Understanding the Variability and Predictability of Seasonal Climates over West and Southern Africa using Climate Models

Kamoru Abiodun Lawal
(LWLKAM001)

Thesis Presented for the Degree of

Doctor of Philosophy (PhD)

Department of Environmental and Geographical Science

Faculty of Science

University of Cape Town

Supervisors:

Dr. Babatunde J. Abiodun and Dr. Dáithí A. Stone

August 2015

Declaration

I, Kamoru Abiodun LAWAL, solemnly declare that this dissertation or thesis is my own work. To the best of my knowledge, it contains neither materials previously written or published by any other person nor materials which have been accepted for the award of any other degree or diploma from the university or other institutions of higher education. However, due acknowledgement has been made in the texts where necessary. I authorize the University to reproduce for the purpose of research either the whole or any portion of the contents in any manner whatsoever.

Parts of the texts of this dissertation include material from a published manuscript in the International Journal of Climatology entitled "Trends in the potential spread of seasonal climate simulations over South Africa". I confirm that the above declaration holds true for this publication too, and authorship of my two supervisors, and the other two co-authors, represents their assistance with improving style and grammar, provision of datasets and advice in managing the paper through the peer-review process.

Signature:..Signed by candidate Date: …… August 28, 2015 …….

Abstract

A good understanding of seasonal climate and the limit to which it can be predicted is crucial in addressing various socio-economic challenges in Africa. However, how to improve the capability of the dynamical models of the climate system in reproducing the regional seasonal climate variability and in replicating the role of various atmospheric circulation anomalies on the regional variability remains a major challenge. Thus far, understanding of seasonal climate over these regions, as well as the ability of climate models to predict them, has focused on the agreement of simulations of dynamical models of the climate system, rather than considering outliers as potentially vital contributors to understanding and predictability. This thesis uses discrepancy in a large ensemble of climate simulations as a tool to investigate variability in dominant seasonal rainfall and temperature patterns (i.e. classes) over West and Southern Africa, to examine the capability of climate models in reproducing the variability, and to study the predictability of the seasonal climates over South Africa.

The dominant classes of variability (of rainfall and maximum temperature fields) in both regions are examined based on the Self-Organizing Map (SOM) classifications. The sequences in which each class occurs cannot be linked simply to a single common index of global scale atmospheric circulation anomalies, implying that the chaotic regional atmospheric circulations that modulate the global scale modes of variability are indispensable. The climate model examined adequately reproduces the dominant classes of seasonal climate over West and Southern Africa. Some simulations perform substantially better and others substantially worse than the average of all the simulations, but the best simulations for a particular region/variable combination may not be exceptional for another region/variable. While identification of the best simulations in an array of simulations can provide substantial improvement over usage of the average of all the simulations, the possibility of misidentifying those simulations poses a serious risk to seasonal forecasting. Over South Africa, significant long-term trends in both observations and measures of the spread of climate model simulations suggest the existence of inter-annual variations in the degree to which a particular year's seasonal climate may be

forecast. Moreover, the year-to-year variations in simulation spread are linearly related to the skill of the model at predicting the seasonal climate for that year, indicating that the ability of dynamical models of the climate system to skillfully predict seasonal climate depends on the ability of the model to capture the real atmospheric trends. The co-variability between the indices of large-scale climate variability and the variations in the spread of atmospheric model simulations over South Africa indicate that all significant predictors of simulation spread over South Africa are of tropical origin.

The study suggests that utilizing dissimilarity in multi-ensemble simulations (multi-analysis ensemble of Global and multi-analysis ensemble of Regional Climate Models) can aid in understanding the variability and predictability of seasonal climate in Africa.

Dedication

To

my Family (Chizoma – my beloved wife and kids – Gbenga, Gbemi and Ope)

and

all Orphans - that refused to bow to harsh realities of life.

Acknowledgments

This doctoral degree (PhD) program is funded by grants from the South African Water Research Commission (WRC: Project K5/2067/1 entitled – "The Limits of Predictability of the South African Seasonal Climate"). Partial funding and assistance was also received from the Applied Centre for Climate and Earth Systems Science (ACCESS). I am sincerely grateful for these gigantic contributions.

I am also grateful to my supervisors for their contributions, guidance, supports and patience. I am specifically thanking them for helping to improve my scientific writing and computational prowess. I appreciate both of them for the freedom of inquiry they afforded me during these tough years. The late-night online meetings and over 2000 e-mails really paid off. Their contributions to a better 'me' are immeasurably immense. Thank you!

The development of CAM5.1 datasets used in this study was funded by the United States Department of Energy (DOE) and it was obtained freely from the Earth System Grid Federation data portal under project "c20c" http://portal.nersc.gov/c20c/data/LBNL/CAM5-1-1degree/All-Hist/est/v1-0/mon/atmos/. I would also like to thank many volunteers who generously ran the weather@home/SAF model simulations on their personal computers.

The Climate System and Analysis Group (CSAG) of the Department of Environmental and Geographical Sciences, University of Cape Town played crucial roles in the successful completion of this work. In this regard, I am grateful to Professor Bruce Hewitson (the director of CSAG), Phillip Mukwena, Sharon Barnard, Vuyo Mafanya, staffs and students of CSAG for their friendliness, scientific discussions, seminars, warmth and logistic supports. I also appreciate the roles played by my extended family members, in-laws, friends (at home, in South Africa and in abroad), and CSAG office mates. You guys are just too great.

Many thanks to the Nigerian Meteorological Agency (NiMet), under the stewardship of Dr. Anthony C. Anuforom (DG / CEO); for giving me the rare opportunity to be a doctorate degree holder and also for approving study-leave with pay in my favour.

The unconditional and lovely supports, prayers and encouragements I received from my family during the course of this work are highly commendable. My sincere thanks my beloved wife (Chizoma) and my great kids (Gbenga, Gbemi and Ope) for their patience, and tolerance of a physically and mentally absent daddy from home and family activities. I love you!

Above all, I give all glory to God – the benevolent and the merciful for His love and protection over my family and me, and for making this thesis a reality. **Thank you God!**

Table of Contents

List of Figures

List of Tables

List of Abbreviations and Acronyms

AAO	Antarctic Oscillation
ACCESS	Applied Centre for Climate and Earth Systems Science
AEJ	African Easterly Jet
AEW	African Easterly Wave
AfDB	African Development Bank
AMIP	Atmospheric Model Inter-comparison Project
AMO	Atlantic Multi-decadal Oscillation
BMU	Best matching unit
CAM3	Community Atmospheric Model version 3
CAM-5.1	Community Atmospheric Model version 5.1
CDC	Center for Disease Control and Prevention
CMIP3	Coupled Model Inter-comparison Project Phase 3
CPDN	Climate*prediction*.net
CRU	Climate Research Unit
CSAG	Climate Systems Analysis Group
CSIR	Council for Scientific and Industrial Research (South African)
DJF	Austral Summer (Boreal Winter)
DOE	Department of Energy (United States)
DWAF	Department of Water and Forestry (South African)
ECMWF	European Centre for Medium-Range Weather Forecasts
ECP	Eastern Cape Province
ENSO	El-Nino Southern Oscillation
FSP	Free State Province
GCM	General Circulation Model or Global Climate Model
GDP	Gross Domestic Product
GGP	Gauteng Province
GHG	Greenhouse Gas
IPCC	Intergovernmental Panel on Climate Change
ITCZ	Inter-Tropical Convergence Zone

ITD	Inter-Tropical Discontinuity
ITF	Inter-Tropical Front
IOD	Indian Ocean Dipole
IPCC	Intergovernmental Panel on Climate Change
JJA	Austral Winter (Boreal Summer)
KZP	KwaZulu Natal Province
LBNL	Lawrence Berkeley National Laboratory
LMP	Limpopo Province
MAM	Austral Autumn (Boreal Spring)
MLP	Mpumalanga Province
MSLP	Mean sea level pressure
NAO	North Atlantic Oscillation
NCAR	National Center for Atmospheric Research
NCEP	National Center for Environmental Predictions
NCP	Northern Cape Province
NiMet	Nigerian Meteorological Agency
NWP	North West Province
PCA	Principal Component Analysis
PSD	Physical Science Division
RCM	Regional Climate Model
RPSS	Ranked Probability Skill Score
rTAI	Reconstructed Tropical Atlantic Index
SAF	Southern Africa
SAM	Southern Annular Mode
SO	Southern-Oscillation
SOM	Self-Organizing Map
SON	Austral Spring (Boreal Autumn)
SPEI	Standardized Precipitation Evapo-transpiration Index
SST	Sea surface temperature
StdDev	Standard deviation

TNA	Tropical Northern Atlantic Index
TSA	Tropical Southern Atlantic Index
TTT	Tropical Temperate Trough
UKMO	UK MetOffice
UNCTAD	United Nation Conference on Trade and Development
UNDESA-PD	United Nations Department of Economic and Social Affairs – Population Division
UNDP	United Nations Development Programme
WCP	Western Cape Province
WHO	World Health Organization
WMO	World Meteorological Organization
WRC	(South African) Water Research Commission
10–90th Percentile Range	The distance between the 90th and 10th percentile values of the ensemble populations

1 Introduction

1.1 Socio-economic Challenges in Africa

African continent is becoming more populous and richer (United Nations Department of Economic and Social Affairs – Population Division (UNDESA-PD), 2013; United Nation Conference on Trade and Development (UNCTAD), 2014). The continent has experienced continuous economic growth for the past three decades (i.e. 1981–2000). As the world's fastest growing continent in terms of economy, the growth rate of its low-income countries is greater than 4.5% in 2012 and it is projected to be greater than 5.5% in the nearest future (African Development Bank (AfDB), 2013). The continent's collective gross domestic product (GDP) per capita has climbed to $953, and about half of African countries (i.e. 26 out of 54) have achieved middle-income status. These economic transformations have opened new developments in the fields of agriculture and food security, infrastructure, economic growth and poverty reduction, water and sanitation, health, environment and clean energy, etc.

However, there have been some economic setbacks. Many countries in the continent are still struggling with numerous development challenges such as high unemployment, environmental degradation, poverty, food insecurity, and natural disasters. The growth rate of the countries' economy does not commensurate with the population's growth rate as the percentage of Africans living on less than US$1 a day also increased from 42% to 46% of the population (United Nations Development Programme (UNDP), 2005; World Bank, 2006). In West and Southern African regions, some of the economic setbacks include unreliable source of livelihood, lack of economic transformation, and low integration of the regions into the continental or global economy (UNCTAD, 2014). Inter-annual variation in seasonal climate has also contributed a major setback to the economy. This is because the majority of the populations in these regions are peasant farmers whose livelihood and economy depend on small scale rain-fed agriculture (Johnston et al., 2004; Omotosho and Abiodun, 2007). The inter-annual variability in seasonal climate makes agricultural planning and production less effective. The influences of the climate variability also extend to other socio-economic activities like

animal and human health, water resources, hydro-energy, natural ecosystems, food security, etc. (Johnston et al., 2004; Intergovernmental Panel on Climate Change (IPCC), 2013). Therefore, the regions are highly susceptible to inter-annual variability in seasonal climate, especially rainfall and temperature (Fauchereau et al., 2003; Collins, 2011; Gbobaniyi et al., 2013).

In view of these, an in-depth understanding and reliable prediction of the inter-annual variability of seasonal climate classifications over West and Southern Africa may help in mitigating the risks of seasonal climate variability on socio-economic activities in Africa. This dissertation will contribute towards achieving that goal.

1.2 The Climate of West Africa

The climate of West Africa (a tropical region located within 20^{o}W-20^{o}E, 0^{o}-25^{o}N) encompasses five major climatic zones, namely: Sub-Tropical Rain Forest (along the Atlantic coast), Tree Savanna, Grass Savanna, Semi-Arid Desert and Arid Desert (in the northern inlands) (Figure 1.1). West African climate can be generalized as having two seasons, the dry season and the rainy season (also known as the monsoon season), resulting from the interactions of two migrating air masses: tropical maritime and tropical continental air masses (Figure 1.2). The dry season, which runs approximately from November to March / April, is characterized by the hot and dry tropical continental air mass of the northern hemispheric high pressure system. The prevailing northeasterly winds bring dry and dusty conditions across the region. The maximum southern extension of this air mass occurs in January between latitudes 5° and 7°N (Figure 1.2). The rainy season is dominated by the moisture laden, tropical maritime or equatorial air mass which produces southwesterly winds. The maximum northern penetration of this wet air mass is in August, averagely between latitudes 19° and 22°N (Figure 1.2). Depending on the climatic region of interest (Figure 1.1), the West African boreal summer rainy season runs, approximately, from April / May to October. At the surface, these two air masses meet at a belt of variable width and stability called the Inter-Tropical Discontinuity (ITD or the Inter-Tropical Convergence Zone (ITCZ) if at upper

level). The north and south migration of ITD and or ITCZ, which follows the apparent movement of the sun, influences the climate of the region (Figure 1.2: Nicholson, 1993; Nicholson and Grist, 2003; Redelsperger et al., 2006; Omotosho, 2007; Omotosho and Abiodun, 2007).

Throughout the year, the climate of West Africa is characterized by uniformly high (near surface) temperatures. Generally, the mean annual temperatures are usually above 18°C (Figure 1.3). On zonal scale, areas within 8° of the equator have a mean annual temperature of about 26°C; between latitudes 8°N and 11°N the mean monthly temperatures can rise to 30°C while beyond these zones the temperatures during the boreal summer seasons can be greater than 45°C during the day. The skies in the inland areas of higher latitudes are usually cloudless as compared to areas close to the coast where skies are cloudier (Collins, 2011; Abiodun et al., 2012; Oguntunde et al., 2012).

However, from year to year, the seasonal climate patterns (spatial seasonal mean of rainfall and temperature) deviate from their long-term averages described above. What makes the patterns deviate from this climatology and to what extent can the deviations be simulated with climate models remain an active area of research. The present study is anticipated to improve knowledge in this area.

1.3 The Climate of Southern Africa

Southern Africa (i.e. 0^o – 55^oE, 40^oS– 0^o) is located south of the equator on the continent of Africa (Figure 1.1). The region is surrounded by Oceans – Atlantic Ocean to the west, Indian Ocean to the east, Antarctic Ocean to the south while northern flanks are land locked (Figure 1.2). Its Climatic zones range from Mediterranean in the southwestern tips, Temperate in the southeastern part, Subtropical in the central zones to Tropical Rain Forest along the equator (Figure 1.2). A small area in the northern parts of the southwest has a desert climate (MacKellar et al., 2006). Most of the region is typified by warm, sunny days and cool nights. Atmospheric temperatures in Southern Africa are more

influenced by variations in orography and ocean currents than by latitude (Kruger and Shongwe, 2004).

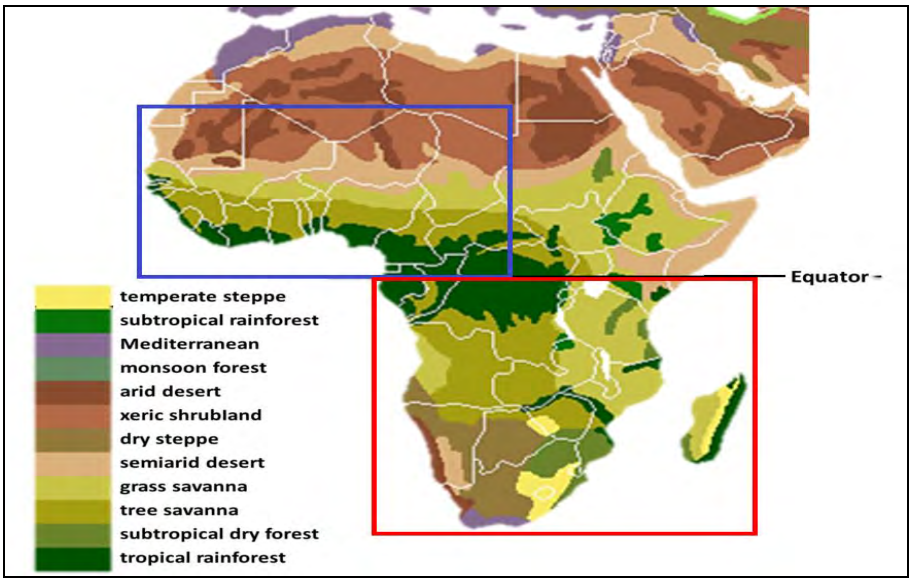

Figure 1.1 The climatic zones of Africa. The blue rectangle indicates the area designated as West Africa, while the red rectangle indicates the area designated as Southern Africa (Source: https://en.wikipedia.org/wiki/Africa#/media/File:Vegetation_Africa.png, with some modifications)

The climate of Southern Africa region is borne out of complex interactions between general circulation, mesoscale and synoptic systems (Tyson, 1987; Buckle, 1996 and Tyson and Preston-Whyte, 2000). Figure 1.4 illustrates some important surface atmospheric circulation over Southern Africa. The region's climate responds to the movements of these synoptic systems. Generally, climatic conditions vary between east and west, largely in response to the warm Agulhas ocean current, which sweeps southward along the Indian Ocean coastline in the east for several months of the year, and the cold Benguela current, which sweeps northward along the Atlantic Ocean coastline in the west (e.g. Chen et al., 2004; Lutjeharms, 2006 and Rouault et al., 2009a). In addition, topography plays more important roles over the region than latitudinal locations (Tyson, 1987).

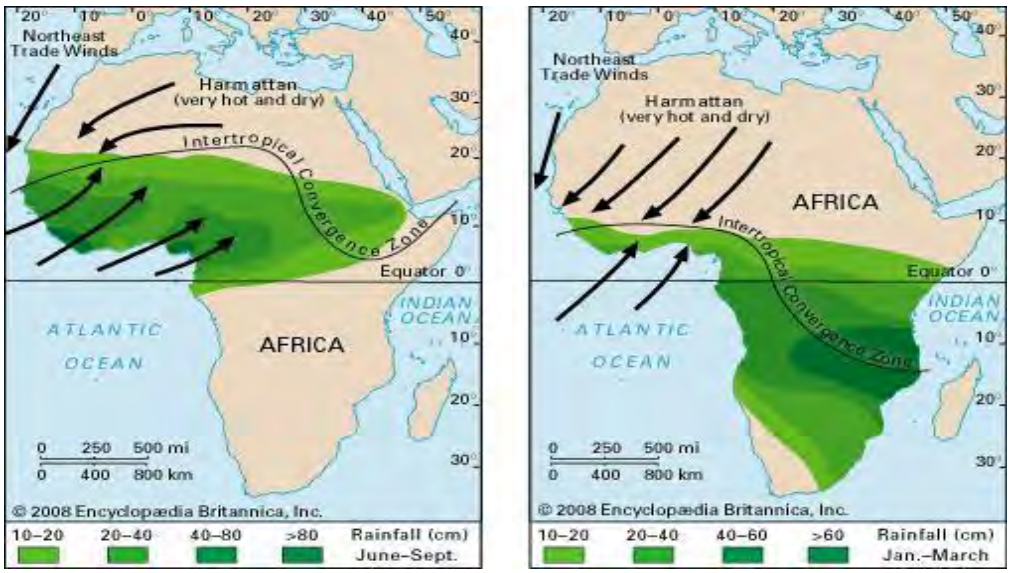

Figure 1.2 Wind and rainfall patterns of West African monsoon during **(left)** the boreal summer and **(right)** the boreal winter. Source: Encyclopedia Britannica via http://global.britannica.com/science/West-African-monsoon

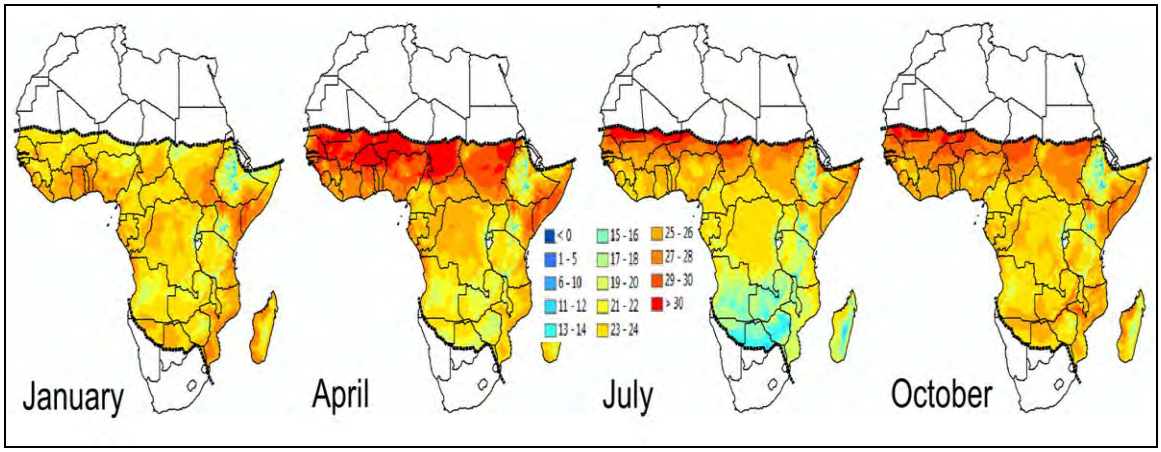

Figure 1.3 The spatial distribution of monthly mean temperatures (^{o}C) over Africa. (Source: https://en.wikipedia.org/wiki/Climate_of_Africa#/media/File:Africa_temperature.png, with some modifications)

Rainfall over Southern Africa is highly seasonal. The peak of the rainy season occurs in austral summers (i.e. the months of December, January and February); except over the south-western corner of the region which is an austral winter (i.e. the months of June,

July and August) rain area. The rainfall has two major gradients (Figure 1.2) – it increases equator ward and from the eastern coast of the region it decreases fairly uniformly westwards (Harrison, 1984). Austral summer rainfall contributes most of the mean annual rainfall over Southern Africa (Preston-Whyte and Tyson, 1988). The rainfall patterns are influenced by several circulation features such as the ITCZ, depressions and associated trough systems, wave interactions between low- and mid-latitude flow, jet streams, anticyclones and associated ridging systems, etc. (Figure 1.4: Lindesay, 1988; Mason and Jury, 1997; Singleton and Reason, 2007; Browne et al., 2009).

The Southern African near-surface air temperature is not as pronounced as the rainfall. Nevertheless, it has distinct variations on seasonal time scales; with austral summer season being the warmest and austral winter the coolest (Figure 1.3; Tyson and Preston-Whyte, 2000). Tropical air masses, as well as rain-bearing clouds which reduce the shortwave radiation reaching the earth's surface, greatly modulate the surface temperature (Hudson and Jones, 2002; Tomczak and Godfrey, 2003). This modulation causes the central parts of the region to experience relatively cooler conditions while the southeastern parts are always warmer. This thesis will also study how classes of seasonal climate (rainfall and temperature) over Southern Africa deviate from their long-term from year to year, why they do so, and how well the deviation can be reproduced by climate models.

1.4 Climate Models

Climate models are tools for simulating climate variability at global, continental and regional scales (Randall et al., 2007; Flato et al., 2013). Climate models use equations of motion that are based on the laws governing the atmosphere to characterize certain properties (e.g. temperature, pressure, moisture content, etc) of the Earth's atmosphere (McGuffie and Henderson-Sellers, 1997). They are usually developed by researchers at climate research centers (e.g. UK Met Office (UKMO)[1], European Centre for Medium-

[1] http://www.metoffice.gov.uk/

Range Weather Forecasts (ECMWF)[2], National Center for Atmospheric Research (NCAR)[3], Climate Systems Analysis Group (CSAG)[4], the Climatic Research Unit[5], etc.). Running these models require supercomputers and the models can be applied seamlessly to any area of the world to produce climate information. Climate models can be regional (regional climate model: RCM) or global (general circulation model or global climate model: GCM).

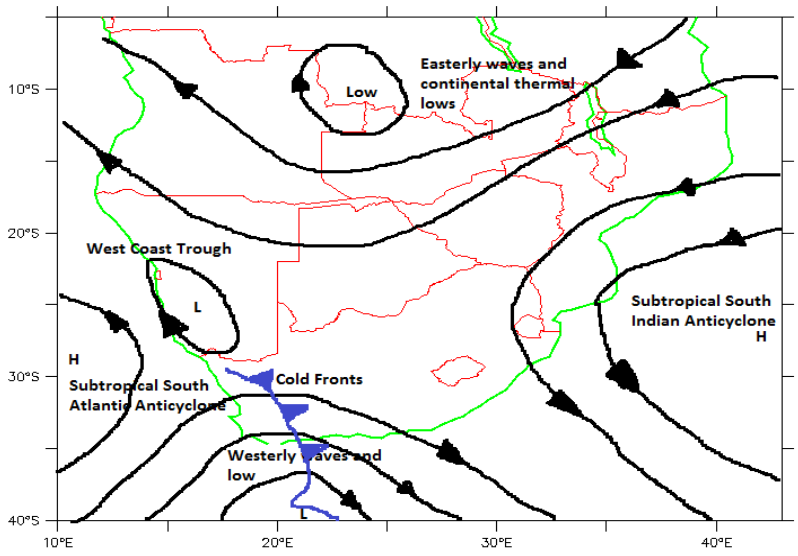

Figure 1.4 Schematic diagrams of important synoptic features of the surface atmospheric circulation over Southern Africa (modified after Tyson & Preston-Whyte, 2000).

1.4.1 General Circulation Model (GCM)

Synonymous with global climate models, GCMs are the tools for simulating climate at global scale (IPCC, 2007 and 2013). They numerically simulate changes in climate as a result of slow changes in some physical parameters (e.g. the greenhouse gas (GHG) concentration) or boundary conditions (e.g. the solar constant, sea surface temperature (SST)). GCMs are the most complex of climate models as they endeavor to represent the

[2] http://www.ecmwf.int/
[3] http://ncar.ucar.edu/
[4] http://www.csag.uct.ac.za/
[5] http://www.cru.uea.ac.uk/cruhome

main mechanisms of the climate system in three dimensional grids over the Earth (New et al., 2000). GCMs provide information on the estimation of large-scale aspects of climate variability, though, with a usually coarse spatial resolution, typically 200km or more (Figure 1.5). Low resolutions contribute to the limitations of GCMs as they prevent GCMs from capturing small scale features that play crucial roles in climate variability and changes (Mitchell and Jones, 2005). For instance, many physical processes such as those related to clouds occur at smaller scales and cannot be properly simulated. Therefore, to represent these small scale features, their known properties are averaged over the larger scale in a technique known as parameterization (Cretat et al., 2012a). This is one source of uncertainty in GCM-based simulations of climate (IPCC, 2007 and 2013). However, newly developed GCMs are more comprehensive as they include more detailed representations of the ocean, land-surface, sea-ice, sulphate and non-sulphate aerosols, the carbon cycle, vegetation dynamics, and atmospheric chemistry, and at finer spatial resolution (Houghton, 2004; Randall et al., 2007; Flato et al., 2013). How well a GCM is able to reproduce the annual variability of the seasonal climate classes over West and Southern is a major focus of this thesis.

1.4.2 Regional Climate Model (RCM)

RCMs are tools for simulating climate change at regional and national levels. In comparison with GCMs, RCMs provide more realistic climate information with finer details because they have higher spatial resolution than GCMs (von Storch et al., 2000; IPCC, 2007 and 2013). RCMs are built in such a way that they can be nested (i.e. made to sit) within a GCM to provide more detailed simulations for a particular location (Figure 1.5: Cocke and LaRow, 2000; Cocke et al., 2007). In this way, information (e.g. GHG and aerosol forcing) of a particular region from a coupled GCM are used as initial conditions, surface boundary conditions, and time-dependent lateral meteorological conditions to drive the RCM. RCMs are usually run over a limited area (Figure 1.5) because they operate at much higher resolution (usually less than 50km); more detailed topographical features (e.g. mountains); more accurate physical parameterizations (Cretat et al., 2012a); and, capture more local extreme climate events (Cocke et al., 2007; Tozuka et al., 2013). However, the qualities of simulations / predictions from a RCM are limited

by the quality of the GCM that drives it. The capability of a RCM in simulating the seasonal climate variability over South Africa will also be discussed in the study.

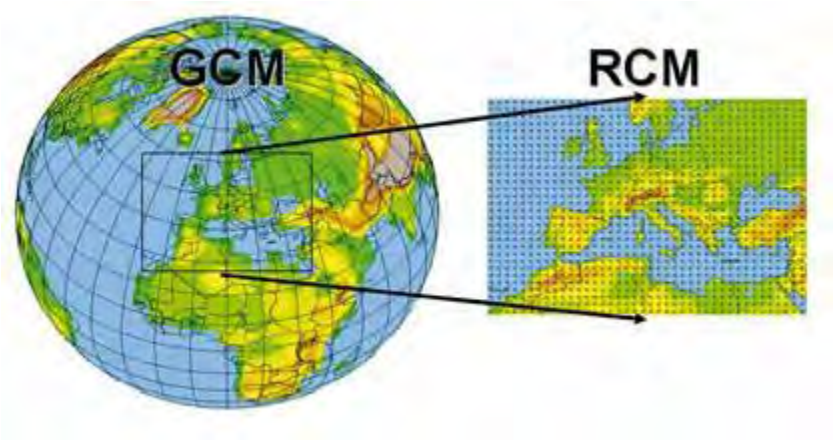

Figure 1.5 Illustration of a nesting approach for RCM that depicts coarse and finer resolutions of GCM and RCM respectively. Source: World Meteorological Organization (WMO: https://www.wmo.int/pages/themes/climate/climate_models.php)

1.5 Seasonal Climate Prediction

A Seasonal climate prediction is a probabilistic statement on the future state of the atmosphere over a season (i.e. 3 months). It is different from weather forecast, which provides a deterministic statement of the atmosphere over a day or two, and not the same as climate changes projection, which provides probabilistic statement on climate condition over a long time (ranging from 20 to 40 years or more). However seasonal climate predictions usually offer the future seasonal climate information as departures from the climatic mean i.e. anomalies. Rainfall and temperature are the main climate variables communicated in seasonal climate forecasts. Seasonal climate predictions in Africa generally relate to the conventional seasons of summer, autumn, winter and spring.

Seasonal Climate predictions usually utilize variety of methods such as dynamical models (Ritchie et al., 1992; Ratnam et al., 2012; Tozuka et al., 2013), statistical methods (Barnston and Ropelewski, 1992), expert judgment (Murphy and Daan, 1984; Stewart and Glantz, 1985) and or combinations of these. Seasonal climate forecasts are generally

expressed in terms of probabilities because of uncertainty in forecasting at long range and also because forecast skill declining at long lead times (Deque and Royer, 1992; Barnston et al., 1994; Landman and Beraki, 2010; Lawal et al., 2014).

Seasonal climate predictions, in West and Southern Africa, are based on expectations obtained from long-term climate trends, shorter-term persistence in the climate system, and the anticipated state of the SSTs (Barnston et al., 1994). Here, the present and future states of the SST anomalies of locally and remotely based oceans are taken into considerations when making seasonal climate predictions (Camberlin et al., 2001; Chen et al., 2004). For instance, during the El Nino-Southern Oscillation (ENSO) event, a natural and periodic phenomenon that can last for up to two years and which occurs whenever the SSTs located across the central and eastern Pacific Ocean are above (for El-Nino, the positive phase of ENSO) or below (for La-Nina, the negative phase of ENSO) average (Camberlin et al., 2001; Mason and Goddard, 2001; Lindesay and Vogel, 1990; Rouault and Richard, 2003; Pohl et al., 2010; Harrison et al., 2014; Zebiak et al., 2014); the chances of West and Southern African sub-regions to experience below normal rainfall and hotter climate are great during El Nino. The situation reverses during La Nina events (Nicholson and Kim, 1997; Landman and Beraki, 2010).

1.5.1 Importance of Seasonal Climate Prediction

The high variability of seasonal climate (i.e. rainfall) from year to year over West and Southern African regions underscores the importance of a timely and reliable prediction of seasonal climate. Timely and reliable prediction of seasonal climate can help reduce the damages caused by extreme climate events. The information from seasonal climate forecasts are needed for planning and risk management in various socio-economic sectors such as agriculture, health, water resources management, environmental management, engineering, etc. (Tenant, 1999; Johnston et al., 2004). Its usefulness also extends to insurance sectors where it assists in the operational task of preparing for major pay-outs. However, a forecast is only useful if it is reliable because a wrong forecast can lead to wrong decisions and can also reduce the trust of the public in using forecast information for planning.

1.5.2 Limits of Seasonal Climate Prediction

However, the skill of seasonal climate forecasts from climate models has limits. This is because a skilful simulation requires (1) a reliable simulation of land surface, ocean and atmospheric interactions (Houghton, 1991; Pennell and Reichler, 2010); (2) knowledge of the initial state of the ocean, the land surface and the atmosphere (Pielke *et al.*, 2006) and (3) knowledge of future changes in boundary conditions, such as the seasonal distribution of solar radiation and variations in chemical composition of the atmosphere (Buckle, 1996; Liniger *et al.*, 2007). The relevance of knowledge of the initial conditions differs between various components of the climate system. The ocean and land surface provide the largest source of skill for seasonal predictions due to the long-time scales of their variations. In contrast to these slow variations, the atmosphere varies rapidly and has a relatively short memory of any initial state. For instance, small perturbations in the state of the atmosphere lead to rapid divergence of future states from the initial state, relative to the timescale of seasonal simulations. This rapid atmospheric departure renders information on the physical state of the atmosphere largely irrelevant; therefore, any predictability must arise from constrains imposed by the slower-varying components of the climate system such as the ocean and variations in land cover (Boer, 2000; Tyson and Preston-Whyte, 2000). The ocean provides the climate with a memory of the system. The memory results in atmospheric deviations that can last for months, or years; because the ocean is highly viscous, it is not mixing rapidly, it is vertically stable (i.e. the heating is at the top), and has a large heat capacity. In view of this, the simulations used in seasonal climate forecasts are conducted with varying initial conditions to scan across multiple possibilities permitted by the relevance of the atmospheric initial state, as well as uncertainty in the ocean and land surface initial states. This method is known as the ensemble forecasting technique[6],[7] (Judd *et al.*, 2007; WMO, 2012).

[6] http://www.metoffice.gov.uk/research/areas/data-assimilation-and-ensembles/ensemble-forecasting/explanation

[7] http://www.wmo.int/pages/prog/www/Documents/1091_en.pdf

1.6 Research Questions, Aims and Objectives

1.6.1 Research Questions

In view of the above, this thesis will investigate the following fundamental questions:

1. What are the dominant classes of seasonal climate (rainfall and temperature) over West and Southern Africa, how do they differ from the long-term climatology, and what controls their year to year occurrence?
2. How well can a GCM simulate the climatology of classes of seasonal climate over West and Southern Africa, their annual and decadal variability, and the associated atmospheric dynamics?
3. What is the theoretical range of forecasts, from a multi-ensemble RCM, for a variety of seasons over South Africa?
4. Does the theoretical range of forecasts from a RCM vary from year to year, and are there long-term trends within these variations? Why?
5. How does predictability of seasonal climate (via ensemble spread) depend on SST?

1.6.2 Aims

This thesis aims are to study the characteristics of dominant classes of seasonal climate (rainfall and temperature) over West and Southern Africa, examine the capabilities of a GCM in reproducing the classifications and the associated atmospheric dynamics, and understand how potential predictability of South African seasonal climate vary from year to year.

1.6.3 Objectives

The objectives of this thesis are to:

- identify and study the characteristics of dominant classes of the spatial distribution of seasonal climate variables (i.e. anomalies of rainfall and maximum air temperature) over the West and Southern Africa.

- evaluate the capability of a GCM in reproducing the dominant classes of seasonal climate, the atmospheric dynamics favouring their occurrence, and their relationship with atmospheric tele-connections.
- estimate the theoretical range of forecasts for a variety of seasons, in the context of a single forecasting model system.
- quantify spreads in seasonal precipitation and temperature over South Africa in a uniquely large ensemble of a RCM simulations.
- examine the co-variability between anomalies of SSTs, large-scale climate indices and variations in the ensemble spread of atmospheric model simulations.

1.7 Thesis Outlines

There are ten chapters in this thesis. After the introduction in **Chapter One**, **Chapter Two** reviews the literature on the past studies while the data and methodology employed by this study are discussed in **Chapter Three**. Presented in the fourth, fifth, sixth and seventh chapter are the evaluations of the capability of a specific multi-ensemble GCM to reproduce the observed characteristics of rainfall and temperature spatial variability (classes) over West and Southern African regions. Specifically, **Chapter Four** examines the ability of the GCM in reproducing the spatial variability of boreal summer (i.e. the months of June, July and August) rainfall over West Africa while **Chapter Five** presents the model's ability to reproduce the spatial variability of near-surface maximum air temperature during the boreal spring (i.e. the months of March, April and May) over the same region. **Chapters Six** and **Seven**, respectively, examine the ability of the GCM in reproducing the spatial variability of rainfall and near-surface maximum air temperature during austral summer (i.e. the months of December, January and February) over Southern African region. **Chapter Eight** examines the spread of ensemble output, from a multi-ensemble RCM run in a hindcast framework, and estimates what the theoretical range of forecasts is for a variety of seasons, in the context of a single forecasting model system, and thus establishes the theoretical limits as to how much we may be able to improve seasonal forecasts. **Chapter Nine** investigates the relative role of SSTs and large scale climate indices as predictors of inter-annual variability of spreads in seasonal

climate. Finally, **Chapter Ten** apart from presenting the summary and conclusions from the findings also discusses the operational applications of the methodology used in this study and provides recommendations for future studies.

2 Literature Review

This chapter reviews the past studies on socio-economic impacts of climate variability in Africa (especially over West and Southern Africa), and the need for better understanding of the spatial variability of climate for mitigation purposes. These are in addition to the descriptions of the documented efforts and the existing knowledge gaps. This chapter also gives an overview of theoretical, statistical, and numerical attempts at investigating the spatio-temporal distribution of climate predictability; as well as the overview of the classification techniques.

2.1 Impacts of Seasonal Climate Variability on West and Southern Africa

Several studies have shown that variability in rainfall and temperature may induce drought (Richard et al., 2001; Lyon, 2009; Sylla et al., 2010), flood (Lindesay and Jury, 1991; Paeth et al., 2010), and heat wave (Robinson, 2001; Lyon, 2009; Fontaine et al., 2013) events. The characteristics (frequency, intensity and duration) of these extreme events are influenced by inter-annual variability in seasonal climate, because their strength may depend on the magnitude of the seasonal climate anomalies (Rouault and Richard, 2003 and 2005; Jones et al., 2008; Nicholson, 2009).

2.1.1 Impacts of Rainfall Variability on West and Southern Africa

Several studies have shown that extremes (excess or deficit) in the inter-annual variations of seasonal rainfall result in environmental, societal, agricultural and economical damages (Makarau and Jury, 1997; Blench, 1999; Hammer et al., 2001; Nicholson, 2001; Keating et al., 2003; Johnston et al., 2004; Paeth et al., 2010) and loss of lives in West Africa. Some studies (Mijindadi and Adegbehin, 1991; Nicholson, 2005; UNDESA-PD, 2013) showed that 60% below-normal seasonal rainfalls that occurred over West Africa in the late 1960s, 1972 and 1980s induced droughts that put the region (with a population of over 300 million people) under the risk of large-scale famine, mass starvation, mal-nutrition and consequently loss of lives. On the other hand, some studies reported that over these regions, heavy rains have induced the flood that rendered thousands of people

homeless (Few, 2003 and 2007), imposed health risks (World Health Organization (WHO), 2008), caused food shortages (Hampshire and Randall, 1999), damaged infrastructure and agricultural products (Tschakert, 2007), etc. Tarhule (2005) and Tschakert et al. (2009) argued that any effort to sustainably increase agricultural production, reduce poverty, enhance food security and livelihoods in West Africa must account for irregularity in the seasonal rainfalls.

Similarly, studies have established that the socio-economic activities in Southern Africa also strongly depend on the seasonal rainfalls over the region (e.g. Jury and Levey, 1993; Unganai, 1994; Hulme et al., 1998; Lindesay, 1998; Rouault and Richard, 2005; Washington and Preston, 2006). For instance, some of these studies showed that the droughts of 1967/1968, 1982/1983, 1991/1992 and early 2000 caused huge economic crisis and resulted in high mortality, while the widespread extreme rainfall of 1974, 1976, 2000/2001 induced floods that destroyed crops and claimed many lives. Assessments from UNDP (2011) showed that, within a season, one particular area of Southern Africa may be experiencing extremely wet conditions while another is experiencing severely dry conditions.

In both West and Southern Africa regions, some rainfall spatial patterns may persist for many years (with its socio-economic impacts), while another pattern may occur only once in many years. Meanwhile, little is known about the atmospheric dynamics that can make a rainfall pattern persist for years or why a pattern easily transits to another pattern in the following year. A good knowledge of this information would enhance the predictability of the seasonal rainfalls and assist in reducing the impacts of seasonal rainfalls on the socio-economic activities of West and Southern African countries. In the present study, we shall study the characteristics of the seasonal rainfall classes, including their frequency, persistence, and transitions.

2.1.2 Impacts of Temperature Variability on West and Southern Africa

Collins (2011) showed that, although in comparison with rainfall variability, temperature variability over West and Southern Africa is low, but these regions are plagued with consistently high temperatures and extreme heat events (i.e. persistently high surface maximum temperatures). It is well documented that extreme heat events exert trauma on human health (WHO, 1998), natural ecosystems (Rutherford et al., 1999; Thompson et al., 2009), water resources and agriculture (Kucharik and Serbin, 2008; Fraser et al., 2013). Bradley (1993) and Kovats and Jendritzky (2006) declare extreme heat events as "silent killers" as they do not leave a trace of devastation in their wake unlike the occurrences of other natural disasters such as hurricanes, earthquakes, floods, etc. Therefore, extreme heat events (proxy for heat wave events) are threats to human lives and properties, especially during summer seasons.

A bio-meteorological study, Tomczyk and Bednorz (2015) showed that persistent high temperature events are the most famous causes of weather-related human deaths worldwide. For example, Center for Disease Control and Prevention (CDC: CDC, 2012) reports that, in the United States of America, extreme heat events are responsible for more human mortality annually than hurricanes, lightning, tornadoes, floods, and earthquakes combined. Robine et al. (2008) estimated more than 70,000 heat related deaths from the catastrophic summer extreme heat event of 2003 in Europe. In Africa, studies have indicated that the frequencies of persistently high temperatures, vis-à-vis extreme heat events, are likely to increase steadily (Robinson, 2001; IPCC, 2007; Lyon, 2009).

Odada and Olago (2005) described West Africa as a unique region because it enjoys varied climates influenced by both northern and southern hemispheric climates; experiences consistently high temperatures; and all countries in the region experience their highest annual near-surface maximum air temperature in boreal spring seasons (i.e. the months of March, April and May: Abiodun et al., 2012; Gbobaniyi et al., 2013; Klutse et al., 2014). Although, studies such as Hulme et al. (2001) and Collins (2011)

have shown that significant changes in temperature observed during the boreal spring season are not as large as those observed during boreal summer and winter seasons, but the impacts associated with high temperatures during spring seasons are surprisingly unpleasant. These impacts cut across some social and economic spheres of lives such as health sectors (Molesworth, 2003; Klutse et al., 2014); agriculture and droughts (Exenberger and Pondorfer, 2011; Waha et al., 2013); risk of civil war (Burke et al., 2009); violent crimes (Anderson et al., 1997); malnutrition (Alfani et al., 2015); etc. Therefore, urgent global and or regional preventive actions to mitigate the socio-economic effects of high temperatures are required. Houghton (2004) argued that if drastic global or regional preventative actions were not taken very soon the upward trends in air temperature are expected to continue for at least some decades.

In West Africa, majority of the influences of high temperatures, as documented by studies, are ecological and health related. For example, Rogers et al. (1996) conclude that high temperatures are the most useful of the predictor variables in the migration of Tsetse Flies[8] across West Africa. Similarly, Klutse et al. (2014) suggest that high temperature is a better predictor of malaria[9] trends than minimum temperature or precipitation. Klutse et al. (2014) further show that the aftermath effects of high temperatures could be more catastrophic than direct effects. They found that maximum air temperature has strong negative correlation with malaria caseloads at zero month lag and significant positive correlations at two- to four-month lags. In addition dehydration, which stresses the cardiovascular system, has been found to be one of the mechanisms underlying high-temperature-related health effects (Flynn et al. 2005; Thornton 2010; Lim et al., 2015). Conversely, Molesworth (2003) and Mera et al. (2014) have shown that one of the good

[8] A blood sucking African fly that transmits sleeping sickness (Ford and Katondo, 1977).
[9] Malaria is a deadly disease caused by sporozoan parasites that are transmitted through the bite of an infected Anopheles mosquito; marked by paroxysms of chills and fever, it accounts for about 90% of the worldwide annual mortality; contributes significantly to the high rates of children and maternal mortality, maternal anemia, low birth-weight, miscarriage and stillbirth; creates significant economic burden on families due to expenditure on malaria treatments, thereby intensifying poverty (Sachs and Malaney, 2002; WHO, 2013).

impacts of high temperature events on socio-economic activities in West Africa is the cessation of the meningitis epidemics during the onset of the wet season, which corresponds to boreal spring season.

Studies have shown that the impacts associated with high temperatures over Southern Africa are also unpleasant. For instance, Thompson et al. (2009) warn that high temperatures, especially during the summers, may likely aid the disappearance of mass of ice on top of Mount Kilimanjaro (coordinates 03°04′S 37°21′E) within few decades. Studies have also shown that the region may witness possible extinction of some species of plants in several nature reserves due to high temperatures (Rutherford et al., 1999). O'Reilly et al. (2003) and Verburg et al. (2003) found that high temperatures are inversely proportional to the oxygen-carrying capacity of water in Lake Tanganyika (coordinates 06°30′S 29°50′E). This may have serious implications on the population of fish in the lake. In addition, there are agreements in the findings of Rasmussen and Collins (1991), Kucharik and Serbin (2008) and Fraser et al. (2013) that high temperatures have the capability to induce droughts, render environments inhabitable and agriculturally unproductive. In the same manner, Bradley (1993), WHO (1998) and Sastry (2002) agree that high temperatures present favorable atmospheric conditions for vectors of both communicable (e.g. cholera and tuberculosis) and non-communicable (e.g. malaria, dengue fever, chronic respiratory and cardiovascular diseases) diseases. Therefore, extreme heat events, vis-à-vis persistently high temperatures, are gateways to devastations.

In spite of all these adversities, attempts to provide operational air temperature forecasts to a variety of end users on seasonal time-scales, in West and Southern Africa, have been less successful than for that of the rainfall forecasts (Mason et al., 1996). Furthermore, studies on the atmospheric processes relating to inter-annual transition of one temperature (spatial) pattern to another are very few. Therefore, good knowledge of this kind of information would enhance the predictability of air temperatures and assist in reducing

the direct and indirect impacts of anomalously high temperatures on the socio-economic activities of West and Southern African countries.

2.2 Factors Influencing the Climate of West and Southern Africa

Several studies (e.g. Thompson and Wallace, 2000; Tyson and Preston-Whyte, 2000; Reason, 2001; Lutjeharms, 2006; MacKellar et al., 2006; Odekunle and Eludoyin, 2008; etc.) have identified some atmospheric processes or phenomena that play major roles in influencing climates of West and Southern Africa. Yarnal (1993) termed these processes or phenomena as atmospheric dynamics and further explain that they determine the changes as well as variability in the climate on seasonal, inter-annual and inter-decadal time-scales. These and many other studies also provide theoretical basis for understanding the mechanisms underlying the linkages between climate and atmospheric dynamics which can either be remote or local. Prominent among the identified atmospheric dynamics are the modulating factors, the feedback processes, atmospheric tele-connections, synoptic scale circulations, etc.

2.2.1 Modulating Factors

Tyson (1987) and Rouault et al. (2009a) explain that modulating factors catalyze the formation of weather and or climate in the areas they are situated. Few examples of modulating factors are natural landmarks or processes such as topography, land cover, ocean currents, etc. Studies have shown that topography mainly inhibits or favors the updrafts of (moist or dry) air parcels (Laing and Fritsch, 2000; Houze, 2004). Numerous studies have also highlighted the fundamental role of topography in the initiation of mesoscale convective systems over Africa (Laing and Fritsch, 1993; Laing et al., 2008); and African rainfalls have been shown to be strongly modulated by the intensity of mesoscale convective systems (Fink and Reiner, 2003). For instance, studies have shown that the contribution of mesoscale convective systems to the annual rainfall amounts is more than 80% in the Sahelian region (Mohr et al., 1999), is about 50% in the Sudanian zone (Omotosho, 1985) while it is between 16% and 32% along the coast of the Gulf of Guinea (Acheampong, 1982; Omotosho, 1985). In Southern Africa, topography has been

shown to play more important roles in the modification of climate than latitudinal locations (Tyson, 1987). Similarly, studies like Chen et al. (2004), Lutjeharms (2006) and Rouault et al. (2009a) have been able to show that Ocean currents do greatly modify the climatic conditions of Southern Africa by supplying moisture to the atmosphere.

2.2.2 Feedback Processes

According to Tyson and Preston-Whyte (2000) climate feedback occurs when an initial change in the climate system starts a process that either strengthens or weakens the initial change. Buckle (1996) and IPCC (2007) identified evaporation, dust, soil moisture, biogenic emissions, water vapor and clouds as parts of many feedback mechanisms in the climate system that can either strengthen (positive feedback) or weaken (negative feedback) changes in the Earth's climate. Take clouds as example, studies (e.g. Vardavas and Taylor, 2011; Pyrina et al., 2013; Ohunakin et al., 2015) have shown that clouds can strengthen or weaken warming because they are effective at absorbing infrared radiation emitted from the Earth; and that they are capable of re-radiating that long-wave energy (heat) back to the ground and consequently exert a large greenhouse effect, thereby warming the Earth. These studies also show that clouds can reflect incoming solar energy, thereby cooling the Earth. Therefore, the climatic feedback involving clouds can either be positive or negative depending on the circumstances.

2.2.3 Atmospheric Tele-connection (Climate Indices)

Buckle (1996) describes atmospheric tele-connection as that process which provides linkages between what is happening in one geographical location to what is happening somewhere else. Camberlin et al. (2001), Manhique et al. (2009), Diatta and Fink (2014), Martin and Thorncroft (2014), and many others have shown that the climate of West and Southern Africa, on spatial and temporal scales, do respond to variations in temperature anomalies over locally and remotely based oceans; and that the climate also respond to normalized pressure differences between some remotely located meteorological stations. Studies describe tele-connections in terms of climate indices such as ENSO (positive and negative phases of which are respectively known as El-Nino and La-Nina: Harrison et al., 2014; Zebiak et al., 2014; Landman and Beraki, 2010; Lindesay and Vogel, 1990;

Nicholson and Kim, 1997), Antarctic Oscillation (AAO: Thompson and Wallace, 2000), Indian Ocean Dipole (IOD: Izumo et al., 2010), etc. Some of these climate indices have been found to play crucial roles in determining seasonal and inter-annual climate variability over West and Southern Africa. For instance, it has been documented that ENSO, among other climate indices, is the most important source of seasonal and inter-annual climate variability in the tropical regions where the majority of the landmass of West and Southern Africa lie (Latif and Grotzner, 2000; Camberlin et al., 2001; Mason and Goddard, 2001; Rouault and Richard, 2003). Camberlin et al. (2001), Latif and Grotzner (2000) and several other studies have shown that West Africa experience abnormally wet and cold climate, during the boreal summer, especially when the sea surface temperatures (SSTs) located across the central and eastern Pacific Ocean is below-average (panels a and b of Figures 2.1 and 2.2). Studies have also shown that above (below)-average SSTs located across the central and eastern Pacific Ocean (Figure 2.1a, b) do modulate abnormally dry (wet) and warm (cold) austral summer (i.e. boreal winter) season over Southern Africa (e.g. Camberlin et al., 2001; Mason and Goddard, 2001; Rouault and Richard, 2003; Pohl et al., 2010: Figure 2.2c, d). In spite of the overbearing influence of ENSO on seasonal climate of West and Southern Africa, studies have shown that ENSO, in most cases, do act in concomitance with other climate indices (Lyon and Mason, 2007; Ujeneza and Abiodun, 2014). It is therefore important to know which of the climate (e.g. rainfall and temperature) spatial patterns are associated to which climate index or indices and hence, can be predicted using such climate index or combination of climate indices as predictor.

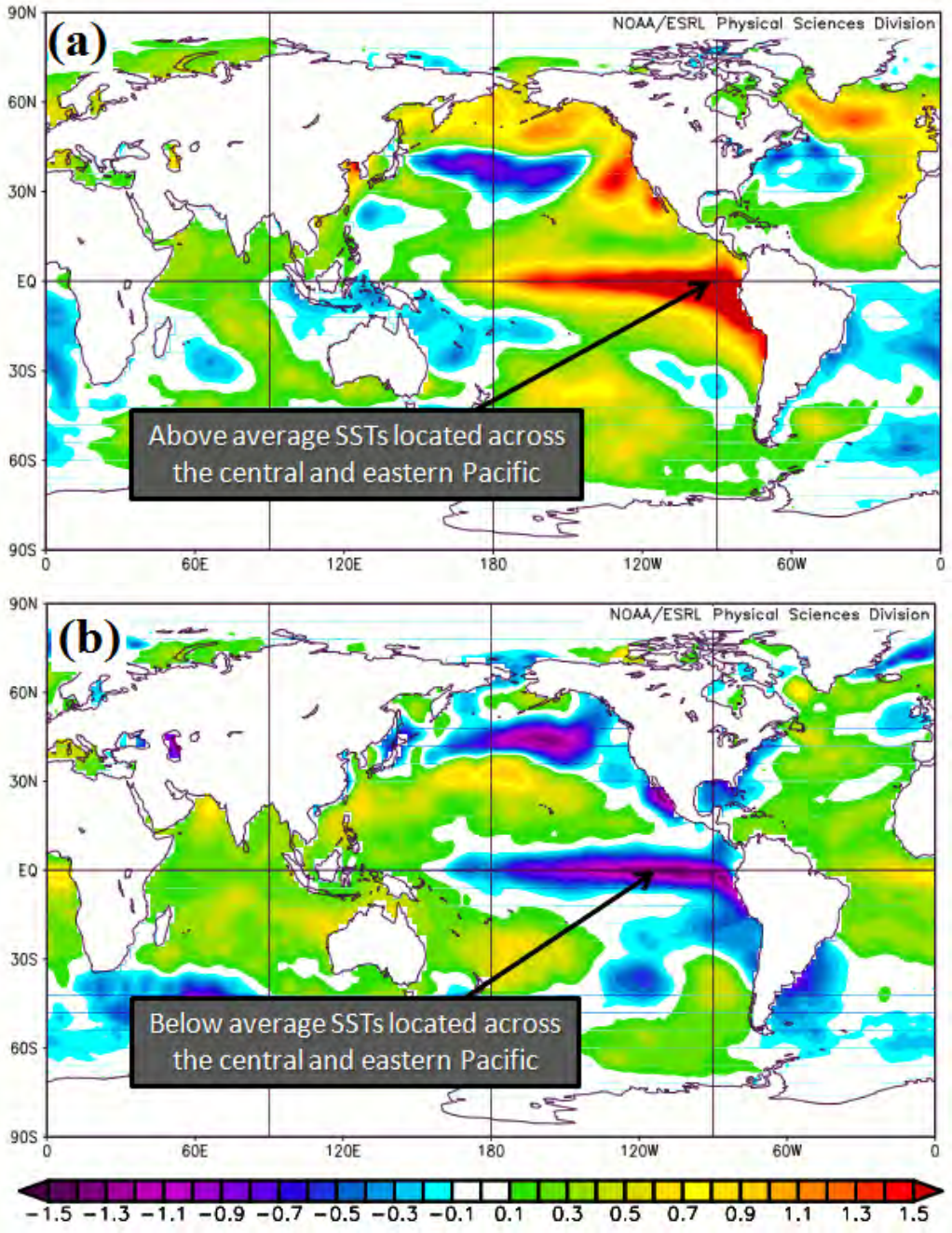

Figure 2.1 Global maps of SST (anomalies) depicting **(a)** the positive phase of ENSO (El-Nino) and **(b)** the negative phase of ENSO (La-Nina). Source: The website of State Climate Office of North Carolina (http://nc-climate.ncsu.edu/climate/patterns/ENSO .html)

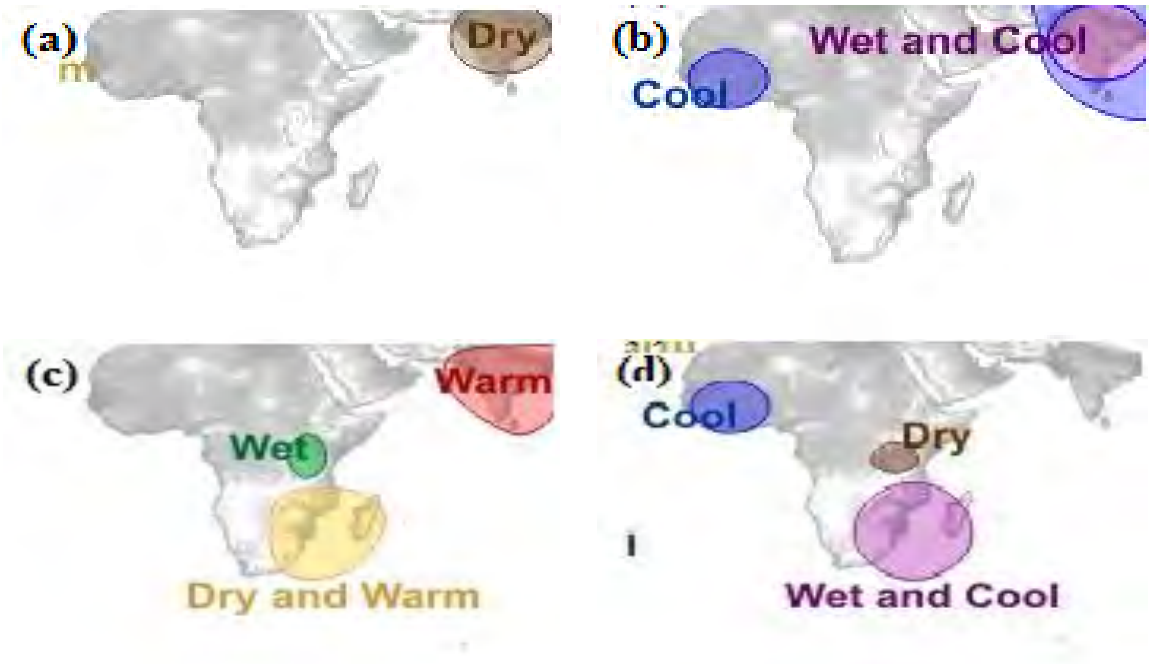

Figure 2.2 Illustrations of the typical effects of **(left column)** El-Nino and **(right column)** La-Nina events on the seasonal climate of Africa during **(top row)** the boreal summer (i.e. the months of June, July and August) and **(bottom row)** the boreal winter (i.e. the months of December, January and February). Source: The website of State Climate Office of North Carolina (http://nc-climate.ncsu.edu/climate/patterns/ENSO.html), with some modifications.

2.2.4 Synoptic Scale Circulations

According to Achberger et al. (2006), Chen et al. (2006), Carleton et al. (2008), Cavazos (1999) and many other studies, synoptic scale circulations govern variations in local climates (rainfall and temperature) and they have strong impacts on surface distribution, vis-à-vis variability, of all climate variables. Documented examples of synoptic scale circulations are tropical high pressure systems over Atlantic and South Indian Oceans (Figure 1.4; Buckle, 1996; Tyson and Preston-Whyte, 2000), Tropical Temperate Trough (TTT: Figure 1.4; Jury and Pathack, 1993; Todd and Washington, 1999), African Easterly Jet (AEJ: Figure 2.3; Fontaine and Janicot, 1992; Grist and Nicholson, 2001), ITD or ITCZ (Figures 1.2 and 2.3: Omotosho, 1985; Nicholson, 1993 and 2009; Sultan and Janicot, 2000; Sultan and Janicot, 2003; Zhang et al, 2006), African Easterly Waves

(AEW: Figure 2.3; Diedhiou et al., 1998 and 1999; Fink and Reiner, 2003; Mathon et al., 2002), etc.

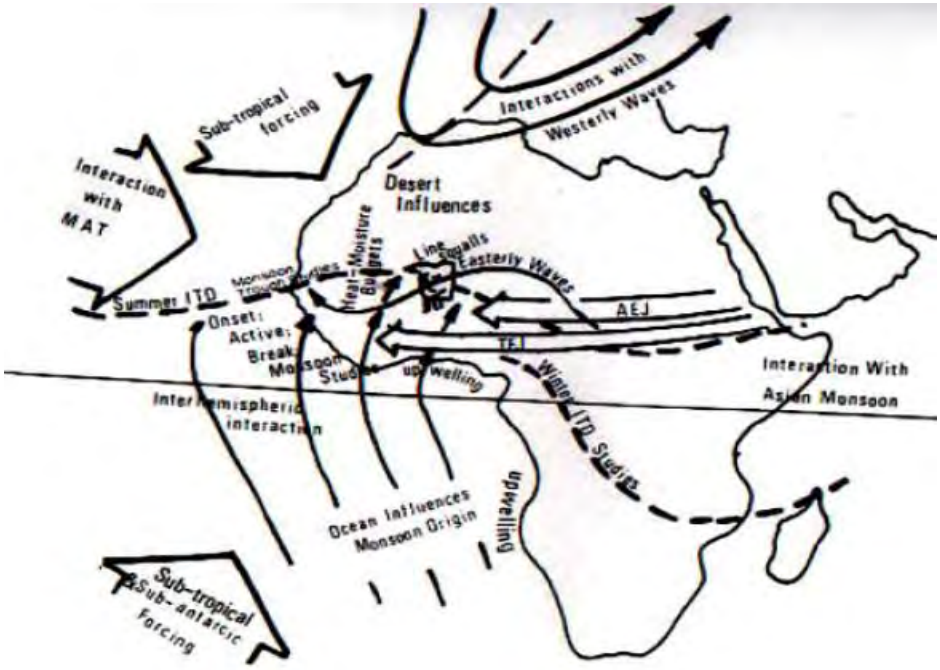

Figure 2.3 A sketch of the dynamics of the West Africa weather systems. Source: Proceedings of the Pre-WAMEX (West African Monsoon Experiment) Symposium on the West African Monsoon, Ibadan, Nigeria 1-3 November, 1978; with some modifications.

Over West Africa, synoptic scale circulation anomalies representing strong upward vertical motion have been shown to accompany positive precipitation composite field (Nicholson and Kim, 1997). However, Newton et al. (2012) have shown that tele-connections also have some influences on surface climate through modifications of synoptic scale circulations. For example, Reason et al. (2000) showed that the ascending and descending branch of the Walker circulation is found over the African continent (most especially over central Indian Ocean) during La-Nina and El-Nino phases respectively. These either strengthen or weaken the sub-tropical high pressure system (an important rain producing mechanism) located over the Indian Ocean (Figure 1.4). Since ENSO has been shown to be inconsistent in the modulation of climate variability (Reason and Jagadheesha, 2005), it is therefore important that further studies on climate

variability over West and Southern Africa should rather focus on changes in atmospheric synoptic scale circulations rather than a tele-connection-related climate variability. This may yield a better understanding of the relative influences of atmospheric dynamics on West and Southern African climate (e.g. rainfall and temperature) variability and could improve forecasting ability over the regions. These would be examined in this study.

2.3 Challenges in Simulating the Variability of Seasonal Climates over West and Southern Africa

Parts of the fundamental challenges facing seasonal climate prediction over West and Southern Africa have been mentioned in Section 1.5.2 of this thesis. Apart from these more of the difficulties encountered in simulating and or forecast of seasonal climate over West and Southern Africa have been highlighted by many studies. Hansen et al. (2011), while reviewing seasonal climate forecasting for agriculture in sub-Saharan Africa, mention that forecast errors, from climate model simulations, grow faster in the tropical region (where majority of West and Southern Africa lie) than in the mid-latitudes; and that poor density of data from equally sparse meteorological observation stations make the challenges worse than thought – unavailability of data for initialization and inability of some countries within these regions to issue seasonal climate forecasts due to financial problems. Furthermore, Harrison (2005), Mason (2008) and Troccoli (2010) hinted that most of the national meteorological and hydrological services in these regions are having serious man-power development issues. Seasonal climate forecasts, if and when are issued at national levels, are not properly disseminated through various channels to the end-users.

Tennant (1999) mentioned the complexity of prediction algorithms on seasonal time-scale, which has to take initial and boundary conditions into consideration, as one of the problems. Barnston et al. (1994) iterated that the degree of complexity, which though provides the platforms for the amount of progress made in forecasting at seasonal time-scale, makes seasonal climate predictions to continue to have lesser skill in comparison to short-range predictions.

Complications in the atmospheric dynamics of West and Southern Africa have been identified by Dike et al. (2015) as another challenge facing the prediction of seasonal climate over these regions. They stated that climate variability over these regions are explained in terms of range of natural conditions such as the connections of SST anomalies to climate indices that are known to play vital roles in modification of seasonal and inter-annual climates. Meanwhile, Held et al. (2005) and many other studies have iterated the inconsistencies inherent in the use of SSTs anomalies in line with its connections to climate indices. For instance, Nnamchi et al. (2013) noted that the apparently well-known relationships between SST anomalies, climate indices and climate variability are still poorly understood. Dike et al. (2015) concluded that many climate indices, in conjunction with continental and extra-continental circulations, including severely complicated internal conditions, are evidently in action.

Guichard et al. (2004) and Sohne et al. (2008) focused on quasi-ability of climate models to represent the true characteristics of the tropical atmosphere as another form of challenges facing seasonal climate prediction over West and Southern Africa. They noted the deficiency of GCMs in capturing the magnitude and phase of deep convection over land as a strong issue because GCMs tend to simulate the onset of convective rainfall earlier than observed. In addition to these, Lebel et al. (2000) suggest fundamental shortcomings of the climate models in the parameterization of the surface, radiative, boundary layer, cloud, and convective processes as another form of challenges. Therefore, uncertainties in local forcings and feedbacks, according to Hegerl et al. (2007), also make it difficult to estimate the contribution of greenhouse gas increases to the observed seasonal climate variability changes.

Friederichs and Paeth (2006) show that the exposure of West and Southern African regions to large expanse of oceanic surfaces makes them prone to different ocean characteristics as air masses with significantly different properties dominate around the coasts of the regions during various seasons of the year. Though, research documents

show that seasonal climate predictions over these regions are derived from tropical and subtropical SST anomalies (Barnston et al. 1994), but climate models, especially the GCMs, are probably not able to reproduce some nonlinear aspects of the atmospheric response to SST. The brilliant idea of using ensemble averaging, also, is not able to enhance the signal-to-noise in the predictor variables (Friederichs and Paeth, 2006). Therefore, climate model output is subject to systematic errors.

Nevertheless, Blench (1999) has declared that, in spite of these challenges, there are potentials for West and Southern African countries to substantially increase the use of information from seasonal climate prediction in planning in order to reduce the threat of climate variability and change to the achievement of development goals. Evidently, ability to predict climate variability on a seasonal time-scale will help the population of the regions to manage and cope with seasonal changes of climate that usually occur in the regions. This will lead to improvement of livelihoods and protection of farmlands against the long-term consequences of adverse extremes.

2.4 Spatial Variability of Rainfall over West Africa

Over the years progress has been made in documenting the spatial variability of West African rainfall. Prominent among this progress are Fontaine et al. (1995), Fontaine and Janicot (1996), Nicholson and Webster (2007) and Nicholson (2009). These studies found two spatial classes of summer rainfall patterns: a north–south dichotomy pattern where rainfall anomalies of opposite signs prevail in equatorial and subtropical sectors (i.e. the semi-arid Sahel zone and the humid Guinea Coast further south: e.g. Sahelian Flood – Guinean drought, and vice versa) and anomalies of same sign across the entire region (i.e. large drought or flood patterns); making a total of four basic spatial classes of boreal summer rainfall.

In order to better understand the complications and irregularities in the distributions of rainfall over West Africa, investigations were also carried out on the regional atmospheric circulations that produce these spatial classes of rainfall anomalies. For

example, Fontaine et al. (1995) utilized a 32-year record, at inter-annual time step, of mean August upper tropospheric wind data to investigate the relationships between the West African rainfall anomaly patterns and tropospheric wind changes in August – the peak of monsoon. They defined wind indexes for differentiating the rainfall patterns. Fontaine and Janicot (1996) examined the sea surface temperature (SST) fields that are associated with West African rainfall anomaly types and found that SST patterns greatly modulate the rainfall-producing systems of West Africa. With the use of observed precipitation and NCEP Reanalysis datasets, Nicholson and Webster (2007) suggest that it is the inertial instability that controls the physical location of the rain belt over the Sahel during the boreal summer. They further show that the criteria for inertial instability are satisfied in wet summers but not in dry ones. Nicholson and Webster (2007) later identified the surface pressure gradient between the continent and the equatorial Atlantic as the major determinant of the inertial instability and that when the gradient is large the inertial instability results in the development of a low-level westerly jet. Nicholson (2009) studied cases of a wet and a dry year respectively in August of 1955 and 1983 over West Africa and found results that are similar to those of Fontaine et al. (1995). Many of these and some unmentioned studies have demonstrated various characteristics of rainfall during wet and dry years. These studies also attempt to identify the underlying causes of rainfall spatial variability which has been identified as the most relevant aspects of rainfall variability in West Africa (Nicholson, 1986). However, no studies have investigated the capability of a GCM to reproduce the spatial variability of the dominant rainfall classes as presented in this thesis. Therefore, it is not yet known which of the spatial classes can a GCM simulate well and or cannot adequately simulate. This present study will use a multi-ensemble GCM to investigate this knowledge gap.

Previous studies that applied GCMs over West Africa have discussed the skill of GCMs in simulating and or predicting rainfall over the region. For example, Abiodun et al. (2011) have established the capability of some GCMs in reproducing the spatial distributions of rainfall over West Africa. Evidences suggest that the skill of GCMs in simulating present-day climate is high; that the ability of models to simulate past changes

in climate changes that have already occurred is high; and, that a comparison of simulated and observed present-day climates shows good agreement for many basic atmospheric variables (Hulme et al., 1998; Landman and Beraki, 2010; Gbobaniyi, et al., 2013). In addition, there have been great improvements in the development and applications of GCMs to seasonal climate simulation or forecasting of rainfall variability over West Africa (Folland et al., 1991; Stockdale et al., 1998; Washington and Downing, 1999). Therefore, assessing GCM simulations using spatial distributions of rainfall over West Africa may aid in identifying those rainfall classes GCMs can simulate well and those they cannot simulate adequately.

2.5 Spatial Variability of (High) Temperatures over West Africa

Apart from the knowledge of north-south temperature gradients and the heat lows (Lavaysse et al., 2010), tangible investigation that has been made concerning the spatial variability of West African (maximum) air temperatures during its annual peak periods – the boreal spring seasons, are very few. Among these few studies are Sultan and Janicot (2003). They investigated the atmospheric circulation changes associated with the summer monsoon onset over West Africa. They attributed the controls of the atmospheric circulations in the low and mid-levels to the heat low dynamics associated with the Inter-Tropical Front (ITF). They found that the meridional circulation intensity of the heat low is highest during this season.

Attempts to aid mitigation efforts for the climate-sensitive epidemics also motivated few studies over West Africa during the boreal spring season (e.g. Seefeldt et al., 2012; Mera et al., 2014). Both studies recognize the critical role of high humidity, resulting from moisture influx, in ending meningitis epidemic outbreaks. Based on these, Molesworth et al. (2003) and Dukic et al. (2012) showed that knowledge of moisture distribution during the spring could aid the mitigation of meningitis by identifying areas where epidemics will end naturally, so that scarce vaccines can be moved elsewhere. The studies hinted that a feedback process may be the mechanism linking temperatures and cessations of

meningitis epidemic. They however failed to take into cognizance the roles played by surface temperature gradients, vis-à-vis extreme heat events, in the initiation and intensification of synoptic disturbances that brought about the increase in relative humidity.

Studies have also utilized the connections between surface temperature distributions and atmospheric tele-connection mechanisms on regional and global scales; and that this effect is greatest in the tropical regions. For example, Halpert and Ropelewski (1992) demonstrated that Southern-Oscillation (SO), an atmospheric tele-connection mechanism, influences surface temperature patterns in West Africa. Here, surface temperatures are always above normal during the positive phases of SO, and vice versa. Interestingly, they also found that surface air temperature anomalies, in West Africa, are always of the same sign as the local SST anomalies and concluded that this is an indication of delayed response to the warming or cooling of equatorial SSTs in the tropical Pacific. Nevertheless, studies have shown that utilization of atmospheric tele-connection mechanisms to determine spatial distributions of climate parameters such as surface temperature has low reliability (Lyon and Mason, 2007 and 2009).

In spite of the economic importance of persistently high temperatures (see Section 2.1.2), studies on the capability of GCMs to reproduce the spatial classes of near-surface maximum air temperatures over West African region are very scarce, if at all they exist. In addition, studies on the atmospheric processes relating to inter-annual transition and or persistence of a temperature (spatial) pattern to another seem indescribable. Good knowledge of these kinds of information would enhance the predictability of air temperatures and also avail us the opportunity to identify temperature classes that GCMs can simulate adequately, those they can simulate moderately and those they cannot simulate at all. That is one of the aims of this study.

2.6 Spatial Variability of Rainfall over Southern Africa

Some studies have used ENSO to classify and or predict rainfall spatial patterns over Southern Africa (e.g. Harrison et al., 2014; Zebiak et al., 2014; Landman and Beraki, 2010; Lindesay and Vogel, 1990; Mason and Goddard, 2001; Rouault and Richard 2003). These studies found that during the positive phase of ENSO (El-Nino event) below normal summer rainfall always occurs over the southeastern (i.e. south of 10^{o}S) part of Southern Africa, and during the negative phase (La-Nina event) above normal summer rainfall usually occurs over the area. On the other hand, some studies have found that not all El-Nino events feature a below normal rainfall over this area, and not all La-Nina events induce above normal rainfall over the area (e.g. Reason et al., 2005; Reason and Jagadheesha, 2005; Lyon and Mason, 2007 and 2009). For instance, Reason et al. (2005), Reason and Jagadheesha (2005) and Lyon and Mason (2007 and 2009) documented the relatively weak 1991/1992 and 2002/2003 El-Ninos and 1997/1998 El-Nino episode, which was one of the strongest events on record in terms of the Southern Oscillation Index and SST anomalies in the tropical Pacific. They also document the relatively weak 1995/1996 and 1999/2000 La-Nina events. The weak El-Ninos reportedly were associated with widespread and severe summer drought across large areas of Southern Africa whereas dry conditions were less intense during the 1997/1998 strong El-Nino. Similarly, the relatively weak 1995/1996 La-Nina event led to significant wet anomalies across the southeastern and Congo basin regions of Southern Africa but many tropical areas of the subcontinent had less than average rainfall; while by comparison, the 1999/2000 event had much more widespread positive rainfall anomalies.

Other studies, e.g. Lyon and Mason (2007) and Ujeneza and Abiodun (2014), have argued that ENSO is not the only atmospheric tele-connection (i.e. climate index) that modulates the spatial variability, vis-à-vis patterns, of rainfall over Southern African. They however identified other climate indices that also play crucial roles in the summer rainfall spatial patterns. These climate indices include the AAO, IOD, the Tropical Southern Atlantic (TSA; Enfield et al., 1999), etc. The rainfall over the southeastern parts of Southern Africa has also been linked to the SST over the South Indian Ocean (i.e.

south of Madagascar), such that positive anomalies in the SST produce above normal rainfall over the southeastern parts of Southern Africa, and vice versa (Reason, 2001; Hansingo and Reason, 2008; Manhique et al., 2009; Reason, 2002). In addition, the rainfall over Angola, and over the west and central parts of Southern Africa, has been shown to depend on SST over the South Atlantic Ocean (i.e. the Benguela El-Nino; Williams et al., 2008; Rouault et al., 2009a, b; Grimm and Reason, 2011). Rainfall over the Republic of South Africa is significantly correlated with the AAO index (also known as Southern Annular Mode, SAM; Pohl et al., 2010). Therefore, ENSO alone may not be sufficient in classifying the rainfall spatial patterns over Southern Africa. Two reasons are suspected: firstly the occurrence of other tele-connections are not limited to the neutral phase of ENSO and, lastly the co-occurrence of strong phases of ENSO and other tele-connections may strengthen or weaken the influence of ENSO on rainfall spatial patterns over Southern Africa. Hence, using the rainfall spatial distributions, instead of ENSO, to classify the rainfall spatial patterns may give a broader and more robust classification.

Some studies have also used daily spatial distribution of some atmospheric variables to classify rainfall over Southern Africa, but none of them have used seasonal rainfall distribution. For instances, Fauchereau et al., (2009), Pohl et al. (2009) and Manhique et al. (2009) applied cluster analysis on daily out-going long-wave radiation anomalies (as a proxy for convective rainfall anomalies) to obtain classes of daily organized large-scale convection. Cretat et al. (2012b) also applied cluster analysis on daily rainfall over South Africa in summer to generate six classes, and studied the role of atmospheric circulations on each class. However, the classification of daily rainfall patterns obtained in these studies may not be a good representation for summer-season-mean rainfall classes.

Recently, Ujeneza and Abiodun (2014) applied the principal component analysis (PCA) to the standardized precipitation evapo-transpiration index (SPEI) to obtain four seasonal drought classes (called regimes) over Southern Africa and showed how various climate indices jointly influence each drought regime. Since SPEI used in Ujeneza and Abiodun

(2014) combined rainfall and temperature data, the characteristics of seasonal SPEI classes discussed in the study may differ from the spatial classes of seasonal rainfall. In addition, the PCA analysis used in the study accounted for only 50% of the drought classes. There is therefore need to spatially classify the summer rainfall using a more robust technique, like the Self Organizing Maps algorithm (SOMs) which will account for all the variability in the summer rainfall distribution. The present study adopts SOM (to be described later) in the spatial classification of seasonal rainfall.

Many studies have established the capability of some GCMs in reproducing the spatial distributions of rainfall over Southern Africa (e.g. Landman and Beraki, 2010; Engelbrecht et al., 2013; Klutse et al., 2015; etc.). For instance, Klutse et al. (2015) showed that the Hadley Centre Atmospheric Model (version 3) and the Community Atmospheric Model (version 3) give realistic simulations of rainfall producing features over Southern Africa. Landman and Beraki (2010) demonstrated the reliability of using multi-model ensemble simulations from the European Centre for Medium-Range Weather Forecasts (ECMWF), Meteo-France, and UK Met Office (UKMO) to predict the rainfall patterns over the region. These studies showed that while these GCMs have some skill in simulating summer rainfall patterns during ENSO years, the models, nevertheless, have no skill in simulating rainfall patterns during the neutral years. In addition, the studies also found that the GCMs can misrepresent the rainfall patterns in some ENSO years, especially when other factors alter the influence of the ENSO events on the rainfall pattern. For example, a multi-GCM ensemble forecasting system simulated below-normal summer rainfall instead of the above-normal summer rainfall that was experienced over Southern Africa during the El-Nino events of 1997/1998 and 2009/2010 (Richard et al., 2001; Landman and Beraki, 2010). Therefore, evaluating the GCM simulations using a classification of rainfall patterns that is based on the rainfall fields (rather than ENSO phases) may help identify the rainfall classes GCMs can adequately simulate, moderately simulate and those they will poorly simulate. Such knowledge can help improve understanding of how to interpret GCM output, as well as offer feed back to model development in order to improve the performance of GCMs over Southern Africa.

2.7 Spatial Variability of (High) Temperatures over Southern Africa

Hitherto, seasonal predictions of temperature variability (patterns) over Southern Africa have been based on ENSO events. Studies have shown that summer air temperatures are significantly cooler during La-Nina events than during El-Nino events over this region[10], [11] (Jury and Pathack, 1993; Raphael, 2003; Arblaster and Alexander, 2012). The theory behind this is that large scale climatic anomalies, which last for few months, are most likely to be a result of persistent large scale anomalies in the ocean-atmosphere behaviors (Rouault and Richard, 2005; Sheffield et al., 2009). These attract monitoring of ENSO events, as well as other tropical SST anomalies by the climate monitoring centers. However, studies have shown that it is not all La-Nina events that present significantly cooler temperatures and vice versa (Reason et al., 2005; Reason and Jagadheesha, 2005; Lyon and Mason, 2007 and 2009). In addition, ENSO events are not the only atmospheric tele-connection or climate indices that influence or modify Southern African climates (Lyon and Mason, 2007; Ujeneza and Abiodun, 2014). Studies such as Washington and Preston (2006) and Hansingo and Reason (2008) have shown that large scale advections of moistures from Atlantic and Indian Oceans (the main sources of moisture for the region) contribute greatly to influence or modulate summer climates, and by extension maximum air temperatures. In view of these, this study will classify the observed summer maximum air temperature anomaly patterns into spatial classes without any recourse to ENSO. The study will evaluate the capability of a GCM at reproducing the spatial classes of maximum air temperature anomalies (as proxy for high temperatures).

GCMs have proven to be capable of reproducing many important elements of observed temperatures, but with some limitations. For example, Lyon (2009) used observed daily maximum air temperature and their corresponding fields from three coupled models from the Coupled Model Inter-comparison Project Phase 3 (CMIP3) to examine the behavior

[10] http://edmc1.dwaf.gov.za/library/Limpopo/Chapter2/Page17/Chapter2Page17.htm
[11] http://www.grida.no/publications/vg/africa/page/3106.aspx

of heat waves; and found that onshore flows are associated with fewer heat waves while land trajectories are associated with several heat wave events over South Africa. Lyon (2009) however found that these processes are not well represented in low-resolution CMIP3 models. Recently, Lazenby et al. (2014) found that a coupled GCM predicts temperatures skillfully, only, when there is a high likelihood of experiencing extremely high air temperature during mid to late summer over Southern Africa. This is therefore bias on the part of the GCM used in that study. Conversely, studies have established the capability of some GCMs in simulating the spatial distributions of climate variables over Southern Africa with great confidence and reliability (e.g. Tadross et al., 2005; Hewitson and Crane, 2006; Browne et al., 2009; Landman and Beraki, 2010; Browne, 2011; Engelbrecht et al., 2013). Furthermore, newly developed GCMs are more comprehensive as they include more detailed representations of the ocean, land-surface, sea-ice, sulphate and non-sulphate aerosols, the carbon cycle, vegetation dynamics, and atmospheric chemistry, and at finer spatial resolution (Houghton, 2004; Randall et al., 2007; Flato et al., 2013). Therefore, using a GCM may be useful to simulate and classify summer maximum air temperature based on its spatial distributions, without recourse to ENSO or any phases of climate indices. The goal here is to identify classes of summer maximum air temperature that GCMs can simulate adequately, moderately and poorly.

2.8 How to Quantify Predictability of Seasonal Climate

There are many efforts on how to quantify the extent to which seasonal climates are predictable. For instance, Rowell (1998), Kumar et al. (2003) and Reichler and Roads (2004) investigated the temporal-spatial distribution of atmospheric predictability. They based their studies primarily on theoretical, statistical, and numerical models and gave qualitative estimates of atmospheric predictability, such as information on regions with either higher or lower predictability. It is however noted that model deficiencies strongly influence their estimates of atmospheric predictability.

Some studies have argued that the limit of atmospheric predictability varies from region to region. For example, Luo et al. (2005 and 2007), Luo (2008) and Keenlyside et al. (2008) showed that tropical climate signals have some degree of predictability from the

order of a few seasons to 1–2 years based on the current state-of-the-art fully coupled models. Luo et al. (2011) further showed that with a perfect warming trend and/or a perfect model, global surface air temperature and precipitation could be predicted beyond two years in advance with an anomaly correlation skill above 0.6. In addition, Li and Ding (2011) used a nonlinear local Lyapunov exponent algorithm to investigate temporal and spatial distributions of predictability limits of the daily geopotential height and wind fields. Although the relevance of the Lorenz two-dimensional vorticity equation that the study analyzed has earlier been disputed by Straus and Shukla (2005) and Rotunno and Synder (2008), Li and Ding (2011) nevertheless noted that limits of atmospheric predictability varies widely with region, altitude, and season; and concluded that limits of noticeable predictability of the daily geopotential height and wind fields are generally less than 3 weeks in the troposphere and approximately 1 month in the lower stratosphere. These imply that a three-dimensional structure of predictability limit exists in the atmosphere.

A large body of research has examined the factors contributing to reliable seasonal forecasts and simulations over Southern African, and South Africa in particular (e.g. Landman and Goddard, 2002, 2005; Johnston et al., 2004; Landman et al., 2005, 2009; Reason et al., 2005; Reason and Jagadheesha, 2005; Friederichs and Paeth, 2006; Landman and Beraki, 2010; Engelbrecht et al., 2013; Ratna et al., 2013; Ratnam et al., 2012, 2013). These studies used various RCMs, embedded in GCMs, at different resolutions and combinations that range from a multi- or single-model ensemble experimental setup to a combination of RCMs and observational datasets. These studies focused mostly on either quantification of internal variability and dynamics in an RCM (Reason et al., 2005; Engelbrecht et al., 2013); prediction and predictability of summer-time precipitation (Landman and Goddard, 2005; Landman et al., 2005; Landman and Beraki, 2010); statistical recalibration and predictions (Landman and Goddard, 2002; Ratnam et al., 2012); or, performance evaluations of statistical and dynamical downscaling of summer-time rainfall peaks and extremes (Landman et al., 2009; Ratna et al., 2013; Ratnam et al., 2013). Though, these studies have helped to improve the

understanding of seasonal climate but none of them have attempted to investigate whether the range of possible seasonal climate simulation or forecast varies from year to year. In addition, the theoretical range of forecasts, from a multi-ensemble RCM, for a variety of seasons over South Africa is still unknown. Also left unattended is the seasonal co-variability between SST anomalies, large-scale climate indices and variations in the ensemble spread, from multi-ensemble RCM simulations; assuming that inter-annual variation in ensemble spread is a reflection of variation in predictability of seasonal climate (Lawal et al., 2014).

In spite of documented efforts aimed at understanding and improving seasonal climate predictions, the aspect of whether the potential predictability (the extent to which a skilful forecast is possible) of climate over West and Southern Africa varies from one year to the next has so far been poorly addressed. The concept of potential predictability to be used in this study is similar to that of Boer (2000 and 2004). The concept suggests that the range of values covered by an ensemble of forecasts or simulations may vary not only as a function of the season but also as a slower function of time, ranging from year-to-year to multi-decadal trends. From a technical point of view, this can be investigated by determining whether long-term trends in the spread of inter-annual ensemble distributions is greater than might be expected from the sampling of a limited number of simulations. This is because there are high possibilities that significant long-term trends in the spread of the simulations could be driven by trends in surface conditions, particularly the anomalous ocean temperature state and by trends in external forcings on the climate system such as anthropogenic emissions. Contextual information on inter-annual variations of simulated skill is therefore necessary. This thesis will, in the context of a single forecasting model system, estimate what the theoretical range of forecasts is for a variety of seasons and establish the theoretical limits as to how much we may be able to improve seasonal forecasts. The study will also investigate the implications of the long-term trends in the potential predictability of seasonal climate.

Consequently, this study will quantify spreads in the ensembles of an RCM simulation over South Africa – a country that is influenced by both temperate and tropical climates. This study will examine the existence and importance of trends in the spread of climate simulations from an RCM that was driven by a dynamical atmospheric model and forced with observed changes in sea surface temperatures, sea ice concentrations and anthropogenic and natural external radiative forcing. Finally, this study will address contextual information on inter-annual variations of simulated skills and examine the co-variability between anomalies of SSTs, large-scale climate indices and variations in the spread of ensembles of atmospheric model simulations over South Africa. These will assist us to better understand the quantitative limits to which seasonal climate can be predicted over South Africa.

2.9 Advantages of Ensemble Forecasting Technique

Ehrendorfer (1997) and Palmer (2000) have shown that an ideal ensemble prediction system accurately accounts for all sources of forecast uncertainty. It provides an approach for integrating both initial conditions and model uncertainty into the forecast processes and at the same time accounts for flow dependence. It has been used to assess the quality of predictions resulting from imperfect initial conditions. Accuracy and reliability of forecasts have been improved through the use of ensemble systems that consist of members with perturbed initial conditions (Hamill and Colucci, 1997) and different physics (Stensrud *et al.*, 2000; Stensrud and Yussouf, 2003; Jankov *et al.*, 2005). On average, the mean of an ensemble of forecasts will, in general, have a smaller error than the mean error of any of the individual forecasts member (Murphy, 1988[12]). In theory, this collection of simulations provides an estimate of the probability distribution of the future behavior of atmospheric variables conditional upon our grasp of the three factors listed in Section 1.5.2 – (1) a reliable simulation of land surface, ocean and atmospheric interactions; (2) knowledge of the initial state of the ocean, the land surface and the atmosphere and (3) knowledge of future changes in boundary conditions.

[12] Murphy JM

2.10 Capabilities and Limitations of Climate Models

As this study intends to employ multi-ensemble simulations from climate models (GCM and RCM), it is therefore necessary to give overviews of their documented capabilities and limitations in real-time applications.

Studies have shown that the performances of climate models are characterized by both capabilities and limitations (IPCC, 2013). Climate models have been known for their capability to reproduce many important elements of observed climates over West and Southern Africa: e.g. the monsoon systems (Hourdin et al., 2010; Xue et al., 2010; Abiodun et al., 2011); the intra-seasonal and the inter-annual variability of rainfall (Sylla et al., 2009); sensitivity to global warming (Hulme et al., 1998); climate change (Hulme et al., 2001); influences of atmospheric tele-connections (Nicholson and Kim, 1997; Martin and Thorncroft, 2014); the spatial distributions of rainfall over West and Southern Africa (e.g. Tadross et al., 2005; Hewitson and Crane, 2006; Abiodun et al., 2011; Landman and Beraki, 2010; Engelbrecht et al., 2013); etc. Therefore, outputs from climate models have enabled us to study and understand, in the practical sense, many atmospheric variables and some aspects of climate system (IPCC, 2007).

On the other hand, some inherently known limitations of climate models include: uncertainties in local forcings and feedbacks (Hegerl et al., 2006 and 2007), these made it difficult for climate models to estimate the contribution of greenhouse gas increases to observed small scale temperature changes; poor depiction of El-Nino climate variability (Hulme et al., 2001); inability of climate models to account for dust, regional changes in land cover and biomass aerosol loadings (Hulme et al., 2001); and, their inability to simulate small-scale processes in anything other than bulk form (IPCC, 2007). Take GCMs as example, their simulations are of less use for some sectors that require high resolutions simulations (e.g. hydrology, agriculture, etc.). At regional and seasonal time-scales, these limitations have negative consequences on the outputs of GCMs. The limitations taint their reputations and erode confidence the end-users have in them. As GCMs are increasingly being considered for seasonal forecasting use, it is therefore

necessary to assess their capabilities, in reproducing spatial classes of the most important climate variables, rainfall and maximum air temperature, over West and Southern African regions. It is equally useful to examine the capability of this GCM in reproducing the atmospheric dynamics favouring the occurrence and dependency on atmospheric tele-connections of these classes. Knowledge of this is relevant to boosting the end-users' confidence in GCMs. The knowledge will help to uncover the spatial characteristic of rainfall and temperature structures that tend to repeat on inter-annual time-scales over these regions. The knowledge will also avail us the opportunity to identify those classes of rainfall and temperature that GCMs can simulate adequately, those they can simulate moderately and those they cannot simulate at all.

2.11 Overview of Classification Technique

A classification technique is a statistical algorithm used to group or partition cases (such as data, individuals or objects) with similar characteristics into homogeneous sub-groups based on responses to the observed input variables (Fraley and Raftery, 1998; Gray and Neuhoff, 1998). There are many classification algorithms that are currently in use for scientific analyses. Among them are the Self Organizing Map (SOM: Kohonen, 1990; Heskes, 2001; Hewitson and Crane, 2002), the Principal Component Analysis (PCA: Reusch et al., 2005 and 2007), the k-Means Clustering (Pham et al., 2003 and 2005), etc.

K-means algorithm is a well known data clustering technique that requires the number of clusters in the data to be pre-specified. In this algorithm, appropriate number of clusters for a given data set depends on a trial-and-error process (Pham et al., 2003). This made it more difficult because of the subjective nature of deciding what constitutes the correct number of clusters (Hardy, 1996). PCA rotates dataset in such a way as to make the maximum variability within the dataset visible i.e. it identifies the most important classes and ignores the rest (Reusch et al., 2005 and 2007). This characteristic prevents users from really categorizing PCA as a clustering algorithm. This thesis utilizes SOM algorithm for classification of climate variability over West and Southern Africa.

2.11.1 Self Organizing Map (SOM) Algorithm

SOM is a neural network based clustering algorithm (Kohonen, 1990; Dermatines and Blayo, 1992; Fritzke, 1994; Su and Chang, 2000). It maps the weight of output data (the output nodes) to conform to the weight of the input data (the input nodes) and accounts for all the variability in the distribution of datasets (Hewitson and Crane, 2002; Schulz and Reggia, 2004; Reusch et al., 2005; Bishop, 2006). SOM calculates the winning nodes that are commonly referred to as the best matching unit (BMU). Any node found within the neighborhood radius of the BMU is regarded as output node. The output nodes in SOM algorithm, therefore, become like and connected to each input node; but are never connected to each other. In view of this, output nodes are ignorant of their nearest neighbor and will only update their weight based on what the input nodes are (Su and Chang, 2000; Barreto and Araujo, 2001; Heskes, 2001).

Studies have shown that SOM has some advantages over other classification and or clustering algorithms such as PCA and k-Means Clustering. For example, SOM algorithm accounts for all the variability in the datasets (Schulz and Reggia, 2004) while PCA mixes both known and unknown classes into single components and does not partition the variance among the components correctly. Classes generated from SOM need no post-processing as they are readily visualized (Bishop, 2006). SOMs algorithm allows users to specify the number of required classes as long as the matrix of rows and columns form a square or rectangular shape (Hewitson and Crane, 2002) while PCA presents wide range of choices which brings confusions. Unlike k-Means Clustering, SOM allows analyses of frequencies of occurrences and transitions (Cavazos, 2000). Furthermore, SOM algorithm is much more flexible than the other algorithms because of its iterative nature, and also because it locates nodes that span the data space. These make the outputs from SOM to be less dependent on a specific data distribution. In view of these, several studies, such as Hewitson and Crane (2002), Reusch et al. (2005 and 2007), Seefeldt et al. (2012), etc. have used SOM algorithm to extract spatial classes and or patterns from climatological datasets and they got robust results.

3 Data and Methods

This chapter describes the data and methods used in this thesis in two parts: the Part A and Part B. Part A discusses the datasets and the methods used to study the spatial variability of seasonal climates over West and Southern African regions; while, Part B explains the datasets and methodology used to analyze the trends in the potential spread of seasonal climate simulations over South Africa.

3.1 Part A: Datasets (Observations, Reanalysis and Simulations)

Three types of datasets analyzed to understand the spatial variability of seasonal climates over West and Southern Africa are the monthly observation from the Climate Research Unit (CRU) of the University of East Anglia; reanalysis obtained from the 20th century reanalysis datasets; and, simulations from a GCM multi-analysis ensemble (the Community Atmospheric Model version 5.1; hereafter known as CAM). Variables obtained for each category of datasets are listed in Table 3.1. Observed rainfall and maximum air temperature were used to evaluate the simulations over West and Southern African regions and also for the classification of spatial patterns of seasonal rainfall and temperature; while other variables were used to obtain the composites of the atmospheric dynamics associated with these classes. The vertical profiles, from 1000 to 100hPa level, of some atmospheric variables were also obtained in order to allow for analyses of upper level dynamics (Table 3.1).

These datasets have different resolutions. Observed variables have a horizontal grid resolution of 0.5^{o}x0.5^{o} longitude-latitude while the extended reconstructed SST datasets have a horizontal resolution of about 2^{o}x2^{o}. Reanalysis datasets, based on historical data, have horizontal resolution of about 200km. Simulations from CAM have a resolution of about 1^{o}x1^{o} and all parameterizations have been tuned for optimal performance at this resolution. Therefore, for uniformity, all simulated (CAM) and reanalysis datasets were

re-gridded to match the horizontal resolution of the observation dataset before they were analyzed.

The time series of all datasets used in the analyses spans from December 1960 to August 2005. Therefore, for example, the 1961 austral summer season is represented by the average of December 1960, January 1961 and February 1961. Similarly, the 1961 boreal summer is represented by the average of June, July and August, all of 1961; while the 1961 boreal spring season is represented by the average of March, April and May 1961, and so on.

3.1.1 Description of CAM

CAM is the most recent in a sequence of global atmosphere models originally developed at the National Center for Atmospheric Research (NCAR). It is technically different from previous family members (e.g. CAM3, 4 and 5.0: Collins et al., 2004[13]; Neale, 2010). CAM has new feature designs in its physics, chemistry and dynamics packages (Eaton, 2010). The physics package (which consists of turbulent mixing processes, cloud and radiation calculations, moist processes, and surface models) provides a less expensive configuration; the chemistry package accounts for short wavelength photolysis in tropospheric chemistry, lengthens the unstructured grid functionality to modal aerosol package and gives flexibility to the units of the emissions datasets; while the dynamics package alters outputs for all high resolution simulations using finite volume dynamic core. Here, the finite volume dynamic core uses a conservative flux form of the semi-Lagrangian scheme in the horizontal to solve the equations for horizontal momentum, pressure thickness, transportation of constituents (e.g. water vapor), and potential temperature (Lin and Rood, 1996). To represent non-convective clouds, CAM uses a bulk microphysical parameterization scheme (Zhang et al., 2003) combined with prognostic condensate scheme (Rasch and Kristjánsson, 1998). It utilizes a mass flux scheme to represent shallow convection (Hack, 1994); uses a plume ensemble scheme to parameterize deep convection in the moist processes (Zhang and McFarlane, 1995); and,

[13] http://www.cesm.ucar.edu/models/atm-cam/docs/description/description.pdf

the Sundqvist (1988) scheme for evaporation of convective precipitation as it falls toward the surface. Detailed descriptions of CAM physics parameterizations can be found in Eaton (2010).

We selected CAM for this project because there are ongoing efforts to include the model as part of multi-model forecasting system over West and Southern Africa by the Climate Systems Analysis Group (CSAG[14]) and other research institutions in Southern and West Africa (Klutse et al., 2015). These institutions are seeking for ways to improve their seasonal forecasts and this requires comprehensive studies of models. However, before adding CAM into the multi-model forecasting system it is essential to identify its weaknesses by evaluating how well it reproduces the rainfall and maximum air temperature characteristics over these important regions of Africa. By so doing, this thesis extends the work of Klutse et al. (2015). While Klutse et al. (2015) studied how well the Community Atmospheric Model (version 3: CAM3[15]) reproduces the inter-annual variability of rainfall over four selected areas in Southern Africa; this thesis investigates the capabilities of 50-member ensembles of CAM in reproducing the characteristics of the rainfall and maximum air temperature classes and or groups identified under the first aim, over West and Southern African regions.

All the CAM used in the study are forced with observed monthly mean sea surface temperature (SST) in accordance with the Atmospheric Model Inter-comparison Project (AMIP) experimental protocol (Gates, 1992). All simulated monthly variables from CAM have 50 ensemble members each; a resolution of about 1^{o} x 1^{o}; differ only in their initial perturbations; and, are continuous for half a century (i.e. from January 1959 to December 2008).

[14] http://www.csag.uct.ac.za/
[15] http://www.cesm.ucar.edu/models/atm-cam/

Table 3.1 List of observation, reanalysis and simulation datasets used in this study

	Variable	Level	Ensemble member	Source and reference
Observation	Maximum air temperature	Near surface (2m)	NA	University of East Anglia Climate Research Unit (CRU, version TS3.22; New et al. 2000; Mitchell and Jones, 2005; and Harris et al., 2013; http://badc.nerc.ac.uk/data/cru/ and http://www.cru.uea.ac.uk/cru/data/)
	Rainfall	NA	NA	
	Total cloud fraction	NA	NA	
	Extended reconstructed sea surface temperature (SST)	NA	NA	National Oceanographic and Atmospheric Administration, USA (Parker et al., 1994; Reynolds et al., 1994; Kaplan et al., 1998; Smith et al., 2008; http://www.esrl.noaa .gov/psd/data and http://www.esrl.noaa.gov/psd/data/ climateindices/).
	Climate indices			
Reanalysis	Vertical velocity (omega)	1000 – 100hPa	NA	20th century reanalysis data provided by the Physical Science Division of the Earth System Research Laboratory – NOAA/OAR/ESRL PSD, Boulder, Colorado, USA (Compo et al., 2011; http://www.esrl.noaa.gov/psd/)
	Zonal (u) wind profile	1000 – 100hPa	NA	
	Meridional (v) wind profile	1000 – 100hPa	NA	
	Air temperature profile	1000 – 100hPa	NA	
	Specific humidity	1000 – 100hPa	NA	
	Mean sea level pressure	NA	NA	
Simulation	Maximum air temperature	Near surface (2m)	50	The Community Atmospheric Model (CAM – version 5.1) from the Earth System Grid Federation data portal (Eaton, 2010; Neale, 2010; http://portal.nersc.gov/c20c/data/LBNL /CAM5-1-1degree/All-Hist/est/v1-0/mon/atmos/)
	Rainfall	NA	50	
	Vertical velocity (omega)	1000 – 100hPa	50	
	Zonal (u) wind profile	1000 – 100hPa	50	
	Meridional (v) wind profile	1000 – 100hPa	50	
	Air temperature profile	1000 – 100hPa	50	
	Specific humidity	1000 – 100hPa	50	
	Total cloud fraction	NA	50	
	Mean sea level pressure	NA	50	

NA = Not Applicable

3.1.2 Climate Indices

Influences of some climate indices on the climate of West and Southern Africa are examined in this study. Table 3.2 gives brief descriptions of the climate indices considered in this study and their major source (the web portal[16] of the Physical Science Division (PSD) of the National Oceanographic and Atmospheric Administration, Boulder, Colorado, USA: Reynolds et al., 1994; Kaplan et al., 1998; Smith et al., 2008). In this study, we enumerate the positive and negative phases of each climate index that correspond to the occurrence of each rainfall and temperature class (observed and simulated) and expressed it as a percentage of the overall events.

3.1.3 Method: The Self Organizing Map (SOM) Algorithm

This study classifies rainfall and maximum air temperature spatial distributions with the aid of the Self Organizing Map (SOM) algorithm. The algorithm software, SOM-PAK 3.2, is freely available via the web portal[17] of the Helsinki University of Technology. Details on the installation of the software can be found via http://www.isegi.unl.pt/ensino/docentes/fbacao/som_pak.pdf and in Kohonen et al. (1995). For the present study, we applied SOM on a dataset that combines the seasonal rainfall and maximum air temperature anomalies from CRU and CAM (i.e. 50-member simulations and the ensemble mean).

Many SOMs classifications were carried out to aid computational stability, avoid class blending and over-generalization. Initially, large matrixes of classes were specified in the SOM algorithm for the rainfall and maximum air temperature anomaly datasets e.g. a 4x4 SOMs archetype. We however discovered that some classes were repeated as they have spatial correlations of more than 0.90 with spatially similar classes. In addition, the frequencies of occurrences of some classes are 0%. Specifications of 4x3 and 3x3 SOMs archetypes did not solve these problems until a 3x2 archetype was specified. The resulting six spatial classes of rainfall and temperature anomalies from the 3x2 SOMs archetype then form the basis of analyses in this study.

[16] http://www.esrl.noaa.gov/psd/data/climateindices/
[17] http://www.cis.hut.fi/research/som_ pak/

Before the SOM analyses, we divide each CAM simulation (including the ensemble mean) by the factor (normalized standard deviation) with which the simulation (averaged over West and Southern Africa) over-estimates the observed rainfall and maximum air temperature anomalies. If these divisions are not done, the large variability of the simulated rainfall and temperature will dominate that of the observation in the SOM analyses and distort the results of the analyses. However, the divisions do not affect the signs of the spatial or temporal variability of the simulated rainfall and temperature anomalies, which are needed in this study. Contributions of CRU and CAM (ensemble mean and ensemble members) datasets to each spatial class of rainfall and temperature anomaly from SOM classifications were then evaluated and assessed.

3.1.4 Synchronization

We computed and compared the inter-annual (and decadal) variability of the spatial classes of the observed and simulated rainfall and maximum air temperature. These enable us to study (and discuss) the transition and persistence of rainfall and temperature classes in both observation and simulations. Synchronization (η), defined by Misra (1991) as

$$\eta = \left(\frac{n'}{n}\right) \times 100\%$$

is used to quantify how well the model simulate (or capture) the timing of the observed rainfall and maximum air temperature classes. η′ is defined as the number of years in which the simulated rainfall and temperature classes are the same with their respectively observed classes while n is defined as the total numbers of years under study (i.e. 45 years: 1961 – 2005). η = 0% if the simulated classes are opposite in sign with the observation (i.e. no synchronisation), while η = 100% if all the simulated classes are of the same sign with observation (i.e. perfect synchronisation). Several studies e.g. Tozuka et al. (2013), Araujo et al. (2014), Klutse et al. (2015), Matthew et al. (2014), etc have also used synchronisation to evaluate the accuracy of phase changes between models and observation datasets.

Table 3.2 Brief descriptions of climate indices used in this study

Climate index	Abbreviation	Description	Reference
Antarctic Oscillation	AAO	Normalized difference in the zonal mean sea-level pressure pattern between 60°S and 40°S. It is a measure of equator-ward / pole-ward shifts in the southern mid latitude storm track. Source: http://www.esrl.noaa.gov/psd/data/20thC_Rean/data/timeseries/monthly/AAO/	Kalnay et al. (1996), Thompson and Wallace (2000), Rayner et al. (2003)
Atlantic Multi-decadal Oscillation	AMO	An unsmoothed index of the North Atlantic temperatures with great effects on temperatures and rainfall over major parts of the Northern Hemisphere. Its area weighted average was computed over the North Atlantic between the equator to 70°N. Source: http://www.esrl.noaa.gov/psd/data/timeseries/AMO/	Martin and Thorncroft (2014)
Benguela Nino	BEN	Measure of SST anomaly gradient by Tropical Southern Atlantic Index (TSA) over the southern parts of equatorial Atlantic Ocean. Source: http://www.esrl.noaa.gov/psd/data/correlation/tsa.data	Enfield et al. (1999), Williams et al. (2008)
El Nino – Southern Oscillation	ENSO	Measure of combined atmosphere – ocean phenomenon, representing shifts of warm surface waters and associated atmospheric convection back and forth across the tropical Pacific Ocean. Synonymous with Multivariate ENSO Index (MEI). Source: http://www.esrl.noaa.gov/psd/data/correlation/mei.data /	Rasmusson and Carpenter (1982), Nicholson and Kim (1997), Camberlin et al. (2001), Wolter and Timlin (2011)
Indian Ocean Dipole	IOD	A shift of SST between positive, neutral and negative phases over the western and eastern Indian Ocean. Constructed from SST variability over the Indian Ocean 35°E – 115°E and 25°S – 20°N domain using the methodology of Behera and Yamagata (2001).	Annamalai et al. (2005), Izumo et al. (2010)
North Atlantic Oscillation	NAO	The normalized pressure difference between an Azores station and another on the Iceland. Source: http://www.esrl.noaa.gov/psd/data/correlation/nao.data	Hurrell (1995 and 2001), Jones et al. (1997), Wanner et al. (2001)
Tropical Southern Atlantic	TSA	Several idealized climate model experiments shows that TSA exhibits a self-evident boost in daily rainfall and rainfall extremes over southern Africa, via locally-based effects such as increased convection and remotely-based effects such as an adjustment of the Walker-type circulation. Source same as BEN.	Enfield et al. (1999), Williams et al. (2008)
Reconstructed Tropical	rTAI	rTAI dataset is similar to those of Tropical Northern and Southern Atlantic Indices (respectively TNA and TSA) described by Enfield et al. (1999). It is a	Enfield et al. (1999)

Atlantic Index	measure of SST anomaly gradient over the Equatorial Atlantic; its construction is however restricted to SST anomalies over the Atlantic Ocean rectangular domain 10^{o}E–20^{o}W and 10^{o}S–5^{o}N in this study.

3.2 Part B: Simulation Datasets

Multi-analysis ensembles from the Hadley Centre Regional Model version 3P (hereafter known as HadRM3P) are the simulated datasets used to study the "Trends in the potential spread of seasonal climate simulations over South Africa". Climate variables from HadRM3P consist of monthly precipitation and near surface air temperature. The simulations were run under the weather@home/SAF[18],[19] project using the climate*prediction*.net (CPDN) facility hosted by the University of Oxford. The project runs the global atmospheric model HadAM3P-N96 that drives the nested regional atmospheric model HadRM3P (Jones et al., 2004) over the Southern African domain. The CPDN framework allows simulations to be run on volunteered home personal computers around the world, thus permitting uniquely large ensemble sizes.

HadRM3P simulations are forced with observed changes in sea surface temperatures, sea ice concentrations and anthropogenic and natural external radiative forcing. They are also constrained every 6hour with lateral boundary conditions supplied by the global atmospheric model. Simulations are run in 1-year segments (starting from 1 December, ending on 30 November) from December 1959 through to November 2010. Simulation sequences are formed by starting new segments from the final state of a simulation for the previous year. Conclusions for December are subject to the rate at which simulations diverge from their perturbed initial states because some of the simulations retained are at the start of a sequence. Those initial states at the start of simulation sequences are random and have no intended relevance to the actual weather observed on that date. This experimental setup is very similar to the Atmospheric Model Intercomparison Project (AMIP: Gates 1992; Zwiers, 1996; Frei and Robinson, 1998). However, it is regionally downscaled to a spatial resolution of 50 km to account relatively better for topographic details that can be very relevant in mountainous South Africa.

[18] http://www.climateprediction.net/weatherathome /regions/
[19] http://weatherathome.org

For this study, the simulations are regarded as hindcasts with perfect skill in forecasting the oceanic and radiative forcing states. However, they have no additional skill in forecasting the atmospheric state beyond what is imposed by the oceanic and radiative boundary conditions. We use 100 simulations per month; subsets of simulations have been rejected because output from at least one of their twelve months fails quality-control tests. These ensembles have two unique advantages: (1) a large sample size that allows more precise sampling of the climate distributions and, (2) a relatively high spatial resolution that allows more detailed analysis within South African territory. This combination of large ensemble size and high spatial resolution has so far only been achieved using theHadAM3P-N96/HadRM3 port on the CPDN facility.

3.2.1 Analysis Procedures

Ensemble spreads are quantified in this study using two measures – the standard deviation (StdDev) and the 10–90th percentile range. StdDev has three distinct features: it describes all of the data; it can be estimated reliably from small samples of the simulations; but, it is also very sensitive to outliers. The 10–90th percentile range, the distance between the 90th and 10th percentile values of the ensemble populations, can essentially be considered the opposite of StdDev in all these three distinct aspects. While interpretation of observed values within the context of StdDev variations requires the assumption of some distributional form, the 10–90th percentile range does not require such an assumption. With these differences, the two measures are complementary and thus give an indication of the sensitivity of conclusions to the particulars of how ensemble spread is measured. Therefore, analysis of spreads of ensembles of simulations from the regional model as depicted in Chapter 8, Section 8.2, will be carried out using these measures.

In order to ascertain the existence of inter-annual variation in the spread of seasonal climate simulations over South Africa, linear trends are evaluated from time series of these two measures of spread. A Monte-Carlo bootstrap resampling method, in line with Buckland (1983), Johnson (2001) and Buhlmann (2002), is used to characterize sampling uncertainty in the results. The values from available simulations for each year are

selected at random, with replacement, and the calculations performed again on these resampled data. The process is repeated 1000 times.

Investigation of "Trends in the potential spread of seasonal climate simulations over South Africa" in this thesis will focus on the Republic of South Africa; a relatively dry country with variable rainfall regimes (Johnston et al., 2004; Kruger, 2006). The country's climatic conditions range from temperate in the southwest and the interior plateau to subtropical in the northeast. Results will be presented on the basis of the republic's nine provinces depicted in Figure 3.1, because many operational decisions in water resource and agricultural management are made administratively at the provincial level. Secondly, there is sharp climate variability from one province to the other (Figure 1.1), although it is acknowledged that the provincial borders do not correspond precisely to borders of regions with different seasonal climate regimes.

It is also important to note that de-trending operations were carried out on the measures of spread and the observed SST during the investigation of the relative role of SSTs and large scale climate indices as predictors of inter-annual variability of spreads in seasonal climate. The reason for de-trending is because this study is interested in the year to year variability relevant to seasonal forecasting rather than the long-term trends. However, analyses without the de-trending showed negligible differences.

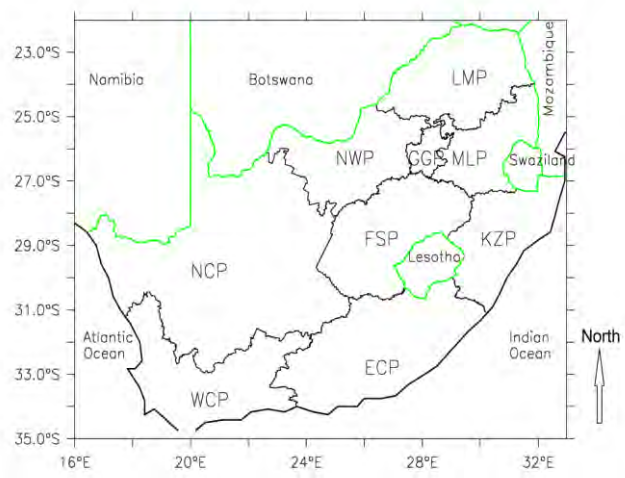

Figure 3.1 Map of the Republic of South Africa showing its provinces: ECP – Eastern Cape Province; FSP – Free State Province; GGP – Gauteng Province; KZP – KwaZulu Natal Province; LMP – Limpopo Province; MLP – Mpumalanga Province; NCP – Northern Cape Province; NWP – North West Province and WCP – Western Cape Province. Provincial abbreviations used here are unique to this study. Source: Council for Scientific and Industrial Research (CSIR) Satellite Applications Centre.

RESULTS AND DISCUSSIONS

4 Characteristics of Summer Rainfall Patterns over West Africa

This chapter presents and discusses the results of our analysis on the characteristics of summer (boreal) rainfall classes over West Africa, as observed by CRU and simulated by CAM. It starts by evaluating the performance of CAM in simulating the climatology of the summer rainfall pattern. Then, it describes the characteristics of the six dominant summer rainfall (anomaly) classes over the region and evaluates how well CAM reproduces them. The six dominant classes were obtained using SOM analysis as described in Chapter 3. The characteristics of the dominant summer rainfall classes considered include their inter-annual and decadal variability, transition, and persistence. The chapter also studies the influence of atmospheric tele-connections on the observed and simulated classes, and examines the capability of CAM in reproducing the atmospheric dynamics that produces each summer rainfall classes.

4.1 Climatology of Summer Rainfall Patterns

Figure 4.1a shows that in most years the inter-annual variability of the simulated summer rainfall (averaged over West Africa), produced by CAM ensemble members, envelope the observed (CRU) summer rainfall. Exceptions are in 1982 and 1997 when CRU is outside the spread of the ensemble members. However, ensemble mean values are very close to, or sometimes the same with, the observed values. Normalized standard deviations of all ensemble members are greater than that of the ensemble mean because the averaging filters out the simulated variability. For example, Figure 4.1b shows that the discrepancy between the ensemble mean and CRU is smaller (< 4.6) than the discrepancies between individual ensemble members and CRU (generally > 4.7). Furthermore, the figure also shows that the relationship between the ensemble members and the observation is linear, as the correlations between them range from 0.4 to about 0.67. Similarly, the correlation between the ensemble mean and the observed rainfall variability is moderate ($r = 0.63$). All these imply that model give a realistic simulation of the inter-annual variation of the summer rainfall (area averaged) over West Africa.

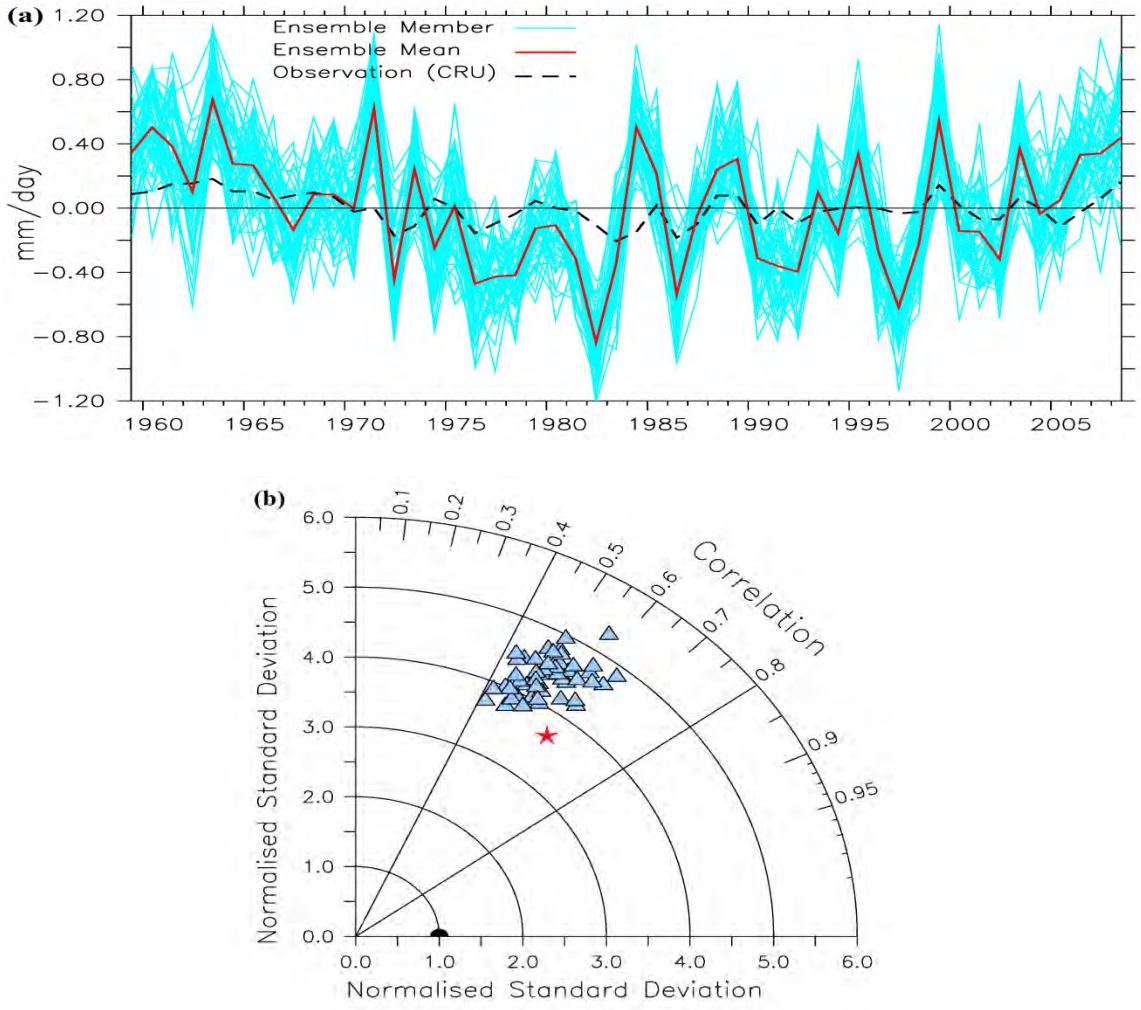

Figure 4.1 (a) Inter-annual variation of boreal summer rainfall (anomaly; mm day^{-1}), averaged over West African sub-region. **(b)** Taylor diagram, of panel a, showing the normalized standard deviations and the correlation coefficients of CAM ensemble mean (red star), ensemble members (blue triangles) and CRU (black semi-circle). The normalized standard deviations and correlations are with reference to CRU observation.

The observed mean annual cycle of rainfall over West Africa exhibits three different periods – the onset, the zenith and the cessation (Figure 4.2a). The onset period marks the northward movement of the rain belt from the coast to about 7^{o}N within the months of March and May. The zenith period is characterized by the northernmost extension of rain

belt to between 8 - 15^{o}N within the months of June to August. This is the period of high rainfall amounts over the Sahel. The period is however accompanied by a pause in rainfall intensities along the coastal parts of the sub-region. The cessation period marks the retreat of rain belt towards the equator from the month of September. Monthly variation of rainfall closely follows the latitudinal positions of the Inter-Tropical Discontinuity (ITD: an imaginary zone, boundary or line at the surface where the dry continental winds meet the moist maritime winds) and the African Easterly Jet (AEJ: a moderate stream of wind between 700 and 600hPa levels). Figure 4.2b shows that CAM captures the mean annual cycle of rainfall and the core values of AEJ. However, the simulated northernmost extension of rain belt is between 9 - 17^{o}N while the northernmost position of ITD in CAM is around 23^{o}N contrary to around 21^{o}N in observation. These findings are consistent with previous studies such as Le Barbe et al. (2002) and Omotosho and Abiodun (2007).

The observed rainfall distribution over West Africa, during boreal summer season, ranges from maximum along the coastal areas to tropical aridity climates as rain transverses hundreds of kilometers further inland (Figure 4.2c). In this season, the rain belts are mainly dominated by maritime south-westerly components of the winds while the zones of aridity are dominated by continental north-easterly components at 850hPa level. CAM captures the zones of maximum rainfall along the coastal axes of Guinea, Sierra Leone, Liberia and southern parts of Nigeria-Cameroon borders (Figure 4.2d). CAM also captures the north-south rainfall gradients and the zones of aridity. CAM gives realistic simulation of the boreal summer trade winds over West Africa at 850hPa level, i.e. it reproduces both the maritime south-westerly and the continental north-easterly components of the trade winds. The only exception is that the trade winds are a bit stronger in the model than the observation, especially over the Atlantic Ocean (Figure 4.2d). Studies have shown that these wind patterns provide good background for the formations of boreal summer rainfall and the associated convective cloud bands that produce most rainfall over West Africa (Sultan and Janicot, 2000 and 2003; Jenkins et al., 2002).

Figure 4.2e shows that convergence of vertically integrated moisture flux is observed over most of the inland regions of West Africa. The convergence overlaps with the location of rainfall activities, while the divergence is more dominant over the Atlantic Ocean. The southerly components of the vertically integrated moisture flow paths transport moisture from the Atlantic Ocean into the sub-region and the convergence of the moisture results in uplifting and consequently, rainfall. The moistures are however gradually advected westward as soon as they are offshore and rapidly as they approach or go beyond 12^{o}N. Figure 4.2f shows that CAM reproduces the vertically integrated moisture flux convergence, but with greater magnitudes along the coast lines. CAM also captures the westward advections of the vertically integrated moisture flow paths.

Figure 4.2(g and h) depicts the vertical structures of the monsoon system during its peak in August when strongest signals in the West African circulations are captured. Observation, Figure 4.2g, shows three distinct wind systems that are essential for rainfall mechanisms over West Africa: the low level westerly components of the monsoon flow which transports moisture from the Atlantic Ocean into the sub-region; the AEJ at around 700 – 600hPa levels; and, the Tropical Easterly Jet (TEJ), which is nearly twice as strong as AEJ, towards 250 – 150hPa levels. Vertical velocity profile south of 30^{o}N show four local extremes. The first is a descent region around 26^{o}N northward. The second is characterized by low level dry ascent centered between 19^{o} – 24^{o}N at below 600hPa level. It corresponds to the position of ITD. The third is a much deeper (i.e. 850 – 200hPa levels) region of ascent between 8^{o} – 18^{o}N, it corresponds to the position of Inter-Tropical Convergence Zone (ITCZ). The last is a deep descent region centered over the equator up to about 8^{o}N; this is responsible for the brief cessation in rainfall intensities along the coastal parts of the sub-region in August. Figure 4.2h shows that CAM captures the low level westerly components of the monsoon flow, including its vertical and latitudinal extents. CAM also reproduces both the AEJ and TEJ, though the TEJ is stronger in CAM while the AEJ is weaker. The vertical and latitudinal extents of the four local extremes of vertical velocity are also reproduced by CAM. Therefore, the realistic

simulations of these features indicate that CAM captures most of the atmospheric dynamics of the summer rainfall over West Africa.

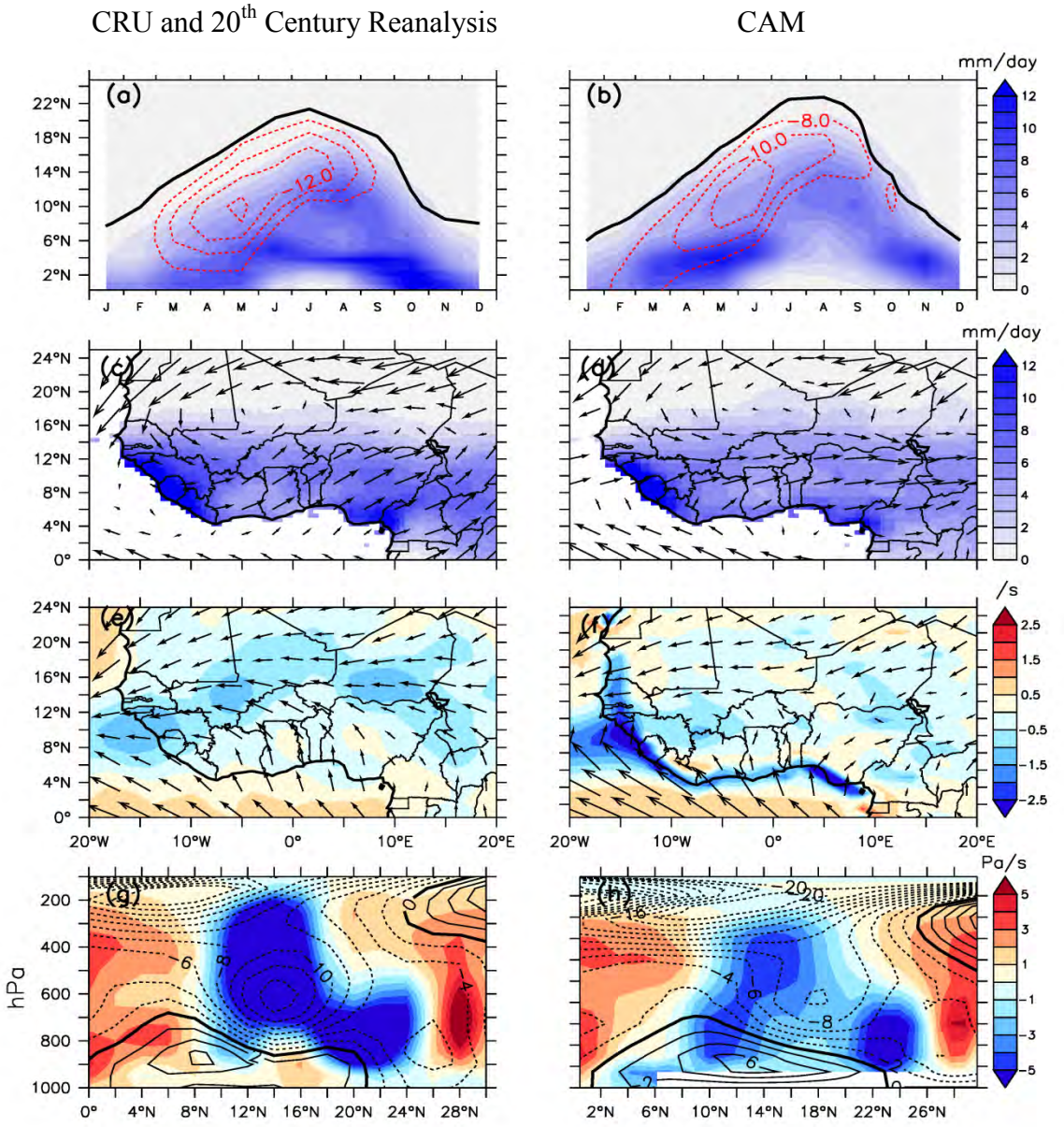

Figure 4.2 (Top row) Time-latitude cross section of monthly mean rainfall (shaded; mm day^{-1}) and the corresponding wind speed at 600 hPa level (dashed contour; ms^{-1}), averaged over 10^{o}W to 10^{o}E. **(Second row)** Mean boreal summer rainfall (shaded; mm day^{-1}) and the corresponding wind directions (arrows) at 850hPa level over West Africa. **(Third row)** Mean summer vertically integrated moisture flux convergence (shaded; x10^{-5} s^{-1}) and the corresponding vertically integrated moisture flow paths (arrows) over West Africa. **(Bottom row)** Mean vertical profile of the monsoon system in August. Zonal wind (contour; ms^{-1}) and vertical velocity (shaded; x10^{-2} Pa s^{-1}) averaged over 10^{o}W to

10^{o}E. Observations and simulations are respectively on the left and right columns while the location of the ITD (the contour of the zero meridional wind at the surface) is indicated by the black solid line in panels a and b.

4.2 Dominant Classes of Rainfall over West Africa in Summer

Figure 4.3 presents the SOMs archetype (2x3 nodes) of the observed (CRU) and the simulated (CAM) summer rainfall anomaly classes over West Africa. These are regarded as the dominant summer rainfall classes over the region. A close examination at the figure shows that the six spatial classes can be categorized into three groups such that each group contains two opposite spatial rainfall classes. Nodes 1 and 6 are categorized as the first group (FG). Node 1 features positive rainfall anomalies that transverse from the coastal regions to around 12^{o}N and longitudinally from south-central Cameroon to Sierra Leone and southern parts of Mali, negative rainfall anomalies over south Senegal – west Guinea axes, and neutral conditions over the rest of the sub-region. Spatial rainfall anomaly class in Node 6 features the opposite of Node 1. Within 1961 – 2005, CRU shows that Node 1 accounts for about 16% of summer rainfall anomaly classes while Node 6 accounts for 11%. Node 1 is adequately simulated by CAM, i.e. ensemble members and ensembles mean agree with CRU on the frequency of occurrence of Node 1. However, CAM overestimates the frequency by 6-9% in Node 4.

The second group (SG) is characterized by rainfall anomalies of one sign throughout West Africa. In this group are Nodes 3 and 4. Spatial rainfall anomaly class in Node 3 features sub-zero rainfall anomalies that cover almost the entire sub-region. Spatial rainfall anomaly class in Node 4 features the opposite of Node 3. While CAM ensemble mean and the average of individual ensemble members simulate good statistics of CRU in Node 3, they however overestimate the frequency of occurrence of the rainfall anomaly class in Node 4. Classes in SG are similar to no-dipole classes found by Nicholson and Webster (2007), and Nicholson (2009).

Nodes 2 and 5 are in the third group (TG). The group features north-south dichotomy of rainfall anomaly classes. Spatial rainfall anomaly class in Node 2 features below-normal rainfall anomalies over the Sahel, to the north, and neutral condition along the Gulf of Guinea, to the south. The core of negative rainfall anomalies is concentrated over Senegal-Guinea axes. Spatial rainfall anomaly class in Node 5 features wetter Sahel; and, drier coastal areas with cores of wetness and dryness over Senegal-Guinea axes and Liberia – south Cote d'Ivoire axes respectively. CAM underestimates the frequency of occurrence of rainfall anomaly classes in this group. For instance, CRU indicates that Node 2 accounts for 18% of summer rainfall classes within 1961 – 2005 while Node 5 accounts for 20%. Meanwhile, CAM suggests that Node 2 only accounts for 9% (ensemble mean) and 14% (ensemble members), while Node 5 accounts for only 13% (ensemble mean) and 16% (ensemble members). Spatial rainfall anomaly classes in TG are similar to those found by Janicot (1992), Fontaine and Janicot (1996), Ward (1998), etc.

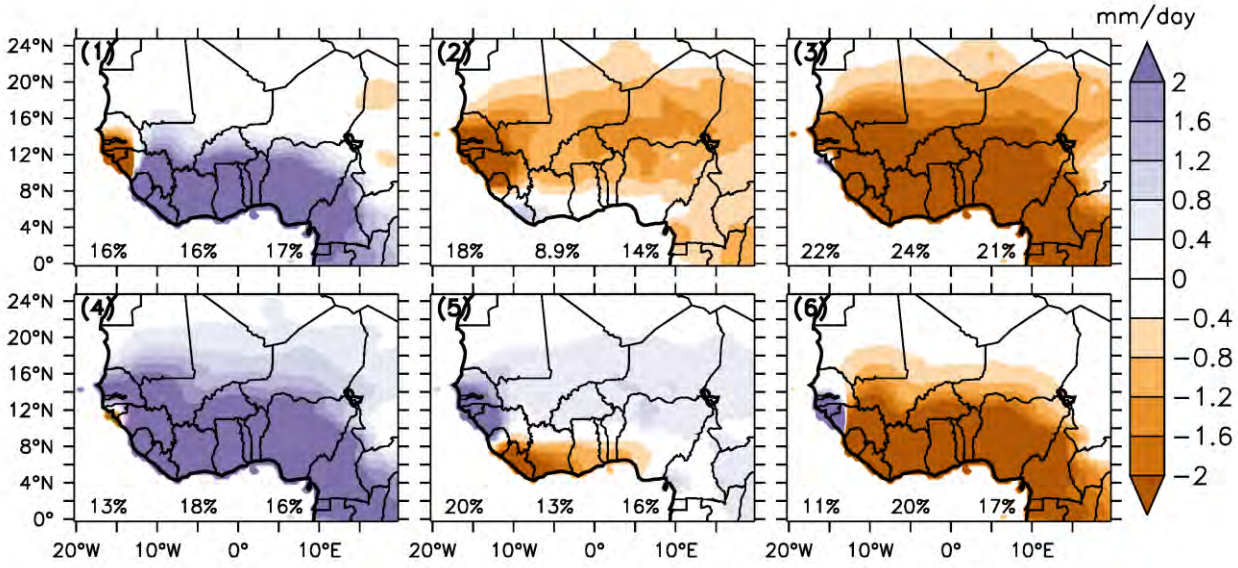

Figure 4.3 SOM classifications of unified spatial patterns of observed (CRU) and simulated (CAM) boreal summer rainfall (anomalies; mm day^{-1}) over West Africa. Class numbers are written on the upper left sides of each panel while the frequencies of occurrences (%) are shown on the lower left, middle and right respectively for CRU, CAM ensemble mean and the average of individual ensemble member simulations.

4.3 Inter-annual Variability of the Dominant Summer Rainfall Classes over West Africa

There are differences on how ensemble mean and ensemble members capture the inter-annual variability of dominant rainfall classes depicted in Figure 4.3. Figure 4.4(a, b) shows that ensemble mean, in agreement with CRU, simulates Node 1 four times, Nodes 2, 5 and 6 once each, Node 3 six times and Node 4 twice (Figure 4.4b). This means that CAM ensemble mean correctly reproduced the observed spatial rainfall anomaly classes in 15 summers, out of 45. Meanwhile, there are only 7 summers where ensembles members disagree with CRU, i.e. when none of the ensemble members simulate the observed class (Figure 4.4a). These imply that ensemble mean has about 33.3% synchronization with CRU while at least one ensemble member will reproduce the right spatial class 84% of the time.

All the 50 ensemble members simulated identical class (Node 1) with CRU in 1963 (Figure 4.4a, b). Similarly, the figure shows that the same numbers of ensemble members agree with both ensemble mean and CRU each time there is agreement between them. This implies that rainfall anomalies in the correct ensemble members dominate those in the wrong members. Nevertheless, Figure 4.4(a, b) suggests that a minimum of 44% of ensemble members (i.e. 22 members) are required for ensemble mean to correctly simulate any of the six observed spatial rainfall anomaly classes over West Africa.

Figure 4.4(a, b) shows that ensemble mean capture some of the transition and persistence of spatial rainfall anomaly classes. Here, persistence means a repetition of the rainfall class consecutively, while transition means change in the rainfall class. For example, ensemble mean reproduces the transition of Node 1 in 1963 to Node 5 in 1964, and then to Nodes 4 and 1 in 1965 and 1966 respectively. Similarly, it also capture the transition of Node 1 in 1989 to Node 3 in 1990, and then to Nodes 2 and 6 in 1991 and 1992 respectively. It however fails to capture the transition of Node 6 in 1978 to Node 1 in 1979, and then to Nodes 2 and 5 in 1980 and 1981 respectively. Ensemble mean also

captures the persistence of Node 3 in 1976 – 1977, but fails to reproduce the persistence of Node 3 from 1972 to 1973 and 1982 to 1983. It also did not capture the persistence of Node 5 from 2003 to 2004.

Observationally, the most persistent rainfall anomaly class is Node 3 (Figure 4.4a, b). Node 3 also has the highest cases of persistence. Ensembles mean however shows that Nodes 1 and 3 are the most persistent nodes; while Nodes 3 and 6 have highest cases of persistence. However, analyses from ensemble members show that Node 3 is the most persistent node and that it is also the node with highest cases of persistence (Figure 4.5). This implies that Node 3 has the greatest tendency to re-occur in the following summer and at the same time persist anytime it occurs than any other nodes. This explains why the sub-region, which thrives on rainfall for all aspects of its socio-economic life, has been struggling with rainfall related disasters.

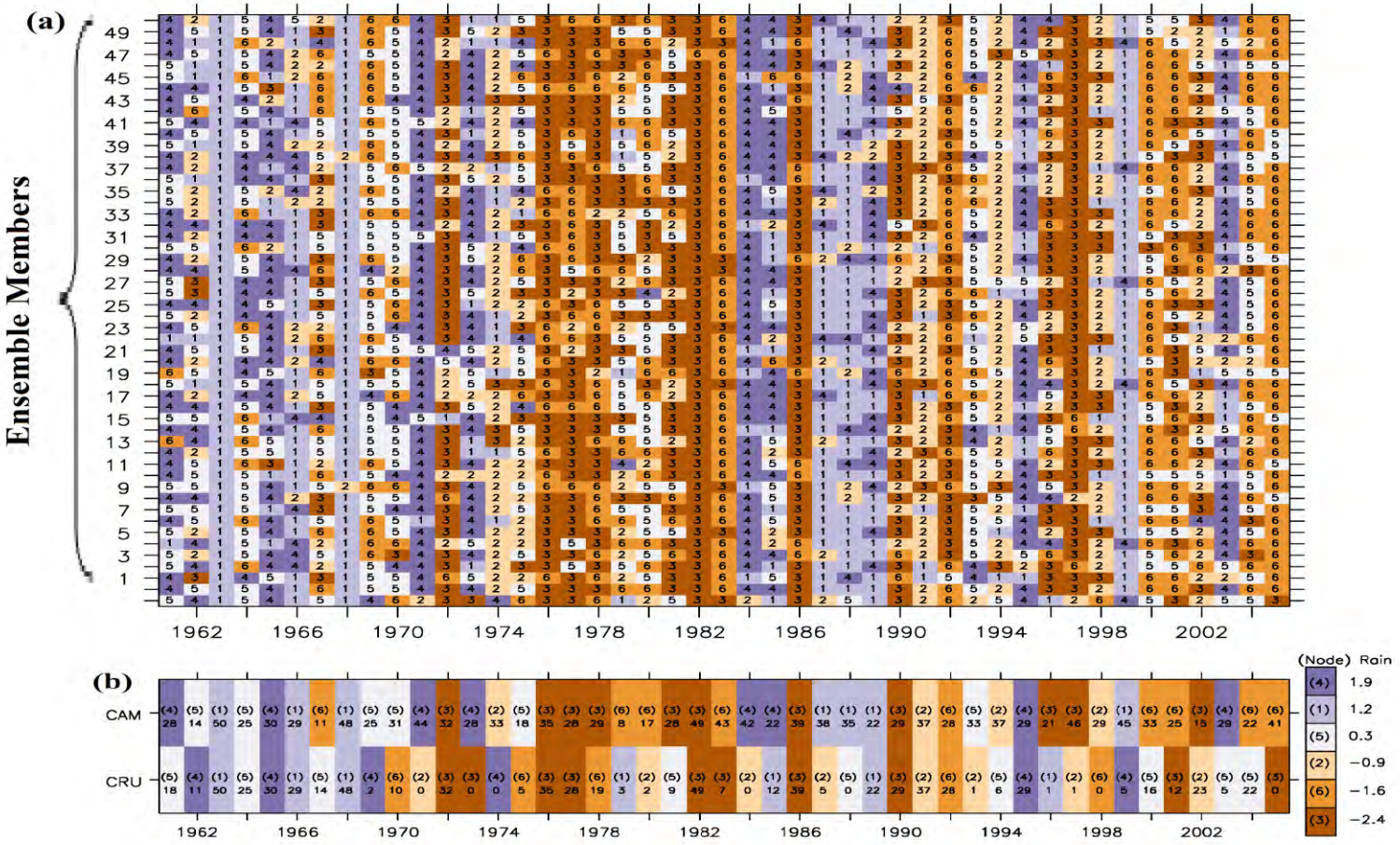

Figure 4.4 Inter-annual variability of spatial classes of rainfall anomalies (mm day^{-1}), depicted in Figure 4.3; **(a)** as simulated by 50 CAM ensemble members, CAM ensemble mean (upper bottom row) and observation (CRU: bottom row) and **(b)** an enlarged last two bottom rows of panel a showing the ensemble mean (upper row) and the observation (bottom row) (the numbers in brackets (i.e. 1 – 6) show the nodes of rainfall classes while the colours indicate the mean rainfall anomalies over the sub-region. The number under the nodes shows the number of the ensemble members that agree with CRU observation or with the CAM ensemble mean simulations on the rainfall class).

Figure 4.5 also shows that 40% of the ensemble members (i.e. 20 ensemble members) have higher synchronization than the ensembles mean. Here, the fifth simulation (SIM05) has the highest synchronization with CRU (i.e. $\eta = 42\%$). The implication of this is that SIM05 captures more rainfall classes than the ensemble mean and any other ensemble members. Therefore, generating an ensemble mean based on performance of individual ensemble members and on the use of different weighting function may give better results than uniformly averaging the members to produce the ensemble mean.

4.4 Decadal Frequency of Dominant Summer Rainfall Classes over West Africa

Figure 4.6 shows that some rainfall classes are frequent; some are recent while some are rare. Rainfall classes in FG have a combination of frequent and rare occurrences. For example, Node 6 occurs only in two decades – 1970s and 1990s, therefore rare. Node 1 occurs every decade except 2000s, hence frequent. While ensemble mean captures the frequentness of Node 1, it does not reproduce the rarity of Node 4. It instead shows that Node 6 is frequent and recent. Node 3 in the SG is recent and frequent as well. It occurs in all decades except 1960s. It has its maximum frequency of occurrence, the highest recorded by any class, in 1970s (4 events). In a warming atmosphere, the recent and frequent nature of Node 3 is consistent with the findings of Zhang et al. (2007) and Stott et al. (2010). It is also consistent with the decadal drying phase observed over the sub-region in 1970s (Folland et al., 1986; Hoerling et al., 2006). Its opposite class, Node 4, is rare. However, ensemble mean does not capture the rarity of Node 4 while it captures the recentness and frequentness of Node 3. Spatial rainfall anomaly classes in TG are frequent, as well as recent in nature. TG's Node 2 occurs almost in all decades, except 1960s and has its maximum occurrences through 1980s and 1990s. Node 5 also occurs in all decades except 1970s. It's the only node that has its maximum occurrences in 2000s after similar occurrences in the 1960s. On the contrary, ensemble mean shows that spatial rainfall anomaly classes of TG are in fact rare.

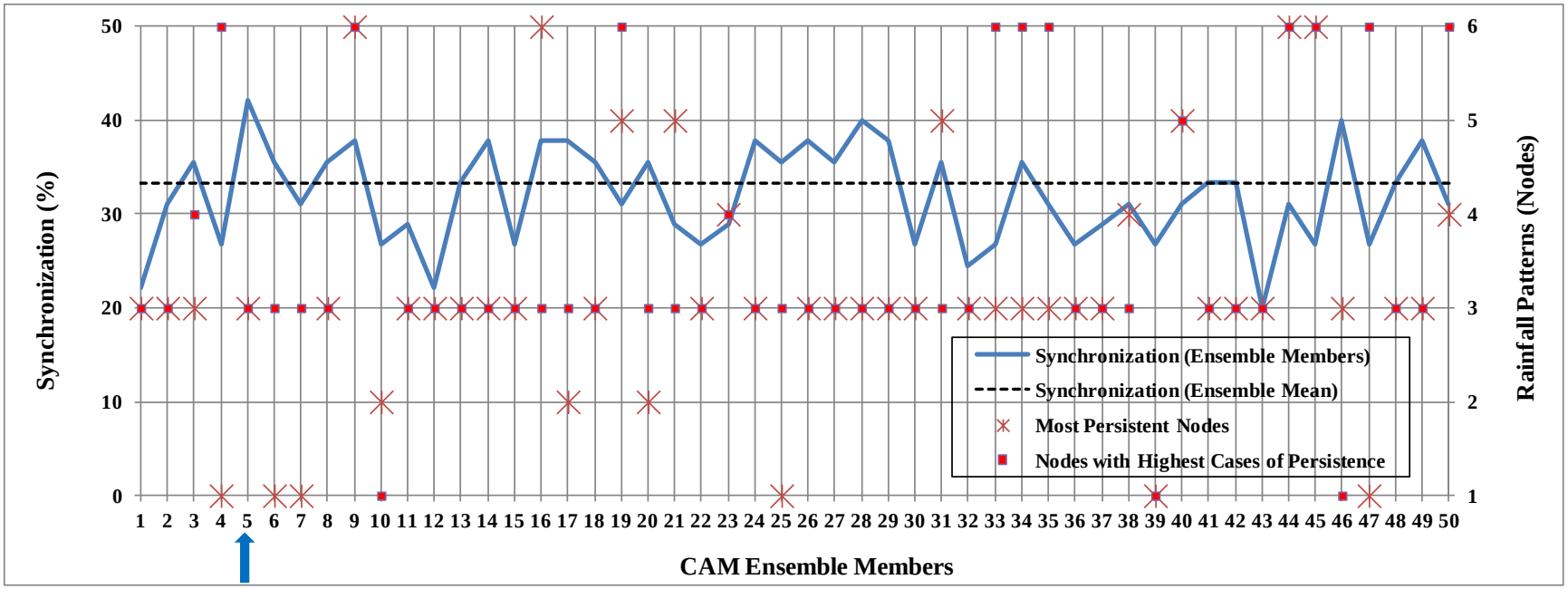

Figure 4.5 Synchronization (%; left vertical-axis) and persistence (nodes; right vertical-axis) of the simulated spatial classes of rainfall in reference to observation. The blue arrow points to the ensemble member with the highest synchronization (the 5th simulation: SIM05).

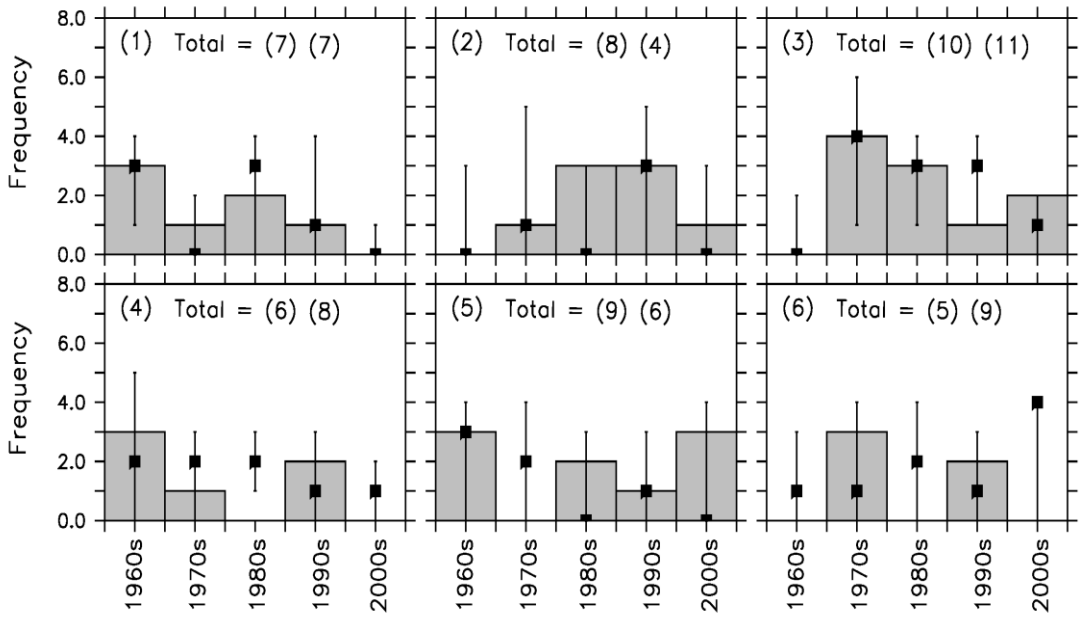

Figure 4.6 Decadal frequencies of spatial classes of rainfall anomalies displayed in Figure 4.3. Grey bars: decadal frequencies of rainfall classes from observation (CRU); black squares: decadal frequencies of rainfall classes from CAM ensemble mean; the upper and lower parts of the error bars, respectively, indicate the maximum and minimum decadal frequencies of rainfall classes produced by CAM ensemble members. In brackets are the tag (or node) of each rainfall pattern shown on the upper left corner of each panel; the total number of occurrence of rainfall pattern as simulated by CRU (nearer to the equal sign) and CAM ensemble mean (farther from the equal sign).

4.5 Atmospheric Tele-Connection and the Occurrence of Dominant Summer Rainfall Classes over West Africa

There are no consistencies in the association between ENSO and rainfall classes, over West Africa, because all classes are associated with both phases of ENSO (Figure 4.7). The only exception is Node 1 where ENSO phases are not observed. Figure 4.7 shows that Nodes 2 and 3 occur during the higher frequencies of positive phase of ENSO. Similarly, Node 4, a wetter than normal class, as well as Node 5 which is a di-pole class are associated with negative phase of ENSO. These are consistent with Conway (2009) whose findings shows that Sahel is characterized with drier than normal conditions during El Nino events (positive phase of ENSO), and vice versa, during La Nina events (negative phase of ENSO). Positive phase of ENSO events tend to result in weak monsoon flow, hence dry conditions over West Africa close to the surface position of the

ITCZ in July–September (Camberlin et al., 2001). On the other hand, Node 6 occurs during negative phase of ENSO, thus highlighting the inconsistency. Therefore, rainfall variability over West Africa may cautiously be predicted / simulated using ENSO phases as predictors. Figure 4.7 shows that CAM ensemble mean capture the dominating phases in Nodes 2, 3, 4 and 5. It is however not able to capture the nil ENSO event in Node 1.

Association between AMO and the rainfall classes are also not consistent, except in Node 6 where it is reliable. Figure 4.7 shows that Node 6 is associated with only the negative phase of AMO while other nodes are associated with both phases of AMO. However, the figure shows that negative phases dominate in Nodes 1 to 4, while positive phase dominates in Node 5. The association of Node 5 with AMO is consistent with the findings of Martin and Thorncroft (2014); they found significantly positive summer rainfall anomalies over the Sahel during positive phases of AMO. In summary, the occurrence of droughts and the recent partial rainfall recovery in the Sahel have been linked to AMO by Sutton and Hodson (2005), Hagos and Cook (2008), and Mohino et al. (2011). Figure 4.7 shows that CAM ensemble mean is able to reproduce the dominating negative phases in Nodes 1, 3 and 4.

Association between NAO and West African rainfall classes is reliable in Nodes 2 and 6 where it features positive phases only. Figure 4.7 shows that other nodes, though dominated by positive phases, are associated with both phases, except Node 4 that has equal frequency of both phases (about 20%). Wanner et al. (2001) describe NAO as a measure of strength of westerly flow. It is in positive phase with strong westerly anomalies which usually dominate maritime monsoon flow during boreal summer periods over West Africa. Therefore, the inconsistencies that characterized the association between NAO and rainfall classes imply that NAO works in tandem with other atmospheric tele-connection indices. Studies, e.g. Hurrell (2001), have shown that NAO, in conjunction with ENSO, is a major source of seasonal to inter-decadal variability in the global atmosphere. NAO-induced predictability arises from the influence of warm SST anomalies in the equatorial Tropical Ocean and fall in station level pressures (Chang

et al., 1997). Therefore, prediction potential of NAO, when compared to that of ENSO, seems to be smaller. Figure 4.7 shows that CAM ensemble mean is able to capture the dominating positive phases in Nodes 1, 3, 5 and 4. Ensemble mean fails to reproduce the scenario in Node 2 by featuring equal frequency of phases, while it also did not capture equal frequency in Node 4.

With the exception of the TG, Figure 4.7 shows that opposing rainfall classes in FG and SG are associated with opposing phases of rTAI. In FG for instance, Node 1 is associated with the positive phase of rTAI while Node 6 is dominantly associated with the negative phase. Rainfall classes in the SG also feature opposing phases. These associations are reliable in Nodes 1 and 4 where they feature positive phases only. Positive phases of rTAI are associated with drier conditions in the Sahel and wetter conditions in the coastal regions (Rowell et al., 1995; Ward, 1998). This is due to anomalous southward displacement of the ITCZ (Polo et al., 2008; Losada et al., 2010). The opposite effect is experienced during the negative phases. However, positive phase of ENSO events determine the Sahelian rainfall anomalies by overriding the Sahel rainfall enhancement signal from the concurrent negative phase of rTAI, and vice versa; thereby resulting in rainfall anomalies of the same sign throughout the sub-region, e.g. Nodes 3 and 4 (Latif and Grotzner, 2000; Rodriguez-Fonseca et al., 2011). These indicate that rainfall anomalies over West African sub-region can be reliably predicted / simulated using SST anomalies over tropical Atlantic and Pacific Oceans as predictors. CAM ensemble mean is able to capture the dominating positive phases in Nodes 1, 2 and 4; and, dominating negative phases in Nodes 3 and 4. Ensemble mean however fails to reproduce the positive phase of rTAI in Node 5.

Inferences from Figure 4.7 indicate that it is difficult to associate any of the rainfall classes with a particular climate index. This is because each class is associated with more than one dominant climate index. Inconsistency in the associations may be attributed to three physical reasons: existence of different forms of a climate index, for example, El Nino Modoki and conical El Nino are both forms of ENSO (Johnson, 2012; Hoell et al.,

2014; Ratnam et al., 2014), whereas we used only one form of each climate index; influence of local or regional forcing conflicting with climate indices; and, the possibility of ensemble members producing different spatial anomaly classes for a particular climate index whereas we used ensemble mean where the classes are averaged together. These may be the reasons why CAM finds it difficult to simulate correctly some of the associations. Nevertheless, the investigation has assisted us to know the abilities of CAM in capturing the association between climate indices and rainfall anomalies over West African sub-region.

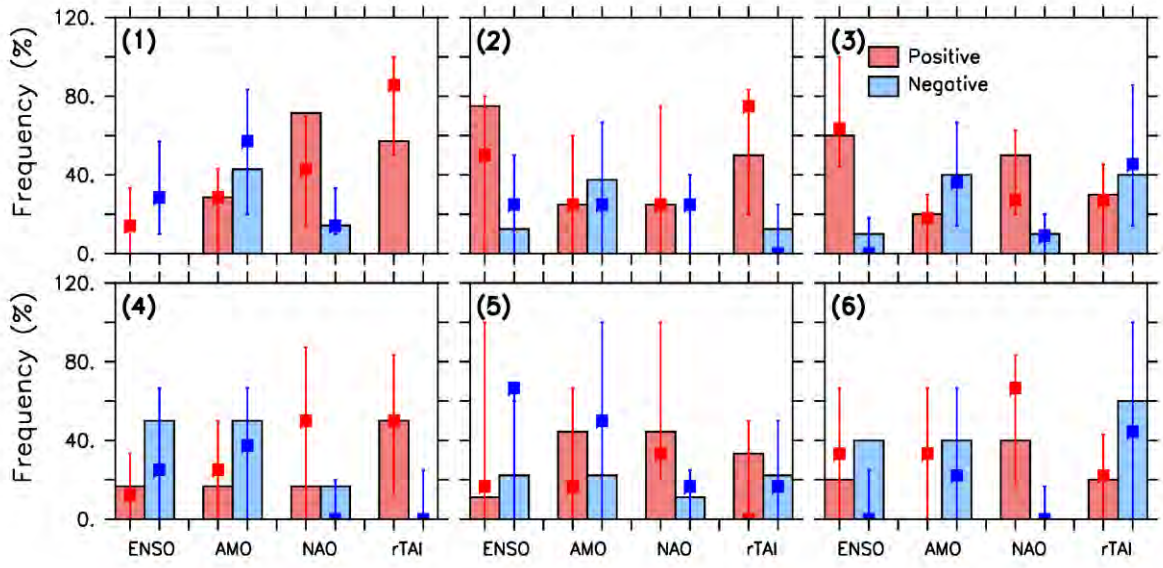

Figure 4.7 Frequency of occurrence of climate indices associated with spatial classes of rainfall anomalies depicted in Figure 4.3, expressed as percentage of frequency of occurrence. Red and blue colors indicate, respectively, positive and negative phases of each climate index; bars, squares, and the upper and lower parts of the error bars, respectively, denote the frequencies of the climate indices associated with observation (CRU), CAM ensemble mean, and the maximum and minimum frequencies of the climate indices produced by CAM ensemble members. The tag (or node) of each rainfall class is shown in bracket on the upper left corner of each panel. See Table 3.2 for brief descriptions of the climate indices considered in this study.

4.6 Global SST Anomalies and the Dominant Summer Rainfall Classes

In this sub-section, we further investigate how well CAM reproduces the link between different oceanic SST conditions and the rainfall classes depicted in Figure 4.3. Observation shows that rainfall class in Node 1 is associated with below-normal SST anomalies over the eastern and central equatorial Pacific, cold SST anomalies over the entire Indian Ocean and warm equatorial Atlantic Ocean (Figure 4.8a). Warm equatorial Atlantic Ocean provides the sub-region with large areas of boundary layer moisture build-up which makes the moisture laden southwesterly wind more buoyant in terms of moisture and energy (Odekunle and Eludoyin, 2008) and eventually results in above-normal rainfall (Omotosho and Abiodun, 2007), especially along the coast. Both the composites of SIM05 and CAM ensemble mean capture the SST anomaly conditions in Node 1 (Figure 4.8b, c).

Figure 4.8a shows that rainfall class in Node 2 is associated with above-normal SST anomalies that extend from eastern Pacific to central equatorial Pacific Ocean (i.e. El Nino phase), mildly warm SST anomalies over most of the Indian Ocean and moderately warm equatorial Atlantic Ocean. The local effect of El Nino over West Africa is to strengthen the easterly component of the trade winds anomalies across the Sahara Desert, thereby, depriving the sub-region of some substantial moisture necessary for rainfall formations during the northern hemispheric summer (Camberlin et al., 2001). The composites of SIM05 and CAM ensemble mean adequately capture SST anomaly conditions in this node (Figure 4.8b, c).

The states of SST anomalies in Node 3 are almost the same with those in Node 2, except that equatorial Atlantic Ocean features below-normal SST anomalies in Node 3 (Figure 4.8a). The cold SST anomaly extends westward beyond 25^{o}W along the equator, northward along the western flanks and almost encircle the sub-region. These conditions deprive the sub-region of boundary layer moisture, makes the little available moisture non-buoyant because of lack of kinetic energy and eventually results in extremely below-

normal rainfall. The composites of SIM05 and CAM ensemble mean adequately capture the SST anomaly conditions in Node 3 (Figure 4.8b, c).

Observed global SST conditions in Node 4 shows that its spatial rainfall anomaly class is influenced by mildly cold SST over the Pacific and Indian Oceans, and mildly warm Atlantic Ocean (Figure 4.8a). The mildly warm SST anomaly over the equatorial Atlantic dynamically ensures a quasi-static situation where the ITCZ is pushed deeply into the northern end of the sub-region. These enable the ascent and enhanced convection to lie over the Sahel, thus producing the anomalously wet conditions deep further inland. Contrary to the mildly cold SST conditions observed over the Pacific Ocean, composites of SIM05 and CAM ensemble mean feature La Nina events over the Pacific Ocean (Figure 4.8b, c). They however capture the sub-zero SST conditions over Indian Ocean and moderately warmer SST anomaly over the equatorial Atlantic.

Rainfall class in Node 5 is associated with sub-zero SST anomalies over the eastern domain of equatorial Pacific Ocean, relatively warm SST anomalies over west Pacific and Indian Oceans, sub-zero SST anomaly over the Gulf of Guinea and warmer pool off the coast of Guinea and Senegal northward (Figure 4.8a). Odekunle and Eludoyin (2008) are of the opinion that rainfall anomaly types of Node 5 are common during upwelling periods. They explained that the upwelling effect produces a localized offshore high pressure system which strengthens the maritime southwesterly air mass, forming coastal divergence while enhancing deep northward penetration of the summer rain producing mechanisms. This accounts for the occurring rainfall dipole which is the anomalously dry conditions over the coastal areas and vice versa over the Sahel. Composites of SIM05 and CAM ensemble mean, though, agree with observation on the state of SST anomalies over the eastern Pacific, they however simulate SST condition over Indian and Atlantic Oceans differently (Figure 4.8b, c).

Rainfall class in Node 6 is associated with below-normal SST anomalies that extend from eastern Pacific to central equatorial Pacific Ocean (i.e. la Nina), near-zero SST anomalies

over most of the Indian Ocean and moderately cold Atlantic Ocean (Figure 4.8a). A La Nina driven below-normal SST over the Atlantic Ocean has the tendency to reverse the local effect of El Nino over West Africa (Fontaine and Janicot, 1996; Ward, 1998). The consequence is a strengthened moisture influx into the Sahel. The available little moistures are non-buoyant due to lack of kinetic energy, thereby causing decrease or insignificant change in precipitation (Lutz et al., 2015). Though, the composites of SIM05 and CAM ensemble mean do not capture the SST anomaly conditions over the Pacific Ocean, they however are able to adequately reproduce the near-zero SST anomalies over Indian Ocean and moderately cold SST anomalies over the equatorial Atlantic Ocean (Figure 4.8b, c).

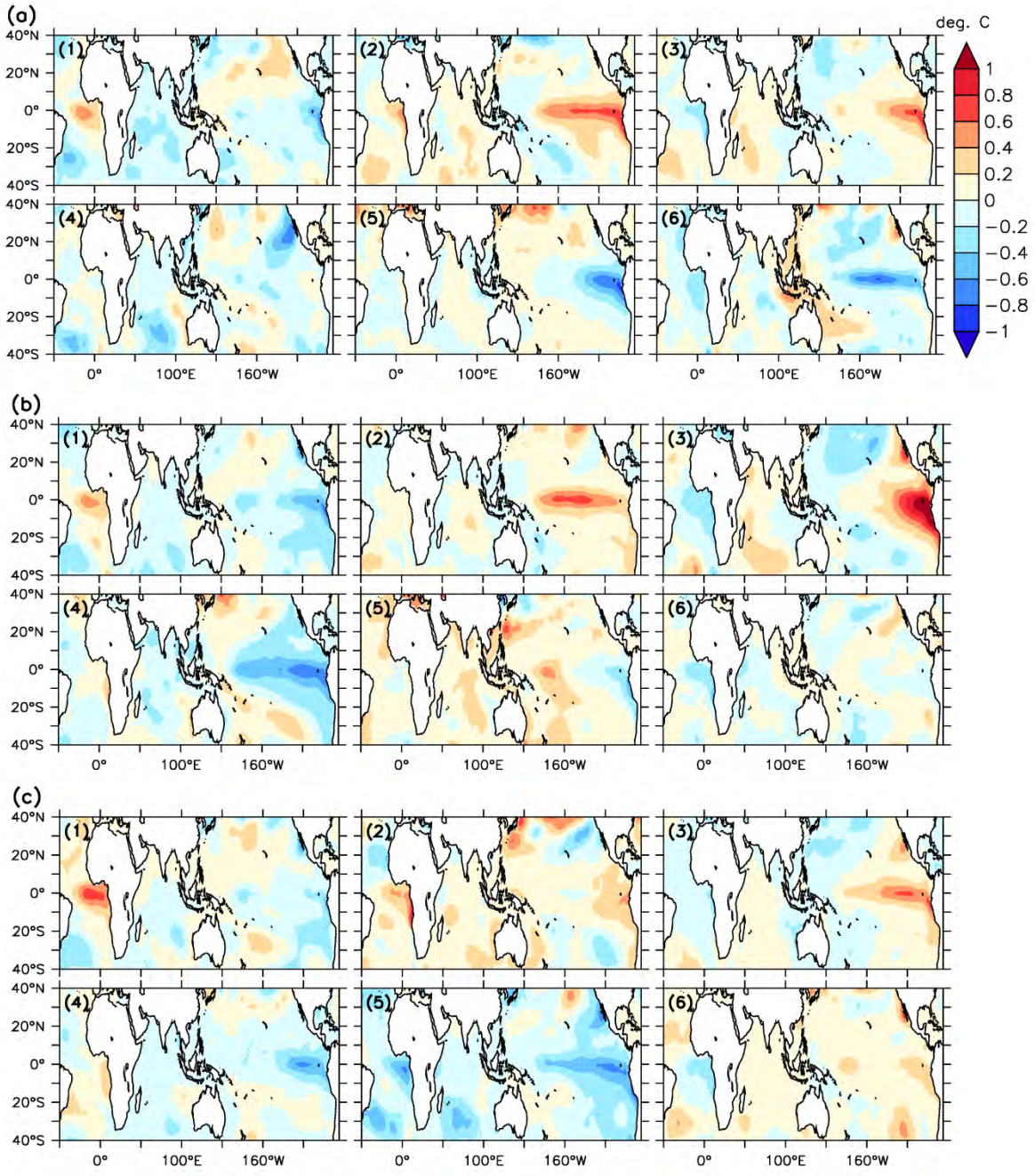

Figure 4.8 Composites of boreal summer global SST anomalies (^{o}C) for **(a)** observation, **(b)** SIM05 and **(c)** CAM ensemble mean classes. Pattern numbers, which correspond to the spatial classes of rainfall anomalies in Figure 4.3, are written on the upper left sides of each panel while the SST anomalies are relative to the 1961-2005 climatological mean.

4.7 Composites of Atmospheric Conditions Associated with the Dominant Summer Rainfall Classes

In this section, we examine how well CAM (SIM05 and the ensemble mean) reproduces the atmospheric conditions that are associated with the rainfall classes. Composites of dataset, i.e. CRU, SIM05, and CAM ensemble mean, in the spatial rainfall classes displayed in Figure 4.3 were separated and presented in Figure 4.9. We then examine the structures of the corresponding atmospheric fields such as the vertically integrated moisture flux convergence with the corresponding 850hPa level winds, vertical velocity field at 500hPa level, and the vertical profiles of vertical velocity with the corresponding zonal winds during the monsoon peak in August (Figures 4.10, 4.11 and 4.12).

CAM has the capability to simulate satisfactorily three of the four already identified rainfall classes over West Africa in summer. The best agreement between the composites of CRU and CAM (SIM05 and ensemble mean) occurs in FG – a north-south dichotomy group, i.e. Nodes 1 and 6 (Figure 4.9). In this group, spatial correlations (r) between CRU and CAM simulations are high ($0.53 \leq r \leq 0.73$); implying that CAM simulates the spatial structures of the group almost as observed. Reanalysis and CAM features comparable patterns in the associated regional dynamics of this group. Both SIM05 and ensemble mean agree with the reanalysis that Node 1 is associated with anomalous moisture laden maritime southerlies which converges the vertically integrated moisture fluxes on encountering the easterlies from the central parts of Africa at 850hPa level (Figure 4.10). These drive anomalous ascent at 500hPa level over the coastal regions (Figure 4.11). The vertical profiles of the peak of monsoon system in August features enhancements of both the AEJ and TEJ, weakened westerly monsoon flow, deep anomalous ascent from 10^{o}N equator ward and deep anomalous descent motion north of 10^{o}N (Figure 4.12). Reanalysis and CAM also agree that anomalies of vertically integrated moisture flux convergence, 850hPa level winds, vertical velocity field at 500hPa level and the vertical profiles of vertical velocity and zonal winds during the monsoon peak in August for Node 1 rainfall class are opposite of those for Node 6 (Figures 4.10, 4.11 and 4.12). Therefore,

CAM simulates adequately the associated regional atmospheric conditions of rainfall classes as observed in FG – a north-south dichotomy group.

There is a split in agreement between the composites of CRU and CAM in SG - a group of same anomaly signs across the entire sub-region. Figure 4.9 shows that spatial correlations between CRU and CAM simulations are high in Node 3 ($0.61 \leq r \leq 0.65$) – a 'large drought' class, but poor in Node 4 ($0.29 \leq r \leq 0.37$) – a 'large flood' class. This implies that CAM simulates the spatial structures of Node 3 almost as observed while it fails to simulate that of Node 4 satisfactorily. There are agreements between reanalysis and CAM on the simulations of regional atmospheric conditions in Node 3. Both SIM05 and ensemble mean agree with the reanalysis that Node 3 is associated with ridges from anomalous anti-cyclonic circulation centered over the Atlantic Ocean around 10 – 20^{o}N at 850hPa level and also with the divergence of vertically integrated moisture fluxes (Figure 4.10). Sahel and the coastal regions experience two different predominant wind directions – northwesterly and easterlies respectively. These drive anomalous descent at 500hPa level over the sub-region (Figure 4.11). The vertical profiles of the peak of monsoon system in August features an enhanced AEJ, weak TEJ, weakened monsoon flow and deep anomalous descent from 12^{o}N equator ward (Figure 4.12). It is only the reanalysis and SIM05 that show that the associated regional atmospheric conditions of rainfall classes in Node 3 are opposite of those in Node 4 (Figures 4.10, 4.11 and 4.12); meaning that there are some disparities between reanalysis and ensemble mean concerning Node 4. Therefore, inferences have shown that CAM does not have the capability to simulate rainfall classes of Node 4 and its associated regional atmospheric conditions adequately.

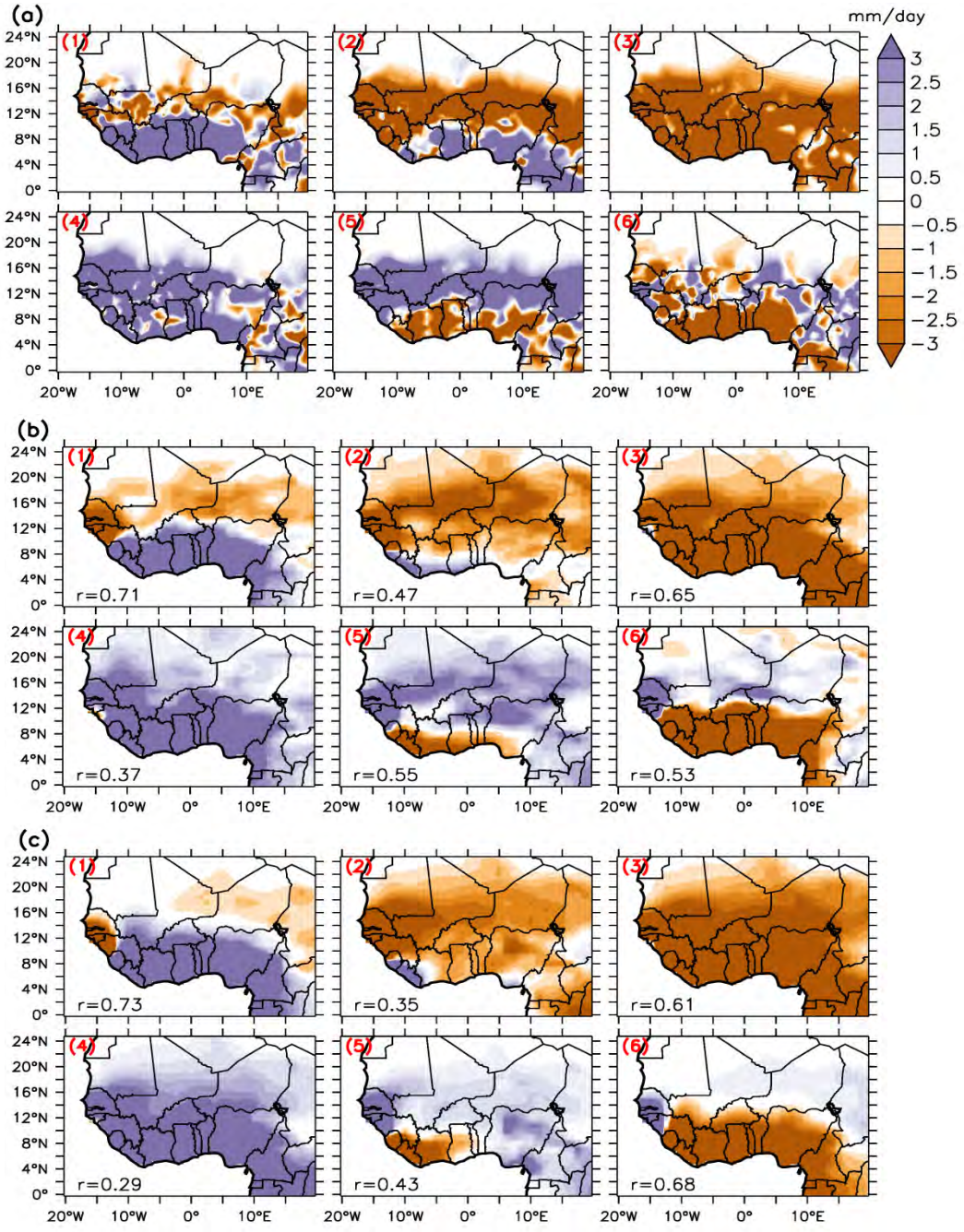

Figure 4.9 Composites of the spatial patterns of boreal summer rainfall anomalies (mm day^{-1}) over West Africa for **(a)** observation, **(b)** SIM05 and **(c)** CAM ensemble mean simulation. Pattern numbers, which correspond to spatial classes of rainfall anomalies in Figure 4.3, are written on the upper left sides of each panel while the values of spatial correlations of SIM05 and ensemble mean with corresponding observed rainfall class are written on the bottom left of panels **b** and **c** respectively.

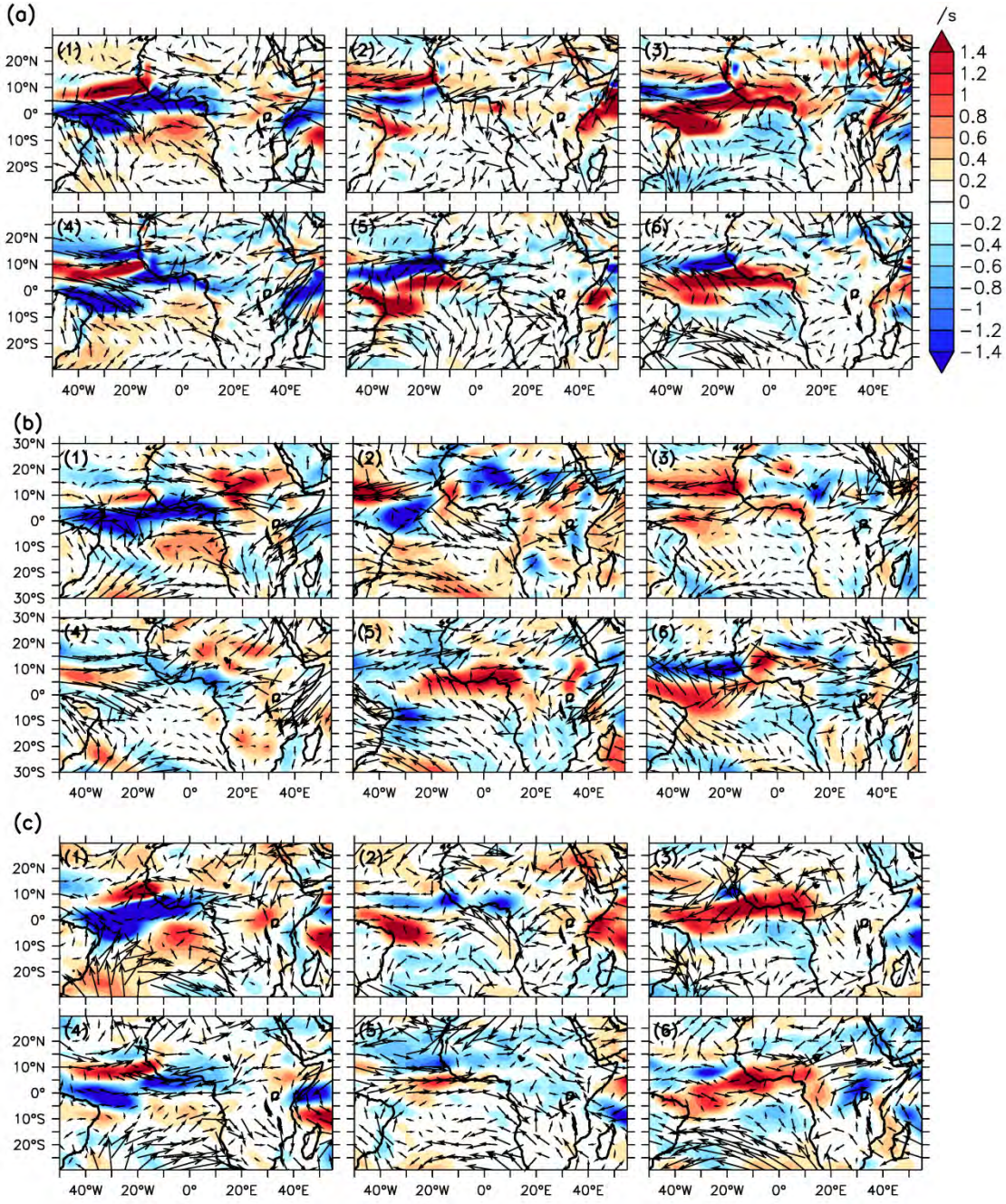

Figure 4.10 Composites of the spatial patterns of boreal summer vertically integrated moisture flux convergence anomalies (shaded; $x10^{-5}$ s^{-1}) and the corresponding 850hPa level wind anomalies (arrows; ms^{-1}), relative to the 1961-2005 climatological mean, for **(a)** observation, **(b)** SIM05 and **(c)** CAM ensemble mean simulation. Pattern numbers, which correspond to spatial classes of rainfall anomalies in Figure 4.9, are written on the upper left sides of each panel. Blue shading indicates resultant convergence while red shading indicates resultant divergence.

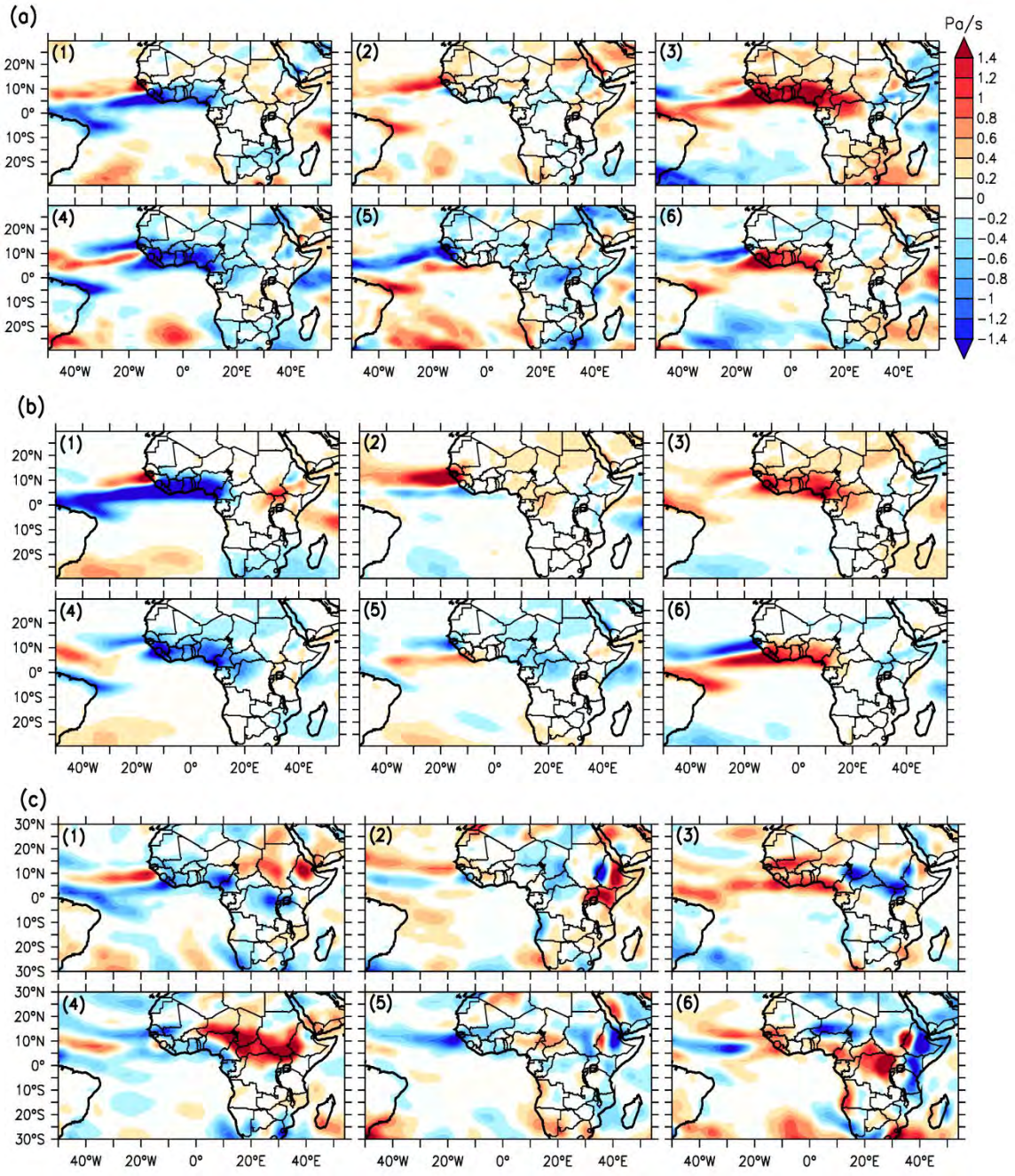

Figure 4.11 Composite of the spatial patterns of boreal summer vertical velocity anomalies (omega; x10^{-2} Pa s^{-1}) at 500hPa level, relative to the 1961-2005 climatological mean, for **(a)** observation, **(b)** SIM05 and **(c)** CAM ensemble mean simulation. Pattern numbers, which correspond to spatial classes of rainfall anomalies in Figure 4.9, are written on the upper left sides of each panel. Blue shading indicates resultant ascent (i.e. upward motions) while red shading indicates resultant descent (i.e. downward motions).

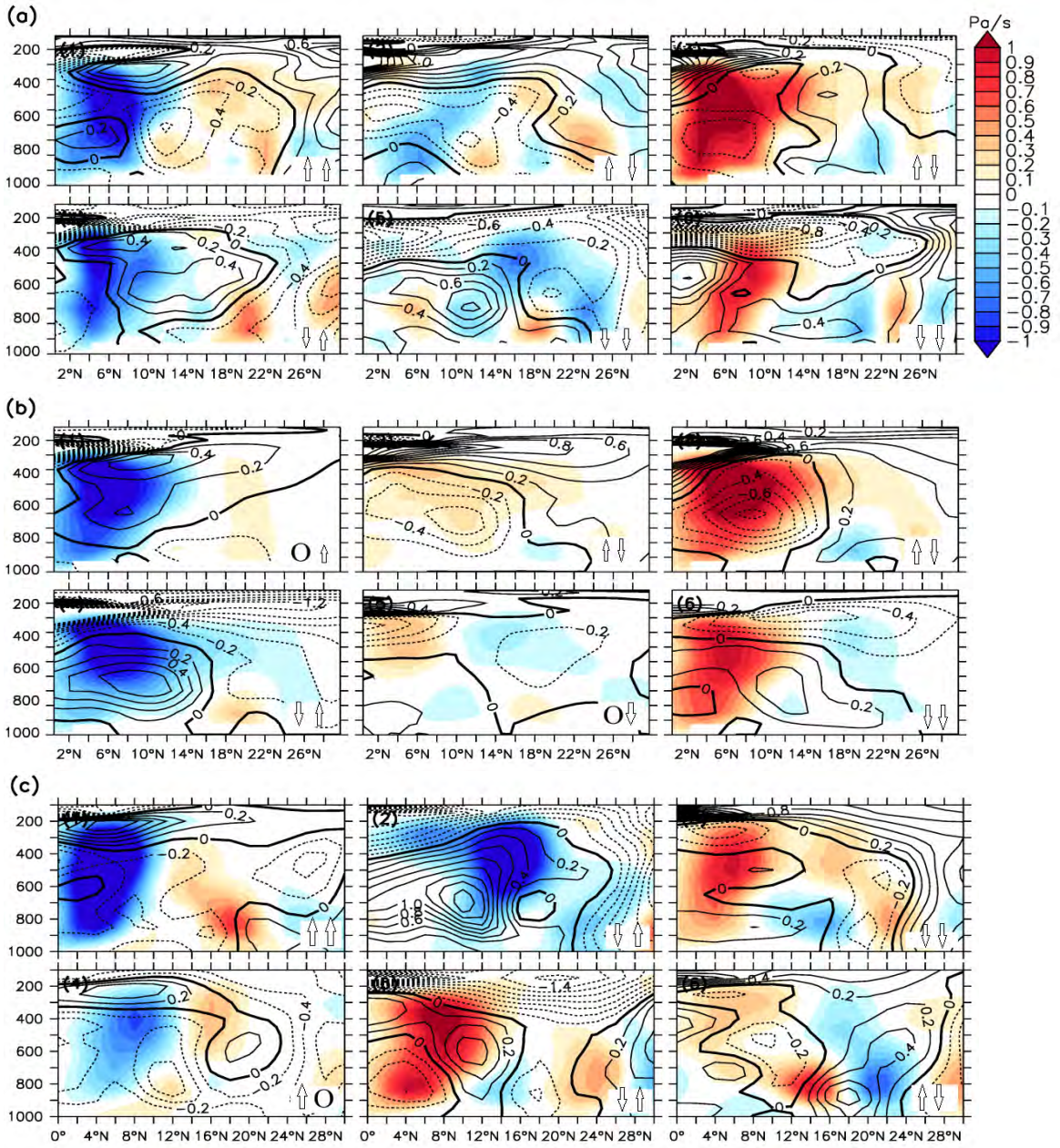

Figure 4.12 Composites of vertical profile of monsoon system in August – anomalies of zonal wind (contour; ms^{-1}) and vertical velocity (shaded; $x10^{-2}$ Pa s^{-1}) averaged over 10^{o}W to 10^{o}E, relative to the 1961-2005 climatological mean, for **(a)** observation, **(b)** SIM05 and **(c)** CAM ensemble mean simulation. Pattern numbers, which correspond to classes of rainfall anomalies in Figure 4.9, are written on the upper left sides of each panel. Blue shading indicates resultant ascent (i.e. upward motions) while red shading indicates resultant descent (i.e. downward motions). ↑, ↓ or O signs, at the bottom right of each panel, respectively represent strengthened, weakened and nil change in the strength of (where the first sign concerns) AEJ and (the second sign) TEJ.

The worst agreements between the composites of CRU and CAM are in TG, i.e. Nodes 2 and 5. Figure 4.9 shows that the spatial correlations between the simulated and observed patterns are weak ($0.35 \leq r \leq 0.55$). This means that CAM (SIM05 and ensemble mean) does not simulate the spatial rainfall anomalies of TG as observed. There are also some disagreements between reanalysis and CAM on the simulations of regional atmospheric conditions for this group (Figures 4.10, 4.11 and 4.12). Observation attributes Node 2 spatial rainfall anomaly class with anomalous northeasterly winds at 850hPa level, divergence of vertically integrated moisture fluxes, mild descent motions at 500hPa level, enhanced AEJ and weak TEJ. In disagreement with observation, SIM05 fails to reproduce the divergence of vertically integrated moisture fluxes, as well as the vertical velocity conditions during the peak of monsoon in August. Ensembles mean, in addition to inability to capture the anomalous winds at 850hPa level; also fails to reproduce respectively the enhanced and weakened AEJ and TEJ. Similarly, only few of the simulated anomalies of the associated regional atmospheric conditions in Node 5, the opposite of Node 2, are consistent with their corresponding rainfall anomalies.

4.8 Summary

In summary, this chapter has shown that CAM can give realistic simulation of the observed boreal summer rainfall climatology over West Africa. The model gives a realistic simulation of the inter-annual variation of the summer rainfall (area averaged); in addition to its capability to realistically capture most of the atmospheric dynamics of the summer rainfall over West Africa. CAM has the capability to simulate satisfactorily three of the four already identified summer rainfall classes over West Africa – the north-south dichotomy classes (i.e. wet Sahel – dry Guinea or vice versa) and the 'large drought' classes. The model however links these dominant rainfall classes to more than one climate index making it difficult to associate any of the rainfall classes with a particular climate index. Nevertheless, the composites of global SST patterns are however consistent with the observed rainfall patterns over West African sub-region. On inter-annual time scale, CAM ensemble mean, in addition to being able to capture the occurrence and persistence of the dominant rainfall classes, is capable of reproducing any

of the observed dominant rainfall classes once out of three simulations (i.e. η = 33%); while at least one ensemble member, out of the 50 members, has 84% chance to randomly reproduce the right rainfall class. However, if the 'one ensemble member' happens to be SIM05, then it is capable of reproducing any of the observed spatial rainfall anomaly classes twice out of five simulations (i.e. η = 42%) on inter-annual time scale. This chapter has therefore identified the spatial classes of rainfall anomalies that CAM can adequately simulate and those it struggles to reproduce over West Africa during summer seasons. The result is consistent with Fontaine et al. (1995) who investigated the relationships between the West African rainfall anomaly patterns and tropospheric wind changes in August – the peak of monsoon.

5 Characteristics of Spring Maximum Air Temperature Patterns over West Africa

In this chapter, we present and discuss the results of the characteristics of boreal spring near-surface (2m) maximum air temperature patterns over West Africa, as observed by CRU and simulated by CAM. Firstly, we carried out the performance evaluation of CAM in simulating the climatology of the spring maximum air temperature pattern. Secondly, the characteristics of the six dominant spring (maximum) temperature classes (anomalies), obtained using SOM analysis as described in Chapter 3, and the evaluations of how well CAM reproduces them are then discussed. The characteristics of the dominant spring temperature classes considered are the inter-annual and decadal variability, transition, and persistence. Lastly, the chapter examined the influence of atmospheric tele-connections on the observed and simulated classes, and investigates the capability of CAM in reproducing the atmospheric dynamics that produces each spring temperature classes.

5.1 Climatology of Spring Maximum Air Temperature over West Africa

5.1.1 Inter-annual Variations of Spring Maximum Air Temperature over West Africa

There are upward trends in the observed (CRU) temperature, averaged over the West African sub-region. Figure 5.1a shows that the observed temperature majorly featured sub-zero anomalies before 1982 and above-zero anomalies after then. This is consistent with the upward trends in temperatures over Africa and the world in general (Hulme et al., 2001; Collins, 2011). The figure also shows that CAM simulations (ensemble mean and members) capture the upward trends. There are however disagreements within 1990 and 1993 when the ensemble mean and observation feature different anomaly signs. The inter-annual variability as produced by CAM ensemble members spread around and envelope the observed temperature, in most of the years; and they also exhibit upward trends.

The relationships between the ensembles mean, ensemble members and the observation are strongly direct. For instance, the correlation coefficient (r) between CRU and the ensemble mean is significantly large, $r \approx 0.8$ (Figure 5.1b). Figure 5.1b also shows that the correlation coefficient between CRU and the individual ensemble member ranges between 0.4 and 0.8. On inter-annual basis, the ensemble mean matches closely the observed temperature (Figure 5.1a). The closeness is also supported by the low normalised standard deviation of the ensemble mean (Figure 5.1b). The normalised standard deviations of all ensemble members are greater than that of the ensemble mean (Figure 5.1b); because the averaging performed to derive the ensemble mean may have filtered out the simulated variability. CAM has therefore demonstrated the ability to reproduce the inter-annual variations of the observed maximum air temperature anomaly, with low discrepancies, over West Africa.

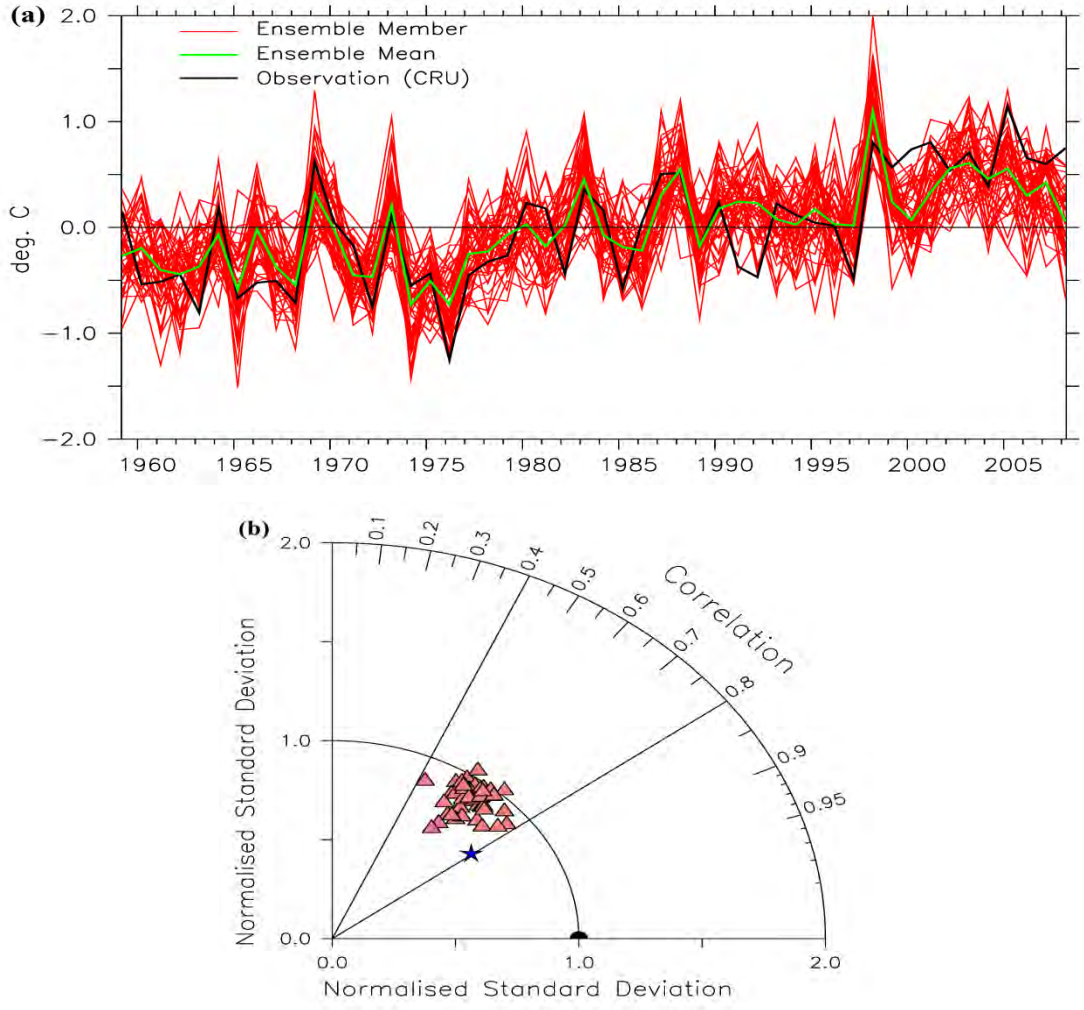

Figure 5.1 (a) Inter-annual variations of boreal spring near-surface maximum air temperature anomalies (^{o}C) averaged over West Africa. **(b)** Taylor diagram, of panel a, showing the normalized standard deviations and the correlation coefficients of simulations (CAM ensemble mean: blue star; and, ensemble members: red triangles) with observation (CRU: black semi-circle).

5.1.2 Monthly Variations of Spring Maximum Air Temperature over West Africa

Both the model and observation agree that, annually, all climatic zones in West Africa experience two peaks of maximum air temperature; the primary being in boreal spring season (i.e. the months of March, April and May) while the secondary peak, which is lower in value, is observed during the late days of boreal autumn (Figure 5.2a). They also agree that Sahel region is always warmer / hotter than both the Savannah and coastal

Guinea regions, except during the boreal winter. Coastal Guinea is the coolest among the three zones year in year out. Annual minimum maximum temperatures are observed over all climatic zones during the core rainy season (i.e. boreal summer: Figure 5.2a). These could be attributed to increased cloud cover and moisture influx during these periods. Figure 5.2b shows that CAM ensemble mean is able to reproduce the observed monthly means of (maximum) temperature distributions in all climatic zones of West Africa. CAM is also able to reproduce the peaks as well as the boreal summer minimum. Though, it appears that CAM under-estimates the temperature in all climatic zones (Figure 5.2b).

Similarly, the month-latitude distribution of temperature over the sub-region shows that the core of hottest temperature oscillates annually with the Inter-Tropical Discontinuity (ITD). Figure 5.2c shows that the hot core, which extends to the equatorial region during the boreal spring season, gradually moves northward with ITD as the year progresses. It is almost bisected by the ITD. Lavaysse et al. (2009) have shown that the hot core corresponds to the position of thermal-heat-depression known as the West African heat low – a vital constituent of the West African monsoon system. The heat low however lags behind the ITD during the southward retreat after the monsoon season. CAM ensemble mean adequately captures the observed mean annual cycle of maximum temperature over West Africa (Figure 5.2d). The model captures the annual oscillation of temperature hot core, its bisection by the ITD, the observed lagging during the southward retreat periods, as well as the relatively lower temperature over the equatorial regions during the monsoon peak periods.

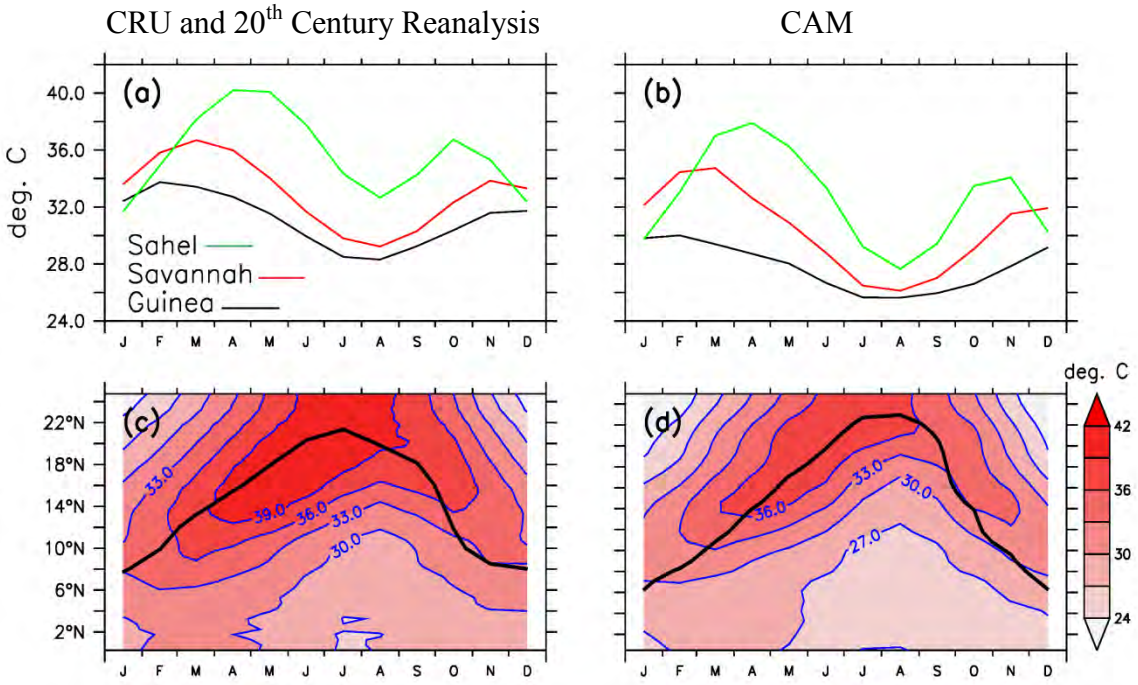

Figure 5.2 West African monthly mean maximum air temperature (^{o}C) averaged over 10^{o}W to 10^{o}E for **(top row)** the climatic zones and **(bottom row)** the time-latitude cross section (shade; contour; ^{o}C). Observations and simulations are respectively on the left and right columns while the location of the ITD (the contour of the zero meridional wind at the surface) is indicated by the black solid line in panels **c** and **d**.

5.1.3 Spatial Variations of Spring Maximum Air Temperature over West Africa

Spatial distribution of the observed mean maximum air temperature features two types of gradients over West Africa during boreal spring seasons (Figure 5.3a). These are the meridional (north-south) and zonal (east-west) gradients. In both cases, the least temperature are observed at the coastal zones as temperature then increases northward or eastward, respectively, for meridional or zonal gradients. Meridional gradient prevails over the coastal zones of the Gulf of Guinea at about 0.75^{o}C per latitude; while the stronger zonal gradient (> 3^{o}C per longitude) can be found west of the sub-region in coastal parts of Mauritania and Senegal. Center of maximum temperature extends in the east-west directions from around 12^{o}N to about 18^{o}N. Figure 5.3b shows that CAM ensemble mean is able to capture the spatial distribution of maximum air temperature over West Africa. The model reproduces the temperature gradients as well as the position

of the center of maximum temperature. Though, some under-estimations are noticed when physical comparisons of Figure 5.3 (a, b) are conducted; nevertheless, the evaluated ranked probability skill score (RPSS: Mason, 2004; Weigel et al., 2006) reveals that CAM has skill in simulating maximum air temperature over West Africa (not shown). Here, the RPSS is generally positive but less than 0.4. This however could be attributed to poor parameterization of physical processes over the sub-region (Rusticucci and Kousky, 2002; Flocas et al., 2004).

The total cloud fraction over West Africa, during boreal spring, is though reproduced by CAM ensemble mean, but with some discrepancies (Figure 5.3c, d). Both the observation (Figure 5.3c) and simulation (Figure 5.3d) show that the coastal zone of the Gulf of Guinea is cloudier than both Savannah and Sahel regions and that the cloud coverage decreases northward. The cloudier areas coincide with areas of relatively lower temperature and vice versa (Figure 5.3a, b, c, d). However, the model is not able to adequately capture the observed north-south gradient in total cloud fraction as the simulated gradient smoothly extends in east-west orientation. The ability of CAM to reproduce total cloud fraction has shown that cloudiness has impact on the degree of hotness or coldness of air temperature over the sub-region.

The simulated vertical velocity (i.e. the omega field) at 850hPa level, over West Africa in spring, has the same magnitudes with the observation (reanalysis: Figure 5.3e, f); exceptions are the location of the maximum upward motion (> 12E-02 Pa s^{-1}). While the observed maximum upward motion stretches in the east-west direction from the coast of Senegal, grazes the edges of northern Nigeria and terminates over the northern parts of Cameroon (Figure 5.3e); the simulated maximum upward motion is isolated over the borders of Senegal, Mauritania, Mali and Guinea (Figure 5.3f). Observation and simulation also agree that downward motions dominate from latitude 17^{o}N pole ward, and also over the coastal zones of Gulf of Guinea, though at different magnitudes. These disparities have been attributed to some atmospheric processes that are not well replicated or represented over some areas in the model (Trenberth et al., 2000). Therefore, Figure

5.3(e, f) has shown that CAM adequately simulates the spatial distributions of the omega field, vis-à-vis atmospheric energy budget, but with some disparities.

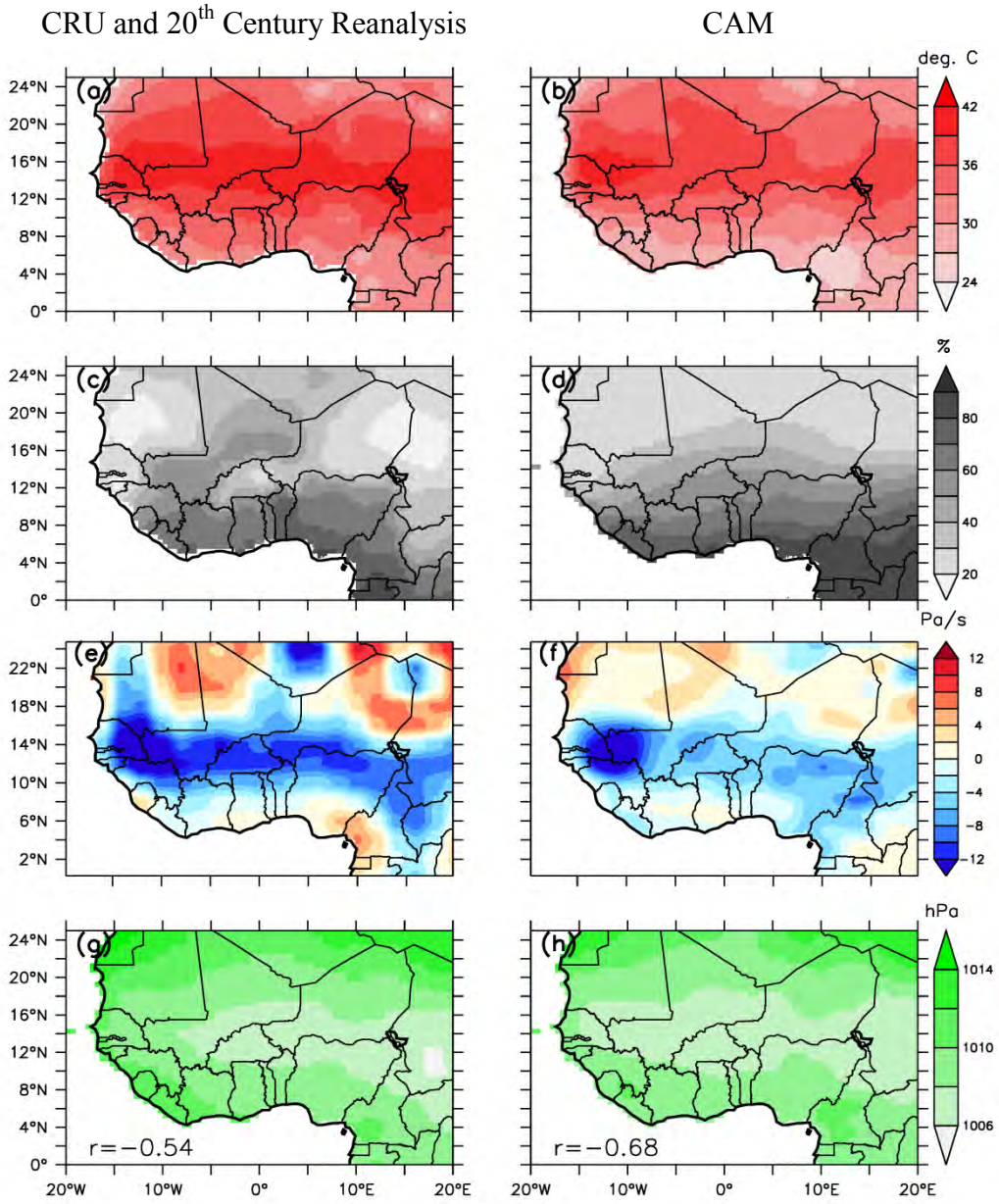

Figure 5.3 Spatial distribution of mean boreal spring **(top row)** maximum air temperature (^{o}C); **(second row)** total cloud fraction (%); **(third row)** vertical velocity (omega; 10^{-2} Pa s^{-1}) at 850hPa level; and **(bottom row)** mean sea level pressure (MSLP: hPa), over West Africa. Observations and simulations are respectively on the left and right columns while the values of the spatial correlation, r, between MSLP (panels **g** and **h**) and maximum air temperature (panels **a** and **b**) are written on the bottom left of panels **g** and **h** respectively.

The mean sea level pressure (MSLP) over West Africa, during boreal spring, is adequately reproduced by CAM ensembles mean (Figure 5.3g, h). Both the observation (Figure 5.3g) and simulation (Figure 5.3h) agree that the coastal zone of the Gulf of Guinea is characterized by higher MSLP which decreases northward. East-west elongation of minimum MSLP is positioned over 11^{o}N to about 17^{o}N, MSLP then increases pole ward. Spatial distribution of MSLP also exhibit meridional and zonal gradients that are similar to those of spatial distribution of maximum air temperature (Figure 5.3a, b). The center of minimum MSLP coincides with the positions of the maximum temperature (Figure 5.3a, b). This supports the definition of the West African heat low, by Lavaysse et al. (2009), as a region of low surface pressures and high surface temperatures. In addition, the spatial correlations, r, between maximum air temperature and MSLP range from -0.54 to -0.68; meaning that the relationship between maximum air temperature and MSLP is strongly inverse (Figure 5.3g, h). These imply that the deepening of West African MSLP induces higher temperatures, and by extension the stronger heat low, while the filling of the MSLP does the opposite. Therefore, CAM is effectively capable of simulating the West African heat lows. The realistic simulations of the total cloud fraction, the omega field and MSLP indicate that CAM captures the atmospheric dynamics that influence and modulate the boreal spring maximum air temperature over West Africa.

5.2 Dominant Classes of Maximum Air Temperature over West Africa in Spring

A 3x2 SOMs archetype of the observed (CRU) and the simulated (CAM) spring maximum air temperature anomaly classes over West Africa is presented in Figure 5.4. The figure depicts the dominant spring temperature classes over the region. These dominant classes can be classified into three groups in such a way that each group contains two opposite classes of temperature anomaly. Nodes 1 and 6 are classified as the first group (TMG1). Node 1 features below-normal temperature anomalies over the entire

Sahel regions, with coldest anomalies positioned over the northern parts of Niger Republic, and a band of neutral anomalies that stretch from the coast to Savannah (at about 11^{o}N: Figure 5.4). Node 6 is the opposite class of Node 1. Observation (CRU) shows that Node 1 accounts for 18% of boreal spring temperature classes while Node 6 accounts for 16%. These imply that the observed TMG1 accounts for a total of 34% of occurrences of maximum air temperature classes within the experimental time frame (1961 – 2005). However, there are disparities in the frequencies of occurrences of TMG1 as simulated by CAM (ensemble mean and ensemble members). While CAM ensemble members' average agree with CRU on the frequency of occurrence of TMG1; CAM ensemble mean however grossly under-estimates the frequencies of occurrences of both nodes. That is, CAM accounts for 18% (ensemble mean) and 36% (ensemble members' average) of the entire datasets.

Nodes 3 and 4 are classified as the second group (TMG2). Node 3 features above-normal temperature over the entire West Africa, with warmest anomalies positioned over the northern parts of Mali (Figure 5.4). Node 4 is the opposite class of Node 3. CRU shows that Node 3 accounts for 20% of boreal spring temperatures while Node 4 accounts for 24%. These imply that the observed TMG2 accounts for a total of 44% of occurrences of temperature classes within the experimental time frame. However, while CAM ensemble mean over-estimates the frequencies of occurrences of both nodes (totaling 56%), CAM ensemble members' average under-estimates their frequencies of occurrences (34% in total).

In comparison to TMG1 and TMG2, the third group (TMG3) lacks extreme anomalies (Figure 5.4). TMG3 consists of classes in Nodes 2 and 5; and they feature normal temperature anomaly conditions almost over the entire sub-region. The only exception is the sub-zero anomalies over the northern parts of Niger-Chad borders in Node 2 and vice versa in Node 5. The observed frequencies of occurrences are equal in both nodes (11% a-piece). The frequency of occurrence of Node 2 is adequately captured by CAM ensemble mean but CAM ensemble members' average over-estimated it by 4%. The

frequency of occurrence of Node 5 is generally over-estimated by CAM. CAM therefore accounts for 28% (ensemble mean) and 32% (ensemble members) of the entire datasets in TMG3.

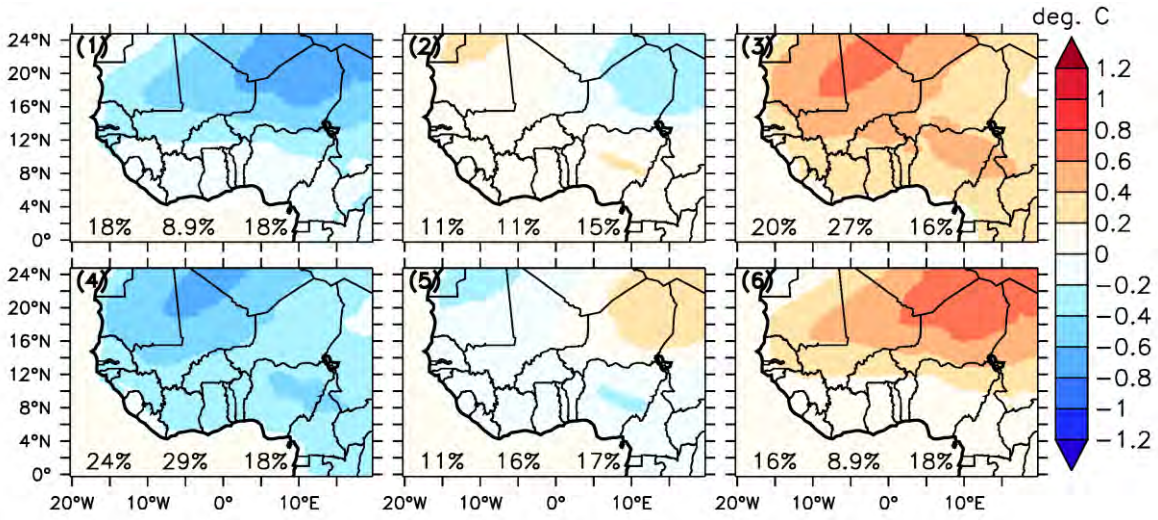

Figure 5.4 SOM classifications of unified spatial patterns of boreal spring maximum air temperature anomalies (^{o}C) over West Africa for observation and simulations. Class numbers are written on the upper left sides of each panel while the frequencies of occurrences (%) are shown on the bottom left, middle and right respectively for CRU, CAM ensemble mean and the average of individual ensemble member simulations.

5.3 Inter-annual Variability of the Dominant Spring Maximum Air Temperature Classes over West Africa

There are disparities in the ways CAM ensemble mean and CAM ensemble members reproduce the inter-annual sequence of the dominant spring temperature anomaly classes over West Africa. Figure 5.5(a, b) shows that ensemble mean is unable to reproduce the inter-annual variation of all temperature classes; i.e. Node 1 is synchronized once, the nodes in TMG2 were synchronized six times each while TMG3 and Node 6 are not featured in the synchronization process. Meaning that, out of 45 spring seasons, ensemble mean only have 13 seasons of agreement with CRU. Meanwhile, there are however no cases of disagreement between CRU and ensemble members. Correct simulation of the observed temperature classes by ensemble members requires a minimum of one ensemble member (e.g. 1964: Figure 5.5a, b). The implication here is that CAM ensemble mean

reproduces CRU temperature classes 29% of the time (i.e. synchronization (η) = 29%) while at least one ensemble member, probably at random, will reproduce the right spatial class throughout the experimental time-frame.

Figure 5.6 shows that 18 ensemble members have higher synchronizations than ensemble mean. It also shows that the 48th simulation (SIM48) has the highest synchronization (η = 44.4%; i.e. 20 cases of agreements with CRU). This shows that, on inter-annual basis, SIM48 have greater ability to correctly reproduce the occurrences of maximum air temperature classes than any other ensemble members and ensemble mean. This therefore calls for review of the practice whereby an ensemble mean is based on uniformly averaging the members rather than the performance of individual ensemble members which may give better prediction.

Figure 5.5 also shows that whenever CRU and CAM ensemble mean synchronizes, the number of CAM ensemble members that agree with CRU and the ensemble mean are always equal (e.g. 1968, 1987, 1998, etc). This number however has a minimum of 14 (in 2001) and a maximum of 31 (in 1974) ensemble members. The reason(s) for this may not be unconnected to the fact that CAM correctly reproduces occurrence of temperature classes because all the correct classes are included in the 13 cases of agreement between CRU and the ensemble mean; or that the correct ensemble members might have dominated the wrong members.

There are agreements, as well as disagreements, between CRU and CAM ensemble mean in the transition and persistence of the observed temperature classes (see Section 4.3 for explanations on transition and persistence). Few instances in Figure 5.5 show that CAM ensemble mean captures the transition of Node 3 to Node 1 from 1988 to 1989; but fails to capture the transition of Node 1 to Node 2 from 1989 to 1990. CAM ensemble mean also captures the persistence of Node 4 from 1974 to 1976 and Node 3 from 1987 to 1988. However, it fails to capture the persistence of Node 1 from 1966 to 1967; and that

of Node 6 from 1980 to 1981. Low synchronization of CAM ensemble mean with CRU ($\eta = 29\%$) may be responsible for these failures.

Observationally, the most persistent temperature classes are Nodes 1 and 4 while the class with highest cases of persistence is Node 3 (Figure 5.5). Nodes 1 and 4 each persist for two years (Node 1 – 1965 to 1967; Node 4 – 1974 to 1976) while Node 3 has two cases of persistence. CAM ensembles mean however captures Nodes 3 and 4 as the most persistent classes and Node 4 as the class with highest cases of persistence. In agreement with both CRU and CAM ensembles mean, ensemble members show that Node 4 is the most persistent temperature class (Figure 5.6). In disagreement with CRU, ensemble members feature Node 4 as the class with highest cases of persistence; here, only 10 ensemble members agree with CRU that Node 3 has the highest cases of persistence.

5.4 Decadal Frequency of the Dominant Spring Maximum Air Temperature Classes over West Africa

The decadal frequencies of maximum air temperature classes feature upward trends in the observed temperature anomalies (Figure 5.7). Sub-zero anomaly classes (Nodes 1 and 4) are frequent within 1960s to 1990s; the positive anomaly classes (Nodes 3 and 6) are frequent with 1980s to 2000s while the near-normal anomaly classes (Nodes 2 and 5) are uniformly distributed within 1970s and 1990s. These observed characteristics are consistent with the upward trends in temperatures over Africa (Hulme et al., 2001; Collins, 2011). Figure 5.7 show that CAM ensemble mean captures the upward trends, especially in TMG2 where ensemble mean depicts its maxima within 1960 and 1970 for Node 4 and within 1980s to 2000s for Node 3. The spread in the decadal frequencies as produced by CAM ensemble member envelopes the observed decadal frequencies, in most years; and they also exhibit upward trends.

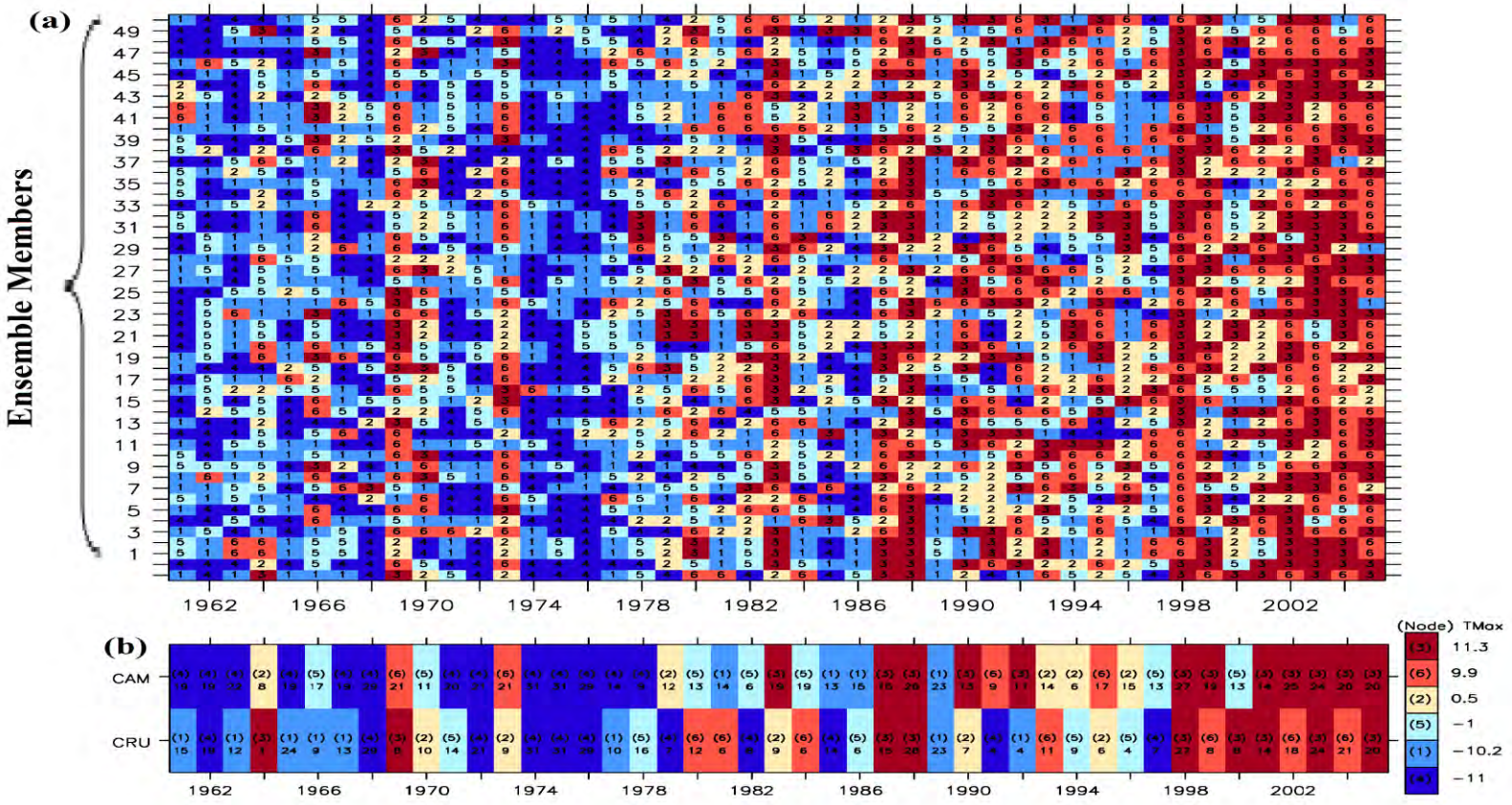

Figure 5.5 Inter-annual variability of spatial classes of maximum air temperature anomalies (^{o}C), depicted in Figure 5.4; **(a)** as simulated by 50 CAM ensemble members, CAM ensemble mean (upper bottom row) and observation (CRU: bottom row) and **(b)** an enlarged last two bottom rows of panel a showing the ensemble mean (upper row) and the observation (bottom row) (the numbers in brackets (i.e. 1 – 6) show the nodes of temperature classes while the colours indicate the mean temperature anomalies over the sub-region. The number under the nodes shows the number of the ensemble members that agree with CRU observation or with the CAM ensemble mean simulations on the temperature class).

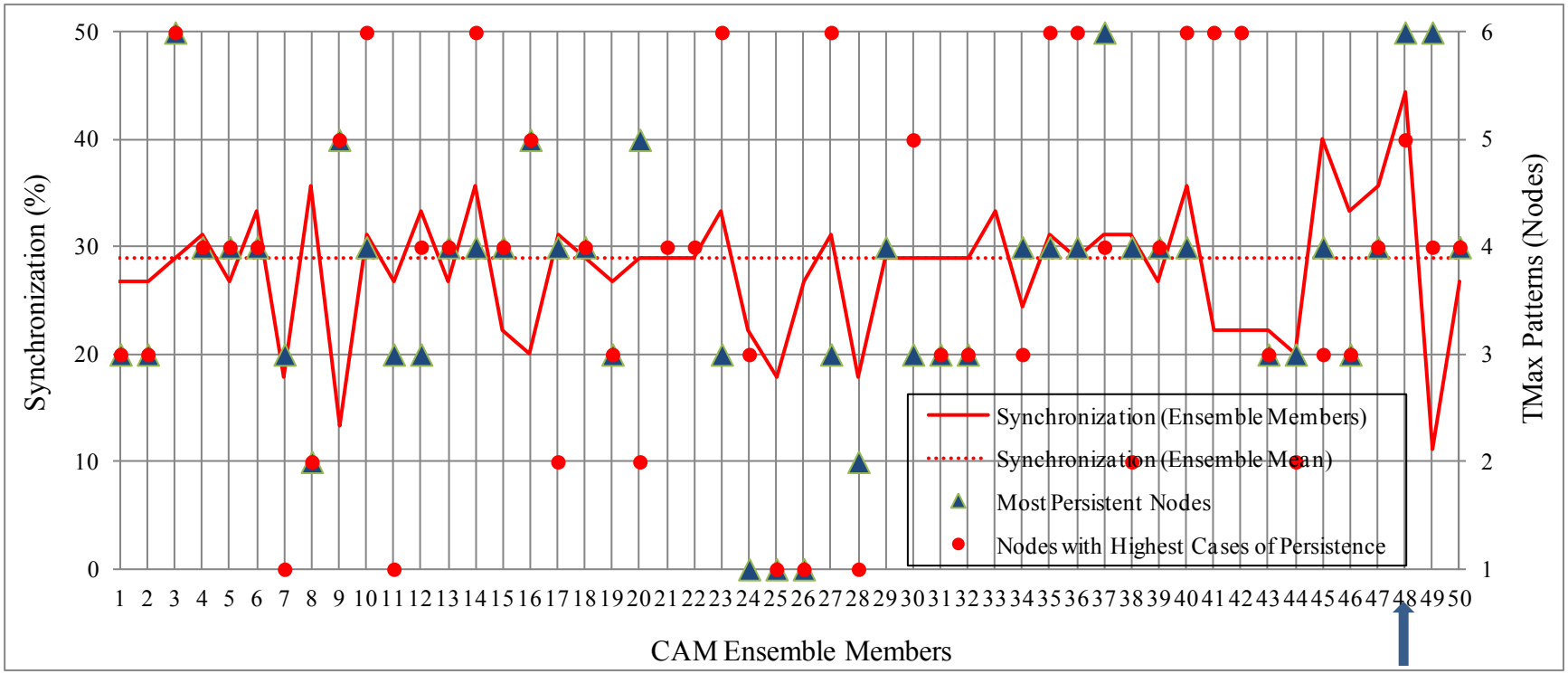

Figure 5.6 Synchronization (%; left y-axis) and persistence (nodes; right y-axis) of simulated temperature classes in reference to observation. The blue arrow points to the ensemble member with the highest synchronization (the 48th simulation: SIM48).

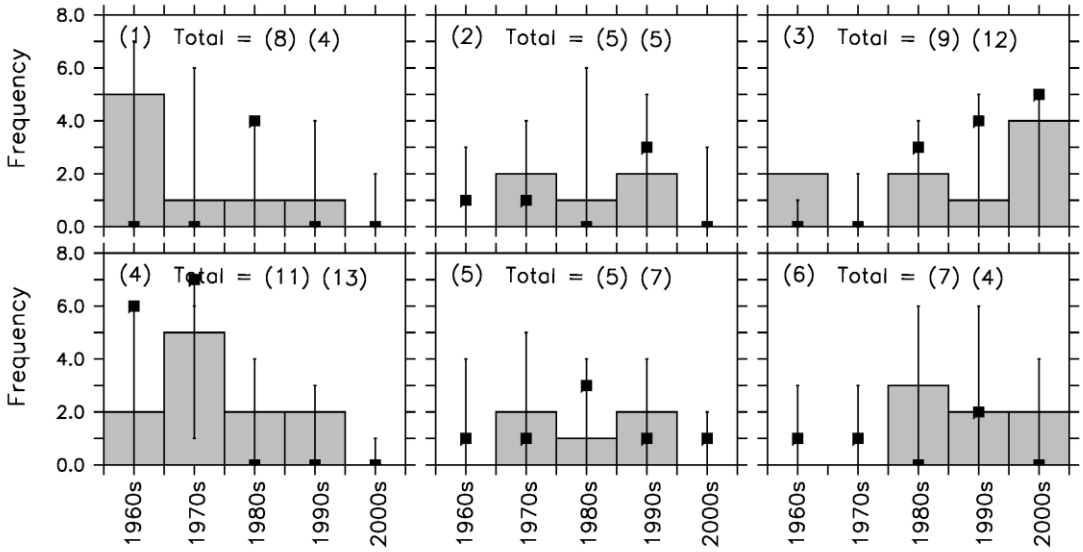

Figure 5.7 Decadal frequencies of spatial classes of maximum air temperature anomalies displayed in Figure 5.4. Grey bars: decadal frequencies of temperature classes from CRU; black squares: decadal frequencies of temperature classes from CAM ensemble mean; while the upper and lower parts of the error bars, respectively, indicate the maximum and minimum decadal frequencies of temperature classes produced by CAM ensemble members. In brackets are the tag (or node) of each class shown on the upper left corner of each panel; the total number of occurrence of class as simulated by CRU (nearer to the equal sign) and CAM ensemble mean (farther from the equal sign).

5.5 Atmospheric Tele-connections and the Occurrence of Dominant Spring Maximum Air Temperature Classes over West Africa

Temperature classes in TMG1 and TMG2 show no consistency in their associations with ENSO because the classes in these groups are associated with both phases of ENSO (Figure 5.8). In TMG1, Node 1 features higher frequency of negative phase of ENSO while Node 6 features the opposite, i.e. the positive phase. The situation in TMG2 is similar to TMG1, Node 3 features higher frequency of positive phase of ENSO while Node 4 features the opposite, i.e. the negative phase. However, association of temperature classes with ENSO is consistent in TMG3 where Node 2 features 60% of its occurrence during El Nino periods only (i.e. positive phase) while Node 5 features 20% of its occurrence during La Nina periods only (i.e. negative phase). The effect of positive phase of ENSO is to abnormally warm up the West African sub-region in concomitance

with dry conditions over the sub-region (Conway, 2009). Figure 5.8 also shows that CAM ensemble mean is able to capture the dominating phases in TMG1 and TMG2. It is however not able to capture the association as observed in TMG3. Therefore, spatial variability of maximum air temperature over West Africa may cautiously be predicted or simulated using ENSO as predictor.

The association between AMO and the temperature classes is not consistent in Nodes 1, 2 and 4 because the classes feature varying percentages of both phases of AMO (Figure 5.8). The classes in Nodes 3 and 5 occur equally during both phases of AMO, hence the association is unreliable. However, the association is consistent in Node 6 where the class features positive phase of AMO only. The association in Node 6 is consistent with occurrence of droughts which, in conjunction with above-normal temperature over West Africa, has been linked to AMO (Hagos and Cook, 2008; Mohino et al., 2011). Figure 5.8 shows that CAM ensemble mean is able to reproduce the dominating negative phase in Node 4 and unreliable association in Node 5. It is however unable to capture the positive phase in Node 6.

The association between NAO and the temperature classes in Nodes 1, 3 and 5 is consistent. These nodes feature only the positive phase of NAO (Figure 5.8). Though, other nodes feature both phases, they are however dominated by positive phase also. NAO-induced predictability, which has been linked to fall in station level pressures and warm SST anomalies in the equatorial Tropical Ocean (Chang et al., 1997), works in tandem with other atmospheric tele-connection indices, one of which is ENSO (Hurrell, 1995). Therefore, in comparison to ENSO the prediction potential of NAO seems to be smaller. Figure 5.8 shows that CAM ensemble mean is able to capture the consistent associations in Nodes 1 and 5. It is also able to reproduce the dominating positive phase in Node 4.

Association between rTAI and the temperature classes is only consistent in Node 3 class. The class occurred during the positive phase of rTAI only (about 79%: Figure 5.8).

Figure 5.8 shows that TMG3, Nodes 4 and 6 feature both phases of rTAI with TMG3 and Node 6 dominated by positive phase; Node 1 features equal frequency of occurrence (about 25%). The scenario in Node 3 has been shown to be attributed to anomalous southward displacement of the ITCZ and consequently hotter and drier conditions over the Sahel (e.g. Rowell et al., 1995; Polo et al., 2008). Figure 5.8 also shows that CAM ensemble mean is able to capture the dominating negative phase in Node 4; also able to capture the dominating positive phase in Nodes 2 and 6, but fails to capture the consistent association in Node 3. The implication here is that the spatial temperature classes over West African sub-region, during the boreal spring, can be cautiously simulated and or predicted using SST anomalies over tropical Atlantic Ocean as predictor.

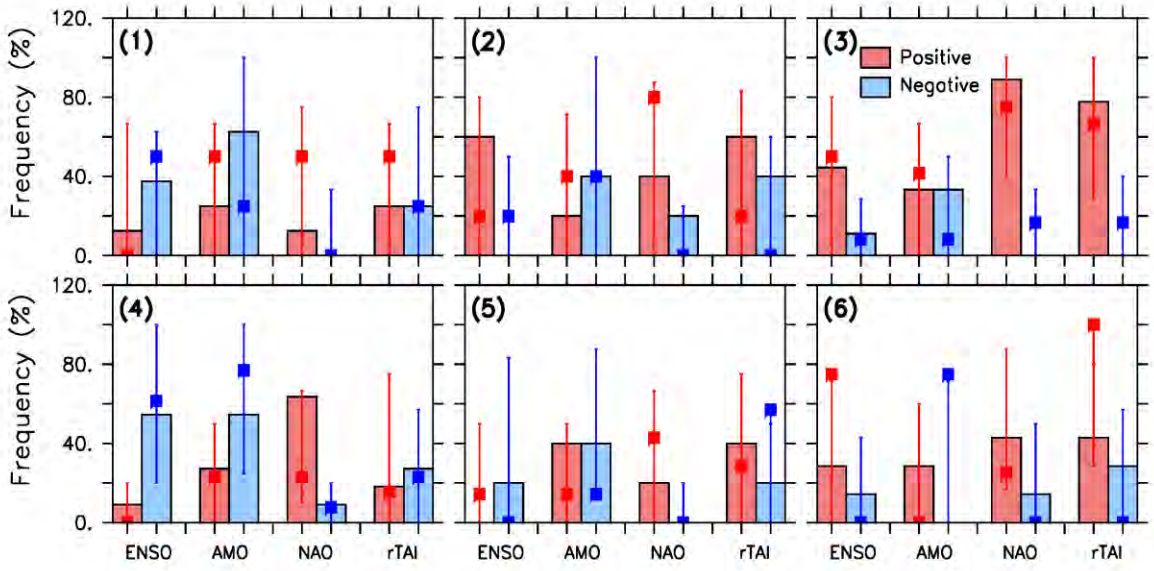

Figure 5.8 Frequency of occurrence of climate indices associated with spatial classes of temperature anomalies depicted in Figure 5.4, expressed as percentage of frequency of occurrence. Red and blue colors indicate, respectively, positive and negative phases of each climate index; bars, squares, and the upper and lower parts of the error bars, respectively, denote the frequencies of the climate indices associated with observation (CRU), CAM ensemble mean, and the maximum and minimum frequencies of the climate indices produced by CAM ensemble members. The tag (or node) of each temperature class is shown in bracket on the upper left corner of each panel. See Table 3.2 for brief descriptions of the climate indices considered in this study.

Summarily, CAM finds it difficult to simulate correctly some of the associations between maximum air temperature and climate indices because of three suspected physical reasons. Firstly, influences of local or regional forcings may possibly conflict with the influences of the climate indices. Secondly, there is possibility of ensemble members producing different spatial temperature classes for a particular climate index in contrast to the use of ensemble mean where the classes are averaged together. Lastly, the use of only one form of each climate index contrary to proven existence of different forms of climate indices, e.g. El Nino Modoki and conical El Nino are both forms of ENSO (Johnson, 2012; Ratnam et al., 2014). Nevertheless, the investigation has assisted us to know the abilities of CAM in capturing the association between climate indices and temperature classes over West African sub-region, during the boreal spring season. We found that spatial maximum air temperature classes over West African sub-region cannot be associated with a particular climate index.

5.6 Global SST Anomalies and the Dominant Spring Maximum Air Temperature Classes

Further investigation into the links between spatial classes of maximum air temperature and global SST anomalies, and the ability of CAM (SIM48 and ensemble mean) to simulate these links are carried out in this sub-section. The results are presented in Figure 5.9(a, b, c). Observationally, temperature classes in TMG1 are associated with near-normal SST anomalies (±0.2^{o}C) over the Atlantic, Indian and Pacific Oceans (Figure 5.9a). The near-normal SST anomalies greatly induce near-normal temperature anomalies over the coastal zones of the sub-region (Figure 5.4). Extreme temperatures observed over the Sahel zone, in TMG1, may however be attributed to the influences of other factors that play important role in the energy budget of the atmosphere. Examples of these are the vertical motions, the temperature profiles, total cloud fraction, etc. that will be discussed later in this study. While the composite of SIM48 adequately reproduces the near-normal SST anomaly conditions over the Atlantic, Indian and Pacific Oceans in Node 1 (Figure 5.9b), the composite of CAM ensemble mean features below-normal SST anomalies over equatorial Pacific and north Atlantic Oceans (Figure 5.9c). The

composites of CAM however fail to reproduce SST scenario in Node 6; they however capture patches of above-normal SST anomalies over the Atlantic, Indian and Pacific Oceans (Figure 5.9b, c).

The spatial classes of maximum air temperature in TMG2 are associated with opposing global SST anomalies. While Node 3 is majorly associated with above-normal SST anomalies over all Oceans, Node 4 features the opposite (Figure 5.9a). Hence, respective maximum air temperatures observed in the nodes of this group (Figure 5.4) may be attributed to large scale advection of air masses, probably, from the Atlantic Ocean; though, influences of other temperature modulating factors are not ruled out. The SST anomaly conditions, in this group, are adequately captured by the composites of SIM48 and CAM ensembles mean (Figure 5.9b, c).

Node 2 is majorly associated with above-normal SST anomalies over the Atlantic, Indian and central equatorial Pacific Oceans while Node 5 is associated with below-normal SST anomalies over the Atlantic, Indian and eastern equatorial Pacific Oceans (Figure 5.9a). However, these SST anomaly patterns seem to be unrelated to their respective spatial classes of temperature anomalies (Figure 5.4). These imply that SST anomalies alone may not be sufficient, as a predictor, to determine the spatial classes of maximum air temperatures over West African sub-region. This means that other factors play important role in the energy budget of the West African atmosphere. The composite of SIM48 captures the SST anomaly conditions in TMG3 (Figure 5.9b), though with little disparities over the Pacific Ocean; but the composite of CAM ensemble mean only succeeded in reproducing the near-normal SST anomalies over the Indian Ocean in Node 5 (Figure 5.9c).

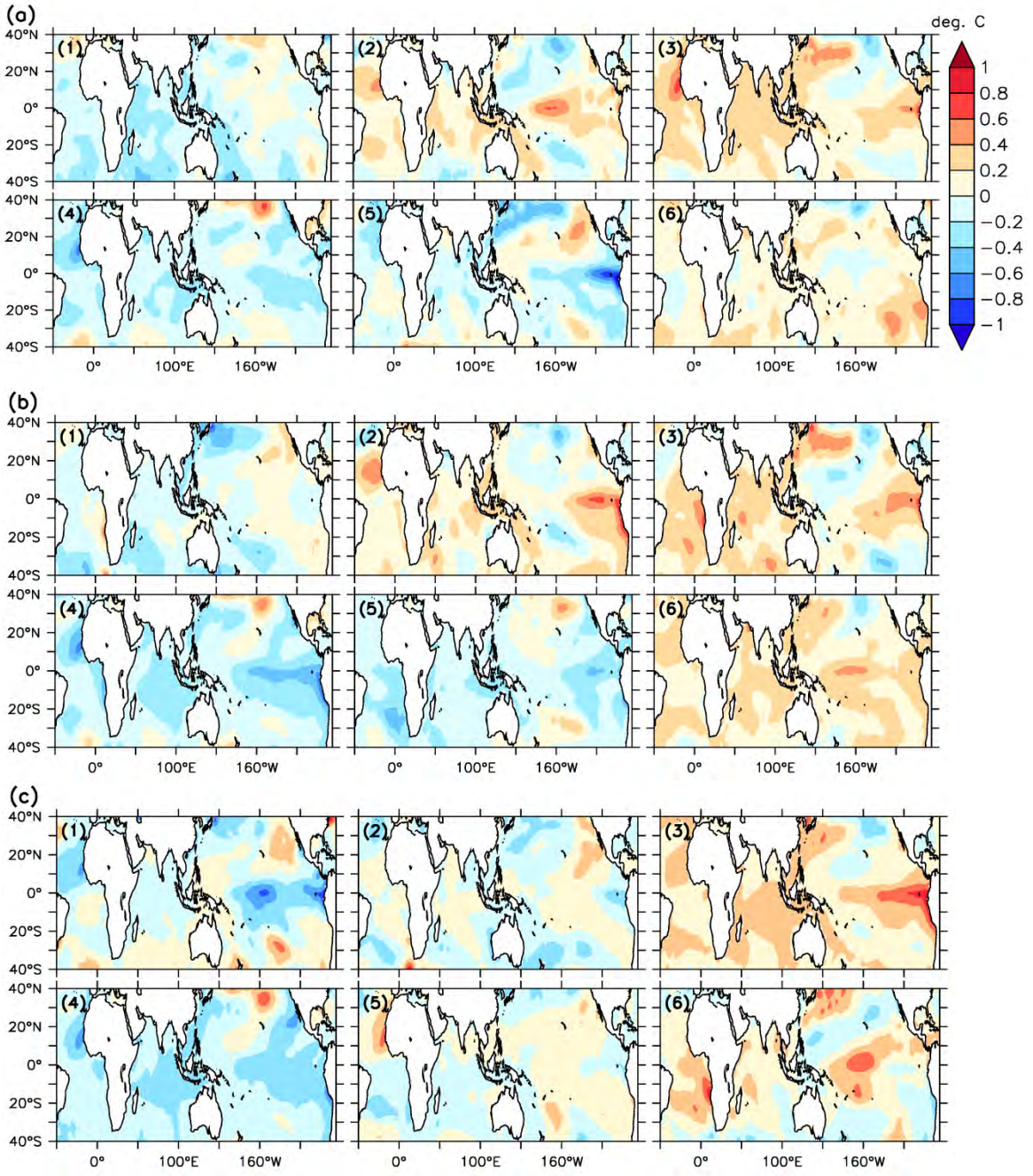

Figure 5.9 Composites of boreal spring global SST anomalies (°C) for **(a)** observation, **(b)** SIM48 and **(c)** CAM ensemble mean classes. Pattern numbers, which correspond to the spatial classes of temperature anomalies in Figure 5.4, are written on the upper left sides of each panel while the SST anomalies are relative to the 1961-2005 climatological mean.

5.7 Composites of Atmospheric Conditions Associated with the Dominant Spring Maximum Air Temperature Classes

Spatial classes of maximum air temperature anomalies displayed in Figure 5.4 were separated into their various composites, i.e. the observation (CRU), SIM48 (the most synchronized ensemble member), and CAM ensemble mean (Figure 5.10). The temporal characteristics of these composites were then used to derive the composites of atmospheric conditions associated with each spatial temperature class. The composites of atmospheric dynamics analyzed are the boreal spring spatial structures of the anomalies of the latitudinal distributions of vertical profiles of zonal wind speed and the corresponding vertical velocity, both averaged over 10^oW to 10^oE (Figure 5.11); the latitudinal distributions of the vertical profile of air temperature averaged over 10^oW to 10^oE (Figure 5.12); the total cloud fraction (Figure 5.13); and, the MSLP (Figure 5.14). We then conclude with how well these composites of atmospheric dynamics are reproduced by CAM (SIM48 and ensemble mean).

SIM48 has greater ability to correctly reproduce the occurrences of maximum air temperature classes than any ensemble members and ensemble mean. For instance, Figure 5.10 shows that SIM48 satisfactorily simulates four of the spatial classes of temperature anomalies (TMG1 and Nodes 2 and 4) while CAM ensembles mean simulates three (TMG1 and Node 2). The best agreement between the composites of CRU and CAM occurs in TMG1, i.e. Nodes 1 and 6. In this group, spatial correlations (r) between CRU and CAM simulations range from 0.49 to 0.86. r are greater in SIM48 ($0.82 \leq r \leq 0.86$) than in CAM ensemble mean ($0.49 \leq r \leq 0.7$). These imply that CAM simulates the spatial structures of the group almost as observed. The composites of CRU and reanalysis show that Node 1, which features sub-zero temperature anomalies over the entire Sahel regions with a band of neutral anomalies that stretch from the coast to Savannah (Figure 5.10a), is associated with: strong upper level ascents and low level subsidence coupled with deep westerly anomalies which weaken the African Easterly Jet (AEJ – a year-round synoptic system found within 4^o – 7^oN at around 650hPa level over

West Africa during the boreal spring, highly known for its precipitation and temperature modulating abilities (Afiesimama, 2006): Figure 5.10a); very deep sub-zero anomalies of air temperature profiles where near-zero anomalies are observed over Guinea and Savannah zones (Figure 5.12a); weak, but positive, anomalies of total cloud fractions (Figure 5.13a); and, anomalous filling (i.e. positive anomalies) of MSLP which induces lower than normal maximum air temperatures (Figures 5.3g, h and 5.14a). Node 6 features the opposite of the spatial classes of these atmospheric dynamics (panel a of Figures 5.10, 5.11, 5.12, 5.13 and 5.14).

Though, reanalysis and CAM feature comparable classes of the associated atmospheric dynamics, they also feature some disparities. CAM is able to reproduce the strong upper level ascents and low level subsidence as well as weak anomalies of AEJ in Node 1, but fails in Node 6; though ensemble mean captures the stronger than normal AEJ in Node 6 (Figure 5.11b, c). CAM, in TMG1, captures the vertical profile of boreal spring temperature anomalies over the sub-region (Figure 5.12b, c) while it fails to reproduce the anomalies of the total cloud fractions (Figure 5.13b, c). CAM adequately reproduces the spatial patterns of MSLP anomalies in Node 1 while it fails in Node 6 (Figure 5.14b, c). Hence, CAM simulates adequately some of the associated regional atmospheric dynamics of the spatial classes of maximum air temperature anomaly as observed in TMG1.

There is a split in agreement between the composites of CAM in the simulations of TMG2 (Nodes 3 and 4). SIM48 adequately simulates the Node 4 of this group while CAM ensemble mean fails to correctly simulate the spatial classes of temperature anomalies in TMG2 (Figure 5.10a). The spatial correlation, r, between CRU and SIM48 in Node 4 is greater than 0.8 while it is 0.26 in Node 3 (Figure 5.10b); while CAM ensemble mean shows that r is generally less than 0.45 in TMG2 (Figure 5.10c). Node 4, described in Figure 5.4 as featuring below-normal temperature anomalies over the entire West Africa, with coldest anomalies positioned over the northern parts of Mali, is associated with the anomalies of atmospheric dynamics that are almost similar to Node 1.

In Node 4, the westerly anomalies are not as deep as in Node 1, there is no significant change in AEJ and the upper level ascents and low level subsidence are not as strong as what was observed in Node 1 (Figure 5.11a). The entire atmospheric column over the sub-region features below-normal temperature profiles (Figure 5.12a), positive anomalies of total cloud fractions (Figure 5.13a) and anomalous filling (especially over Mauritania and Mali) and deepening (over eastern Niger and Chad) of MSLP (Figure 5.14a). These atmospheric dynamics work in tandem to induce lower than normal maximum air temperature. Here, the composites of SIM48 capture some of the atmospheric dynamics while it failed to reproduce some. For example, SIM48 manages to reproduce the nil significant change in AEJ and the westerly anomalies which terminate at around 7^{o}N up to the depth of about 500hPa level while the captured upper level ascents and subsidence are not as strong as what was observed (Figure 5.11b). SIM48 captures the below-normal temperature profiles over the entire atmospheric column of the sub-region (Figure 5.12b) and positive anomalies of total cloud fractions up to south of Sahel zone (Figure 5.13b). It however generally does not reproduce the anomalies of MSLP (Figure 5.14b).

While the TMG3 described in Figure 5.4 lacks extreme anomalies, probably as a result of data combination which dampens, smoothens and suppress variability; the composites of observation in Figure 5.10a show that Node 2 features an isolated cold anomalies over northern parts of Niger Republic and Chad, a band of neutral zones over the Sahel that separates the cold anomalies from the above-normal anomalies along the coasts. CAM is able to simulate the spatial structures of Node 2 in TMG3 almost as observed (i.e. generally, $r > 0.7$; Figure 5.10b, c). The temperature class described in this node is associated with: interwoven upper level subsidence and ascents coupled with low level easterly anomalies below 800hPa level and strong upper level westerly anomalies which weaken the AEJ (Figure 5.11a); deep and mildly above-normal air temperature profiles (Figure 5.12a); positive and negative anomalies of total cloud fractions that correspond with negative and positive temperature anomalies respectively (Figure 5.13a); and,

anomalous filling and deepening of MSLP which, respectively, induces below- and above-normal temperature anomalies (Figure 5.14a).

There are disparities in the ways the composites of CAM capture atmospheric dynamics in Node 2. Composites of CAM failed to reproduce the status of AEJ and the associated profiles of vertical wind motions; SIM48 however manages to capture the low level easterly anomalies below 800hPa level and strong upper level westerly anomalies (Figure 5.11b, c). The composite of SIM48 captures the deep and mildly above-normal air temperature profiles southwards of 13^{o}N (Figure 5.12b) while the vertical gradient of the air temperature profiles as featured by the composite of CAM ensemble mean is too weak to be assessed (Figure 5.12c). Composites of CAM failed to reproduce the anomalies of the total cloud fractions (Figure 5.13b, c), as well as the spatial patterns of MSLP anomalies (Figure 5.14b, c). Knippertz et al. (2011) opine that difficulties experienced by climate models to simulate the West African climate may be due to large deviations in the simulations of solar radiation, cloudiness, and low-level winds; furthering that these deviations could strongly affect the regional budgets of moisture and energy.

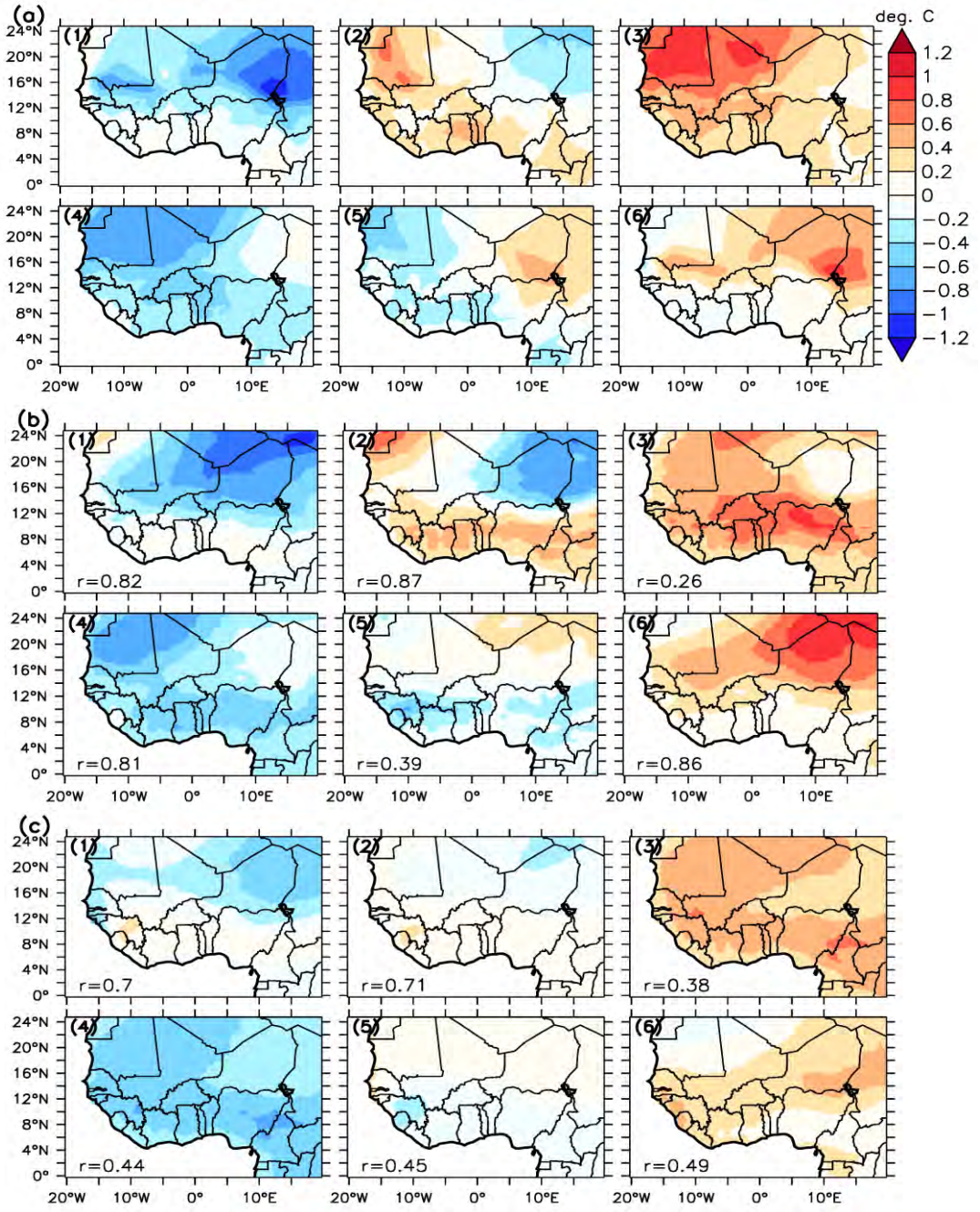

Figure 5.10 Composite of the spatial patterns of boreal spring maximum air temperature (^{o}C) anomalies over West Africa for **(a)** observation (CRU), **(b)** SIM48 and **(c)** CAM ensemble mean. Pattern numbers, which correspond to spatial classes of temperature anomalies in Figure 5.4, are written on the upper left sides of each panel while the values of spatial correlations of SIM48 and ensemble mean with corresponding observed temperature pattern are written on the bottom left of panels in **b** and **c** respectively.

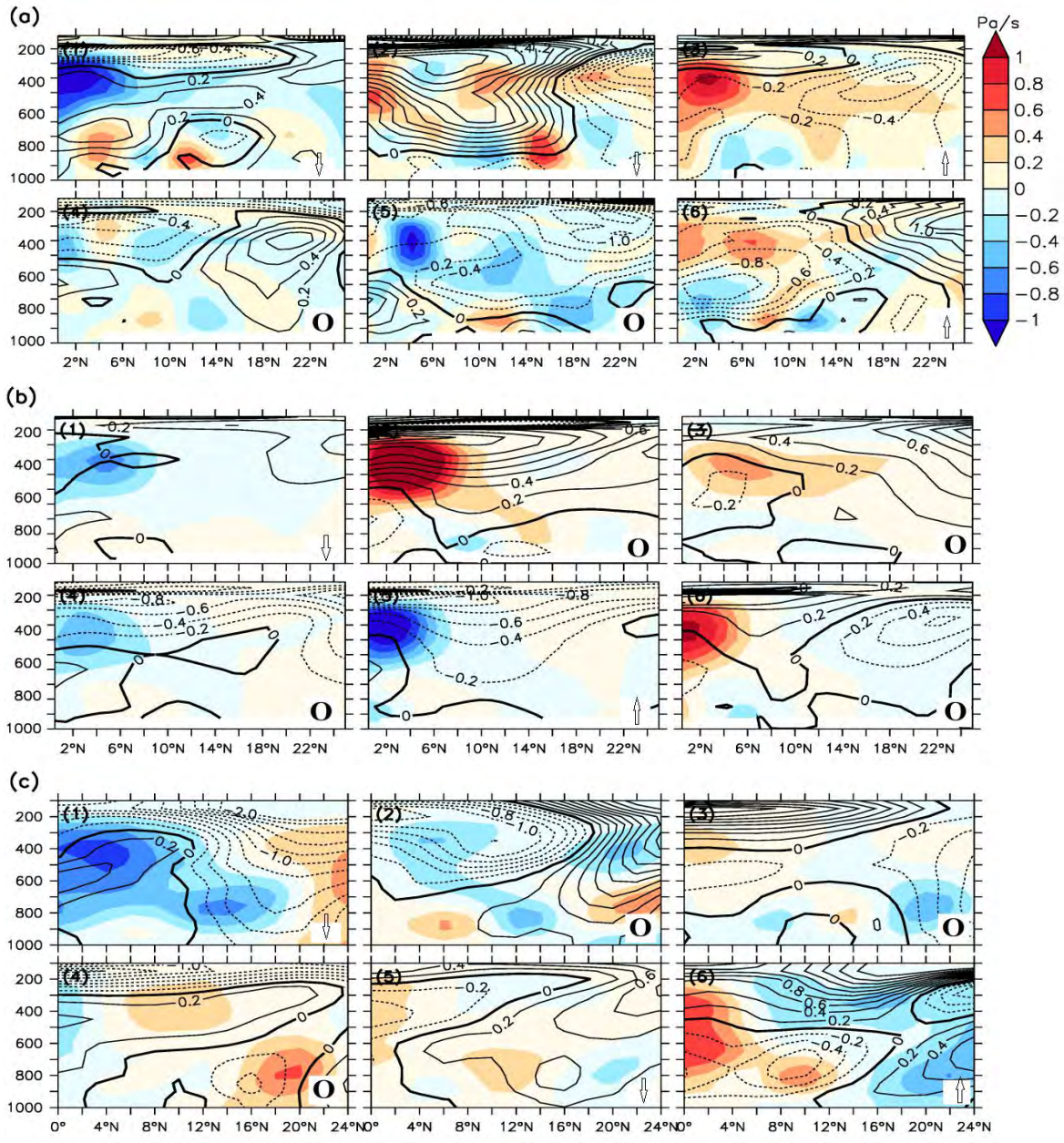

Figure 5.11 Composites of the vertical profiles of boreal spring zonal wind speed (contour; ms^{-1}) and vertical velocity (omega; shade; $x10^{-2}$ Pa s^{-1}) anomalies averaged over 10^{o}W to 10^{o}E, relative to the 1961-2005 climatological mean, for **(a)** observation (reanalysis), **(b)** SIM48 and **(c)** CAM ensemble mean simulation. Pattern numbers, which correspond to classes of temperature anomalies in Figure 5.10, are written on the upper left sides of each panel. Blue shading indicates resultant ascent (i.e. upward motions) while red shading indicates resultant descent (i.e. downward motions). ↑, ↓ and O sign at the bottom right of each panel respectively represent enhanced, weak and no significant change in African Easterly Jet (AEJ).

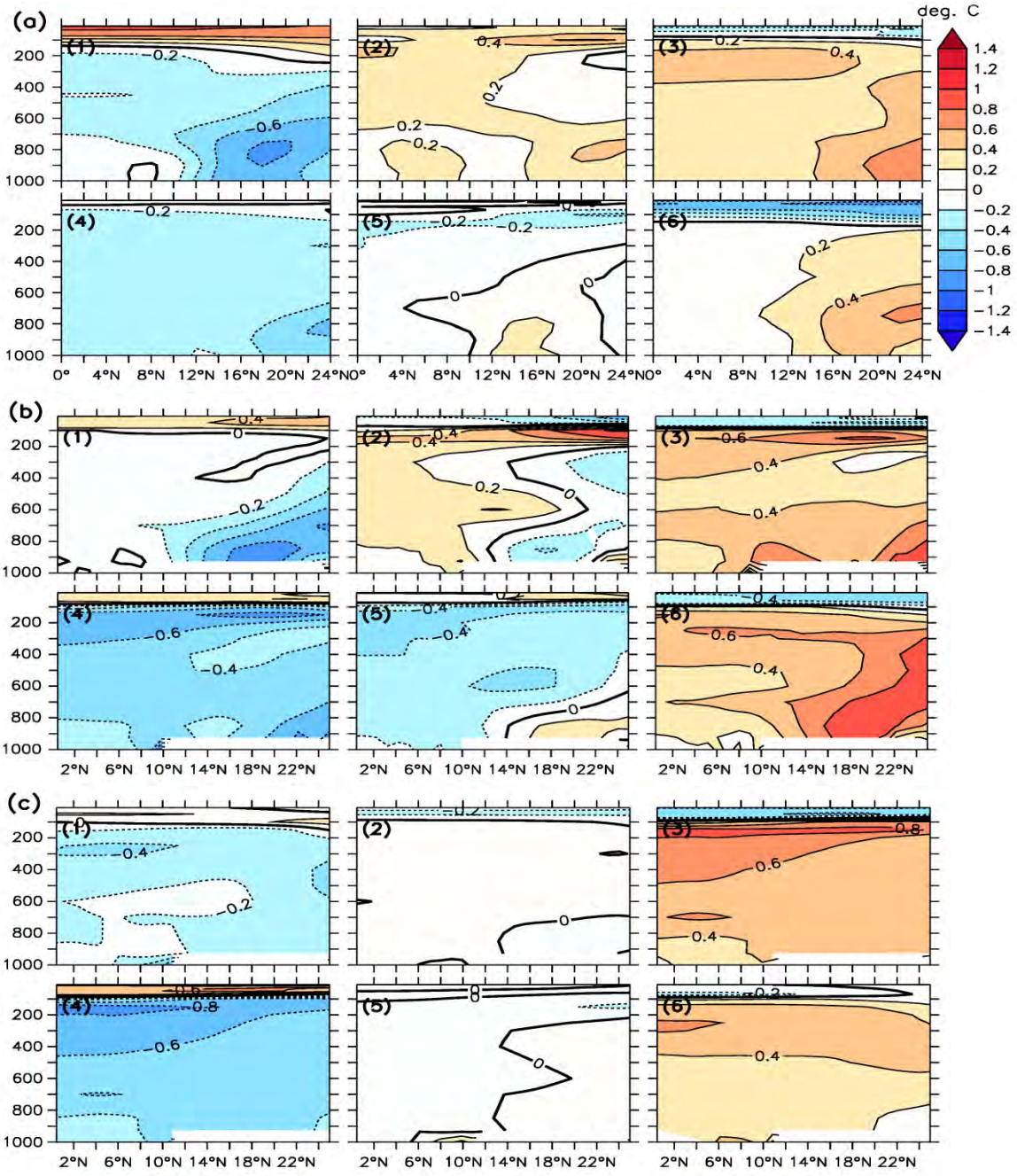

Figure 5.12 Composites of the vertical profile of the boreal spring temperature anomalies (shade and contour; ^{o}C) averaged over 10^{o}W to 10^{o}E, relative to the 1961-2005 climatological mean, for **(a)** observation (reanalysis), **(b)** SIM48 and **(c)** CAM ensemble mean simulation. Pattern numbers, which correspond to classes of temperature anomalies in Figure 5.10, are written on the upper left sides of each panel.

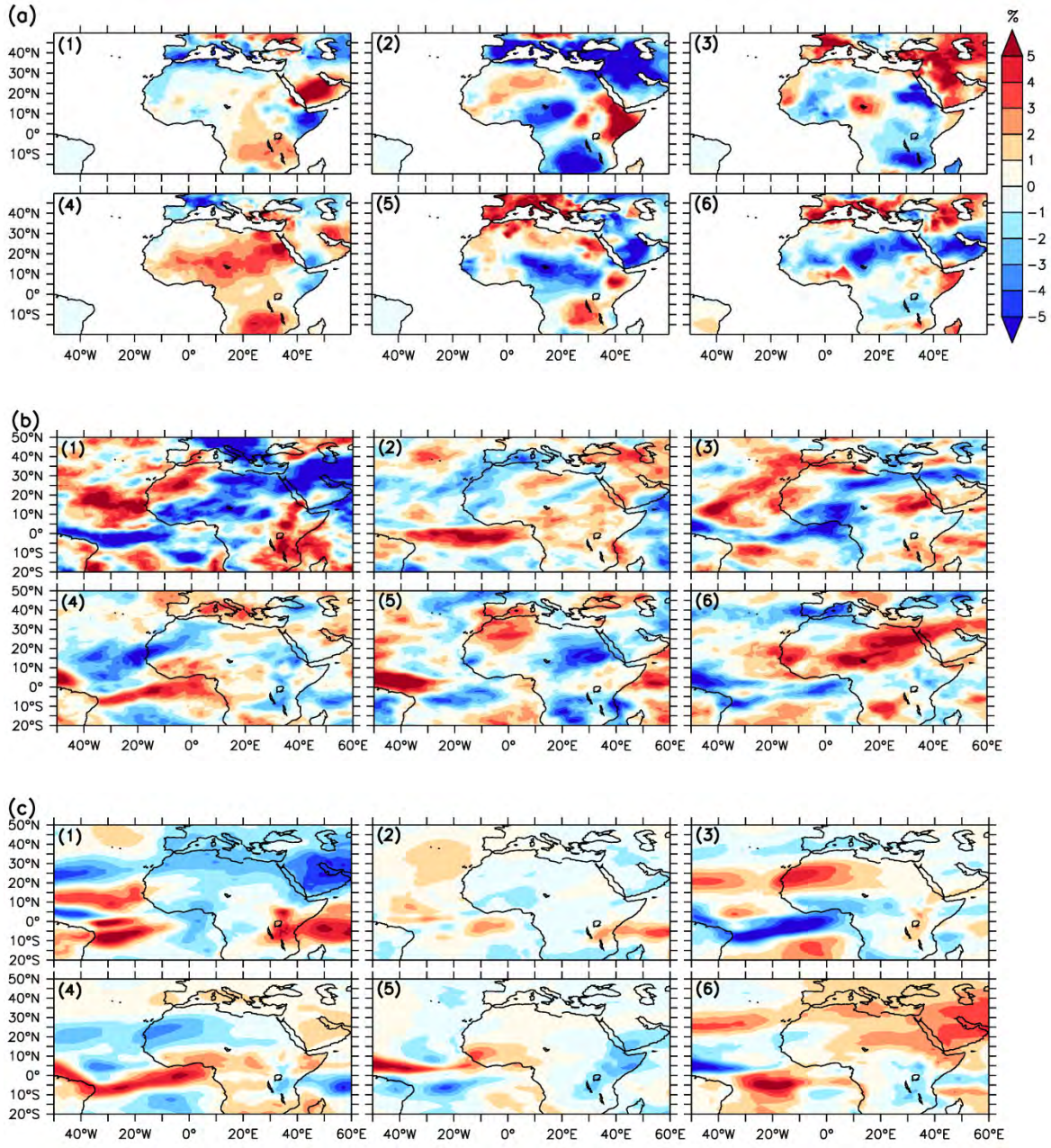

Figure 5.13 Composite of spatial patterns of boreal spring total cloud fraction anomalies (%) for **(a)** observation (CRU), **(b)** SIM48 and **(c)** CAM ensemble mean, relative to the 1961-2005 climatological mean. Pattern numbers, which correspond to classes of maximum air temperature anomalies in Figure 5.10, are written on the upper left sides of each panel. Blue shading (negative value) indicates resultant reduction in cloud coverage while red shading (positive value) indicates resultant increase in cloud coverage.

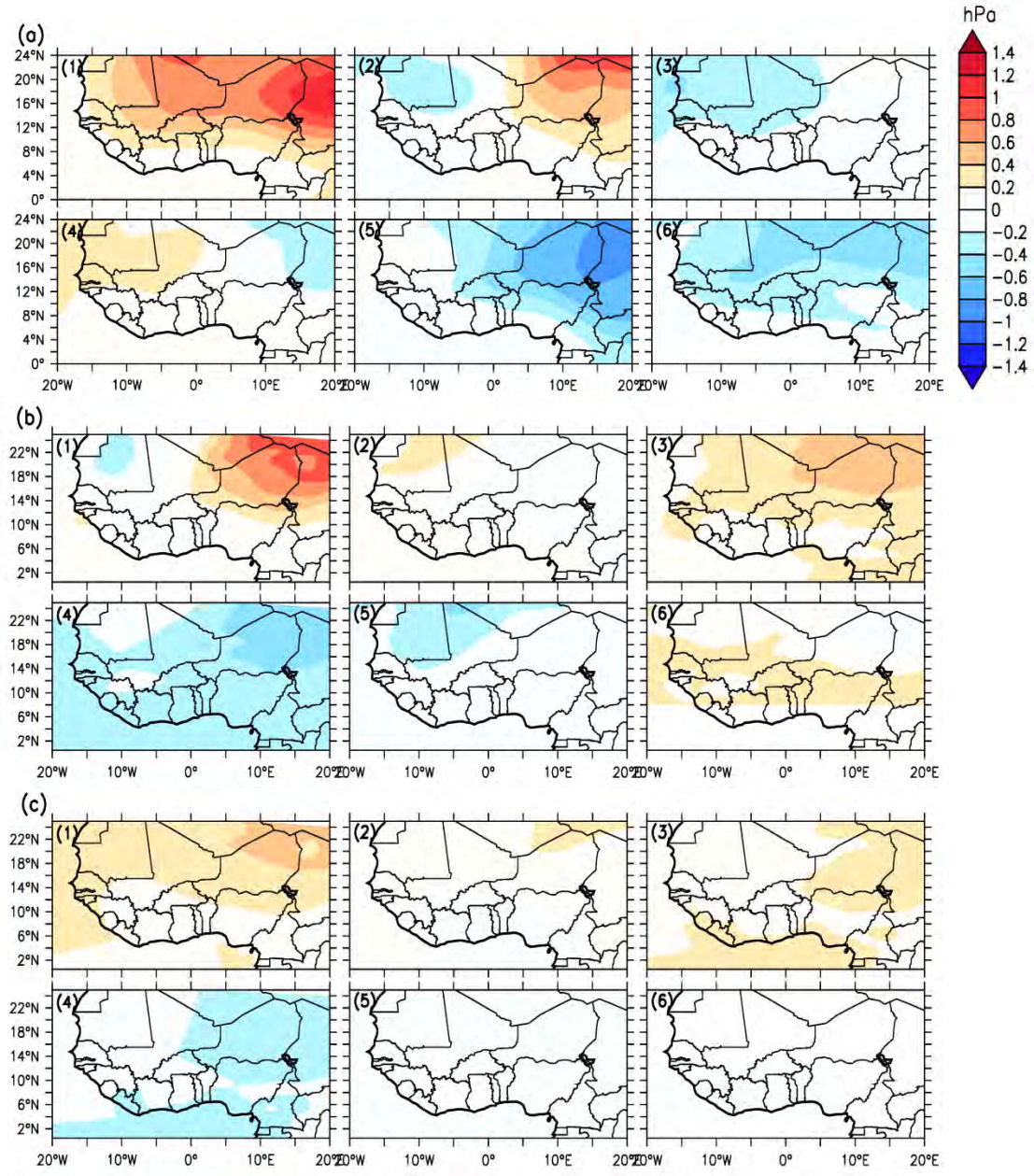

Figure 5.14 Composite of the spatial patterns of boreal spring MSLP anomalies (hPa) for **(a)** observation (reanalysis), **(b)** SIM48 and **(c)** CAM ensemble mean, relative to the 1961-2005 climatological mean. Pattern numbers, which correspond to classes of maximum air temperature anomalies in Figure 5.10, are written on the upper left sides of each panel. Blue shading (negative value) indicates resultant deepening of (i.e. reduction) MSLP while red shading (positive value) indicates resultant filling of (i.e. increase) in MSLP.

5.8 Summary

We have demonstrated in this chapter that CAM is adequately capable of reproducing the inter-annual and spatial variations of the observed boreal spring maximum air temperature over West Africa. It is also capable of simulating the atmospheric conditions that influence and modulate the boreal spring maximum air temperature over West Africa. Though, CAM adequately reproduces the "extreme temperatures over Sahel" and "near normal temperatures over the region" classes almost as observed and also succeeded in reproducing some of their associated regional atmospheric conditions; however, the disparity between SIM48 and the ensemble mean shows that SIM48 (η = 44%) adequately simulates four of the spatial classes of the temperature variability while CAM ensembles mean (η = 29%) simulates three, out of the six dominant classes. This lends credence to the utilization of the best performing ensemble member in issuance of seasonal forecasting rather than the use of ensemble mean that is based on uniformly averaging the members. Conversely, our investigation shows that CAM struggles to simulate correctly some of the associations between the dominant temperature classes and climate indices as the investigation also shows that these dominant temperature classes cannot be associated with a single climate index. These failures have been attributed to three physical reasons – influences of local or regional forcings; the possibility of ensemble members producing different spatial classes of maximum air temperature anomaly for a particular climate index in contrast to the use of ensemble mean where the classes are averaged together; and, the use of only one form of each climate index contrary to proven existence of different forms of climate indices. Nevertheless, our results have identified the dominant spring maximum air temperature classes that CAM can simulate well and those it struggles to reproduce over West Africa.

A comparison of the results in this chapter with those in Chapter (4) shows no preference in CAM's ability to simulate the seasonal variability in rainfall and temperature over West Africa. That is, while the model captures some aspects better in the temperature than in the rainfall, it also simulates some aspect worse in the former than in the later. For instance, the correlation, r, between observation and simulations is higher for temperature

(i.e. $0.4 < r < 0.8$; $r = 0.8$ for the ensemble mean) than for rainfall (i.e. $0.4 < r < 0.65$; $r = 0.64$ for the ensemble mean); the normalized standard deviation is closer to 1.0 in former than in later (see Figures 4.1 and 5.1). On the other hand, the synchronization of the ensemble mean (with observation) is higher for rainfall ($\eta > 33\%$) than for temperature ($\eta < 30\%$). While the best simulation for temperature ($\eta_{best} = 44\%$) has better synchronization (with observation) than the best simulation for rainfall ($\eta_{best} = 42\%$), the worst simulation for temperature ($\eta_{worst} = 11\%$) is worse than the worst synchronization for rainfall simulation ($\eta_{worst} = 20\%$). For rainfall, 40% of the ensemble members perform better than the ensemble mean, while, for temperature, only 36% of the ensemble members perform better than the ensemble mean (Figures 4.5 and 5.6). However, the discrepancy among the simulations (or the degree of spread among the simulations) is higher for temperature than for rainfall. This suggests that, over West Africa, the seasonal predictability may be lower for temperature classes than for rainfall classes.

6 Characteristics of Summer Rainfall Patterns over Southern Africa

Our analysis on the characteristics of summer (austral) rainfall classes over Southern Africa, as observed by CRU and simulated by CAM are presented and discussed in this chapter. The chapter evaluates the performance of CAM in simulating the climatology of the summer rainfall patterns over Southern Africa. We then describe the characteristics of the six dominant summer rainfall (anomaly) classes over the region and evaluate how well CAM reproduces them. The six dominant classes were obtained using SOM analysis as described in Chapter 3. We also consider the characteristics of the dominant summer rainfall classes such as the inter-annual and decadal variability, transition, and persistence. The chapter also studies the influence of atmospheric tele-connections on the observed and simulated classes, and examines the capability of CAM in reproducing the atmospheric dynamics that produces each summer rainfall classes.

6.1 Model Evaluations

6.1.1 Inter-annual Variability of Summer Rainfall over Southern Africa

The inter-annual variability of the observed and simulated rainfall over Southern Africa (Figure 6.1a) shows that, in most years, the CAM ensemble simulations spread around CRU and the ensemble mean closely follows CRU. There is only one year (i.e. 1997) in which the ensemble member simulations fail to enclose the observation, and the largest discrepancy (about 0.6 mm day^{-1}) between the ensemble mean and CRU occurs in that year. Both CRU and CAM ensemble mean show no trend in the rainfall series, but they suggest increased rainfall variability in the last three decades. However, all the CAM simulations overestimate the magnitude of the inter-annual variability, and have weak correlations with the observed variability. Figure 6.1b, which presents the normalised standard deviation (σ, which is simulated standard deviation normalised by the observed standard deviation) and the correlation between the simulation and observations (r),

shows that $1.9 < \sigma < 3.1$ and $-0.1 < r < 0.54$ for the ensemble members. The ensemble mean produces a lower σ (≈ 1.4) than all the ensemble members (because the averaging filters out the simulated variability), but has r (≈ 0.39) that is still within those of ensemble members. These results are similar to what Klutse et al. (2015) obtained with the previous version of the CAM model (version 3) over Southern Africa (i.e. $0.5 < \sigma < 2.0$ and $0 < r < 0.3$).

6.1.2 Spatial Distribution of Mean Summer Rainfall over Southern Africa

Figure 6.2 shows that the CAM ensemble mean gives a realistic simulation of mean summer rainfall patterns over Southern Africa. In agreement with observation, the model simulates the zone of maximum rainfall (inter-tropical convergence zone, ITCZ) over the central part of Southern Africa (i.e. over Angola, Zambia, and North Mozambique), although the simulated zone extends to about 5^o south (i.e. 25^oS) of the observed position (20^oS) (Figure 6.2a, b). The model also reproduces the east-west rainfall gradient south of 25^oS, except that the simulated rainfall extends too far westward (by about 5^o). As in the reanalysis, CAM simulates anti-cyclonic flows (at 850hPa level) over the Atlantic and Indian Oceans, and produces a convergence of easterlies (from the Indian Ocean) and westerlies (from tropical Atlantic Ocean) over the ITCZ. The simulated easterlies are stronger in CAM than in the reanalysis. However, the simulated vertical wind (omega at 500hPa level) has the same magnitudes with the reanalysis, except that the location of the maximum upward motion (about 8×10^{-2} Pa s^{-1}) extends 5^o more westward than observed (Figure 6.2c, d); this is consistent with the bias in the location of ITCZ. The simulated easterlies and westerlies transport moisture (from the Indian and Atlantic Oceans, respectively) into the sub-continent and the convergence of the moisture roughly overlaps with location of the maximum vertical winds and agrees well with that of reanalysis, except that the magnitude of the convergence is weaker in CAM than in reanalysis. Furthermore, CAM captures the position of a col over the southwestern tip of the sub-region (around 33^oS, 20^oE). This col provides a link through which a maritime trough connects the continental depression to a mid-latitude low system. Several studies have shown that these wind patterns provide a good background for formations of tropical-

temperate-troughs (TTTs) and the associated cloud bands that produce most of the summer rainfall (i.e. Jury and Pathack, 1993; Todd and Washington, 1999; Hansingo and Reason, 2008; Manhique et al., 2009). Hence, the realistic simulation of these features indicates that CAM captures general dynamics behind the summer climate.

However, there are some biases in the simulated rainfall (Figure 6.2e). The maximum dry bias (about -4 mm day^{-1}) occurs over north-west Angola and north Mozambique, and the maximum wet bias (about 4 mm day^{-1}) occurs over the borders of Namibia and Botswana, and over the Drakensberg Mountains. However, the ranked probability skill score (RPSS), a measure of skill (Wilks, 1995; Murphy, 1988; Mason, 2004; Weigel et al., 2006), shows positive values over most Southern African countries, meaning that the model has good skill over those countries (Figure 6.2f). The skill of the model is poor over some countries (especially over Mozambique and Angola). Nevertheless, in general, CAM skill over Southern Africa compares well with those reported for other GCMs over the region (i.e. Landman and Goddard, 2005; Landman et al., 2005; Batte and Deque, 2010).

6.2 Dominant Classes of Rainfall over Southern Africa in Summer

Figure 6.3 presents the SOM classification (3 x 2 nodes) of the observed (CRU) and simulated (CAM) rainfall (anomaly) classes over Southern Africa. Figure 6.3 depicts the dominant summer rainfall classes over the region. These dominant classes can be divided into three groups, such that each group contains two opposite rainfall classes. The first group (hereafter, RPA) consists of Nodes 1 and 6. Node 1 features a wet condition (positive rainfall anomalies) over the eastern part of Southern Africa (i.e. over Mozambique and Tanzania), a dry condition (negative rainfall anomalies) over the north-western part (i.e. over DRC – Democratic Republic of Congo) and southern part (i.e. South Africa and Botswana) of the sub-continent, and a band of neutral condition that extends from the wet area to the west coast (i.e. over Angola) and separates the two dry areas at about 10 - 20^{o}S. Node 6 features the opposite class of Node 1. However, CRU

observation shows that the Node 1 class accounts for about 18% of summers within 1961 – 2005 while Node (6) accounts for 13%; hence RPA classes account for 31% the rainfall. CAM simulates the statistics of both classes well. The ensemble members and ensemble mean agree with CRU on the frequency of Node 1, but they slightly overestimate the frequency of Node 6 by 3%; hence RPA classes account for 34% of the summers.

The second group, which consists of Nodes 3 and Node 4 classes (hereafter, RPB), has similar features with the RPA (Nodes 6 and 1, respectively). The main difference is that the band of neutral conditions that separates the dry areas in Node 1 and the wet areas in Node 6 does not extend to the west coast in Nodes 4 and 3, respectively; instead, it stops at the centre of the sub-continent (around 20^{o}E). Therefore, in Node 4, the two dry areas are connected at west of 20^{o}E; and, in Node 3, the two wet areas are linked at west of 20^{o}E. However, CAM grossly overestimates the frequency of RPB classes. For instance, while CRU shows that the RPB classes account for only 6.7% (each) of the dataset, CAM shows that Node 3 class accounts for 20% (ensemble members) and 22% (ensemble mean), while Node 4 accounts for 16% (ensemble members) and 27% (ensemble mean).

The third group (hereafter, RPC), which consist of Node 2 and Node 5, features different rainfall classes from RPA and RPB. Node 2 shows a dry condition over the south-eastern half of Southern Africa (with a maximum value over Zimbabwe), and a wet condition over eastern half of the tropical area (with a maximum over Angola), while the north-east and south-west Southern Africa experience a neutral condition. Node 5 features the opposite class to Node 2. CAM underestimates the frequency of RPC. For instance, CRU indicates that Node 2 accounts for the 31% of summers within 1961 – 2005 while Node 5 accounts for 24%. Meanwhile, CAM suggests that Node 2 only accounts for 14% (ensemble members) and 13% (ensemble mean), while Node 5 accounts for only 17% (ensemble members) and 4.4% (ensemble mean).

(a)

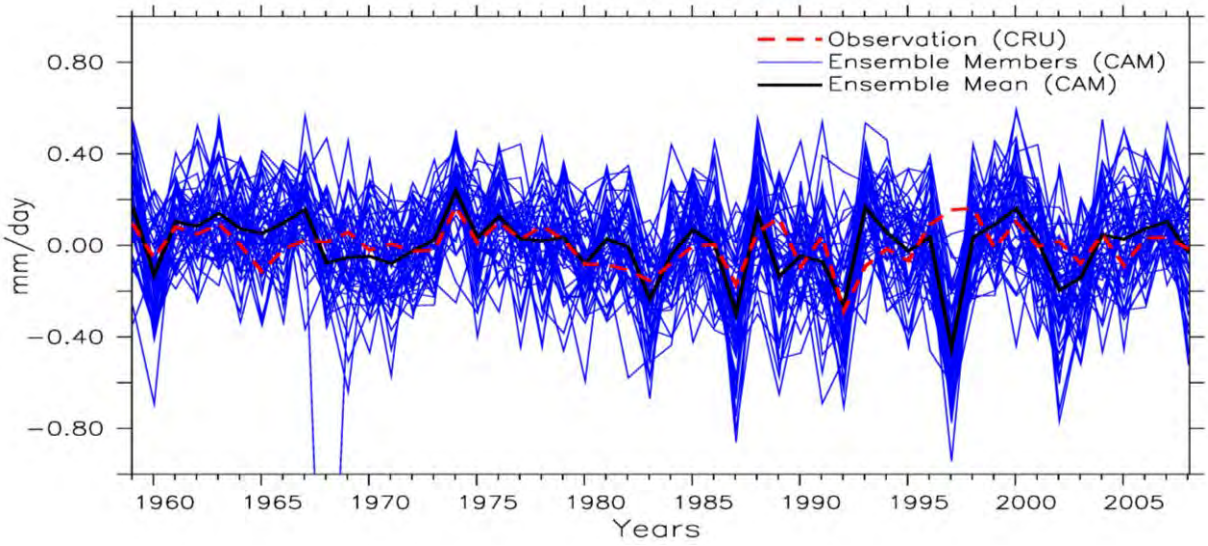

(b)

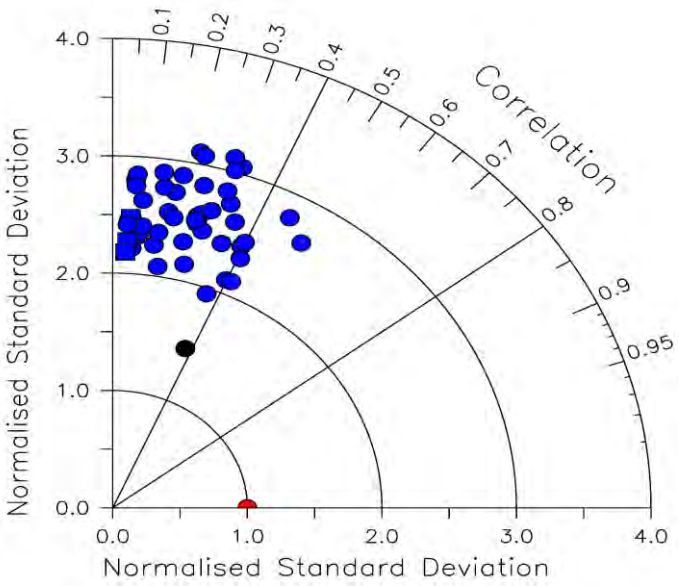

Figure 6.1 (a) The inter-annual variation of austral summer rainfall (anomaly, mm day^{-1}), averaged over the Southern Africa (including Madagascar); **(b)** Taylor diagram showing the normalized standard deviations and the correlation coefficients of CAM ensemble simulations (blue circles; blue squares for negative correlations), the ensemble mean (black star), CRU observation (red semi-circle). The normalized standard deviations and correlations are with reference to CRU observation.

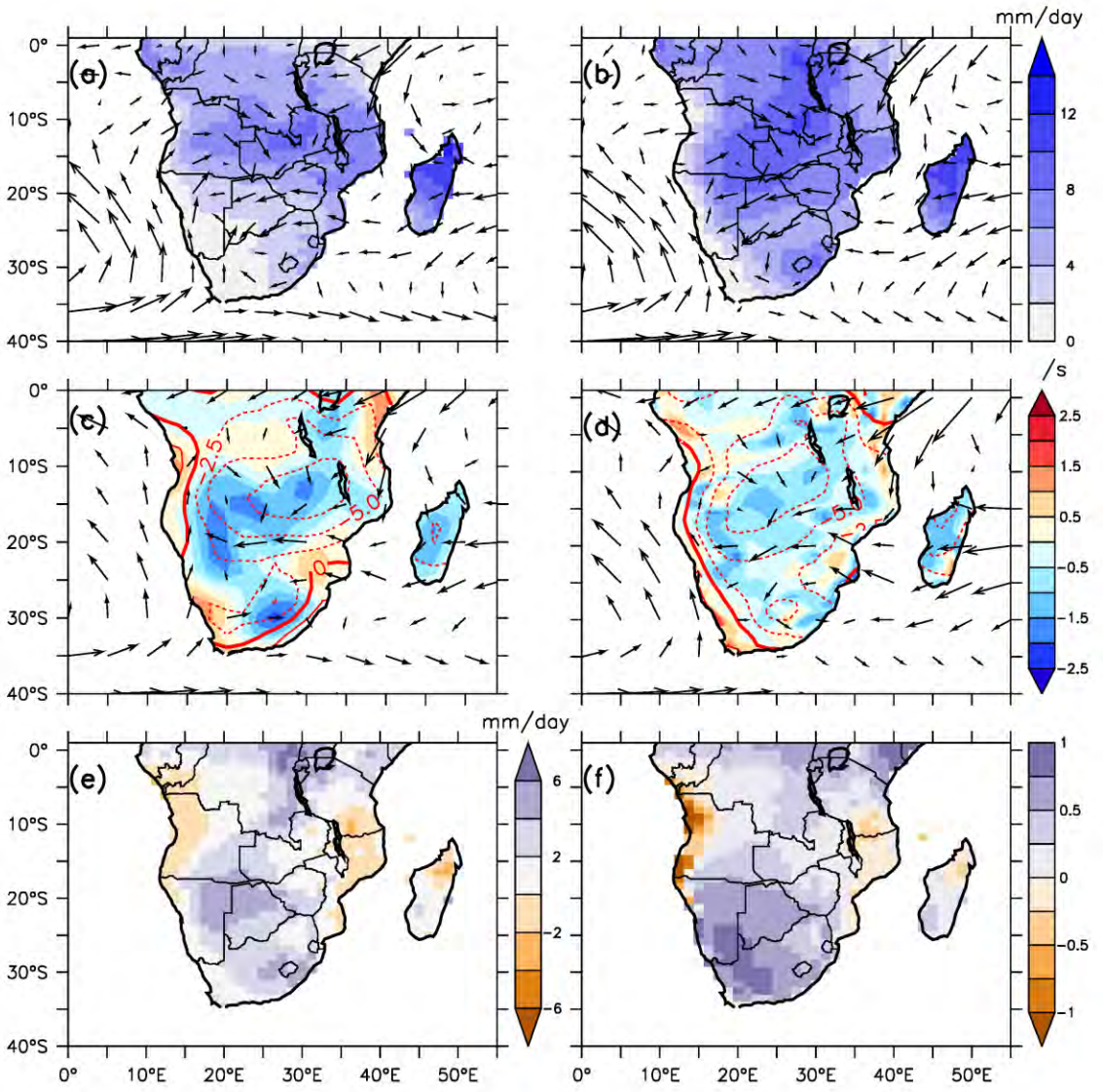

Figure 6.2 Spatial distribution of mean austral summer **(top row)** rainfall (shaded; mm day^{-1}) with the corresponding 850hPa level winds (arrows); **(middle row)** vertical velocity at 500hPa level (omega; contour; x10^{-2} Pa s^{-1}) with the corresponding vertically integrated moisture flux (arrows) and the vertically integrated moisture convergence (shaded; x10^{-5} s^{-1}) over Southern Africa. Observations and simulations are respectively on the left and right columns. **(e)** The bias in the simulated rainfall (i.e. simulated minus observed) and **(f)** the ranked probability skill score (RPSS) of the simulated rainfall.

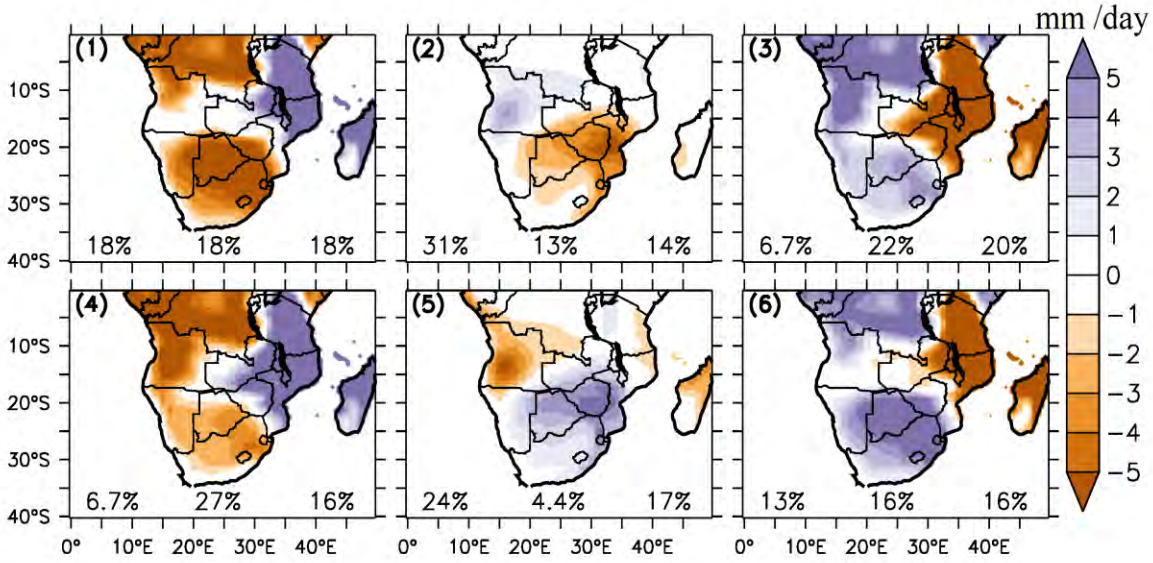

Figure 6.3 SOM classification of the observed (CRU) and the simulated (CAM) austral summer rainfall patterns (anomalies, mm day^{-1}) over Southern Africa. Class numbers are written on the upper left sides of each panel while the frequencies of occurrences (%) are shown on the lower left, middle and right respectively for CRU, CAM ensemble mean and the average of individual ensemble member simulations.

6.3 Inter-annual Variability of the Dominant Summer Rainfall Classes over Southern Africa

There are differences in how well CAM ensemble members and the ensemble mean reproduce the inter-annual variation of the dominant rainfall classes (Figure 6.4a, b). For instance, there are only 13 summers (out of 45) of agreement between CRU and the ensemble mean; meanwhile, there are only 5 summers where all CAM ensemble members disagree with CRU. In other words, the ensemble mean only captures the observed classes 29% of the time, while at least one ensemble member reproduces the right classes 89% of the time. The problem is how to pre-select the ensemble member(s) that will produce the right classes. However, this supports the notion that using different weighting functions to generate an ensemble mean (based on performance of ensemble members) may give a better forecast than uniformly averaging the ensemble members to produce the ensemble mean. Nevertheless, Figure 6.5 indicates that only three ensemble members have higher synchronization (a measure of right class at the right time) than the

ensemble mean. The best CAM simulation (hereafter, Run 49) agrees with CRU 40% of the time (i.e. $\eta = 40\%$; Fig. 5).

Figure 6.4(a, b) also shows that for all the 13 cases of agreement between CRU and the CAM ensemble mean the same number of CAM ensemble members agree with both CAM and CRU, but not all the 50 members agree. It could be that the rainfall anomalies in the correct ensemble members dominate those in the wrong members. However, Figure 6.4 suggests that the agreement between the CAM ensemble mean and CRU requires at least 13 (i.e. 26%) of the ensemble members to agree with the CRU (see year 1993 in Figure 6.4b). However, CAM may correctly reproduce occurrence of any rainfall class, because all the rainfall classes are included in the 13 cases of the agreement between CRU and the CAM ensemble mean (i.e. Nodes 3 and 4 occur once; Nodes 1 and 5 occur twice; Node 6 occurs thrice while Node 2 occurs four times).

Furthermore, CAM also captures the transition and persistence of some rainfall classes as in CRU (see Section 4.3 for explanations on transition and persistence). For instance, CAM ensemble mean correctly reproduces the transition of Node 6 to Node 5 in 1974–1975, Node 5 to Node 6 in 1975–1976, and Node 2 to Node 1 in 1983–1984. It also simulates the persistence of Node 6 in 1976–1977 and that of Node 2 in 2003–2004. However, the ensemble mean fails to capture the persistency of Node 2 in 1964–1965, 1979–2000, and 2001–2005, or that of Node 5 in 1989–1990. In addition, CRU shows that Node 2 is the most persistent rainfall class (persisting for 4 years, 2001–2005), and it is also the node with highest cases of persistence (i.e. 3 cases). CAM ensemble mean fails to capture this. Instead, it suggests that Node 3 is most persistent node (persisting for 4 years, 1966–1970) and that Node 4 has highest cases of persistency (i.e. 3 cases) (Figure 6.4). Meanwhile, at least five of the ensemble members (including Run 49) agree with CRU that Node 2 is the most persistent rainfall class and is the node with highest number of persistence (Figure 6.5). However, most ensemble members suggest Node 3 as the most persistent node and Node 4 as the node with the highest cases of persistency.

6.4 Decadal Frequency of the Dominant Summer Rainfall Classes over Southern Africa

The decadal frequency of the rainfall classes has different distributions and there is no distinct trend in the distributions (Figure 6.6). The rainfall classes exhibit their maximum frequency in different decades. For example, Node 1 features the maximum frequency (3 events) in 1980s while Node 6 features it (3 events) in 1970s. Node 3 produces it (2 events) in 1960s but Node 4 produces it (2 events) in 1990s. Node 2 shows the maximum frequency (5 events) in 2000s while Node 5 attains the maximum values (3 events) consistently for three decades (1970s, 1980s and 1990s). CAM (ensemble mean) captures few characteristics of the decadal frequency as observed in CRU. For instance, it correctly simulates the magnitude and period of the maximum decadal frequency in Node 1 class, although the simulated distribution is different from observed. It also captures the period of the maximum decadal frequency in Nodes 3 and 6, but the magnitude is higher than the observed. However, in most cases, the spread of decadal frequency simulated by CAM ensemble members encompasses or overlaps the observed values. This indicates that at least one ensemble member simulate the decadal frequency of the observed value. However, CAM fails to capture the distribution and maximum decadal frequency of Node 4; it simulates the maximum decadal frequency in 1980s, instead of 1990s. Nevertheless, the worst performance of CAM in simulating the decadal frequency is when the model simulates high decadal frequency for a rainfall class in a decade, but the class does not feature at all in that decade. Examples of this include Nodes 1 in 2000s, Node 3 in 1970s, and Node 4 in 1980s and 2000s.

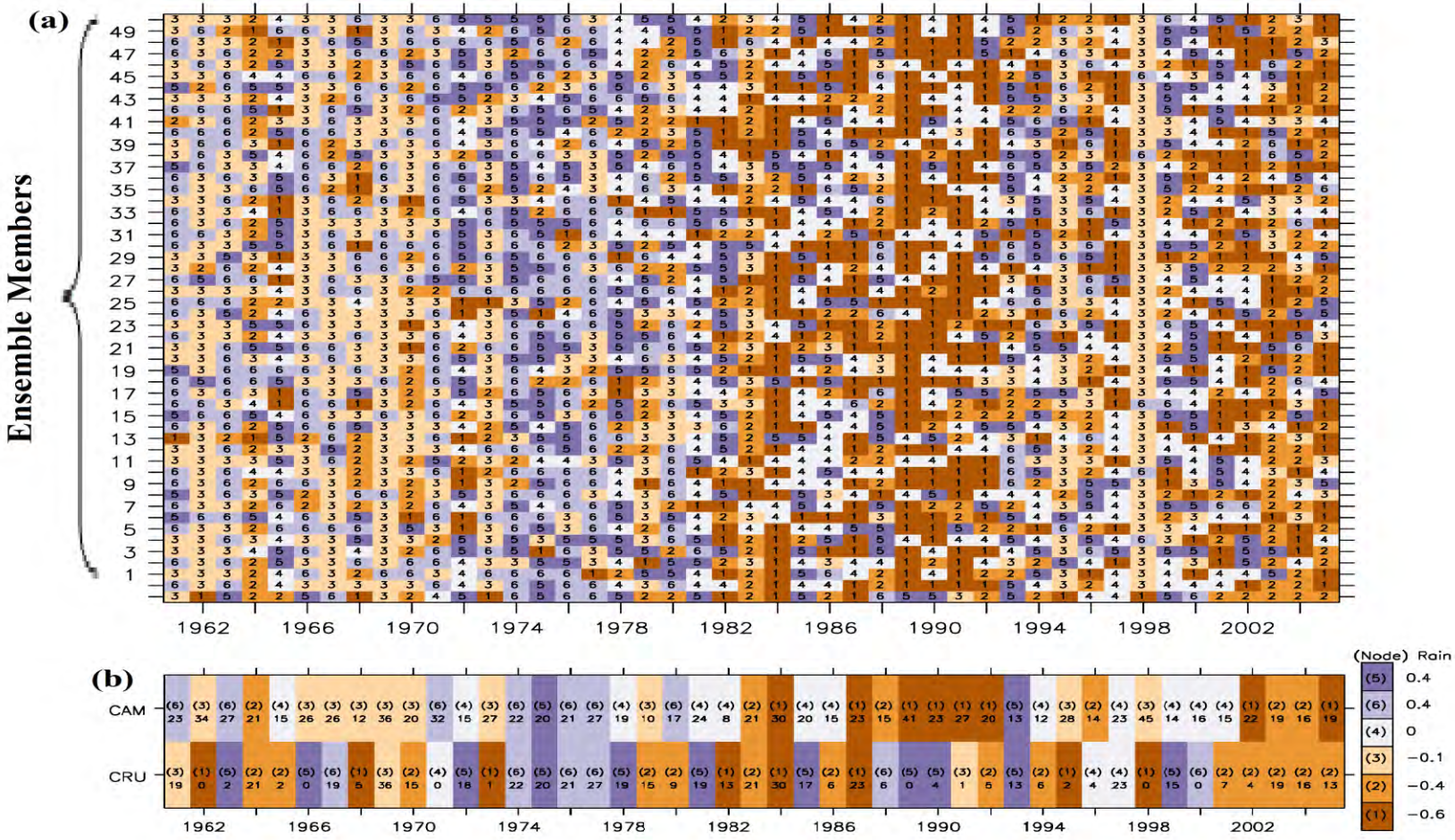

Figure 6.4 Inter-annual variability of spatial classes of rainfall anomalies (mm day^{-1}), depicted in Figure 6.3; **(a)** as simulated by 50 CAM ensemble members, CAM ensemble mean (upper bottom row) and observation (CRU: bottom row) and **(b)** an enlarged last two bottom rows of panel a showing the ensemble mean (upper row) and the observation (bottom row) (the numbers in brackets (i.e. 1 – 6) show the nodes of rainfall classes while the colours indicate the mean rainfall anomalies over the sub-region. The number under the nodes shows the number of the ensemble members that agree with CRU observation or with the CAM ensemble mean simulations on the rainfall class).

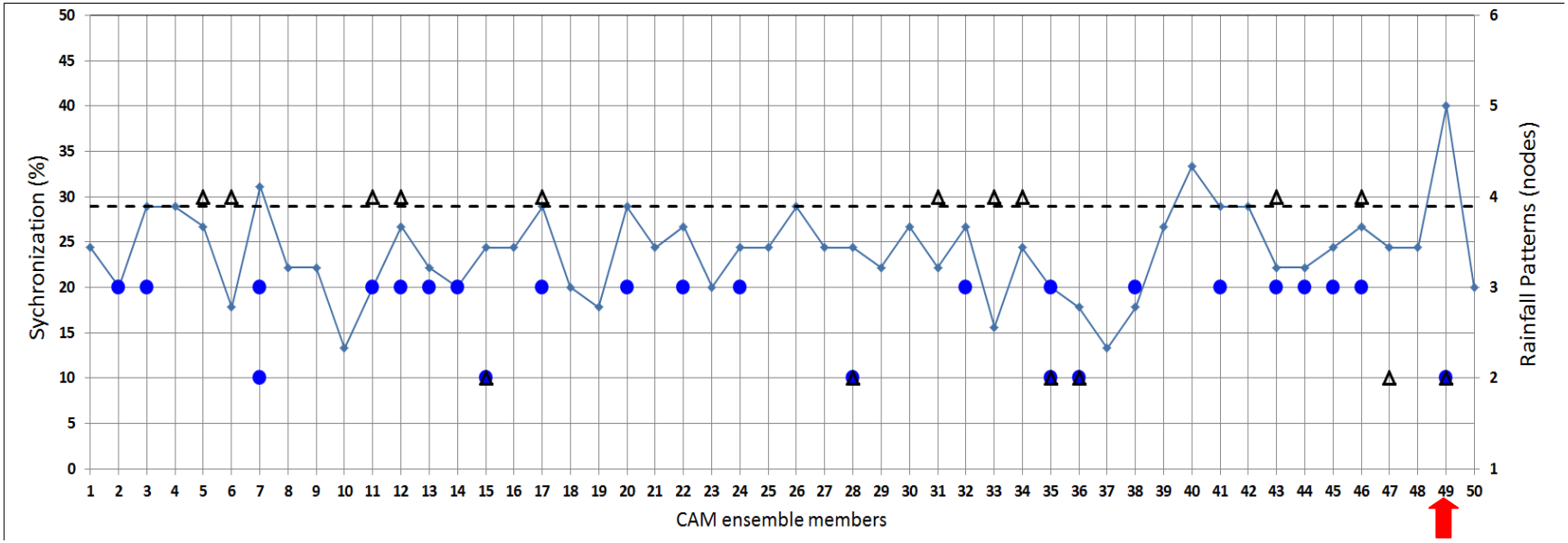

Figure 6.5 Synchronization (%; left y-axis) and persistence (nodes; right y-axis) of simulated rainfall classes in reference to observation. The red arrow points to the ensemble member with the highest synchronization (the 49th simulation: Run 49).

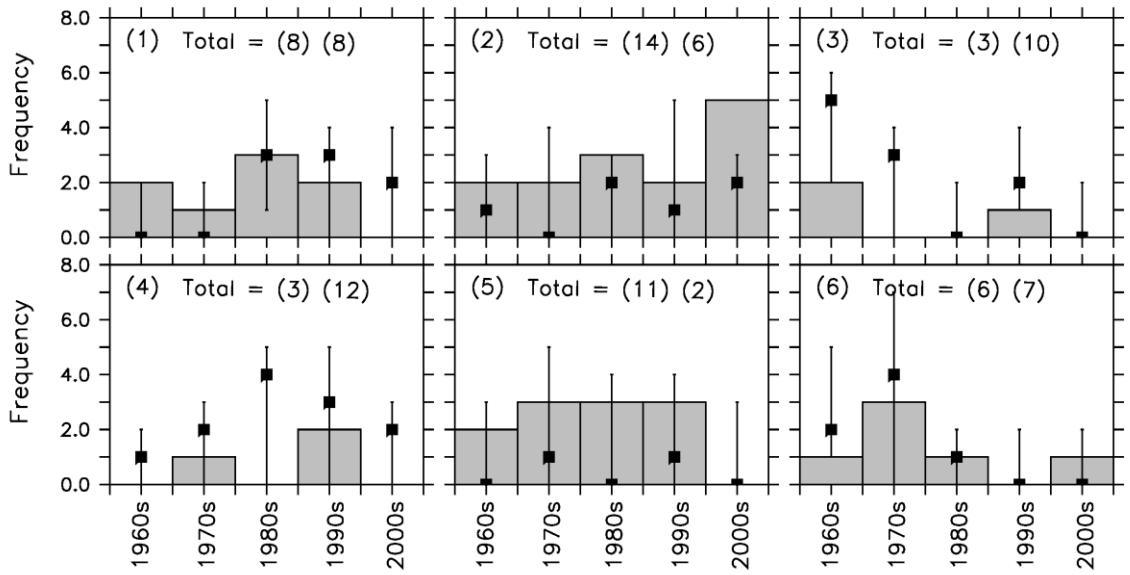

Figure 6.6 The decadal frequency of rainfall classes (shown in Figure 6.3) as observed (CRU) and simulated (CAM). The grey bars indicate the observed values; the black squares show the CAM ensemble mean, while the error bars depict the spread (i.e. minimum and maximum values) among the CAM ensemble members. The tag (i.e. node) of each rainfall class is shown at the upper left corner of each panel, and the total number of the rainfall class occurrences in CRU and CAM (ensemble mean) datasets are shown in the panel, i.e. (CRU; CAM).

6.5 Atmospheric Tele-Connections and the Occurrence of Dominant Summer Rainfall Classes over Southern Africa

CRU observation shows that ENSO has a substantial relationship with all the rainfall classes, and the relationship is consistent with three of the rainfall classes (i.e. Nodes 2, 3 and 4: Figure 6.7). For example, Node 2 and 3 feature more than 38% and 65%, respectively, of their events during the positive phase of ENSO (i.e. El Nino) and none during the negative phase (i.e. La Nina). In contrast, Node 4 has more than 68% of its events during La Nina and none during El Nino. However, the relationship between ENSO and other rainfall classes (i.e. Nodes 1, 5 and 6) is not consistent. For instance, Node 1 features more than 50% of its event during El Nino, and yet features more than 25% during La Nina. In contrast, Node 6 features 70% of its events during La Nina, but shows at least 18% during La Nina. Node 5 has the most unreliable relationship with

ENSO, because it features equal number (25%) of its events in both El Nino and La Nina. CAM fails to capture the consistent association between ENSO and Node 2, 3 and 4; instead, it indicates an inconsistent relationship between ENSO and these rainfall classes. However, the model capture the inconsistent relationship between ENSO and other rainfall classes as observed in CRU. For example, the model agrees with CRU that Node 1 features more events during El Nino than during La Nina, and that Node 6 occurs more during La Nina than during El Nino conditions. It also captures that Node 5 has the most unreliable relationship with ENSO, because the simulated class also features equal number (50%) of events in both El Nino and La Nina.

In CRU observations, IOD has a substantial relationship with five of the rainfall classes, and the relationship is consistent for two of the rainfall classes (i.e. Node 1 and 3: Figure 6.7). The two rainfall classes feature about 35% of their events during the negative phase on IOD and none during the positive phase. Meanwhile, Node 4 features all its events during the neutral phase of IOD. Other rainfall classes (Nodes 2, 5 and 6) show inconsistent relationship with IOD. While Node 2 shows about 40% and 30% of its events in positive and negative (respectively) phases of IOD, Node 5 shows about 40% and 10% (respectively), and Node 6 shows 20% and 70% (respectively). CAM also fails to reproduce the consistent relationship IOD with Nodes 1 and 3; and contrary to CRU, it simulated Node 4 during the active phases of IOD. Nevertheless, in agreement with CRU, the model simulate that Node 5 features more during the positive phase of IOD than during the negative phase, and that Node 6 occurs more negative phase of IOD than during the positive phase.

CRU also indicates that AAO has substantial relationship with all the rainfall classes, but the relationship is only consistent with Node 4, which features about 30% of its events during the positive phase of AAO and none during the negative phase (Figure 6.7). Node 3 has the most unreliable relationship with AAO, in that it features equal number of events (38%) during the positive and negative phase of the tele-connection. CAM does not capture the consistent relationship between AAO and Node 4, but simulate well the

inconsistent relationship between AAO and other rainfall classes. The observation also show that BEN has a substantial relationship with the rainfall classes (except Node 3), but the relationship is inconsistent. CAM simulates the inconsistent relationship, but could only reproduce observed portioning of the events between positive and negative phases of the tele-connection for only one rainfall class (Node 4).

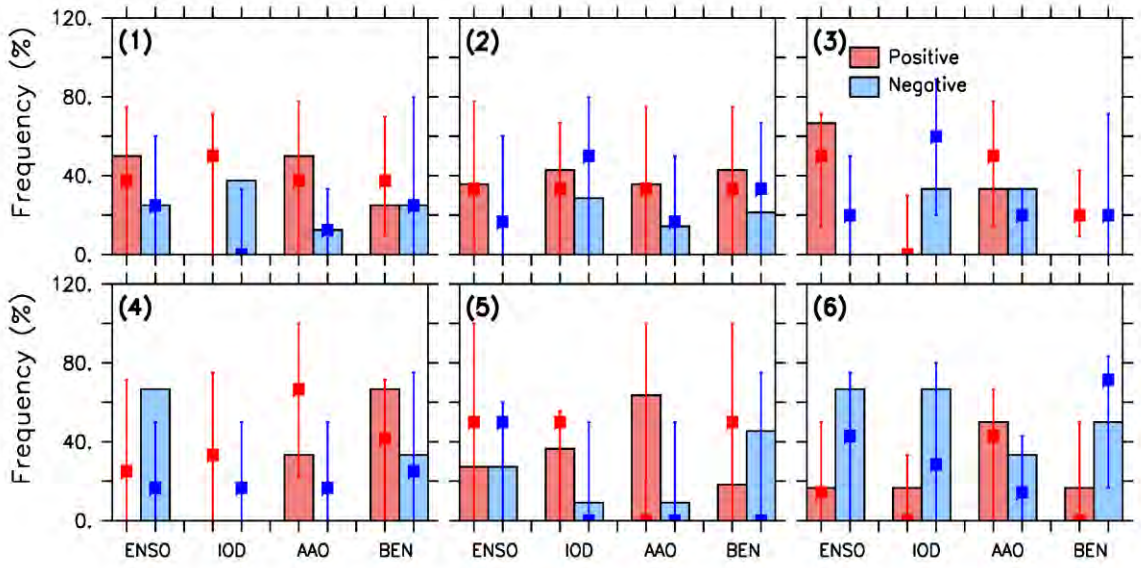

Figure 6.7 Frequency of occurrence of climate indices associated with spatial classes of rainfall anomalies depicted in Figure 6.3, expressed as percentage of frequency of occurrence. Red and blue colors indicate, respectively, positive and negative phases of each climate index; bars, squares, and the upper and lower parts of the error bars, respectively, denote the frequencies of the climate indices associated with observation (CRU), CAM ensemble mean, and the maximum and minimum frequencies of the climate indices produced by CAM ensemble members. The tag (or node) of each rainfall class is shown in bracket on the upper left corner of each panel. See Table 3.2 for brief descriptions of the climate indices considered in this study.

In summary, Figure 6.7 shows that each rainfall class links with more than one tele-connection, making it difficult to associate any class with a particular tele-connection. However, the figure can guide on identifying the unfavorable and favorable tele-connection conditions for each rainfall class. For example, the figure suggests that Node 3 does not occur during the negative phase of ENSO and/or positive phase of IOD. Meanwhile, Node 4 does not occur during the positive phase of ENSO and/or negative

phase of AAO. The reason for the inconsistent relationship between tele-connection and the rainfall classes is not clear, but may be attributed to a number of reasons. As there are different flavors of these tele-connection (i.e. conical El Nino versus El Nino Modoki; Johnson, 2012; Hoell et al., 2014; Ratnam et al., 2014), it could be that each rainfall class has preference for different flavor of a tele-connection; and here, we only used a flavor of each tele-connection. In addition, apart from conflicting impacts of the tele-connection on the rainfall classes, the influence of local or regional forcing may be more important than that of the tele-connections in some rainfall classes. All these could also explain or contribute to the poor performance of CAM in simulating the relationship of the rainfall classes with the tele-connection. However, using the ensemble mean for the evaluation may also compromise the evaluation because for a particular tele-connection the ensemble members may produce different rainfall classes, yet all the classes are averaged together to obtained the ensemble mean for that condition.

6.6 Global SST Anomalies and the Dominant Summer Rainfall Classes

To further investigate how well CAM simulates the link between the rainfall classes and ENSO flavors, we present the composite of SST patterns associated with the observed and simulated rainfall classes (Figure 6.8) in comparison with the SST patterns of ENSO flavors (obtained by Johnson, 2012 and Hoell et al., 2014). For CRU, all the SST patterns associated with the rainfall classes compare well with those of ENSO flavors. For example, Node 1 and Node 6 SST patterns (Figure 6.8a) are similar to Hoell et al. (2014) El Nino pattern 3 (hereafter, EN3) and La Nina pattern 3 (hereafter, LN3), respectively. In agreement with EN3, Node 1 SST pattern features warm tropical SST (i.e. positive anomaly) over eastern and central Pacific Ocean and the warmest SST is between 180^{o}E - 120^{o}W, while Node 6 SST features the opposite. Interestingly, our Node 1 rainfall class agrees well with the EN3 rainfall pattern over Southern Africa, and our Node 6 rainfall class resembles their LN3 rainfall pattern over Southern Africa. For CAM, the ensemble mean shows similar Node 6 SST patterns to CRU, but Run 49 does not (Figure 6.8b, c). However, neither the Ensemble mean nor Run 49 features the characteristics of Node 1

SST patterns as depicted by CRU. This implies that CAM fails to associate Node 1 rainfall class with EN3. Furthermore, While CRU associates Node 3 and node 4 with EN1 and LN1 respectively, Run 49 associates them with EN4 and LN4 (Figure 6.8b), respectively, and the ensemble mean associate them with EN2 and LN4, respectively (compare Figure 6.8c with Hoell et al, 2014). CRU generally attributes Nodes 2 and 5 to EN2 and LN2, respectively (Figure 6.8a), Run 49 does not associate them with a notable ENSO flavor (Figure 6.8b), while the ensemble mean associates them with EN3 and LN4 (Figure 6.8c), respectively.

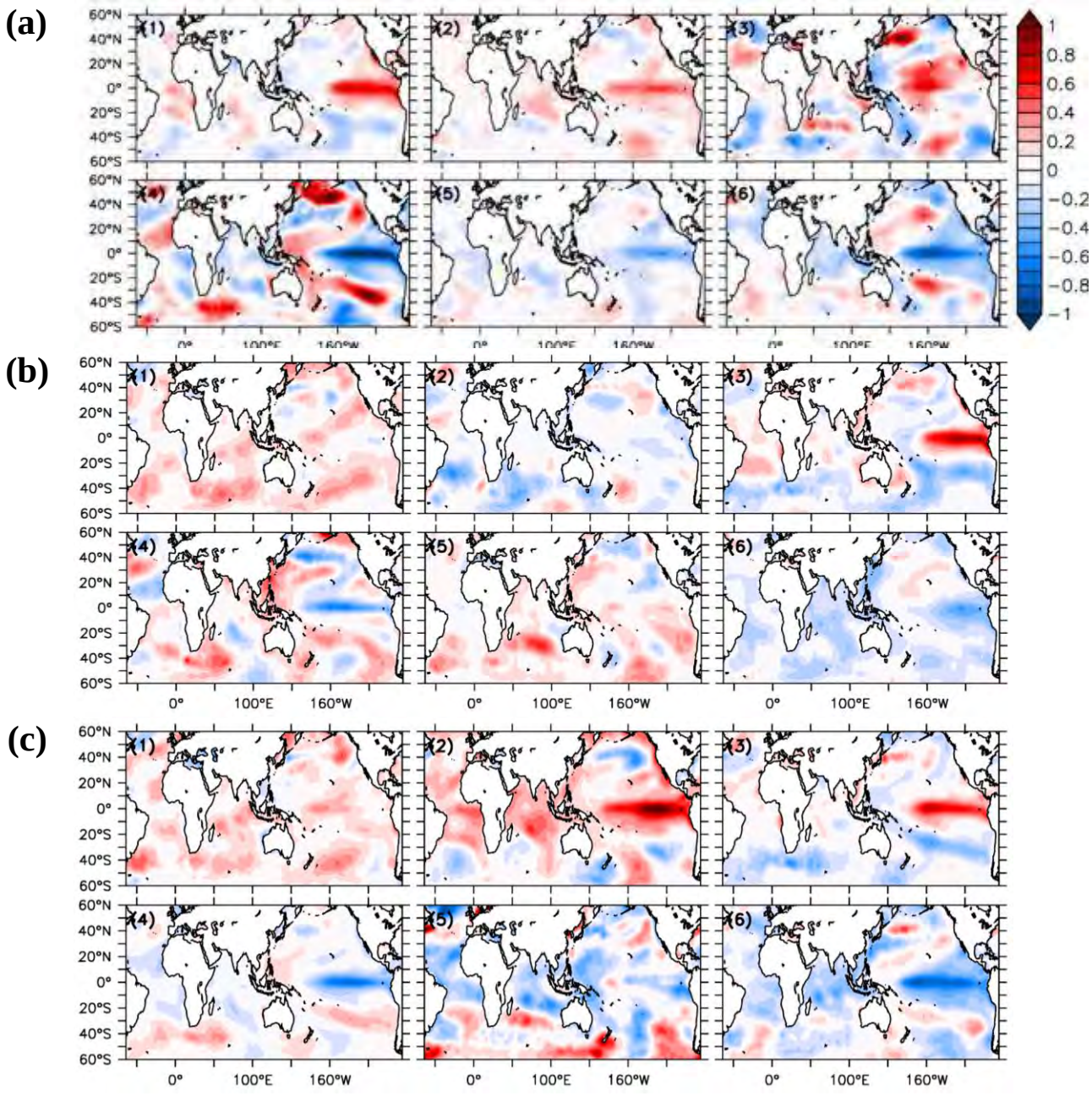

Figure 6.8 Composites of austral summer global SST anomalies (^{o}C) for **(a)** CRU, **(b)** CAM Run 49 and **(c)** CAM Ensemble in the SOM classification (shown in Fig. 6.3). Pattern numbers, which correspond to the spatial classes of rainfall anomalies in Figure 6.3, are written on the upper left sides of each panel while the SST anomalies are relative to the 1961-2005 climatological mean.

6.7 Composite of Atmospheric Conditions Associated with the Dominant Summer Rainfall Classes

In this section, we examine how well CAM simulates the atmospheric condition associated with the rainfall classes. For clarity and consistency, we separate the composite of each dataset (i.e. CRU, Run 49, and the ensemble mean) in the rainfall classes (i.e. nodes; Figure 6.9) and examine the structure of the corresponding atmospheric fields (i.e. 850hPa level winds, vertical velocity, and vertically integrated moisture flux convergence; Figure 6.10 and 6.11). The composites of CRU and CAM (Run 49 or the ensemble) rainfall classes agree in some nodes but differ in others (Figure 6.9). The best agreement between CRU and CAM composites occurs in Nodes 1 and 6 rainfall classes, where the correlation (r) between the observed and simulated classes is high ($0.64 \leq r \leq 0.76$). The reanalysis and CAM features similar patterns in the associated dynamic fields (anomalies). For instance both datasets agree that Node 1 rainfall class is associated with net cyclonic flow (i.e. weaker anticyclone flow) over the India Ocean. The net cyclonic flow induces a stronger tropical westerly flow over the continent and Indian Ocean (between 0^o and 10^oS), and a stronger southerly flow over the eastern part of Southern Africa (south of 20^oS). The convergence of these tropical westerlies and southerly flows over the Indian Ocean, Tanzania and northern Mozambique produces the moisture convergence (Figure 6.10), enhanced convection (stronger upward motion; Figure 6.11), and positive rainfall anomalies over these areas (Figure 6.9). The negative rainfall anomalies over continent (i.e. south of 20^oN) can be attributed to the transport of cold and dry polar air (by the southerly flow) into the area. Furthermore, the reanalysis and CAM also agree that anomalies in winds, moisture flux convergence, and vertical motion fields for Node 6 rainfall class are opposite of those for Node 1. Hence, in addition to reproducing the frequency of the Nodes 1 and 6 rainfall classes as observed (see Figure 6.3), CAM simulates the regional atmospheric condition associated with these rainfall classes well.

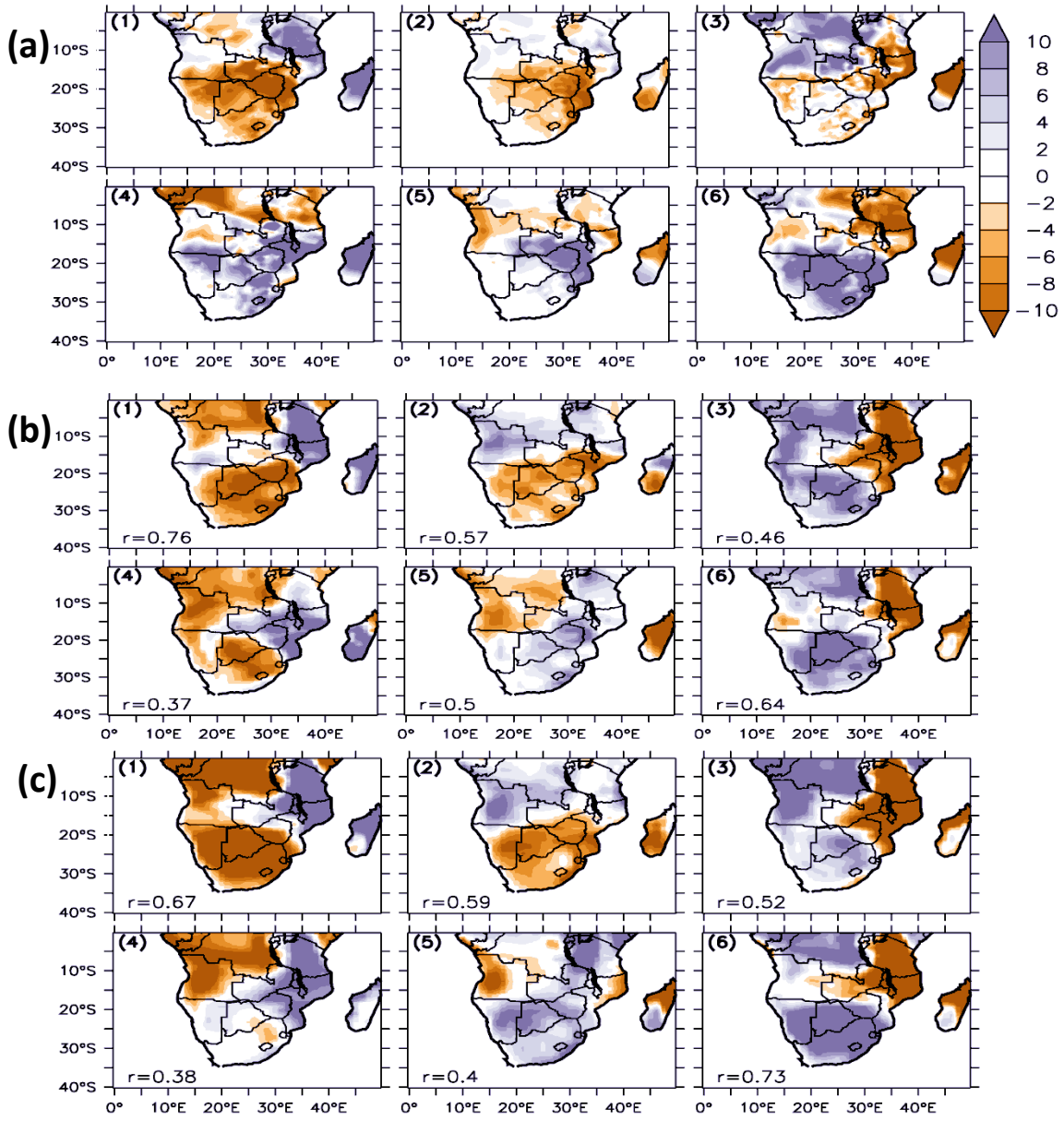

Figure 6.9 Composite of the spatial patterns of austral summer rainfall anomalies (mm day^{-1}) over Southern Africa for **(a)** observation (CRU), **(b)** CAM Run 49 and **(c)** CAM ensemble mean. Pattern numbers, which correspond to spatial classes of rainfall anomalies in Figure 6.3, are written on the upper left sides of each panel while the values of spatial correlations of Run 49 and ensemble mean with corresponding observed rainfall pattern are written on the bottom left of panels in **b** and **c** respectively.

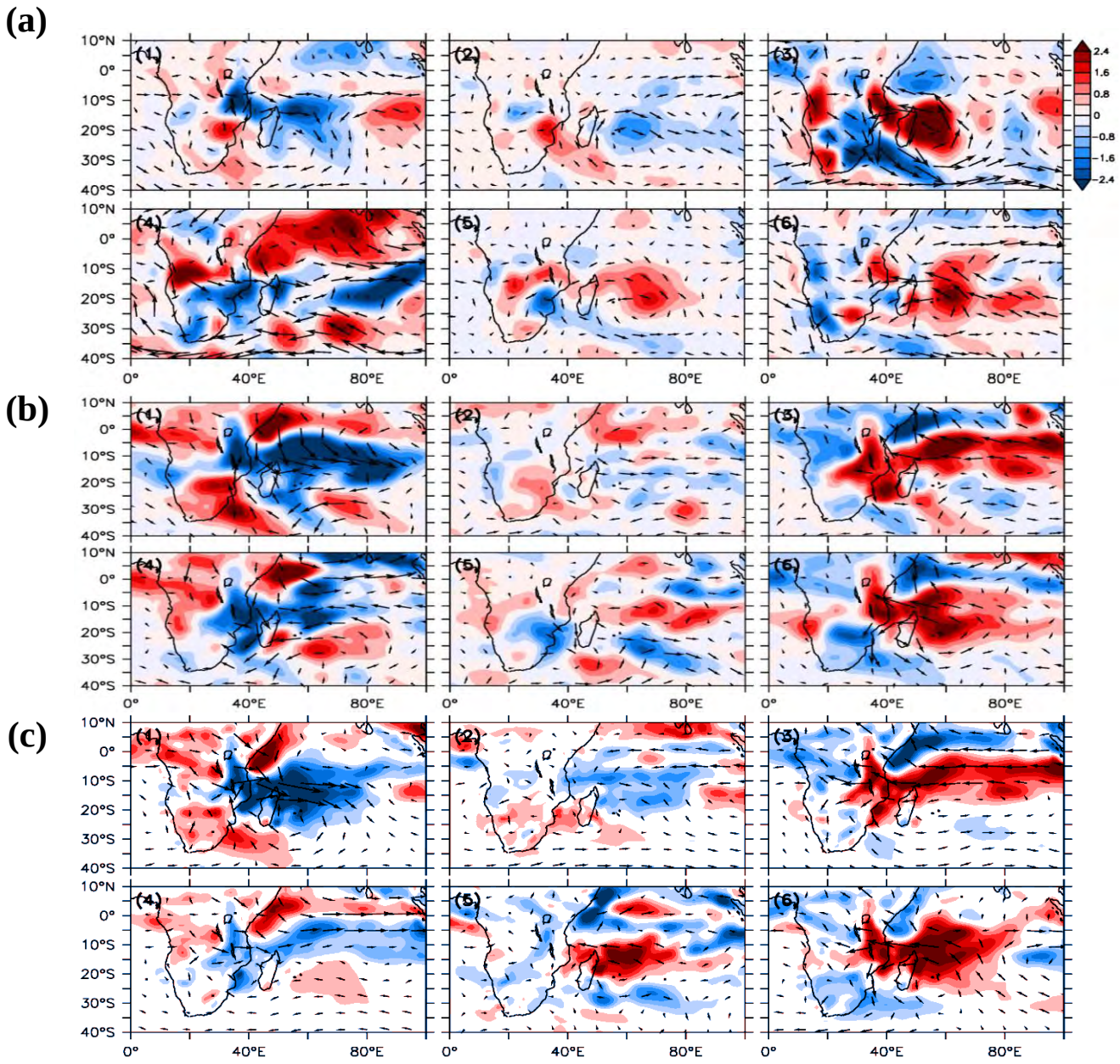

Figure 6.10 Composite of the spatial patterns of austral summer wind anomalies at 850hPa level (arrows) and vertically integrated moisture flux convergence (shaded; anomalies, $x10^{-5}$ s^{-1}) for **(a)** CRU, **(b)** CAM Run 49 and **(c)** CAM Ensemble in the SOM classification (shown in Figure 6.9). The anomalies are with reference to 1961-2005 mean; a positive value (red) indicates resultant divergence while a negative value (blue) denotes resultant convergence. Pattern numbers, which correspond to spatial classes of rainfall anomalies in Figure 6.9, are written on the upper left sides of each panel.

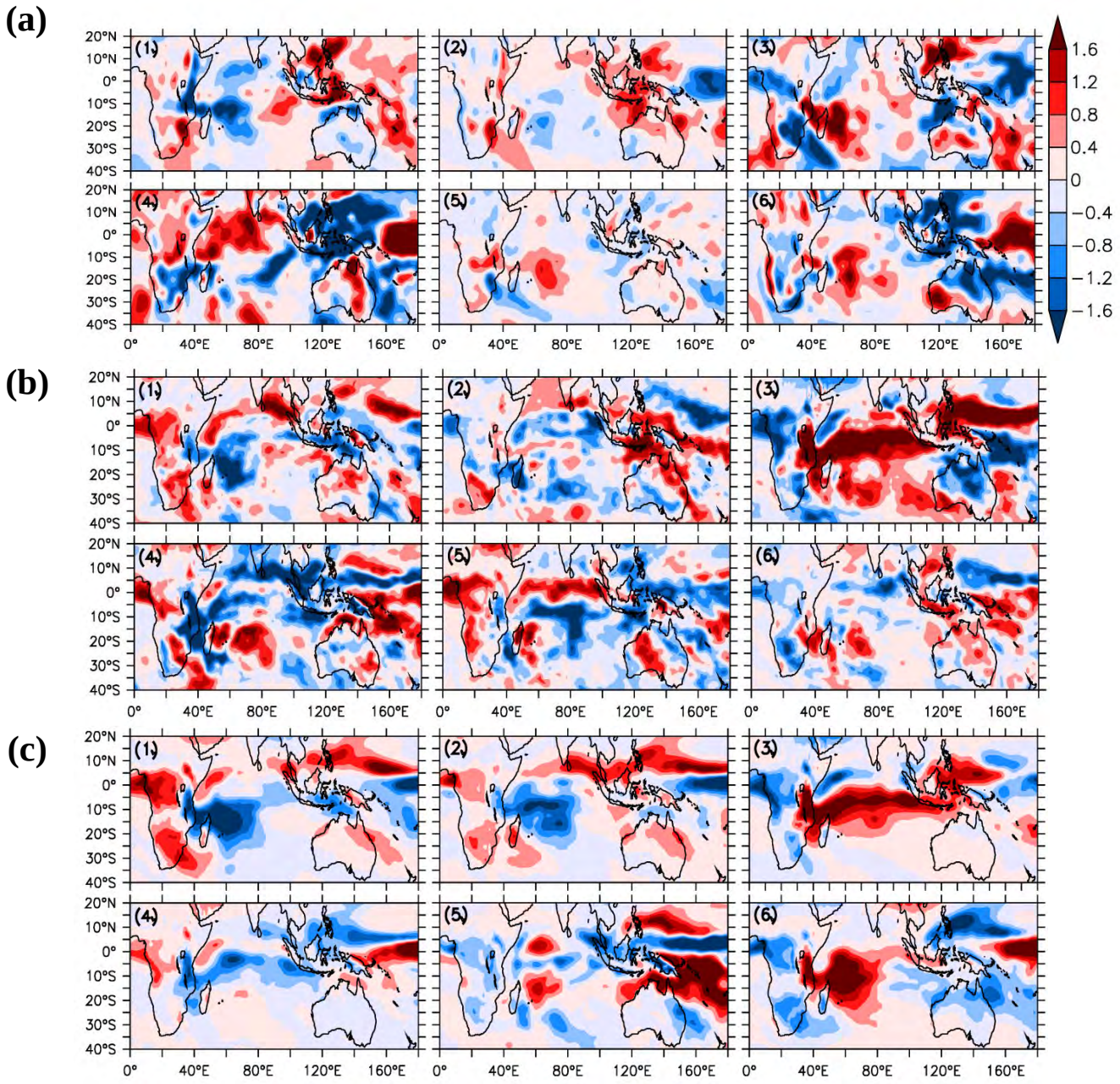

Figure 6.11 Composite of the spatial patterns of austral summer vertical velocity at 500hPa level (anomalies, x 10^{-2} Pa s^{-1}) for **(a)** CRU, **(b)** CAM Run 49 and **(c)** CAM Ensemble in the SOM classification shown in Figure 6.9. The anomalies are with reference to 1961-2005 mean; a positive value indicates resultant descent (downward motion) while a negative value denotes resultant ascent (upward motion). Pattern numbers, which correspond to spatial classes of rainfall anomalies in Figure 6.9, are written on the upper left sides of each panel.

The worst agreement between CRU and CAM composites is in Nodes 3 and 4. The correlation between the simulated and observed patterns is weak ($0.37 \leq r \leq 0.52$; Figure 6.9). Apart from overestimating the frequency of these rainfall classes (Figure 6.3), CAM does not simulate the rainfall distribution as observed. For instance, in Node 3, CRU features a negative rainfall anomaly over some areas south of 20°S, but CAM simulates positive a rainfall anomaly over these areas; the reverse is the case in Node 4. As expected, the simulated atmospheric conditions for these also differ from the observed (Figures 6.10 and 6.11). The reanalysis attributes Node 3 rainfall class with anomalous anti-cyclonic flow (centered over Madagascar) and stronger westerly flows in the mid-latitudes (south of 30°S), and Node 4 with a weaker easterly flow in the mid-latitudes (south of 30°S). On the other hand, CAM attributes Node 3 rainfall class with enhanced tropical easterly flows in the tropics (within ±20°N), and Node 4 rainfall class with a stronger westerly flow in the tropics (within ±20°N). However, the observed and simulated anomalies of the vertical motion and moisture flux convergence fields for Node 3 and 4 are consistent with their corresponding rainfall anomalies.

6.8 Summary

This chapter has shown that CAM is able to adequately simulate the observed austral summer rainfall climatology over Southern Africa. In addition to its capability to realistically capture most of the atmospheric dynamics of the summer rainfall, the model gives a realistic simulation of the inter-annual variation of the summer rainfall (area averaged) over Southern Africa. CAM has the capability to simulate satisfactorily the "wet eastern part – normal central parts – dry northwest and southern parts or vice versa", averagely simulates the" normal conditions over the entire region" but poorly reproduces the "wet eastern part – dry northwest and southern parts or vice versa". On inter-annual time scale, CAM ensemble mean, in addition to being able to capture the occurrence and persistence of the dominant rainfall classes, is capable of reproducing any of the observed dominant rainfall classes 29% of the time; a minimum of one ensemble member, out of the 50 members, has 89% chance to randomly reproduce the right rainfall class; while the best simulation (Run 49) simulates it 40% of the time. The model however struggles to link these dominant rainfall classes to ENSO flavours and also shows that any of the

dominant rainfall classes may be associated with more than one climate index. This chapter has therefore identified the spatial classes of rainfall anomalies that CAM can adequately simulate and those it struggles to reproduce over Southern Africa during the austral summer seasons.

A comparison of results in this chapter with those in chapter (4) indicates that the model simulates the seasonal rainfall better over West Africa than over Southern Africa in all aspect, except in reproducing amplitude of the rainfall variability as observed (i.e. normalized standard deviation). First, the correlation, r, between observed and simulated summer rainfall is higher over West Africa (i.e. $0.4 < r < 0.65$; $r = 0.64$ for ensemble mean) than over Southern Africa (i.e. $-0.1 < r < 0.54$; $r = 0.4$ for ensemble mean), although the normalized standard deviation is closer to 1.0 over Southern Africa than over West Africa (see Figures 4.1 and 6.1). Second, the synchronization of the ensemble mean (with observation) is also higher over West Africa ($\eta > 33\%$) than over Southern Africa ($\eta < 30\%$). Both the worst ($\eta_{worst} = 20\%$) and the best ($\eta_{best} = 42.2\%$) simulations over West Africa have higher synchronizations than their counterparts over Southern Africa ($\eta_{worst} = 15.6\%$; $\eta_{best} = 40\%$) respectively (Figures 4.5 and 6.5). Third, over West Africa, about 40% of the simulations perform better than their average, but, over Southern Africa, only 6% of the of the simulations perform better than their average. However, the discrepancy among the simulations (or the spread among the simulations) is higher over West Africa than over Southern Africa, suggesting that the predictability of dominant seasonal rainfall may be lower over West Africa than over Southern Africa.

7 Characteristics of Summer Maximum Air Temperature Patterns over Southern Africa

We present and discuss the results of the characteristics of austral summer near-surface (2m) maximum air temperature patterns over Southern Africa, as observed by CRU and simulated by CAM in this chapter. Firstly, we carried out the performance evaluation of CAM in simulating the climatology of the summer maximum air temperature patterns. Secondly, the characteristics of the six dominant summer (maximum) temperature classes (anomalies), obtained using SOM analysis as described in Chapter 3, and the evaluations of how well CAM reproduces them are then discussed. The characteristics of the dominant summer temperature classes considered are the inter-annual and decadal variability, transition, and persistence. Lastly, the chapter examined the influence of atmospheric tele-connections on the observed and simulated classes, and investigates the capability of CAM in reproducing the atmospheric dynamics that produces each summer temperature classes.

7.1 Validation of the Model

CAM ensembles mean realistically simulate the mean austral summer maximum air temperature over Southern Africa. The model (CAM) is able to reproduce the spatial structures of the temperature over the borders of Namibia, Botswana and South Africa, and captures the cut-off structure over the north-western parts of the sub-region (Figure 7.1a, b). CAM, in agreement with the observation (CRU), also reproduces the relatively lower temperature over the eastern parts of Madagascar, Lesotho environs and those that extend from the Angolan coast through the central parts to the north-eastern parts of the sub-region. Visual comparison of the observed temperature (Figure 7.1a) to the simulation (Figure 7.1b) shows that CAM exhibits cold biases of up to about -5^{o}C (bias maps not shown). Ranked probability skill score (RPSS - a measure of skill: Mason, 2004; Weigel et al., 2006) also reveals that the model has skill in simulating temperature over Southern Africa. Computed, but not shown, RPSS is generally positive over the sub-region; though it is widely less than 0.5. The low skill may be attributed to poor

parameterization of physical processes as suggested by Rusticucci and Kousky (2002), and Flocas et al. (2004).

CAM ensembles mean also captures the spatial distributions of austral summer total cloud fraction over Southern Africa (Figure 7.1c, d). Agreements between observation and simulation show that the total cloud fraction is highest over the central-northern axis of the sub-region (> 80%) while it is least over the south-west corner of the sub-region (generally less than 40%). Cloudy areas coincide with areas of relatively lower temperatures and vice versa (Figure 7.1a, b, c, d). The agreements also show that the north-eastern parts of Madagascar are cloudier than the southern parts. These suggest that cloudiness has impact on the degree of hotness or coldness of air temperature over the sub-region.

The simulated vertical velocity (omega) at 500hPa level has the same magnitudes with the reanalysis, except that the location of the maximum upward motion (about 8 x 10^{-2} Pa s^{-1}) extends 5^{o} more westward than observed (Figure 7.1e, f). Similarly, as in the reanalysis, CAM simulates anti-cyclonic flows over the Atlantic and Indian Oceans at 850hPa level. The model also reproduces a convergence of easterlies from the Indian Ocean and westerlies from tropical Atlantic Ocean over the central parts of the sub-region. These easterlies and westerlies transport moisture, respectively from the Indian and Atlantic Oceans, into the sub-region and the convergence of the moisture roughly overlaps with locations of lower temperature, cloudier areas and areas of maximum upward motions (Figure 7.1a, c, e). In these cases, CAM agrees well with the reanalysis except that the magnitude of the convergence is weaker in CAM than in reanalysis and the simulated easterlies are stronger in CAM than in the reanalysis (Figure 7.1b, d, f). A col, at the southwestern tip of the sub-region (around 33^{o}S, 20^{o}E), which provides links through which a maritime trough connects the continental depression to a mid-latitude low system is also captured by CAM (Figure 7.1e, f). These wind patterns provide necessary mechanisms for formations of tropical-temperate-troughs (TTTs) and the associated convective cloud bands that produce most of the summer rainfall, and in turn

modulate surface temperatures (i.e. Jury and Pathack, 1993; Todd and Washington, 1999; Hansingo and Reason, 2008; Manhique et al., 2009). Therefore, the realistic simulation of these features implies that CAM adequately captures the general dynamics behind the summer temperature climate.

Figure 7.2a shows that both CRU and CAM exhibit increasing trend in maximum air temperature. That is, temperature anomalies are majorly sub-zero within 1960 to around 1980 and majorly positive after 1980, except in few cases (e.g. 1989, 2000, etc). The figure also show that the observed temperature anomalies falls within probable ranges of CAM ensemble members in most of the years under consideration. However, ensemble members fail to envelop the observation in 1989, 1992 and 2006; and the largest discrepancies (about 0.4^{o}C) between the ensembles mean and observation occur in these years. Ensembles mean closely follows CRU and the disagreement between them, though visible, is not so large. For instance, Figure 7.2b, which depicts the normalised standard deviation (σ, which is the simulated standard deviation normalised by the observed standard deviation) and the correlation (r) between the simulations and observation, shows that σ ($\approx$ 0.95) and r ($\approx$ 0.85) for ensembles mean are within those of ensemble members ($0.8 < \sigma < 1.3$ and $0.6 < r < 0.88$). Respectively, these imply low discrepancies and strong direct linear relationship between the simulations and the observation. Therefore, CAM is able to represent the temperature climate of Southern Africa and the variability therein but with some bias.

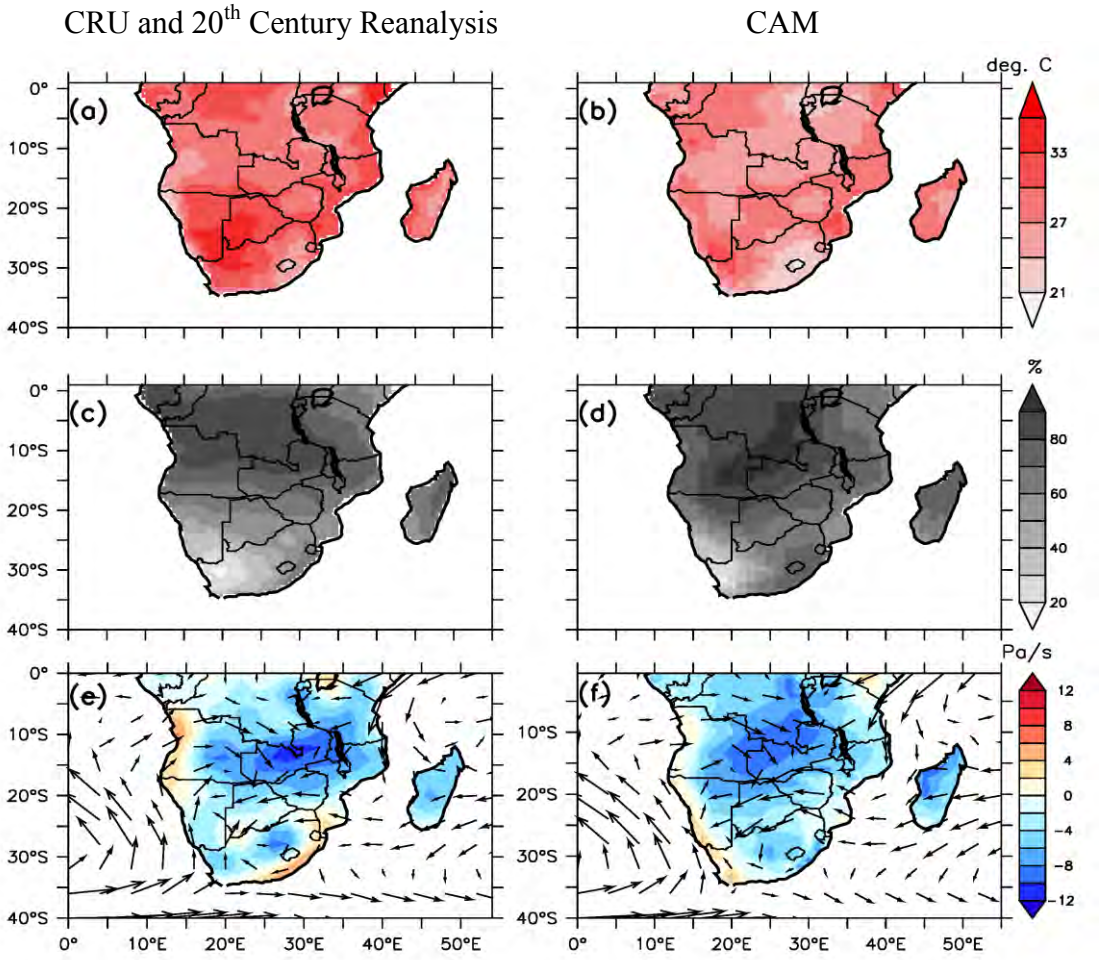

Figure 7.1 Spatial distribution of austral summer mean **(Top row)** near-surface maximum air temperature (2m; ^{o}C); **(Second row)** total cloud fraction (%); **(Bottom row)** vertical velocity (omega; x10^{-2} Pa s^{-1}) at 500hPa level with the corresponding wind vectors at 850hPa level, over Southern African. Respectively on the left and right columns are the observations (CRU or reanalysis) and simulations (CAM ensemble mean).

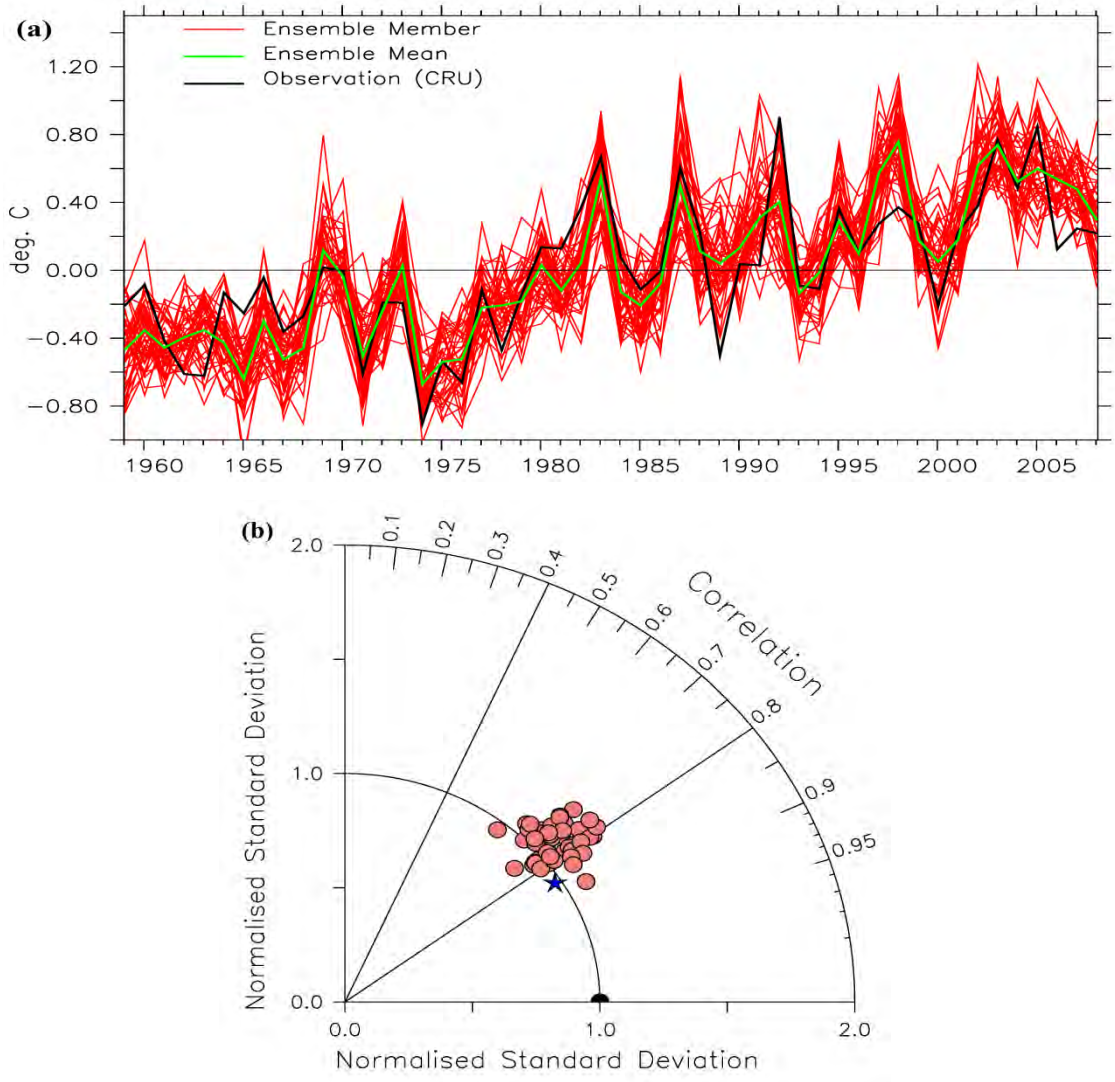

Figure 7.2 (a) The inter-annual variations of maximum air temperature anomalies, averaged over Southern Africa (including Madagascar). **(b)** Taylor diagram, of panel a, showing the normalized standard deviations and the correlation coefficients of CAM ensemble mean (blue star), ensemble simulations (red circles) and CRU observation (black semi-circle). The normalized standard deviations and correlations are with reference to CRU observation.

7.2 Dominant Classes of Maximum Air Temperature over Southern Africa in Summer

Figure 7.3 presents the SOM categorization (3 x 2 nodes) of the observed (CRU) and simulated (CAM) maximum air temperature (anomaly) classes over Southern Africa in summer. The figure depicts the dominant summer temperature classes over the region. These dominant classes can be categorized into three groups in a way that each group contains two opposite temperature classes. Group-one (hereafter known as GRP1) consist of anomaly classes of Nodes 1 and 6. Node 1 features below-normal temperature over the entire Southern Africa with coldest anomalies situated over the Kalahari Desert (i.e. Namibia, south-west Botswana and north-western parts of the Republic of South Africa), and an isolated normal condition over the western parts of Angola. Node 6 features the opposite class of Node 1. Node 1, according to observation, accounts for 18% of summer temperature classes within the experimental time frame (1961 – 2005) while Node 6 accounts for 20%. GRP1 therefore accounts for 38% of the dataset. CAM (ensemble mean and ensemble members) agrees with CRU in Node 1 on the frequency of occurrence; it however under-estimate the frequency of occurrence of Node 6 by about 2 – 4%. CAM, in GRP1, therefore accounts for 36% (ensemble mean) and 33% (ensemble members) of the entire datasets.

Group-two (hereafter known as GRP2) consists of anomaly classes of Nodes 3 and 4. This group has similar features with classes in GRP1 (i.e. Nodes 6 and 1 respectively); except that, in Node 3, there exist a tongue of normal condition which connects eastern coast of the sub-region (i.e. the entire Tanzania and northern parts of Mozambique), through the central areas (Zambia), to the western coast (over Angola). The warmest areas in Node 3, just like in Node 6, are confined to larger areas of Kalahari Desert while the relatively less warm areas are confined to the north-west equatorial parts of the sub-region (i.e. northern Angola and central parts of Democratic Republic of Congo). Node 4 is exactly the opposite of Node 3. Observation shows that GRP2 accounts for 29% of the datasets (i.e. 13% in Node 3, 16% in Node 4). There are disparities in the way CAM reproduces frequencies of occurrences in GRP2. For instance, ensemble members

overestimate both nodes in GRP2 while ensemble mean rightly captures frequency of occurrence in Node 4 but underestimates that of Node 3 by about 2%. CAM, in GRP2, therefore accounts for 27% (ensemble mean) and 36% (ensemble members) of the entire datasets.

Apart from below-normal anomalies over Tanzania and northern Zambia in Node 2 and vice versa in Node 5, group-three (hereafter known as GRP3) which consists of anomaly classes of Nodes 2 and 5, in comparison to GRP1 and GRP2, lacks severely extreme maximum air temperature anomalies. This means that GRP3 features normal temperature anomaly conditions almost over the entire sub-region. CRU shows that GRP3 accounts for 34% of summer temperature classes (i.e. 16% in Node 2, 18% in Node 5). The frequency of occurrence of Node 2 is adequately captured by ensemble members but ensemble mean over-estimated it by 6%. The frequency of occurrence of Node 5 is however under-estimated by CAM. CAM therefore accounts for 38% (ensemble mean) and 30% (ensemble members) of the entire datasets in GRP3.

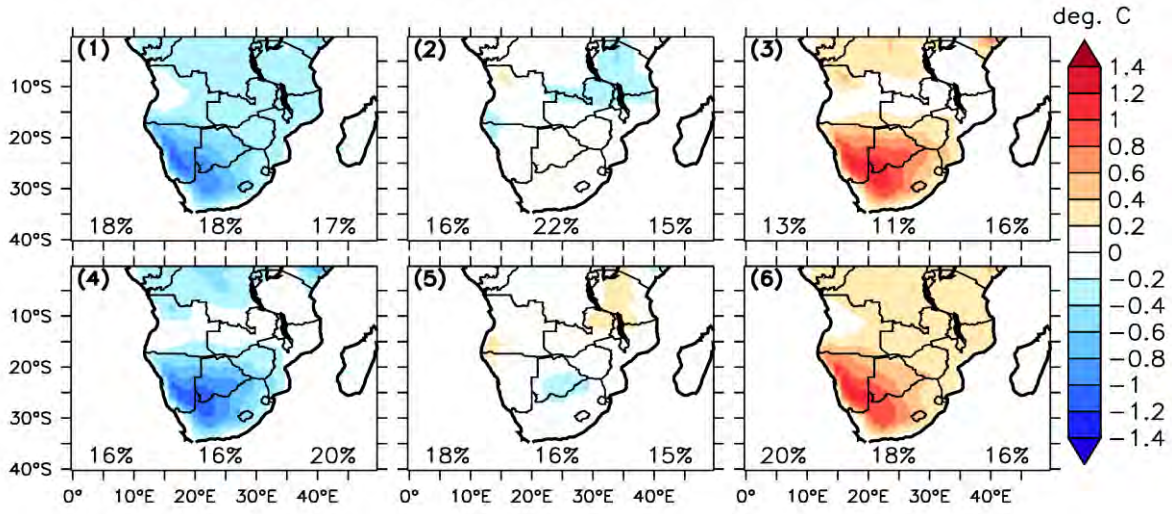

Figure 7.3 SOM classifications for the observed and simulated maximum air temperature over Southern Africa (anomalies; 2m; ^{o}C), relative to the 1961-2005 climatological mean, during austral summer season. Class numbers are written on the upper left sides of each panel while the frequencies of occurrences (%) are shown on the lower left, middle and right respectively for CRU, CAM ensemble mean and the average of individual ensemble member simulations.

7.3 Inter-annual Variability of the Dominant Summer Maximum Air Temperature Classes over Southern Africa

Figure 7.4(a, b), which depicts the inter-annual variability of the dominant maximum air temperature anomaly classes displayed in Figure 7.3, shows that the mean values of the temperature classes over Southern Africa are steadily increasing. In the CRU rows (Figure 7.4), sub-zero anomalies dominate in 1960s to late 1970s; while positive anomalies dominate from 1980s onward with intermittent occurrences of normal and negative anomalies. CAM ensemble mean captures these upward trends, though with few discrepancies. For example, it fails to capture the occurrence of normal condition in 1977 and above-normal conditions in 1982, 1984 and 2001. These upward trends in temperature are in agreement with Figure 7.2a and also consistent with findings from other studies (e.g. Collins (2011), Tett et al. (1999), Stott et al. (2004 and 2010), Christidis et al. (2012), etc).

CAM ensemble mean and ensemble members reproduce the inter-annual variation of the temperature classes in different ways. There are 17 cases of agreement, out of 45, between CRU and the ensemble mean, meaning that CAM ensemble mean correctly reproduce the observed anomaly classes 38% of the time (Figure 7.4a, b). Meanwhile, there are only two cases of disagreement between CRU and ensemble members (e.g. 1969 and 1981, when none of the ensemble members simulate observed temperature classes); and that correct simulation of observed anomaly classes by ensemble members requires a minimum of two ensemble members. These imply that CAM ensemble members have at least 95% probability of reproducing the observed temperature classes correctly, if and only if two right CAM ensemble members are selected. This poses a problem of pre-selection of the right ensemble members that will reproduce the correct classes.

Figure 7.4(a, b) also shows that the number of CAM ensemble members that agree with CRU and CAM ensemble mean, whenever CRU and CAM ensemble mean simulate the

same temperature classes, are equal (e.g. 1965, 1980, 1998, etc). This number however has a minimum of 16 (in 1979) and a maximum of 48 (in 1998). The implication here is that at least 32% of ensemble members are required for CAM ensemble mean to correctly simulate any of the six observed temperature anomaly classes. The reason(s) for this remains unclear. It may be that CAM correctly reproduces the occurrence of a temperature class because all the correct classes are included in the 16 cases of the agreement between CRU and CAM ensemble mean; or that the correct ensemble members might have dominated the wrong members.

Figure 7.5 shows that 5 ensemble members out-perform the ensemble mean, i.e., they have higher synchronizations than ensemble mean. Among these 5 ensemble members, the 49th simulation (hereafter known as SIM49) has the highest synchronization (η = 48.9%). That is, SIM49 have 22 cases of agreements, out of 45, with CRU and therefore have greater ability to correctly reproduce occurrences of any of the temperature classes than any other ensemble members and ensemble mean. Therefore, generating an ensemble mean based on performance of individual ensemble members may give better predictions than uniformly averaging the members to produce the ensemble mean.

Transition and persistence of the observed temperature classes are captured by CAM (see Section 4.3 for explanations on transition and persistence). For example, Figure 7.4(a, b) shows that CAM ensemble mean captures the transition of Node 1 to Node 5 in 1979 – 1980, Node 2 to Node 3 then to Node 6 in 1986, 1987 – 1988, etc. It also captures the persistence of Node 6 in 2004 and 2005. It however fails to capture the persistence of Node 5 in 1981, 1991 and 1997, and that of Node 2 in 1969 and 1970. CAM also does not capture the transition of Node 2 to Node 4 within 1993 to 1994 and that of Node 6 to Node 3 in 1983 to 1985. These failures are attributed to low synchronization of CAM ensemble mean with CRU (η = 38%). The most persistent temperature anomaly class, according to CRU, is Node 6 (Figure 7.4a, b). It persists for 3 years (2003 to 2005), while the class with highest cases of persistence is Node 5. It has 3 cases of persistence. However, CAM ensembles mean is not clear on the issue of the most persistent node; it

shows that Nodes 1, 4 and 6 persist for 2 years each while it shows that Node 2 is the node with highest cases of persistence. Contrary to CRU and CAM ensemble mean, majority of the CAM ensemble members suggest that Node 4 is the most persistent node as well as the node with highest cases of persistence (Figure 7.5). Only 8 ensemble members agree with CRU that Node 6 is the most persistent temperature anomaly class while 5 ensemble members agree with CRU that Node 5 has the highest cases of persistence. However, in agreement with CRU and CAM ensemble mean, SIM49 captures Node 6 as the most persistent node; though, it failed, like ensemble mean, to capture Node 5 as the node with highest cases of persistence, it captured Node 4 instead.

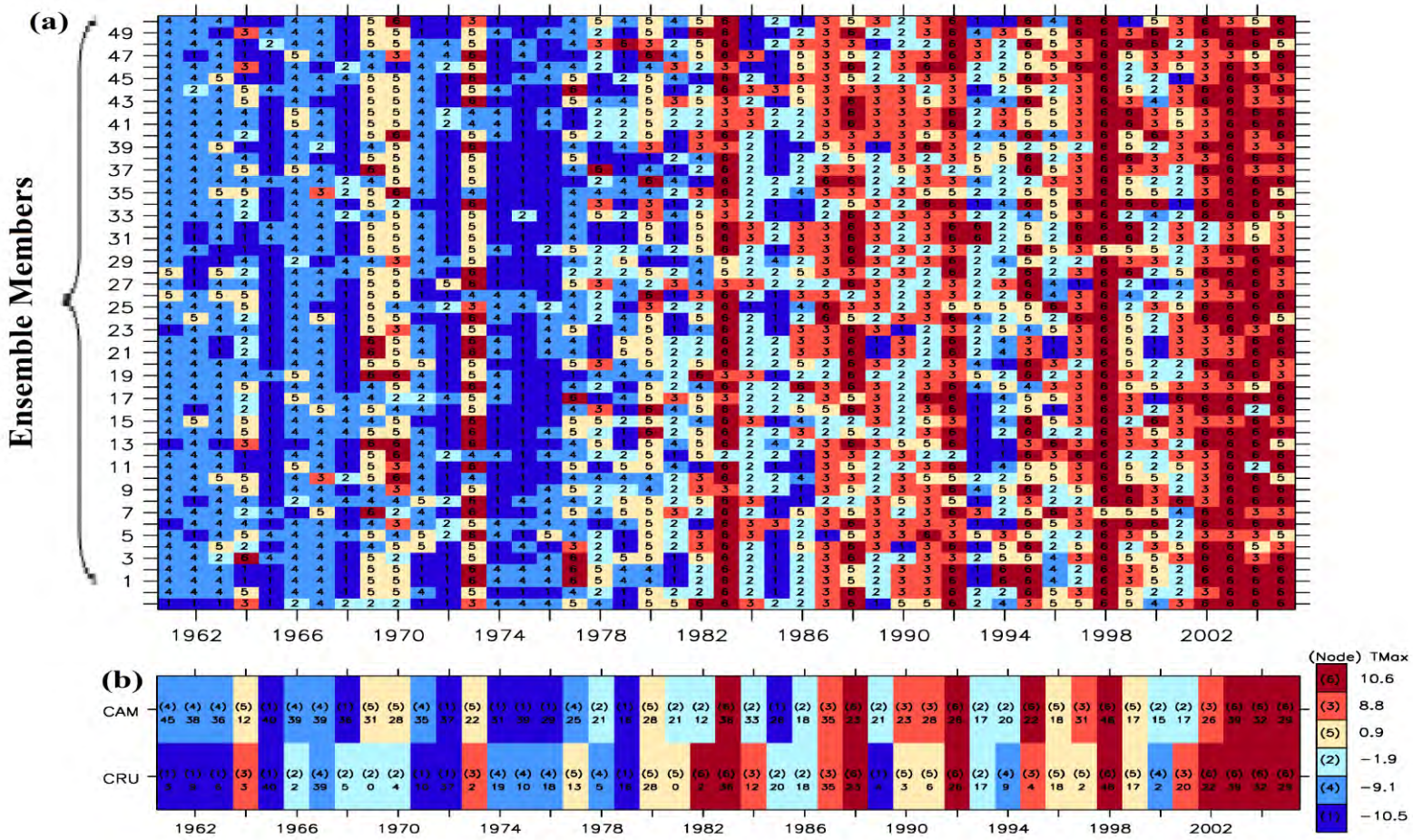

Figure 7.4 Inter-annual variability of spatial classes of maximum air temperature anomalies (^{o}C), depicted in Figure 7.3; **(a)** as simulated by 50 CAM ensemble members, CAM ensemble mean (upper bottom row) and observation (CRU: bottom row) and **(b)** an enlarged last two bottom rows of panel a showing the ensemble mean (upper row) and the observation (bottom row) (the numbers in brackets (i.e. 1 – 6) show the nodes of temperature classes while the colours indicate the mean temperature anomalies over the sub-region. The number under the nodes shows the number of the ensemble members that agree with CRU observation or with the CAM ensemble mean simulations on the temperature class).

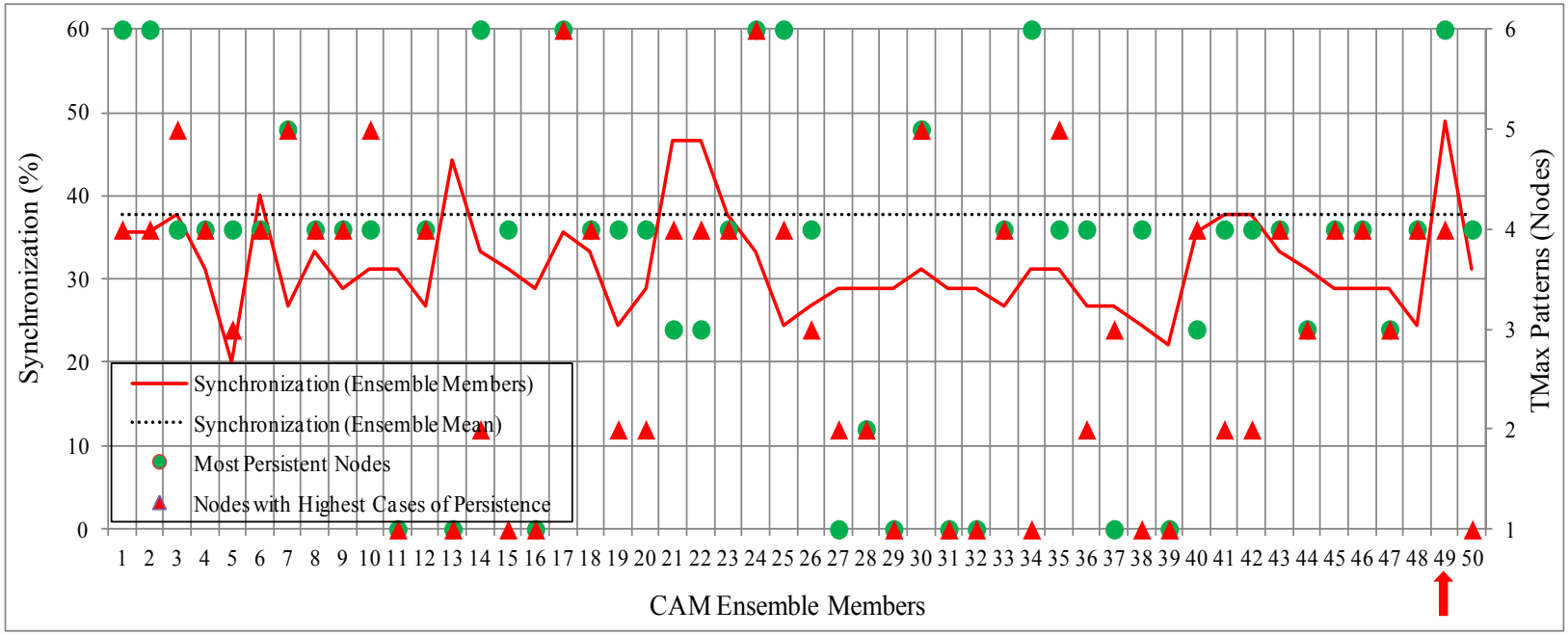

Figure 7.5 Synchronization (%; left y-axis) and persistence (nodes; right y-axis) of simulated temperature classes in reference to observation. The red arrow points to the ensemble member with the highest synchronization (the 49th simulation: SIM49).

7.4 Decadal Frequency of the Dominant Summer Maximum Air Temperature Classes over Southern Africa

Figure 7.6 shows that some classes are recent; some are common while some are rare. Recent classes occur within the last two decades, e.g. Nodes 2, 3, 4, 5 and 6; common classes occur in almost every decade after 1960s, e.g. Nodes 2, 3, 4 and 5; while rare classes do not occur within the last two decades, e.g. Node 1. Though, the decadal frequencies of the maximum air temperature anomaly classes as observed (CRU) and simulated (CAM ensemble mean) have different distributions, CAM ensemble mean is however able to reproduce few of these observed trends. For instance, it captures non-occurrences of Node 1 in 1990s and 2000s, and Node 6 in 1960s and 1970s. Hence, it captures the rarity of Node 1 and recentness of Node 6 even though it fails to capture years of their maximum frequency (i.e. 1960s for Node 1, 2000s for Node 6). Nevertheless, the magnitudes of the observed decadal frequencies are, most of the time, within the ranges of what CAM ensemble members produce. In addition, ensemble members simulate a minimum of 1 event for Node 1 in 1970s, Node 2 in 1980, Node 6 in 1990s, and a minimum of 2 events for Node 4 in 1960s.

Furthermore, in agreements with CRU, the spread produced by the ensemble members shows that there are evidences of warming in the distributions of decadal frequencies (Figure 7.6). For instance, the maximum decadal frequency produced by CAM ensemble members in averagely below-normal classes (Nodes 1 and 4) is highest in the 1960s and 1970s (i.e. 6 events in Node 1 in the 1970s and more than 8 events in Node 4 in the 1960s) and it constantly reduces towards the 21st century. On the contrary, the maximum decadal frequency produced by CAM ensemble members is lowest in above-normal classes (Nodes 3 and 6) during the 1960s and constantly increases towards the 21st century (more than 4 events from 1980s). It ranges between 2 to 5 events in normal condition classes (Nodes 2 and 5) throughout the experimental time-frame of 1961 – 2005. These imply that the decadal frequencies of occurrences of below-normal classes are decreasing, those of above-normal classes are increasing while those of normal condition classes are quasi-constant.

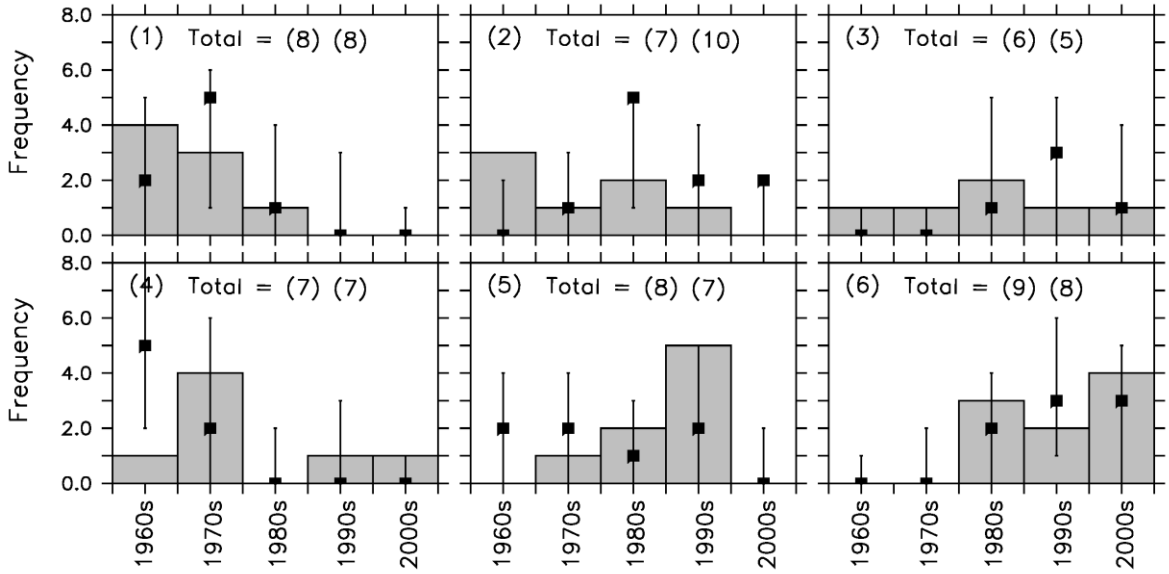

Figure 7.6 Decadal frequencies of maximum air temperature anomaly classes, displayed in Figure 7.3, as observed and simulated. Grey bars show the observed values; black squares show CAM ensemble mean; while the error bars indicate the maximum and minimum decadal frequencies by CAM ensemble members (i.e. the spread). Shown in brackets on the upper left corner of each panel is the tag (or node) of each class. The total number of class occurrences in CRU and CAM (ensemble mean) datasets are also shown in each panel, i.e. (CRU; CAM).

7.5 Atmospheric Tele-connection and the Occurrence of Dominant Summer Maximum Air Temperature Classes over Southern Africa

Figure 7.7 presents the number of tele-connection events (in frequency; %) in which maximum air temperature anomaly classes occur during the positive and negative phases of the tele-connection as observed by CRU and simulated by CAM. We defined here three types of associations between a climate index and an observed temperature class – consistent, inconsistent and unreliable. An association is consistent when the observed class exists only during one of the phases of a climate index and vice versa for inconsistent (i.e. the observed class exists during both phases of a climate index) while an association is unreliable when the observed class features equal frequency of occurrences of both phases of a climate index.

There exist substantial associations between ENSO and all observed temperature classes. The association is however consistent in only two classes (Nodes 2 and 6). Both nodes feature more than 40% of their events during El Nino periods (i.e. positive phase) and none during La Nina periods (i.e. negative phase). Association between ENSO and other classes (i.e. Nodes 1, 3, 4 and 5) is not consistent. Instances reveal that Nodes 1 and 4 feature 38% and 72% of their events, respectively, during La Nina periods and at the same time feature 12% and 30% of their events, respectively, during El Nino periods. On the contrary, Node 3 features more than 30% of its event during El Nino periods, and still features almost 20% during La Nina periods. An unreliable association occurs in Node (5). The node features equal number (about 25%) of its events during both phases of ENSO. CAM ensemble mean captures the consistent association between ENSO and temperature class of Node 6 but captures inconsistent association for Node 2. It also reproduces the inconsistent associations between ENSO and other classes. For instance, CAM ensemble mean agrees with CRU that Nodes 1 and 4 feature more events during La Nina than during El Nino periods, and that Node 3 occurs more during El Nino than during La Nina events. It however fails to reproduce the unreliable association in Node 5; instead, it shows that the node features more of its events during La Nina than during El Nino periods.

Observation shows that IOD has inconsistent associations with all observed temperature classes, except Node 1 with which it has consistent association. Though, with low frequency (about 12%), Node 1 features its events during the negative phase of IOD and none during the positive phase. Nodes 2, 3 and 4 feature more than 30% of their events during the negative phase and, yet, features more than 10% of their events during the positive phase. On the contrary, Nodes 5 and 6 feature more than 25% of their events during the positive phase and at the same time features more than 10% of their events during the negative phase. CAM ensemble mean fails to reproduce the consistent association between IOD and Node 1; though it shows that the class occurs more during negative phase than during positive phase. However, in agreement with CRU, the model

simulates that Nodes 4 and 6, respectively, feature more of their events during the negative and positive phases of IOD than during the positive and negative phases. CAM ensemble mean fails to agree with CRU in Nodes 2, 3 and 5. It captures the opposite of what is observed in these nodes.

Observationally, there is substantial association between AAO and all temperature classes, but the relationship is only consistent in Nodes 5 and 6. These nodes, respectively, feature about 50% and 30% of their events during the positive phase of AAO and none during the negative phase. Positive phase of AAO dominates in other nodes (i.e. Nodes 1, 2, 3 and 4) as well. In these nodes, observed temperature classes feature more events during positive phase (ranging from 28% in Node 2 to 70% in Node 1) than during negative phase (ranging from 13% in Node 2 to 35% in Node 3). While CAM ensemble mean captures consistent association in Node 6, it however shows that the association of AAO with Node 1 is unreliable, because it features equal number of events (about 38%) for the positive and negative phases AAO. While it captures the inconsistent associations in Nodes 2, 3 and 4 by showing that they occur more during positive phase than during negative phase, it also captures inconsistent association in Node 5 instead of consistent association.

Figure 7.7 shows that BEN has no consistent association with all observed temperature classes. The association between BEN and the temperature classes is inconsistent and unreliable. The figure shows that averagely below-normal temperature classes (i.e. Nodes 1 and 4) occur more during negative phase than during positive phase of BEN and vice versa for averagely above-normal temperature classes (i.e. Nodes 3 and 6); while the association between BEN and normal temperature classes (i.e. Nodes 2 and 5) is not consistent because they feature equal number of events (about 12% in Node 2 and more than 35% in Node 5) during the positive and negative phases of BEN. While CAM ensemble mean captures unreliable association in Node 5, it also captures inconsistent associations in Nodes 3, 4 and 6; but fails to capture the scenarios in Nodes 1 and 2.

It is therefore difficult to associate any maximum air temperature anomaly class with a particular climate index because each class is associated with more than one climate index (Figure 7.7). Nevertheless, this investigation has helped to know which of the classes are, favorably and or unfavorably, associated with which of the atmospheric tele-connection and hence, can be simulated or predicted reliably from such climate index. The rationale behind the inconsistent association between tele-connection and the classes may be attributed to the facts that each atmospheric tele-connection may exist in different forms. Examples abound in ENSO where different flavors of ENSO have been uncovered, e.g. conical El Nino and El Nino Modoki: Johnson, 2012; Hoell et al., 2014; Ratnam et al., 2014). Therefore, each class may have inclination for different forms of tele-connection. Meanwhile, in this study, we only used a flavor of each tele-connection. Furthermore, the influence of local or regional forcing may be more important than that of the tele-connections in some classes and, hence adds to the conflicting impacts of the tele-connection on the classes.

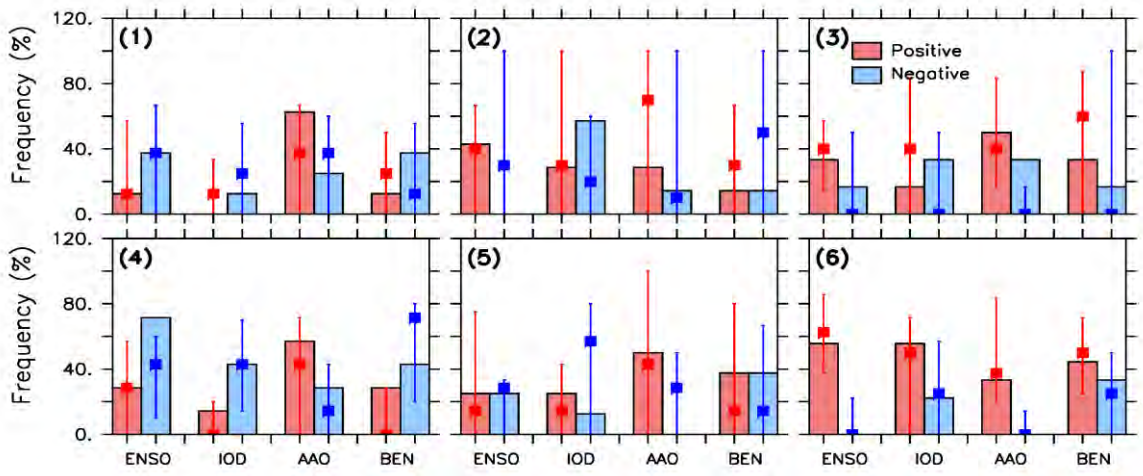

Figure 7.7 Frequency of occurrence of climate indices associated with spatial classes of temperature anomalies depicted in Figure 7.3, expressed as percentage of frequency of occurrence. Red and blue colors indicate, respectively, positive and negative phases of each climate index; bars, squares, and the upper and lower parts of the error bars, respectively, denote the frequencies of the climate indices associated with observation (CRU), CAM ensemble mean, and the maximum and minimum frequencies of the climate indices produced by CAM ensemble members. The tag (or node) of each temperature class is shown in bracket on the upper left corner of each panel. See Table 3.2 for brief descriptions of the climate indices considered in this study.

So, what makes a summer warmer or colder than its predecessor? This depends on a number of factors that play important roles in the energy budget of the atmosphere. These factors are volcanic eruptions (Kelly and Jones 1996; Johns et al., 2002), global SST and oceanic circulations (Gadgil et al., 1984; Xie et al., 2009; Abraham et al., 2013), surface reflectivity (i.e. albedo: Henderson-Sellers and Hughes, 1982; Henderson-Sellers and Wilson, 1983), absorptions of solar energy due to emissions of green-house gases (GHG: WMO, 1990a, b and 1992; Staehelin et al., 2001; Jones et al., 2008; Collins, 2011; Christidis et al., 2012), etc. These factors engage in complex interactions with the atmosphere and therefore, their effects are being controlled by atmospheric circulations (Kysely, 2007). Interestingly, temperature fluctuation is one of the outcomes of complex interactions between atmospheric variables, processes and circulations. Anomalies of global SST, among others like anomalies of vertical motions and total cloud fraction are fundamentally associated with seasonal temperature fluctuations and variations over Southern Africa (Breaker, 1989; Mullan, 1998; Abraham et al., 2013). Therefore, analyzing the composites of the spatial patterns of these anomalies in comparison with the spatial classes of maximum air temperature anomalies will assist in furthering the investigation into how well CAM simulates the link between these classes and factors modulating the atmospheric energy budgets.

7.6 Global SST Anomalies and the Dominant Summer Maximum Air Temperature Classes

7.6.1 ENSO Flavors and Temperature Classes

This sub-section furthers the investigation into how well CAM simulates the link between the temperature anomaly classes and different ENSO flavors. Figure 7.8 depicts additional analyses of the composites of SST anomaly patterns in comparison with the SST patterns of ENSO flavors obtained by Hoell et al. (2014). All SST anomaly patterns associated with the observed temperature anomaly classes compare well with those ENSO flavors described by Hoell et al. (2014). For instance, SST anomaly patterns for

Nodes 1 and 6 (Figure 7.8a) are respectively similar to La Nina pattern 1 (hereafter known as LN1) and El Nino pattern 3 (hereafter known as EN3). In agreement with LN1, Node 1 SST anomaly pattern features cold SST (negative anomaly) over the eastern and central equatorial Pacific and it is coldest between 180^{o}E - 120^{o}W. SST anomaly patterns for Node 6 features the opposite (i.e. EN3). Both SIM49 and CAM ensemble mean simulate similar SST anomaly patterns for these nodes (Figure 7.8b, c). Furthermore, CRU associates Nodes 3 and 4 with El Nino pattern 4 (hereafter known as EN4) and LN1 respectively (Figure 7.8a). EN4 is, though, similar to EN3 but its positive SST anomaly is more confined to central Pacific Ocean. However, SIM49 associates Nodes 3 and 4 with normal SST condition and LN1 respectively (Figure 7.8b); while ensemble mean associates them with El Nino pattern 1 (hereafter known as EN1) and normal SST condition respectively (Figure 7.8c). These imply that SIM49 fails to associate Node 3 with EN4 and that ensemble mean also fails to associate Nodes 3 and 4 temperature classes with EN4 and LN1 respectively. Nevertheless, while SIM49 does not associate Nodes 2 and 5 with normal SST conditions (Figure 7.8a, b), the ensemble mean adequately associate Node 5 with normal SST conditions but instead associate Node 2 with La Nina pattern 3 (hereafter known as LN3 – characterized by uniformly negative SST anomalies over the eastern and central equatorial Pacific and normal SST conditions over the west Pacific, Indian and Atlantic Oceans: Figure 7.8c). Therefore, CAM has the ability to adequately reproduce LN1 (as in Nodes 1 and 4) and EN3 (as in Node 3).

7.6.2 Caveats on ENSO-based Predictions

The dominant temperature classes have two points of agreements and one point of disagreement with the earlier mentioned ENSO-based prediction frame-works[20,21]. Figures 7.3, 7.8 and 7.9 show that summer air temperatures are significantly cooler during La Nina events and vice versa during El Nino events; though inconsistent (Figure 7.7). The classes, in agreement with the ENSO-based prediction frame-works, also show that the coldest and warmest anomalies are located south of 10^{o}S over the sub-region.

[20] http://edmc1.dwaf.gov.za /library/Limpopo/Chapter2/Page17/Chapter2Page17.htm
[21] http://www.grida.no/public ations/vg/africa/page/3106.aspx

They however disagree on the occurrence of extreme temperature anomalies over Madagascar. Contrary to the ENSO-based prediction frame-works, jointly simulated dominant groups (Figures 7.3 and 7.9) show no extremes over Madagascar. This indicates that unusually higher or lower than normal temperatures, as suggested by the frame-works, may however not be occurring over this Island. This is highly possible because the Island is, throughout the year, dominated by onshore flows which have been associated with none or fewer anomalously higher than normal temperatures (Lyon, 2009). Therefore, while the ENSO-based prediction frame-works may be adequate for the prediction of rainfall extremes during ENSO events, it may however not be adequate for the prediction of summer temperature over the sub-region.

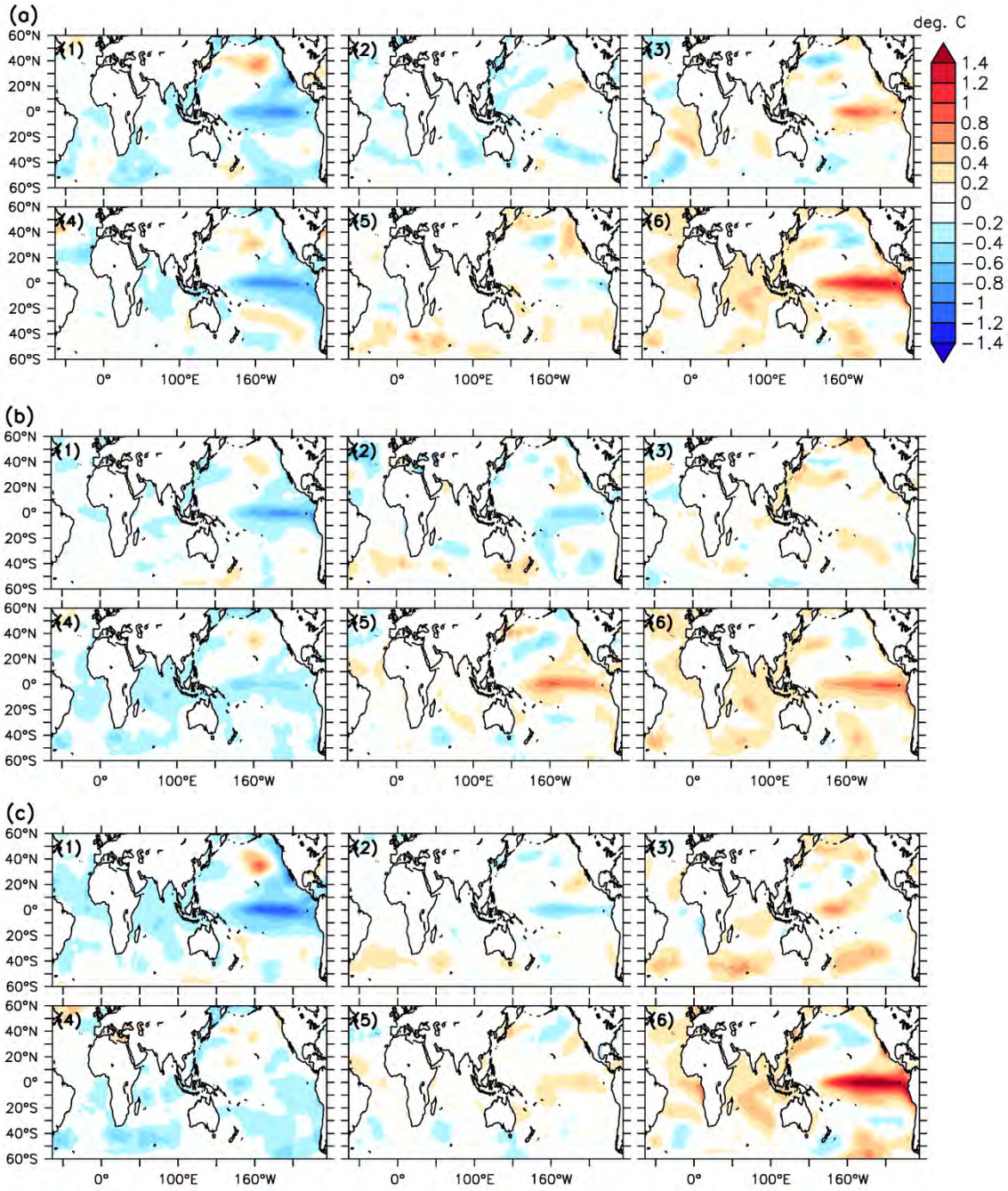

Figure 7.8 Composite of austral summer global SST anomalies (^{o}C) for **(a)** observation, **(b)** SIM49 and **(c)** CAM ensemble mean patterns. Pattern numbers, which correspond to the spatial classes of temperature anomalies in Figure 7.3, are written on the upper left sides of each panel while the SST anomalies are relative to the 1961-2005 climatological mean.

7.7 Composite of Atmospheric Dynamics Associated with the Temperature Classes

Atmospheric conditions associated with each dominant maximum air temperature class, and how well they are simulated by CAM, are examined in this sub-section. Temperature anomaly classes displayed in Figure 7.3 were separated into the composites of each dataset (i.e. CRU, SIM49 and CAM ensemble mean; Figure 7.9). Anomalies of vertical velocity at 500hPa level with the corresponding anomalies of wind vectors at 850hPa level and those of the total cloud fraction are then used to examine the structure of the corresponding atmospheric fields (Figures 7.10 and 7.11).

While there are agreements between the composites of CRU and CAM (SIM49 and ensemble mean) in some patterns, there are discrepancies in other patterns (Figure 7.9a, b, c). For instance, the best agreement is in GRP2 (i.e. Nodes 3 and 4). In this group, spatial correlations (r) between CRU and CAM simulations are high ($0.58 \leq r \leq 0.76$); implying that CAM simulates the spatial structures of the group almost as observed. Though, reanalysis and CAM feature comparable patterns in the associated atmospheric dynamics, they also feature some disparities. CRU shows that Node 3, a majorly above-normal anomaly, is associated with anomalous mid-latitude cyclonic flows, at 850hPa levels, over south Atlantic and Indian Oceans (Figure 7.10a). The cyclonic flows stimulate maritime southerly flows almost over the entire sub-region as they induce strong anomalous subsidence at 500hPa level (downward motion; Figure 7.10a) and below-normal total cloud fraction (Figure 7.11a) over the sub-region. Apart from the agreements between CRU, SIM49 and CAM ensemble mean on these atmospheric dynamics; both SIM49 and CAM ensemble mean also agree with the composite of CRU that the below-normal anomalies over Tanzania (Figure 7.9) can be attributed to an enhanced convection (upward motion; Figure 7.10) and anomalous increase in cloud fraction (Figure 7.11) over the country. SIM49 and ensemble mean agree with CRU that anomalies of vertical motion fields and total cloud fraction for Node 4 class are opposite of those for Node 3. Therefore, in addition to the capturing of the frequency of occurrence by the ensemble mean in GRP2 (Figure 7.3), CAM (SIM49 and ensemble

mean) also simulate adequately the atmospheric conditions associated with the maximum air temperature anomaly classes in GRP2.

GRP1 (Nodes 1 and 6), as agreed by CRU and CAM (SIM49 and ensemble mean), is the most poorly simulated group. In this group, the spatial correlations (r) between CRU and CAM simulations are weak ($0.17 \leq r \leq 0.29$); implying that CAM does not simulate the spatial structures of the group as observed (Figure 7.9a, b, c). Though both CAM and CRU, in Node 1, feature below-normal anomalies over the entire sub-region; CRU locates the coldest temperature anomalies over Botswana-Zambia-Zimbabwe axes while CAM placed the coldest anomalies over the Kalahari Desert (i.e. Namibia, south-west Botswana and north-western parts of the Republic of South Africa). Node 6 features the opposite of these, i.e. above-normal anomalies over the entire sub-region and with peak centers corresponding to those found in Node 1. Reanalysis attributes Node 1 to anomalous cyclonic flows over mid-latitude parts of south Indian Ocean and also to an anomalous anti-cyclonic flow centered over the southern tip of the sub-region (Figure 7.10a). These flows resulted in weak and unorganized wind anomalies almost over the entire Southern Africa. The flows induce weak anomalous ascent (upward motion; Figure 7.10a) and weak above-normal total cloud fraction (Figure 7.11a) over the sub-region. Observation and CAM feature comparable patterns in the associated dynamic fields (Figures 7.10 and 7.11), but the observed vertical motions do not correspond to areas of below- and above-normal temperature anomalies (Figures 7.9a and 7.10a). Similar scenarios apply to Node 6, the opposite pattern of Node 1. Here, the observed vertical motions are also not consistent with the corresponding temperature anomalies (Figures 7.9a and 7.10a), but the anomalies of total cloud fraction are reproduced by the composites of SIM49 and ensembles mean (Figures 7.10 and 7.11).

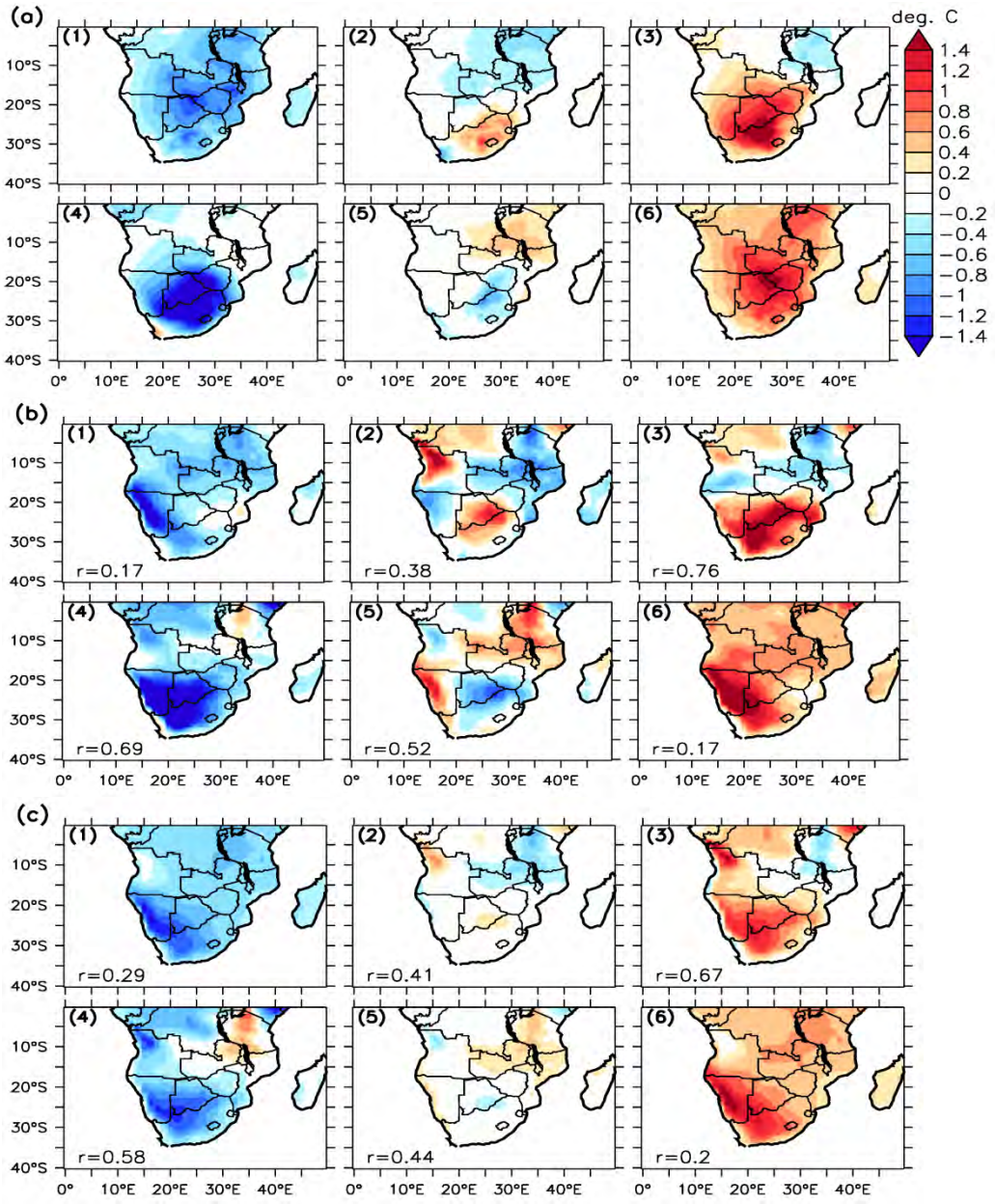

Figure 7.9 Composite of the spatial patterns of austral summer maximum air temperature anomalies (^{o}C) over Southern Africa for **(a)** observation (CRU), **(b)** SIM49 and **(c)** CAM ensemble mean in SOM classifications depicted in Figure 7.3, relative to the 1961-2005 climatological mean. Pattern numbers, which correspond to classes in Figure 7.3, are written on the upper left sides of each panel while the values of spatial correlations of SIM49 and ensemble mean with corresponding observed pattern are written on the bottom left of panels in **b** and **c** respectively.

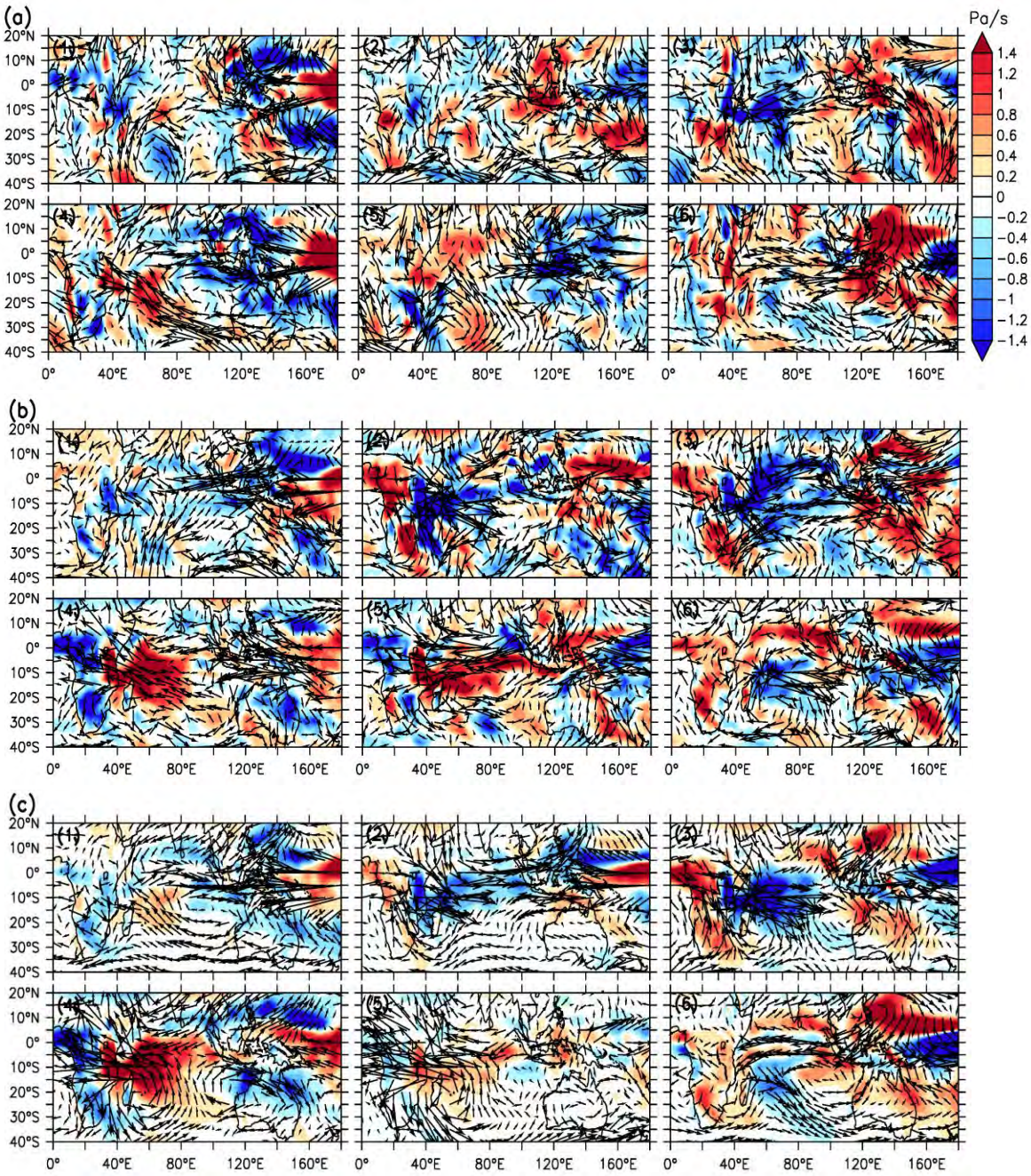

Figure 7.10 Composite of the spatial patterns of austral summer vertical velocity anomalies at 500hPa level (omega; $x10^{-2}$ Pa s^{-1}) with the corresponding anomalies of wind vectors at 850hPa level for **(a)** observation (reanalysis), **(b)** SIM49 and **(c)** CAM ensemble mean, relative to the 1961-2005 climatological mean. Pattern numbers, which correspond to classes in Figure 7.9, are written on the upper left sides of each panel. Blue shading (negative value) indicates resultant ascent (i.e. upward motion) while red shading (positive value) indicates resultant descent (i.e. downward motions).

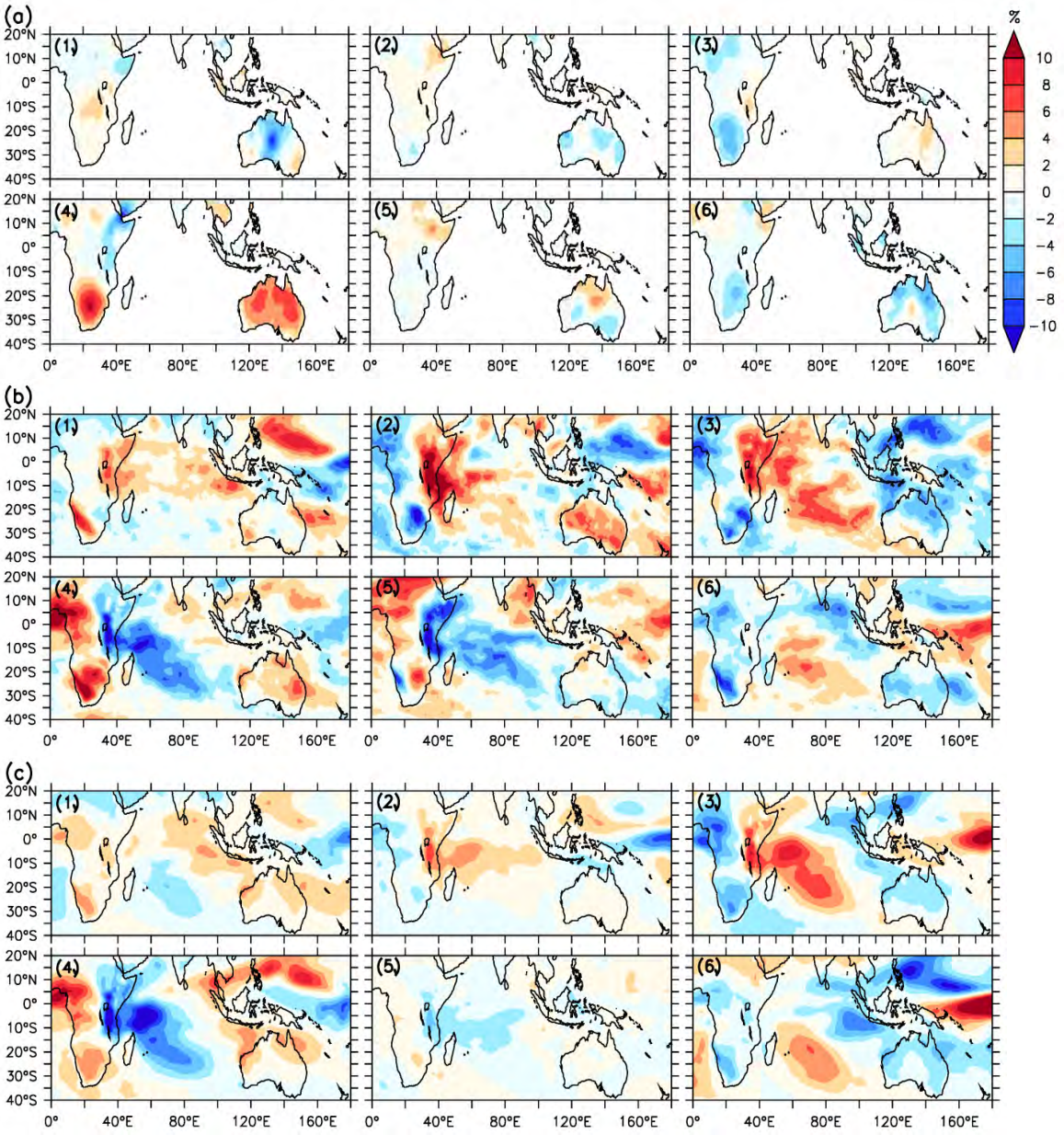

Figure 7.11 Composite of the spatial patterns of austral summer total cloud fraction anomalies (%) for **(a)** observation (CRU), **(b)** SIM49 and **(c)** CAM ensemble mean, relative to the 1961-2005 climatological mean. Pattern numbers, which correspond to classes in Figure 7.9 are written on the upper left sides of each panel. Blue shading (negative value) indicates resultant reduction in cloud coverage while red shading (positive value) indicates resultant increase in cloud coverage.

7.8 Summary

It has been shown in this chapter that CAM is adequately capable of reproducing the inter-annual and spatial variations of the observed austral summer maximum air temperature over Southern Africa. The model is also capable of simulating the atmospheric conditions that influence and modulate the summer maximum air temperature over Southern Africa. Out of the predetermined six dominant temperature classes, CAM reliably reproduces classes of the "temperature extremes over the Kalahari Desert (south of 20^{o}S)" and averagely reproduces classes of the "near-normal temperatures over the entire region". Ensemble mean has the potential to reproduce the right classes 38% of the time, while SIM49 has the capacity to simulate the correct class once out of every two simulations (η = 49%); and the model correctly reproduces the regional atmospheric conditions that modulate the occurrences of these captured classes. The dominant temperature classes, though inconsistently, comply with the ENSO-based prediction frame-works (i.e. summer air temperatures are significantly cooler during La Nina events and vice versa during El Nino events). It however fails to agree with the frame-works on the occurrence of extreme anomalies over the Madagascan Island. Our results have therefore identified the dominant summer maximum air temperature classes that CAM can simulate well and those it struggles to reproduce over Southern Africa.

A comparison of this chapter with chapter (6) suggests that, over Southern Africa, CAM does a better job in simulating temperature than in simulating rainfall. For example, the correlation, r, between observation and simulations is higher for temperature (i.e. $0.6 < r < 0.9$; $r = 0.85$ for ensemble mean) than for rainfall (i.e. $-0.1 < r < 0.54$; $r = 0.4$ for ensemble mean), and the normalized standard deviation is closer to 1.0 in the former than in the later (Figures 6.1 and 7.2). In addition, the synchronization of the ensemble mean (with observation) is higher for temperature ($\eta > 38\%$) than for rainfall ($\eta < 30\%$). Both the best (η_{best} = 49%) and the worst (η_{worst} = 20%) simulations for temperature have higher synchronizations than their counterparts for rainfall η_{best} = 40%; η_{worst} = 13%) respectively. For temperature, 10% of the simulations perform better than the average, while, for temperature, only 6% the ensemble members perform better than the ensemble

mean. The discrepancy among the simulations (or degree of spread among the simulations) is lower for temperature than for rainfall. This suggests that, over Southern Africa, the predictability of dominant seasonal temperature classes may be higher than that of rainfall classes.

Furthermore, a comparison between the results in this chapter and chapter (5) indicates that the model simulates the seasonal maximum temperature better over Southern than over West Africa in all aspect. First, the correlation between observed and simulated summer rainfall is higher over Southern Africa (i.e. $0.6 < r < 0.9$; $r = 0.85$ for ensemble mean) than over West Africa (i.e. $0.4 < r < 0.8$; $r = 0.8$ for the ensemble mean), and the normalized standard deviation is almost 1.0 over Southern Africa but 0.5 over West Africa. Second, the synchronization of the ensemble mean (with observation) is also higher over Southern Africa ($\eta > 38\%$) than over West Africa ($\eta < 30\%$). Both the worst and best simulations over Southern Africa ($\eta_{worst} = 20\%$; $\eta_{best} = 49\%$) have higher synchronization than their counterparts over West Africa ($\eta_{worst} = 11\%$; $\eta_{best} = 44\%$) respectively. However, over West Africa, about 36% of the simulations perform better than their average, while, over Southern Africa, only 10% of the simulations perform better than their average. However, in simulating temperature, the discrepancy among the simulations is higher over West Africa than over Southern Africa, suggesting that the predictability of dominant seasonal maximum temperature may be higher over Southern Africa than over West Africa.

8 Trends in the Potential Spread of Seasonal Climate Simulations over South Africa

This chapter investigates the characteristics of the measures of the limits of predictability of seasonal forecasts over South Africa. It examines the spread of ensemble output from a regional climate model, specifically the regional component of the Hadley Centre Atmospheric / Regional Model version 3 (HadAM3P-N96/HadRM3P-50km) modeling system, run in a hindcast framework. The chapter then estimates what the theoretical range of forecasts is for a variety of seasons, in the context of a single forecasting model system, and thus establishes the theoretical limits as to how much we may be able to improve seasonal forecasts.

8.1 Evaluation of HadRM3P Simulations

Ensembles of simulations can either be evaluated in a deterministic or probabilistic sense. Here, we evaluate monthly precipitation and near surface air temperature output in a deterministic sense using the ensemble means of the HadRM3P simulations. Figures 8.1 and 8.2 respectively depict maps of seasonal precipitation and temperature over the full period of the simulations. The ensemble mean is compared to observed seasonal climatologies of South Africa, represented by the University of East Anglia Climate Research Unit (CRU: Mitchell and Jones, 2005) monthly gridded dataset. HadRM3P is successful in simulating the overall pattern of maximum rainfall over the northeast of South Africa and the decrease towards the southwest (Figure 8.1). Similarly, it successfully simulates the seasonal locations of maximum and minimum temperatures but it displaces slightly the local maximum and minimum over these regions. The ability of HadRM3P to simulate and reproduce these patterns is crucial to reliable seasonal forecasts and simulations over South Africa, and by extension the success of this study.

Model biases range from −2 to 2 mm day^{-1} for precipitation against this observational dataset (Figure 8.1). In all seasons, biases mimic the spatial distribution of precipitation, reflecting the model's ability to capture both spatial and seasonal patterns. Figure 8.2 shows that, for all seasons, overestimation of air temperature is concentrated along

southern and eastern provinces, whereas air temperatures for the majority of inland provinces are underestimated, in some cases by 4 ^{o}C.

We use the ranked probability skill score (RPSS) to evaluate the ability of the model to reproduce the observed year-to-year variations of the climate variables. RPSS is defined as a measure of the accuracy of the forecast in terms of the probability assigned (Wilks, 1995; Mason, 2004). It compares the performance of a forecasting system against a simple climatological reference through an expression:

$$RPSS = 1 - \frac{RPS_{fcst}}{RPS_{clim}}$$

where RPS_{fcst} is the anomaly of the forecast value while RPS_{clim} is the anomaly of climatological reference. RPSS ranges from 1.0 for a perfect forecast, through 0.0 for one that provides no improvement over the climatological reference, to negative values for forecasts that are worse than the climatological reference. Wilks (1995) and Weigel et al. (2006) have shown that positive skills are normally desirable and that they represent a minimal level of acceptable performance by forecasts.

Positive skill appears over the domain in different seasons. For precipitation (Figure 8.1 bottom row), RPSS indicates some positive skill during austral summer (DJF) and autumn (MAM). Skill scores are mostly negative during the dry winter season when rainfall amounts are near-zero [JJA; however, this is a wet season over the Western Cape Province (WCP)]. Skills are generally negative for the important onset season (SON). Studies, e.g. Landman and Beraki, 2010; Li and Ding, 2011, have attributed these lacks of skill during JJA and SON seasons to the influence of transient synoptic systems (Reichler and Roads, 2004). The dominance of tropical atmospheric circulation is almost absent during these seasons. RPSS for temperature (Figure 8.2 bottom row) depicts positive skill throughout the country during DJF, but only in inland areas during MAM and SON. The model rather lacks skill during JJA.

Anomalies of the area average of July inter-annual variations of precipitation and temperature over Limpopo Province (LMP) are plotted in Figure 8.3. The plotted values are anomalies from the full-period climatology and thus have had the biases displayed in Figures 8.1 and 8.2 linearly removed. The figure shows that the observed inter-annual precipitation lies within the range of probable values exhibited by simulated ensemble members for most of the experimental period (Figure 8.3a). The correlation coefficient between rainfall ensemble mean and CRU observation is 0.40 while their strength of association as evaluated from ranked correlation is 0.51. Ensemble mean produces smaller inter-annual variations in temperature than has been observed, leading to the observed values more frequently exceeding the probable range suggested by the simulations (Figure 8.3b). For temperature, the strength of the linear relationship between the ensemble mean and observations in terms of the correlation coefficient is 0.46, or 0.58 for Spearman's ranked correlation.

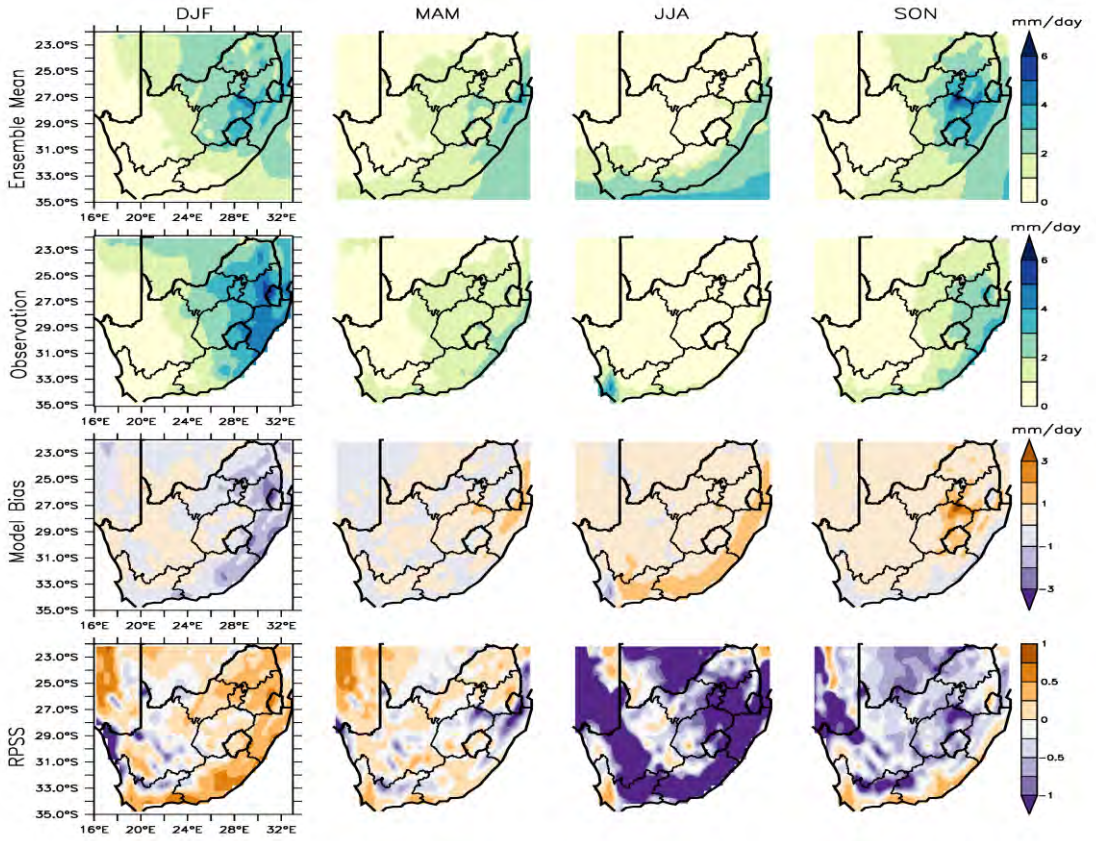

Figure 8.1 Seasonal distribution of precipitation over South Africa during December 1959 through November 2008. **Top row:** Ensemble mean as simulated by HadRM3P. **Second row:** Observation as presented by the CRU dataset. **Third row:** Model bias relative to CRU observations (simulations minus observations). **Bottom row:** Ranked probability skill score, RPSS, of HadRM3P precipitation simulations over South Africa. Columns indicate the austral seasons: DJF – summer; MAM – autumn; JJA – winter; SON – spring.

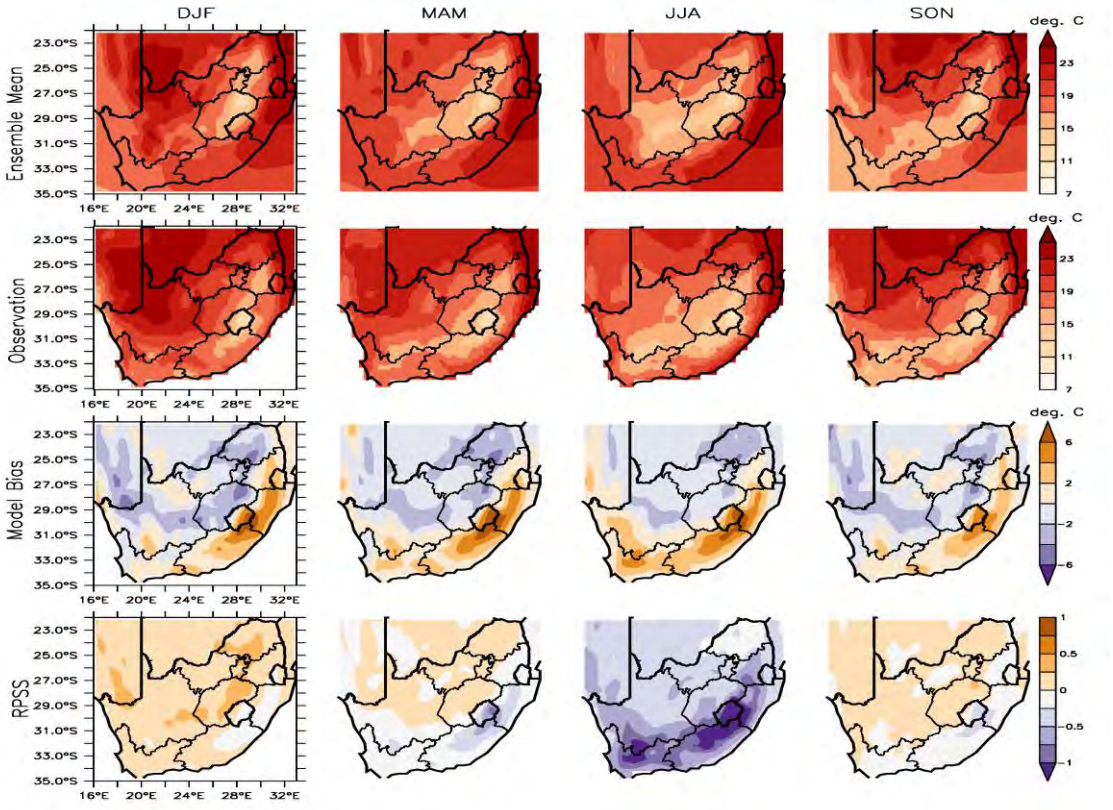

Figure 8.2 Seasonal distribution of near surface air temperature over South Africa during December 1959 through November 2008. **Top row:** Ensemble mean as simulated by HadRM3P. **Second row:** Observation as presented by the CRU dataset. **Third row:** Model bias relative to CRU observations (simulations minus observations). **Bottom row:** Ranked probability skill score, RPSS, of HadRM3P near surface air temperature simulations over South Africa. Columns indicate the austral seasons: DJF – summer; MAM – autumn; JJA – winter; SON – spring.

8.2 Spatial Distribution of Ensemble Spread over South Africa

Ensemble spreads as measured by StdDev and the 10–90th percentile range vary with time and in space (Figures 8.3(a, b), 8.4 and 8.5). The top and middle rows of both Figures 8.4 and 8.5, for precipitation and surface air temperature respectively, show that larger spreads are concentrated where the seasonal average values are higher (see top rows of Figures 8.1 and 8.2). Higher ensemble spreads for precipitation are found over the central and north-eastern areas of the country during the onset (SON), rainy (DJF) and cessation (MAM) seasons (Figure 8.4). The regions of higher precipitation spread are also found in the southwest, southern and eastern coasts during their rainy season (JJA), following the natural patterns of seasonal rainfall distribution (Figure 8.1). Ensemble spreads for temperature are lower and more uniform along the coasts than inland (Figure 8.5). This may be as a result of prescribed sea surface temperature used in the weather@home/SAF setup, in that coastal areas in the HadRM3P model may be constrained to more closely follow the prescribed ocean temperature than inland areas. Higher spreads are found inland where temperature variability is higher (Figure 8.2).

There are strong direct linear relationships between the two measures of spread. Correlation coefficients between the two measures of precipitation spread are generally around 0.7 and relatively uniform across the country and seasons (bottom row of Figure 8.4). Correlation coefficients are less homogenous for temperature spreads (bottom row of Figure 8.5). They are highest, generally greater than 0.7, during the summer (DJF) and winter (JJA). Ranked correlation for both parameters, which is generally greater than 0.9, further confirm that there exist strong associations between the two measures of spread.

8.3 Implications of Spread Variations on Simulation Skill

Whether the inter-annual variations in the spread follow the Grimit and Mass (2007) hypothesis, "*cases with large (small) ensemble spread should be associated with large (small) forecast uncertainty*", can be determined using the model skill, as measured using the RPSS with the CRU observational product, as a function of simulation spread.

Seasonal-provincial values of the measures of spread for each year were ranked in ascending order and sorted into four equally populated bins. Bin 1 contains the narrowest spread values while widest values are in bin 4. Averages of simulations and corresponding observational datasets in each bin are then used to evaluate RPSS. RPSS is then plotted as a function of these bins in Figures 8.6 and 8.7 for precipitation and temperature respectively.

For precipitation, all provinces and seasons have higher skill when the simulation spread is narrower (Figure 8.6). This even holds during the dry season (JJA for most provinces), when the negative scores reflect the difficulty of interpreting probabilistic forecasts for seasons with a very small number of precipitation events. The correspondence of higher skill with lower simulation spread also exists for temperature in all seasons and provinces (Figure 8.7), though it is not as remarkable a relationship as for precipitation. As with precipitation, this relationship curiously continues to hold even when the model skill is poor.

The profiles of RPSS on Figures 8.6 and 8.7 indicate that there is observational support to the hypotheses that there are fundamental variations in potential forecast skill from year to year and that some of these variations are captured by the ensemble spread emanating from HadRM3P. Notably, most El-Nino and La-Nina years, as categorized by Null (2013), fall within bins 1 and 2 for precipitation.

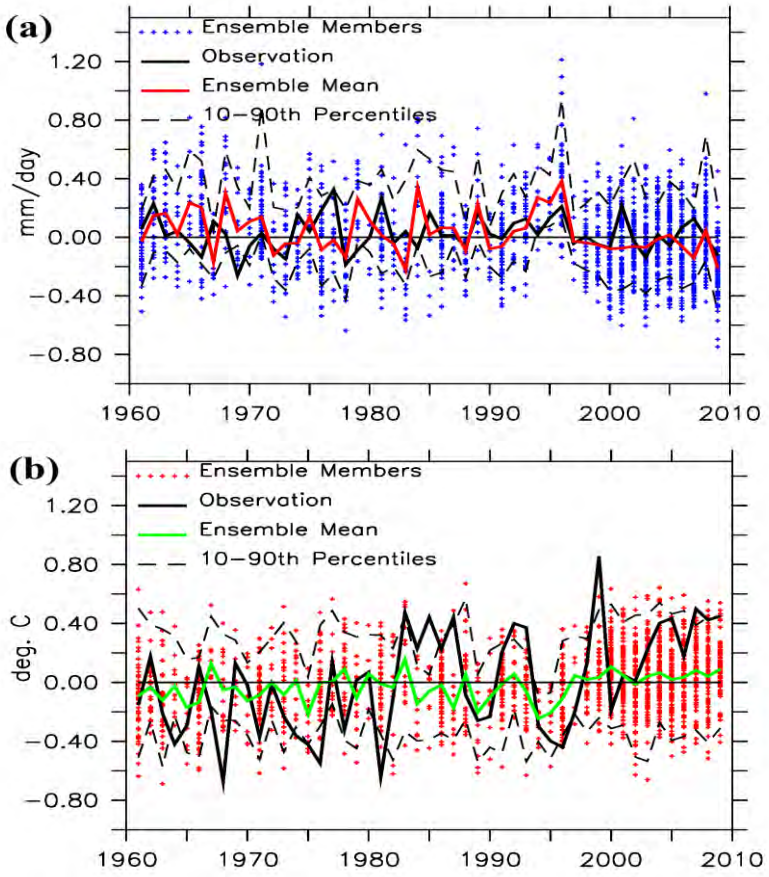

Figure 8.3 Inter-annual variations of **(a)** precipitation and **(b)** near surface air temperature anomalies over Limpopo Province (LMP) from a sample of the simulations for the month of July. Plotted on the panels are the anomalies of individual ensemble members, observation as represented by CRU datasets, the ensemble mean and the 90th and 10th percentiles of the ensemble distribution.

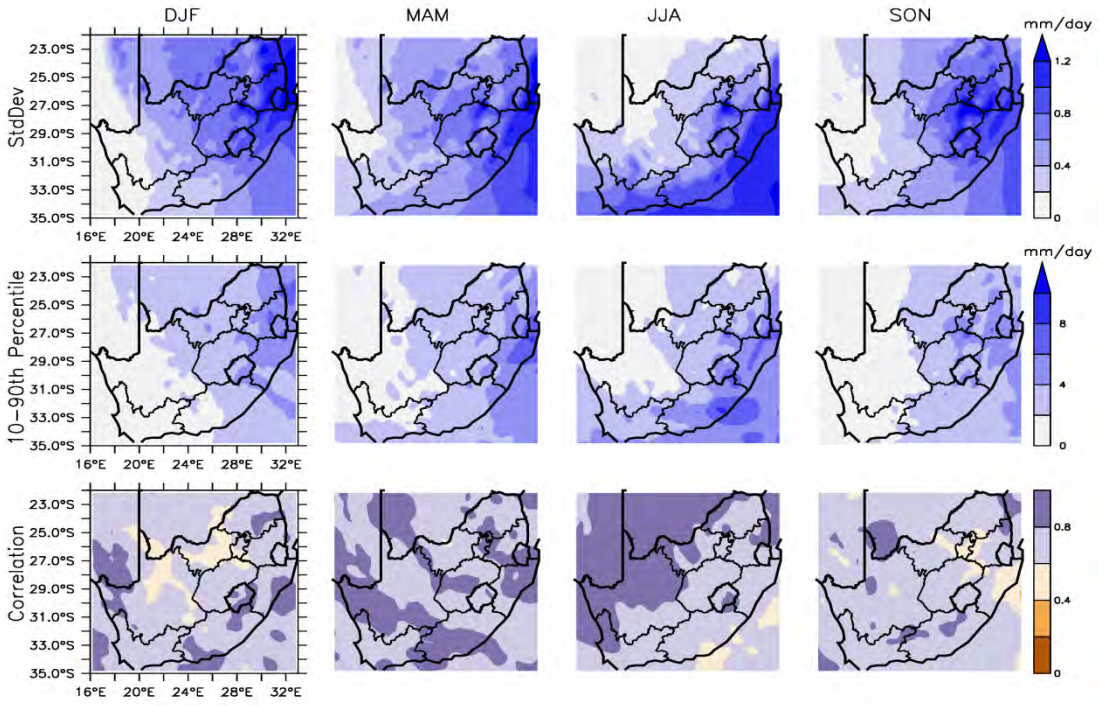

Figure 8.4 Seasonal distribution of average ensemble spread in precipitation calculated using (**top row**) the StdDev and (**middle row**) the 10-90th percentile range during December 1959 through November 208. **Bottom row**: correlation coefficient (r) between StdDev and 10-90th percentile range. Columns indicate the austral seasons: DJF – summer; MAM – autumn; JJA – winter; SON – spring.

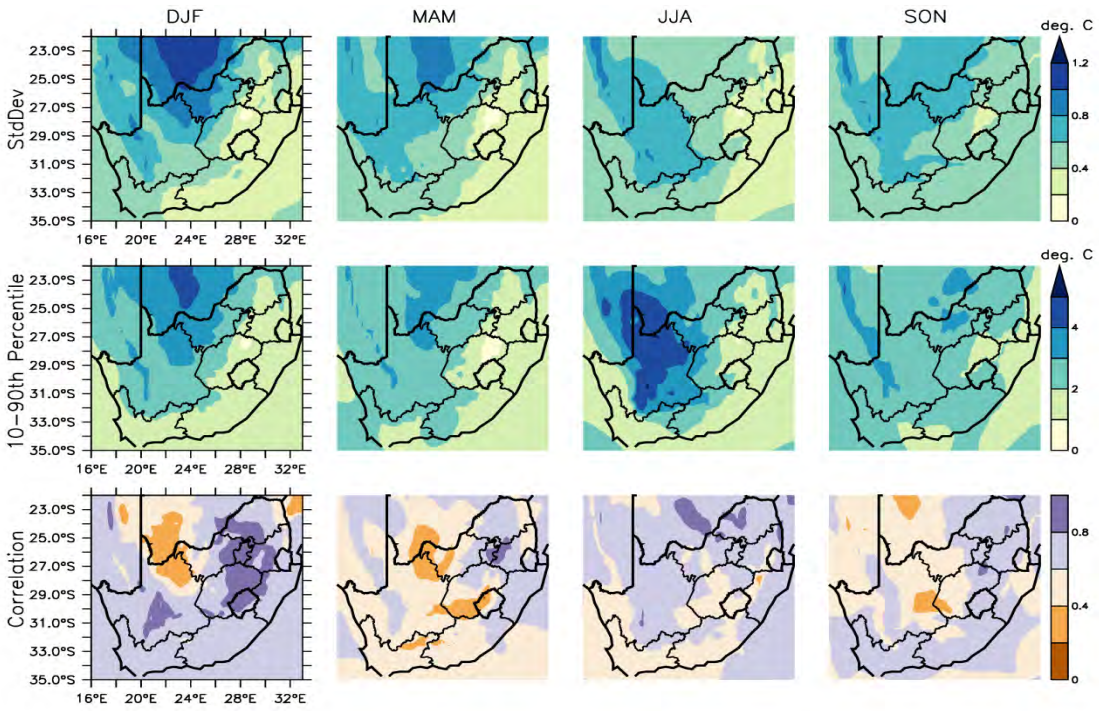

Figure 8.5 Seasonal distribution of average ensemble spread in temperature calculated using (**top row**) the StdDev and (**middle row**) the 10-90th percentile range during December 1959 through November 208. **Bottom row**: correlation coefficient (r) between StdDev and 10-90th percentile range. Columns indicate the austral seasons: DJF – summer; MAM – autumn; JJA – winter; SON – spring.

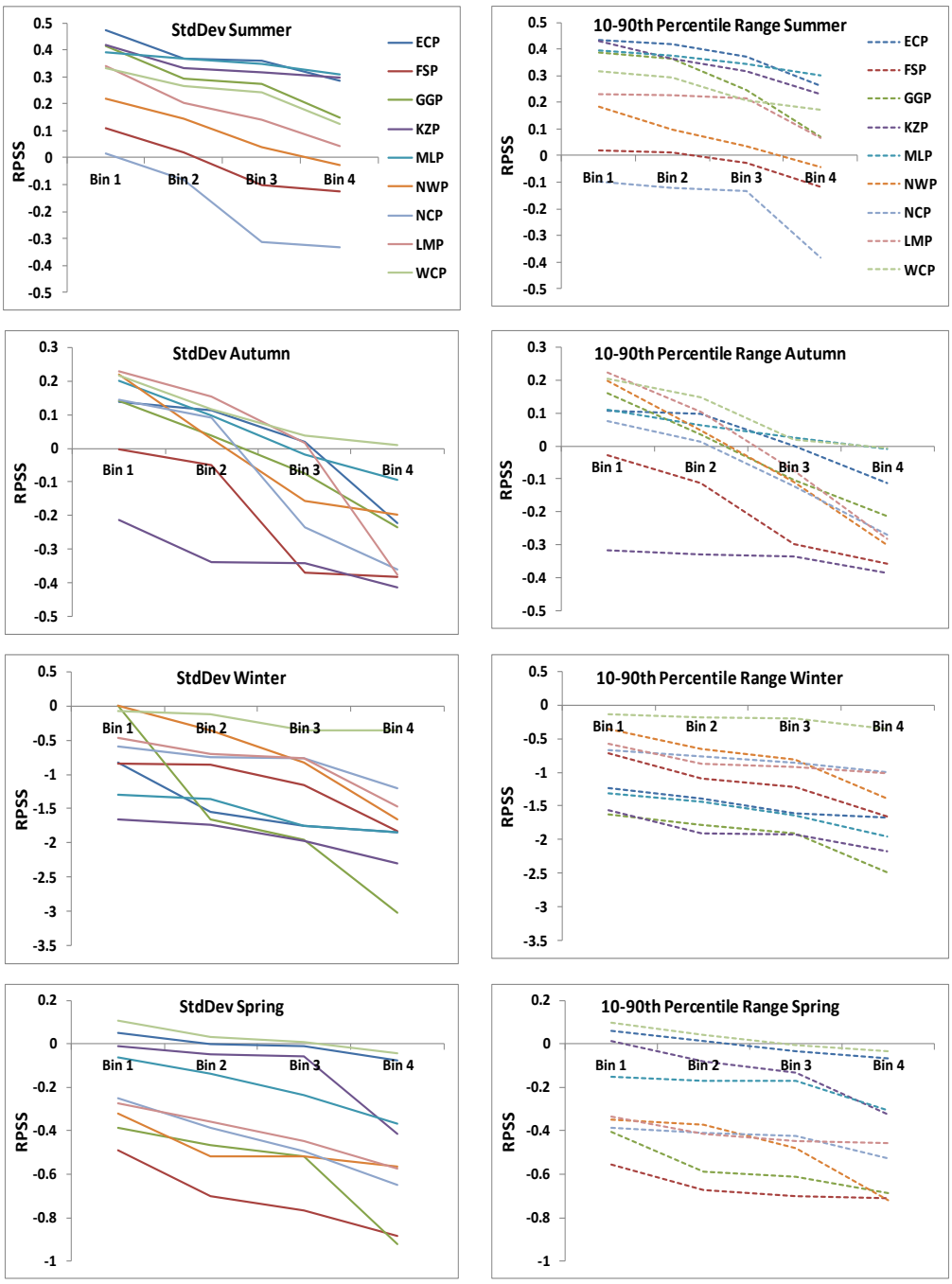

Figure 8.6 Ranked probability skill score, RPSS, for precipitation, as a function of ensemble spread. Years are classified into one of four equally-populated bins (horizontal axis) according to StdDev (**left panels**) and 10-90th percentile range (**right panels**) measures of spread. Bin 1 contains years with the narrowest spread while bin 4 contains years with the widest spread. Provincial abbreviations are as stipulated in Figure 4.3.

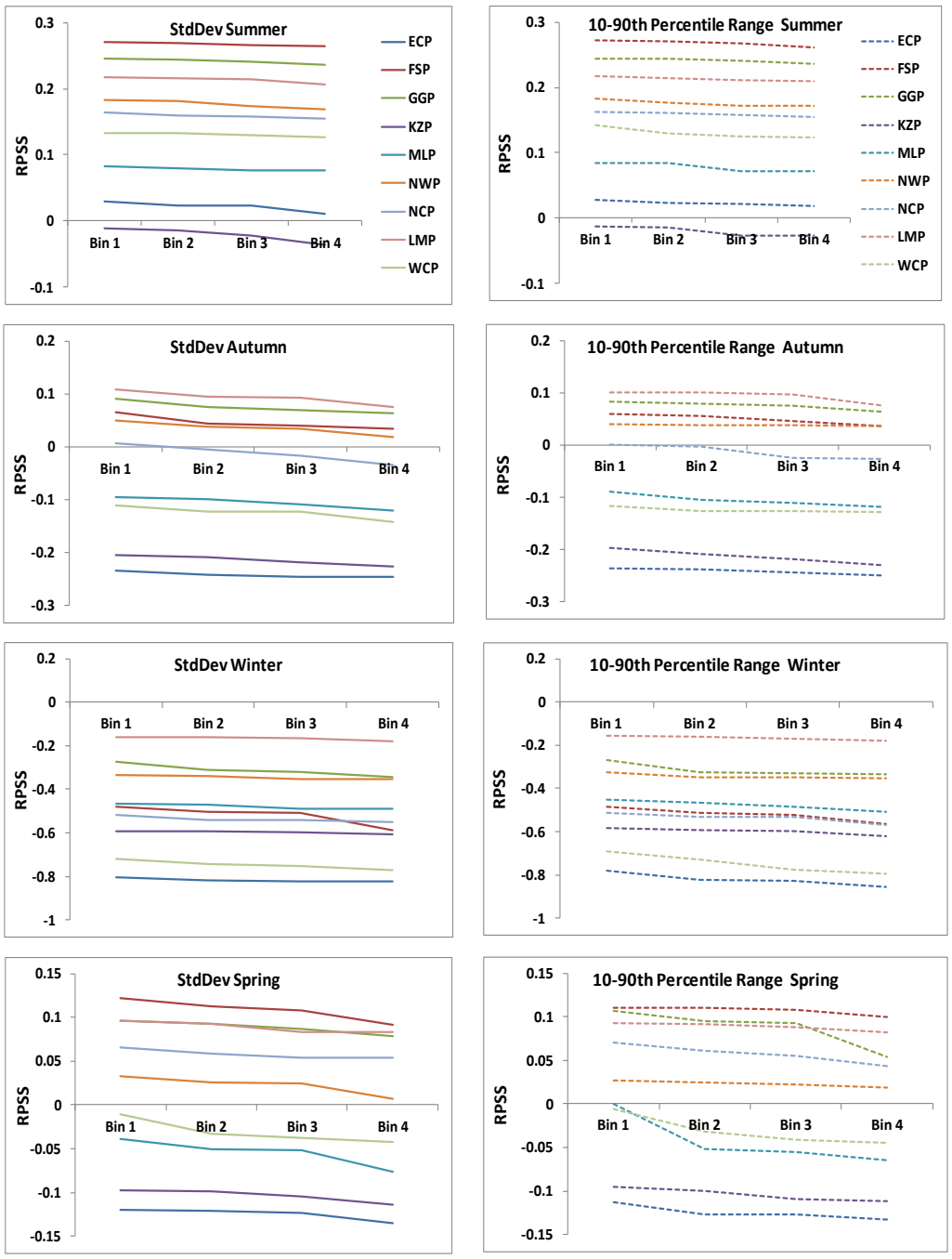

Figure 8.7 Ranked probability skill score, RPSS, for temperature, as a function of ensemble spread. Years are classified into one of four equally-populated bins (horizontal axis) according to StdDev (**left panels**) and 10-90th percentile range (**right panels**) measures of spread. Bin 1 contains years with the narrowest spread while bin 4 contains years with the widest spread. Provincial abbreviations are as stipulated in Figure 4.3.

8.4 Spatial Trends in Ensemble Spread over South Africa

There exist substantial long-term trends in the spread of seasonal climate simulations over South Africa. These trends are evaluated from the inter-annual time series of the two measures of spread – the StdDev and the 10-90th percentile range and the ensemble mean. Their spatial distributions are depicted in Figures 8.8 and 8.9 respectively for precipitation and near surface air temperature. Also included in these figures is the spatial distribution of trends of the observation. Generally, there are some degrees of agreement between the evaluated and the observed trends (in precipitation and in near surface air temperature). All evaluated trends exhibit coastal–inland gradients. As expected for an approximately Gaussian distribution, trends in the 10–90th percentile range are typically around three times larger than the trends in the StdDev.

Trends exhibited by the StdDev of precipitation have a tendency for widening (positive trends), which is similar to trends in 10–90th percentile range (Figure 8.8, top and second rows). Coastal areas are mostly dominated by widening of the spread, the maximum magnitudes of which are approximately 0.0075 and 0.025mm day^{-1} year^{-1} respectively for StdDev and 10–90th percentile range. This implies that, for the seasonal total over the 50-year period, the simulated precipitation spread over these areas have widened by about 34mm (i.e. 0.0075mm day^{-1} year^{-1} * 90 days * 50 years; where 90 days represent a season) around the seasonal climatological mean; and, to a maximum of 110mm (i.e. 0.025mm day^{-1} year^{-1} * 90 days * 50 years) in extreme situations. Narrowing of width (negative trends; maximum magnitude of about 0.005mm day^{-1} year^{-1}) is generally weak and more confined to inland territories especially in DJF and JJA.

Spatial structures of measures of spread in temperature are also similar (Figure 8.9, top and second rows). Both measures of spread indicate a general widening tendency over the majority of inland provinces in spring (SON), through summer (DJF) to autumn (MAM). Width amplitudes are 0.005 and 0.018 ^{o}C year^{-1}, respectively for StdDev and 10–90th percentile range, implying a maximum spread of about 1 ^{o}C (i.e. 0.018 ^{o}C year^{-1} * 50 years) over the 50-year period. The entire coastal area experiences a narrowing

(maximum magnitudes of 0.0025 to 0.006 ^{o}C year^{-1}) of ensemble width in spring (SON). This results in spreads ranging from 0.1 to 0.3 ^{o}C over the same period. However, the spread over the inland territories switches to narrowing in winter (JJA).

Disagreement in rainfall trends could be as a result of the observed trends not being attributable to the effects of increased radiative forcing from greenhouse gases (Zhang et al., 2007; Stott et al., 2010) whereas changes in observed temperature are attributable to anthropogenically forced changes (Solomon et al., 2007). MacKellar et al (2014) attributed models' inability to capture satisfactorily the observed trends to the temporal development of low-frequency climate variations that differs distinctly from the observation. The existence of long-term trends in the spread of seasonal precipitation and temperature simulations over South Africa suggests that there exist variations in the range of possible seasonal climate simulations from year to year, at least within this experimental setup.

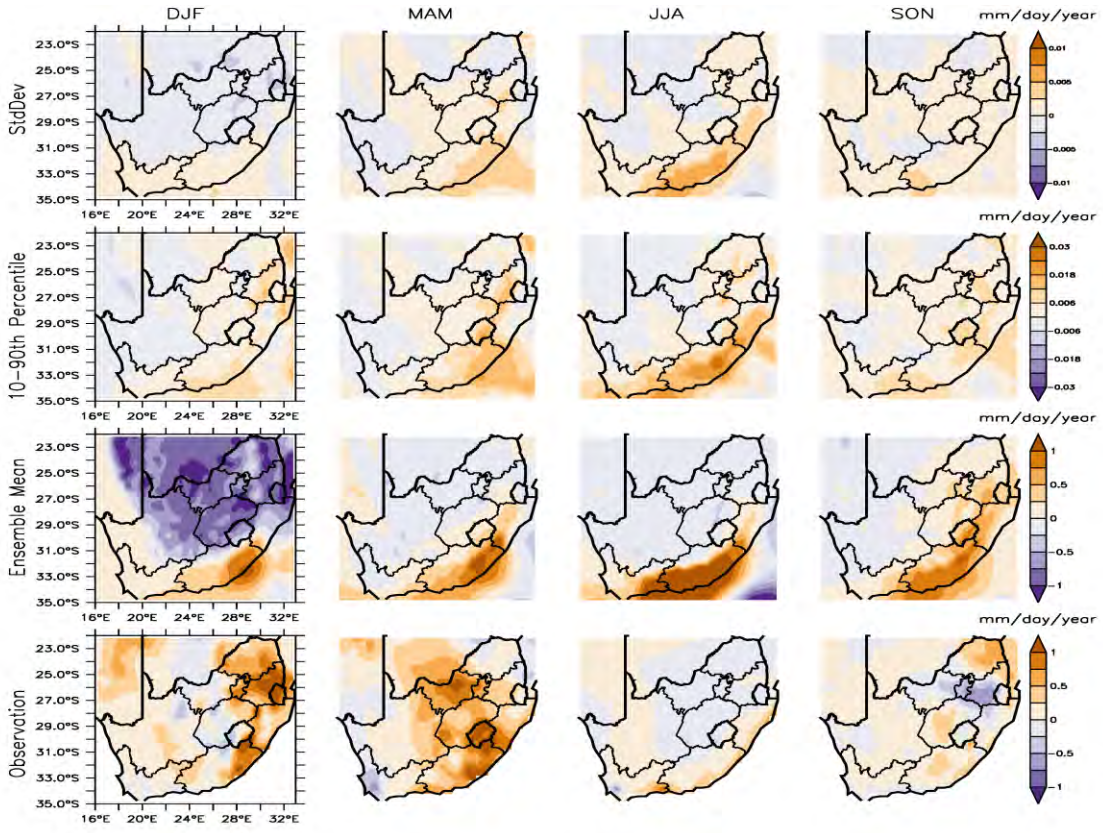

Figure 8.8 Spatial distribution of trends (mm day^{-1} year^{-1}) calculated from the seasonal time series of (**top row**) the StdDev; (**second row**) the 10-90th percentile range; (**third row**) the ensemble mean; and (**bottom row**) the observation of precipitation during the December 1959 through November 2010 period. Columns indicate the austral seasons: DJF – summer; MAM – autumn; JJA – winter; SON – spring.

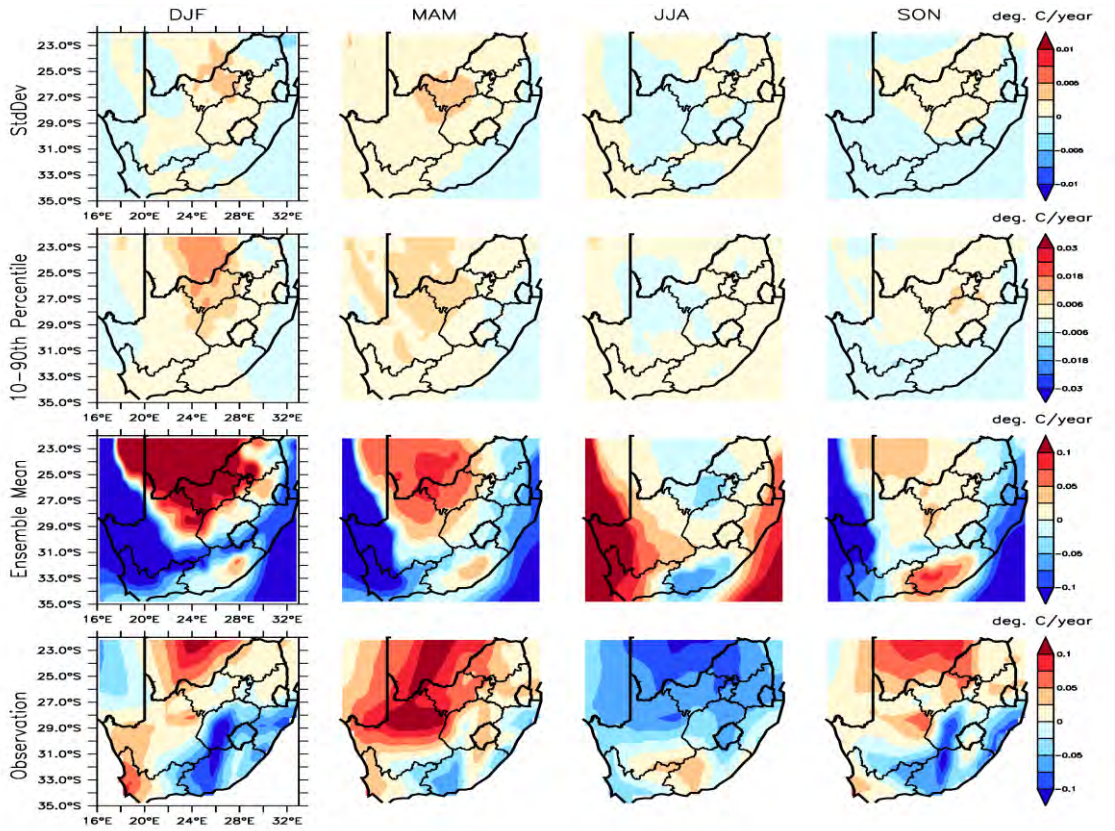

Figure 8.9 Spatial distributions of trends (^{o}C year^{-1}) calculated from the seasonal time series of (**top row**) the StdDev; (**second row**) the 10-90th percentile range; (**third row**) the ensemble mean; and (**bottom row**) the observation of temperature during the December 1959 through November 2010 period. Columns indicate the austral seasons: DJF – summer; MAM – autumn; JJA – winter; SON – spring.

8.5 Monthly Trends in Ensemble Spread on Provincial Basis

Section 8.4 above focused on the spatial details at the expense of sub seasonal details and uncertainty characterization. In this section, we reverse this focus by examining trends on provincial levels on a monthly basis including uncertainty estimation. Trends in measures of spread are estimated from a sample of 100 ensemble members for each month.

Some provinces have experienced a widening (positive trends) or narrowing (negative trends) of the ensemble spreads as indicated in panels (a) and (b) of Figures 8.10 and 8.11. The solid lines in those panels indicate the sample mean, whereas the grey shading indicates the 80% confidence interval estimated through a Monte-Carlo bootstrap

procedure. As expected for Gaussian distributions, trends in the StdDev measure are generally less than half as large as those in the 10–90th percentile range measure.

Majority of the trends (i.e. monthly trends in ensemble spread for precipitation over the nine South African provinces) displayed in panels (a) and (b) of Figure 8.10 are positive during both the onset and cessation seasons (spring and autumn for all provinces other than the Western Cape). Mean estimates of trends in total monthly precipitation spread range approximately from a narrowing of 1.5mm to a widening of 13.5mm over the half-century period according to the StdDev measure, and a narrowing of 15mm to a widening of 68mm according to the 10–90th percentile range measure. In general the central and eastern provinces experience a narrowing or no change of ensemble width from November to January, with some provinces such as Limpopo (LMP) and Mpumalanga (MLP) also experiencing narrowing later into the rainy season. The southern coastal provinces [Eastern Cape (ECP) and Western Cape (WCP)] experience a widening in most months.

Trends in measures of spread for surface air temperature over the South African provinces have a distinct duality between the coastal and inland provinces (Figure 8.11(a) and (b)). For the most part, inland provinces exhibit widening trends. Coastal provinces exhibit narrowing of the ensemble spreads from September to December. The estimated mean trends in the temperature spread range from a narrowing of 0.05 ^{o}C to a widening of 0.45 ^{o}C over the 50-year period according to the StdDev measure, and a narrowing of 0.1 ^{o}C to a widening of 1.4 ^{o}C over the full periods according to the 10–90th percentile range measure.

8.6 Comparison of Trends in Spread, Ensemble Mean and Observation

Spatial correlations between the evaluated trends obtained through vectorization of trends in the measures of spread as well as the ensemble mean trend and the observed trend, displayed in Figures 8.8 and 8.9, are presented in Table 8.1. Results in the table indicate

whether or not the ensemble mean trend of the simulations resembles long-term trends in the observational record. In this respect there are some disparities in the physical spatial structure of the trends in the ensemble mean and the observational records (Figures 8.8 and 8.9, third and bottom rows) that are reflected in Table 8.1, most obviously in summer and autumn precipitation. These similarities and discrepancies vary in magnitude, locations of positive and negative trends, and with season; they resemble previous studies that found similarities and discrepancies between observed and modelled trends, e.g. Hoerling et al. (2006) and MacKellar et al. (2014).

With regard to the trends in simulated ensemble spread, there are significant spatial correlations in some seasons between trends in observed precipitation and trends in the two measures of simulated precipitation spread. For temperature, spatial correlations between trends in observed temperature and StdDev are significant for all seasons. With the notable exception of autumn for both variables, for both precipitation and temperature, statistically significant correlations involving observed trends are small and much smaller than correlations of the measure of spread with the ensemble mean. This would lend support to the possibility that, while trends in the ensemble spread of this particular HadRM3P model may in some cases not be an accurate reproduction of trends in potential predictability in the real world, the real trends may be inferable from the mean observed trend.

On a monthly basis, all provinces exhibit larger magnitudes in observed trends during the summer rainy season (winter rainy season over WCP), and vice versa during winter (summer over WCP) (Figure 8.10c). This characteristic, which commences from late spring through summer to mid autumn, is also displayed by trends in ensemble mean. There exist non-zero trends over ECP, probably because it rains throughout the year over this province. This is however opposite over Northern Cape (NCP), an arid region with a climatologically small amount of winter precipitation (Figure 8.1). We note that these periods of large (small) trends in both the observation and ensemble mean coincide with periods of rainfall peaks (dry season) over each respective province. The coastal–inland

duality is also exhibited by trends in ensemble mean of temperature (Figure 8.11c). This is more obvious in warm summer and autumn periods where majority of the coastal provinces exhibit downward trends. Trends in observed record and ensemble mean oscillate more around the zero axes with largest amplitude of about 0.09 ^{o}C year^{-1} in summer. Generally, the trends in ensemble mean tend to switch signs between summer and the cold winter period. What may be the main reasons for disagreements have been mentioned earlier, i.e. in paragraph 4 of Section 8.4.

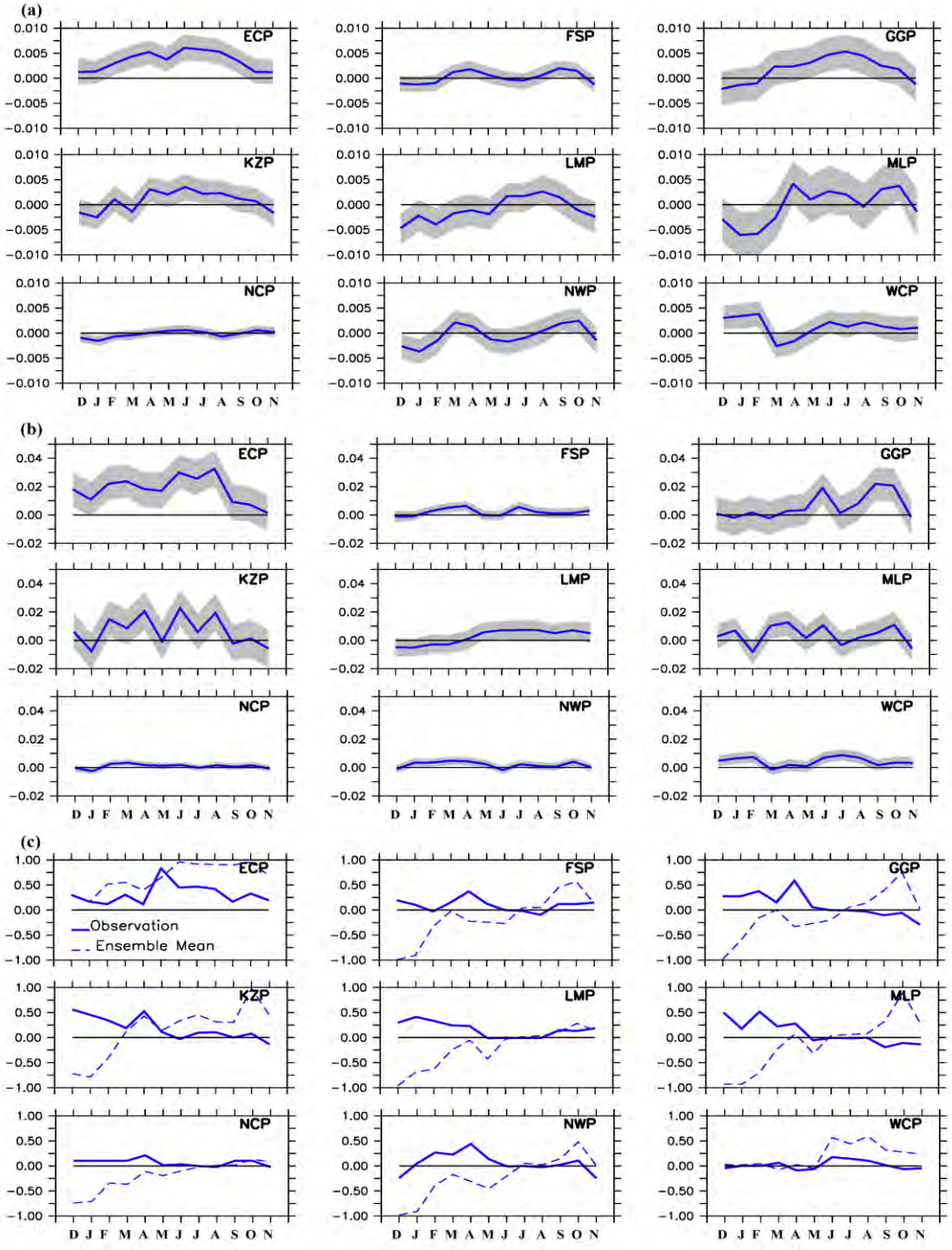

Figure 8.10 Trends (mm day^{-1} year^{-1}) in (**a**) StdDev, (**b**) the 10-90th percentile range, and (**c**) the observational record and ensemble mean of precipitation over the nine South African provinces as a function of month. Provincial abbreviations, written at the top right corner of each panel, are as stipulated in Figure 4.3. Gray shading in panels **a** and **b** indicates 80% confidence intervals estimated through a Monte-Carlo bootstrap procedure.

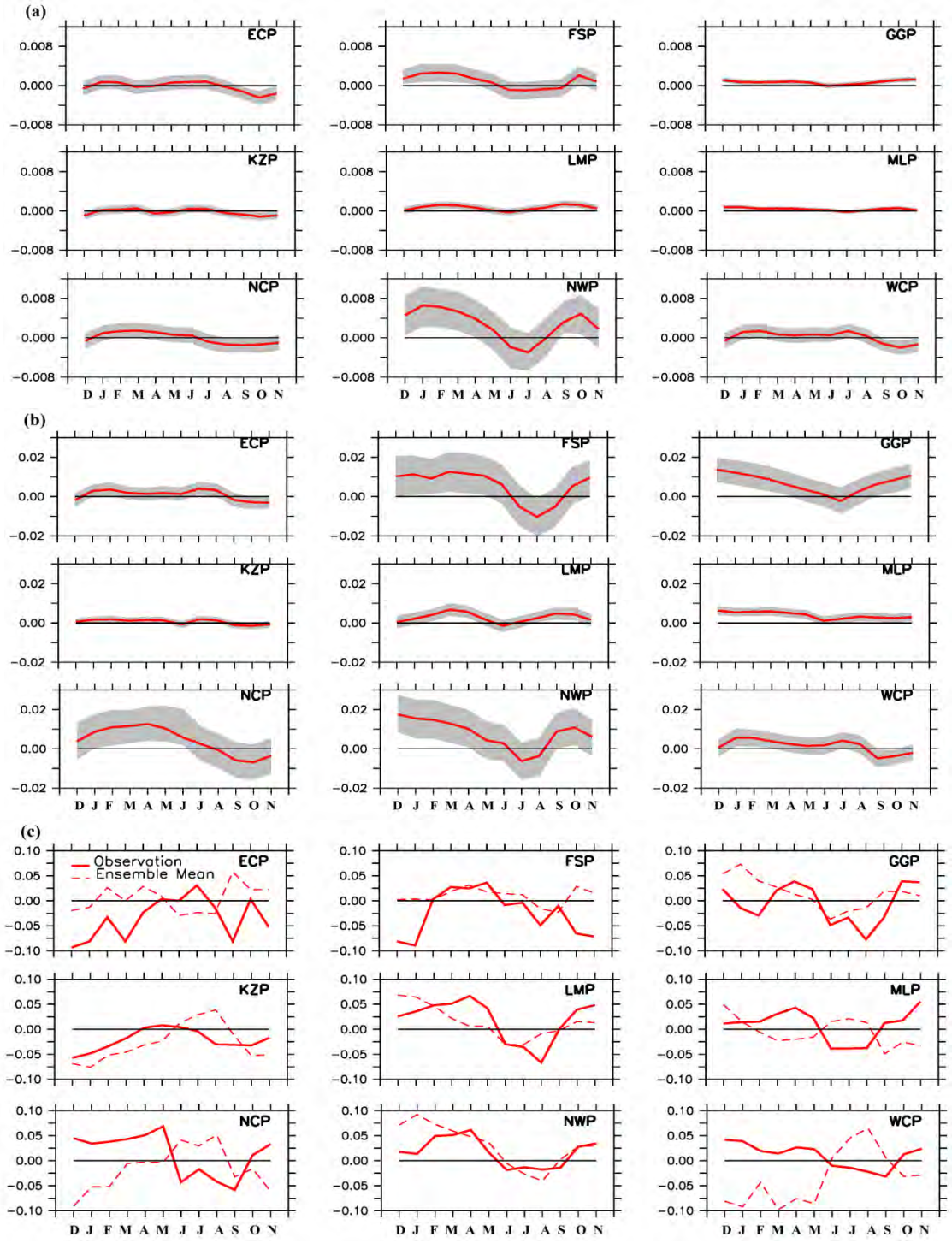

Figure 8.11 Trends (^{o}C year^{-1}) in (**a**) StdDev, (**b**) the 10-90th percentile range, and (**c**) the observational record and ensemble mean temperature over the nine South African provinces as a function of month. Provincial abbreviations, written at the top right corner of each panel, are as stipulated in Figure 4.3. Gray shading in panels **a** and **b** indicates 80% confidence intervals estimated through a Monte-Carlo bootstrap procedure.

8.7 Uncertainty Analysis and Simulation Skill

Careful analysis of panels (a) and (b) of Figures 8.10 and 8.11 show that it is possible for trends to have zero-values outside their 80% confidence level. Of the 108 province-month realizations for each variable and measure, 38 of the StdDev cases and 50 of the 10–90th percentile range cases for precipitation spread have the zero trends outside their 80% confidence intervals; 53 of the StdDev cases and 65 of the 10–90th percentile range cases for temperature spread exhibit these characteristic. At random, only 22 cases, in each case, would be expected to do so. These evidently, thus, suggest real changes in simulation spread occurring within this climate model framework.

Comparison of the model skill (Figures 8.6, 8.7 and 8.12) with the evaluated trends (Figures 8.10 and 8.11) show that there are some relationships between variations in simulation spreads and what is realized in the real world. Irrespective of the direction of trends skills are higher when magnitudes of trends, especially in the observed record and ensemble mean, are large. For both parameters, it is possible that trends in both observation and ensemble mean contribute more to the understanding of skill. Poor precipitation skill over WCP in winter, when trends are higher, may be attributed to the inability of the model resolution to track those transient synoptic systems that are active over this province in winter. Therefore, annual cycles of trends in observations and ensemble mean may have the potential to improve the interpretation of annual cycles of simulation skill. Furthermore, simulation skills are expected, in the nearest future, to further improve as a result of computational improvements in the state-of-the-art climate modeling systems.

Table 8.1 Spatial correlations between the evaluated trends obtained through vectorization of trends displayed in Figures 8.8 and 8.9. Bolded figures represent correlations that are statistically significant at 95% confidence level and are not within the critical value of ±0.22. Evaluated trends are represented are follow: **1** – StdDev; **2** – 10-90th percentile range; **3** – Ensemble mean; and, **4** – Observation.

	Summer				**Autumn**				**Winter**				**Spring**			
	1	2	3	4	1	2	3	4	1	2	3	4	1	2	3	4
Precipitation																
1		**0.25**	**0.42**	**-0.36**		**0.96**	**0.52**	**0.75**		**0.85**	**0.79**	-0.14		**0.8**	**0.59**	0.2
2	**0.25**		**-0.38**	**0.24**	**0.96**		**0.61**	**0.58**	**0.85**		**0.42**	0.18	**0.8**		**0.61**	**0.51**
3	**0.42**	**-0.38**		**-0.39**	**0.52**	**0.61**		**-0.63**	**0.79**	**0.42**		**0.48**	**0.59**	**0.61**		**0.26**
4	**-0.36**	**0.24**	**-0.39**		**0.75**	**0.58**	**-0.63**		-0.14	0.18	**0.48**		0.2	**0.51**	**0.26**	
Temperature																
1		**0.89**	**0.69**	**-0.33**		**0.97**	**0.61**	**0.82**		**0.95**	**0.45**	**-0.24**		**0.93**	**0.85**	**-0.24**
2	**0.89**		**0.84**	0.03	**0.97**		**0.46**	**0.9**	**0.95**		**0.54**	**-0.24**	**0.93**		**0.87**	-0.11
3	**0.69**	**0.84**		0.15	**0.61**	**0.46**		**0.28**	**0.45**	**0.54**		0.07	**0.85**	**0.87**		0.18
4	**-0.33**	0.03	0.15		**0.82**	**0.9**	**0.28**		**-0.24**	**-0.24**	0.07		**-0.24**	-0.11	0.18	

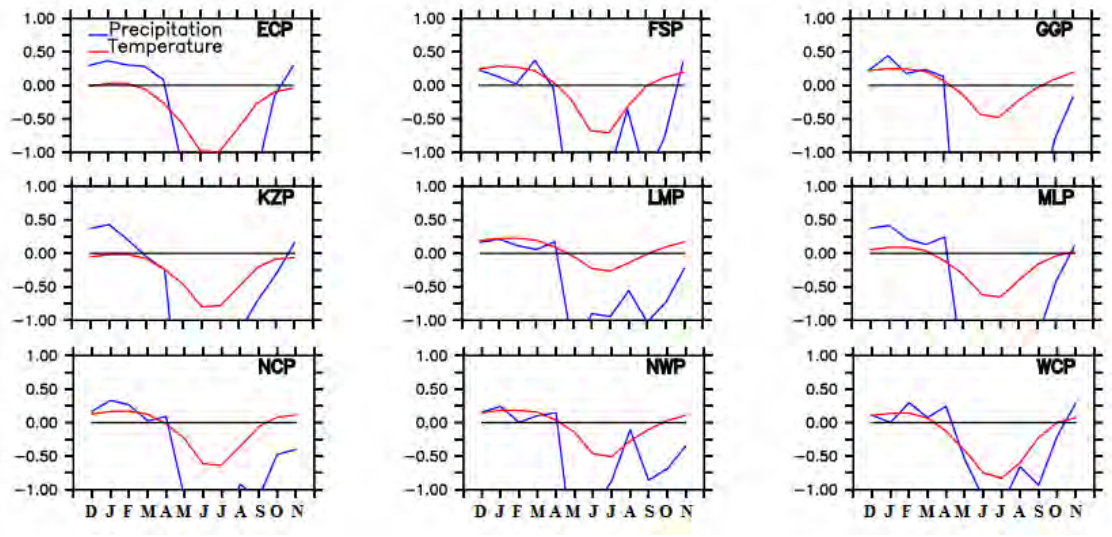

Figure 8.12 RPSS, for precipitation and temperature, as a function of month over the nine South African provinces. Provincial abbreviations, written at the top right corner of each panel, are as stipulated in Figure 4.3.

8.8 Summary

This chapter has revealed the evidence that the spread of seasonal climate (rainfall and temperature), over South African, simulated from an atmospheric model driven by observed boundary conditions exhibit long-term trends and, by inference, can vary from one year to the other. These long-term trends differ across seasons and locations within the country and have the potential to improve the interpretation of long-term simulation skills.

This experiment was carried out within the framework of the HadAM3P-N96/HadRM3P model pair, which is not used in any contemporary seasonal forecast service [though the global HadAM3P is (http://www.gfcsa.net/csag.html); Browne et al, 2009; Browne, 2011]. The use of this model pair was motivated by the large computational expense of the experimental design, which required use of CPDN, and which benefited from the existing HadAM3P-N96/HadRM3P port on that facility. The possibility exists that the exact values of these trends in ensemble spread are specific to this model pair and may not reflect those in other model setups.

The correspondence of higher model skill when the simulation spread is narrower suggests that the long-term trends reflect fundamental trends in the climate system that modern seasonal forecasting systems might thus also be expected to reproduce. In addition, the correspondence of higher model skill when trends are higher also suggests that the skill produced by a dynamical modeling system may not be independent of the model ability to capture the real atmospheric trends in whatever the model is simulating or forecasting. In any case, the presence of these trends in this modeling setup is highly suggestive of possible similar trends in contemporary active multi-model prediction settings. Such trends may thus be useful in the characterization of skills of current forecasts in relation to the assessment of past skill.

9 Investigating the Co-variability of SSTs, Climate Indices and Spreads in the Simulation of South African Climate

This chapter investigates the relative role of SSTs and large scale climate indices as predictors of inter-annual variability in the ensemble spreads of seasonal climate (i.e. rainfall and near surface air temperature) simulations from HadRM3P over South African provinces. The chapter analyzes the co-variability between the measures of seasonal climate predictability and seasonal anomalies of the SST. Seasonal measures of predictability are quantified by ensemble spreads which are in turn measured with the de-trended anomalies of standard deviation (StdDev) and the distance between the 90^{th} and 10^{th} percentiles of the simulations (as described in section 3.2.1 of Chapter 3 and depicted in Figure 8.3).

9.1 Co-variability of Global SST and the Seasonal-Provincial Ensemble Spreads

Figures 9.1 and 9.2 show an illustrative subset of maps indicating correlations between the observed SST and the provincial measures of ensemble spread (the StdDev and the 10–90th percentile range). Specifically, Figure 9.1 depicts correlations between the provincial rainfall 10–90th percentile range and the observed SST during the onset of the rainy season (i.e. austral spring in eight of the provinces and the cessation season for WCP); while Figure 9.2 displays the correlations between the provincial temperature StdDev and the observed global SST during the winter season. The trend was removed from all seasonal data before calculations because we are interested in the natural variability. Generally, **r** ranges from -0.82 to +0.86 for both parameters and measures of spreads for all the seasons (including other seasons that are not shown).

Provincial measures of ensemble spreads for both rainfall and temperature significantly co-vary with SSTs over various ocean regions. However, the co-variability differs from season to season. Most provinces feature considerable positive or negative spread-SST

correlations over the mid latitude to Antarctic / southern zones of the Pacific, Atlantic and Indian Oceans. Many provinces also exhibit some positive or negative correlations over the tropical axis of these Oceans. These imply that oceans may provide useful predictors of variations in the predictability of seasonal climate over these provinces. Interestingly, some aspects of oceanic variability are so generally useful for describing seasonal forecasts; hence they are summarized into climate indices (see Table 3.2). Some of these climate indices represent variations in ocean temperature signals in the tropical, mid latitudinal and southern parts of Pacific, Atlantic and Indian Oceans where we have noted significant correlations. Thus, there is the possibility that along with being useful predictors of seasonal climate over South Africa, these indices may also be useful predictors of the potential skill of that forecast.

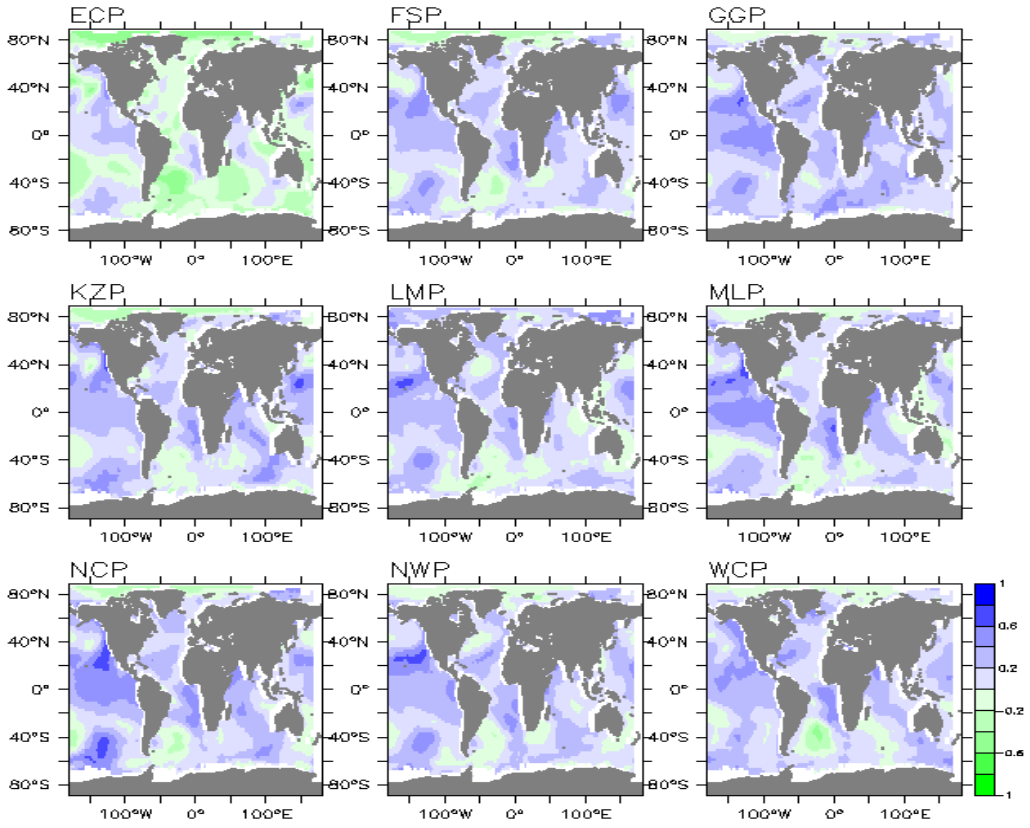

Figure 9.1 Maps of the correlations between the 10–90th percentile range of the provincial rainfall and the observed global SST during spring onset of the rainy season for all provinces except WCP, for which it is the cessation period. The trend was

removed from all data before calculations while the provincial abbreviations, written at the top left corner of each panel, are as stipulated in Figure 3.1.

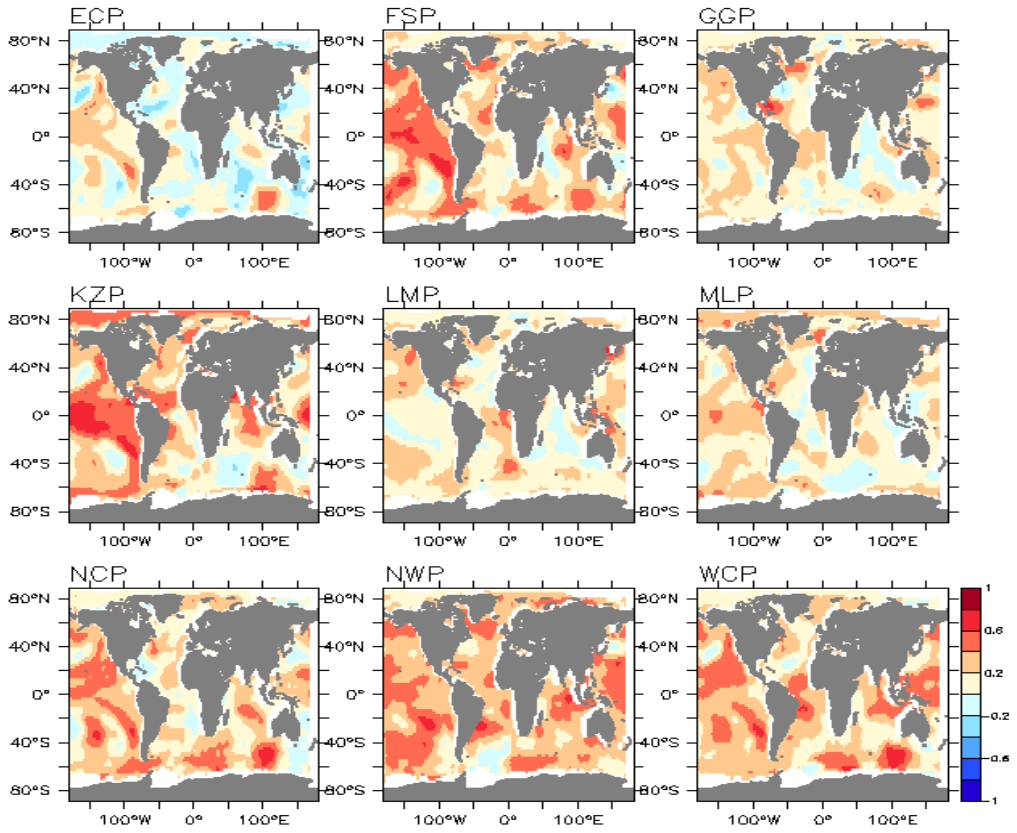

Figure 9.2 Maps of the correlations between the StdDev of provincial temperatures and the observed global SST during the cold winter season. The trend was removed from all data before calculations while the provincial abbreviations, written at the top left corner of each panel, are as stipulated in Figure 3.1.

9.2 Co-variability of Seasonal-Provincial Ensemble Spreads and Climate Indices

9.2.1 Rainfall

Figure 9.3 shows that the average correlation, **r**, between the rainfall measures of spread (for the nine South African provinces) and climate indices spans across +/-0.47; but when the error bars are considered, **r** spread across +/-0.8 which are more notice-able during

rainfall peak (summer) and dry (winter) seasons. The correlations range from significantly weak to strong relationships in both directions of direct and inverse proportions. There are high degrees of agreements between the measures of spread (the 10–90th percentile range and StdDev) when they were correlated with climate indices.

During the dry winter season for instance, Figure 9.3 shows that clear cases of non-zero **r** agreements can be found in MEI (the Multivariate ENSO Index) for Northern Cape Province (NCP) and WCP. In the same season, measures of spread over the Eastern Cape Province (ECP) correlated significantly with AAO while Gauteng Province (GGP) correlated with TSA. However, it is necessary to note that provincial rainfall totals, in all provinces, in this season are so small as to have any impacts, except over ECP and WCP.

Measures of spread over many provinces correlated considerably with more than one climate index during the spring (onset) season. For instance, Free State Province (FSP) and GGP correlate considerably with IOD; FSP, GGP, NCP, North West Province (NWP) and WCP also correlated considerably with MEI while FSP and GGP also responded to TSA (Figure 9.3). In summer (rain peak) season, both measures of spread agreeably correlated considerably with MEI over WCP. In autumn (the cessation period), only FSP measures of spread correlated considerably with TSA. Few instances of major differences are in AAO over Limpopo Province (LMP) and ECP during peak and onset seasons respectively. In general, the degrees of correlations differ from index-to-index, season-to-season and province-to-province. There is therefore no gross spatial pattern to the correlations, vis-à-vis the co-variability, at the national scale.

Summary of Figure 9.3 in Table 9.1 shows the frequency of non-zero correlations at 10% significant level for province-season combinations. For each season in the table, if the indices and the measures of spread are independent, then approximately 1 out of 9 provinces per index would be expected to be significant (i.e. non-zero) by random chance. Counts above 1 are thus suggestive that we are finding evidence of physically-based co-variation. The “1-in-9-expected-by-chance” rule of thumb should be considered

a bare minimum, rather than sufficient; because the provinces are hardly independent of each other climatologically. Therefore, on seasonal time-scale, MEI is the most influential regarding rainfall predictability over South Africa (Table 9.1). MEI is the only index that has more than the required statistical provincial-seasonal realizations during rainfall onset and peak periods. However, its influence is zero during cessation period when TSA dominates. Furthermore, IOD and TSA processes may also determine rainfall predictability during the onset period.

9.2.2 Temperature

The correlations between the seasonal temperature measures of spread (for the nine South African provinces) and climate indices are illustrated on the panels of Figure 9.4 for summer and winter. In similarity to rainfall analysis, no province, and no climate index demonstrates any particular pattern in the seasonal-provincial distributions of **r** during these two seasons. As potential correlations span from -0.6 to +0.8, there exists some degrees of graphical similarities between the 10–90th percentile range and the StdDev (Figure 9.4). In summer, both measures of spread correlated considerably with MEI over ECP, KwaZulu Natal Province (KZP) and WCP; with IOD over ECP and with TSA over FSP, MLP and NWP. In winter, measures of spread over KZP and WCP correlated considerably with MEI.

Table 9.1, where the condition is the same as that of rainfall on seasonal time-scale, shows that IOD and MEI processes possess considerable influences on the predictability of South African near-surface air temperature in both summer and winter. While MEI has more of the required statistical provincial-seasonal realizations than IOD in both seasons; TSA's influences on the measures of predictability for temperature are restricted only to summer season.

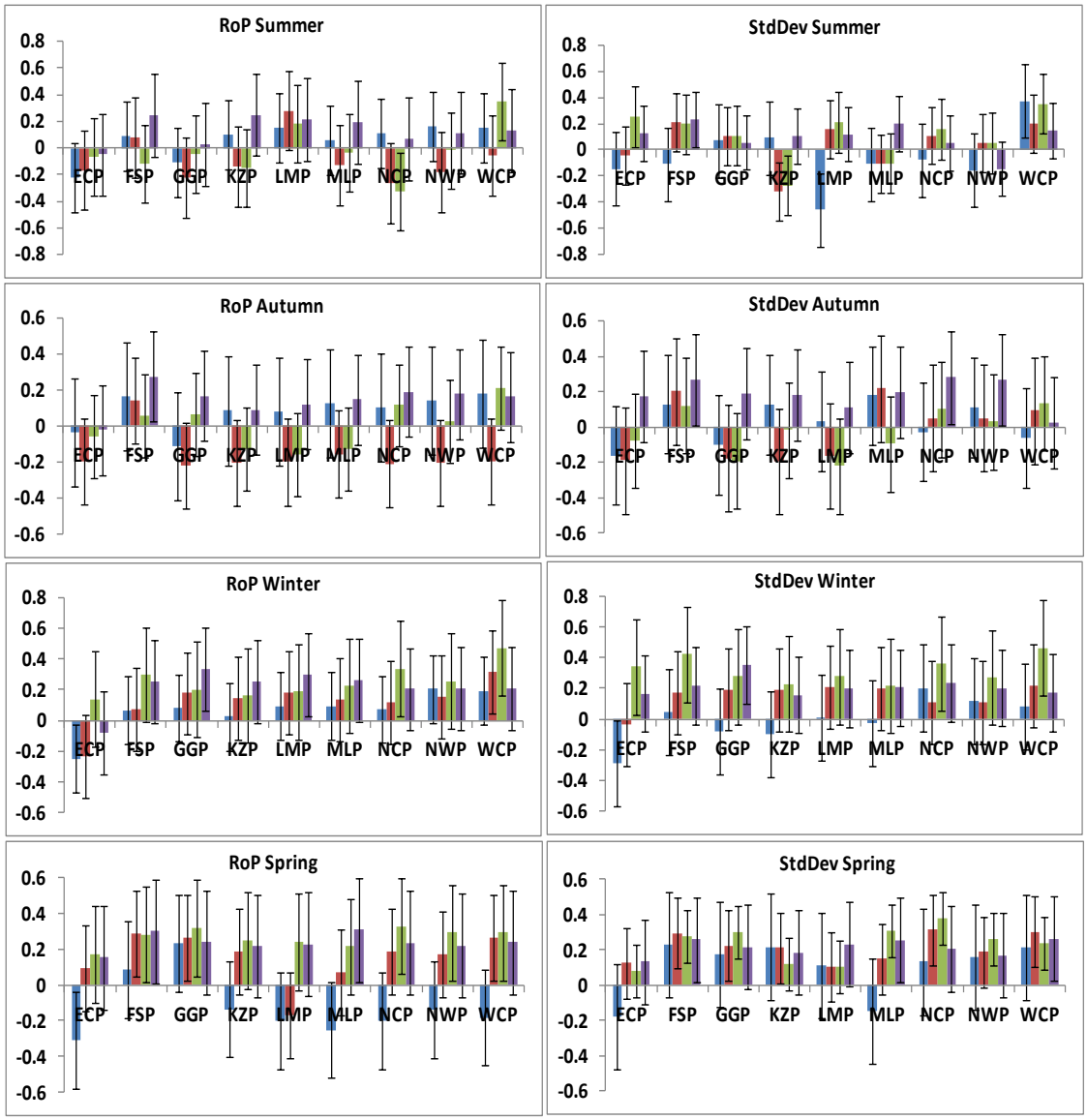

Figure 9.3 Correlations between seasonal rainfall measures of spread (for the nine South African Provinces) and climate indices. Error bars indicate 90% confidence intervals estimated through a Monte-Carlo bootstrap procedure; RoP is the 10-90th percentile range and StdDev the standard deviation.

Table 9.1 Frequency of non-zero correlations between provincial-seasonal measures of spread and large-scale climate indices. At random, only 1 out of 9 provinces per index are expected to have correlations considerably different from zero at the two-sided 10% significant level. On rainfall column, note that the peak and dry seasons are respectively dry and wet seasons for WCP.

Climate index	Rainfall			Temperature		
	Season	The 10–90th percentile range	StdDev	Season	The 10–90th percentile range	StdDev
AAO	Peak (Summer)	0	2	Hot (Summer)	0	0
IOD		0	1		1	2
MEI		2	3		3	7
TSA		0	1		4	4
AAO	Cessation (Autumn)	0	0			
IOD		0	0			
MEI		0	0			
TSA		1	3			
AAO	Dry (Winter)	1	1	Cold (Winter)	0	0
IOD		1	0		1	3
MEI		2	4		2	6
TSA		2	1		0	1
AAO	Onset (Spring)	1	0			
IOD		3	5			
MEI		4	6			
TSA		2	3			

Tyson and Preston-Whyte (2000) noted that rainfall over WCP and ECP, respectively in winter and year-round, results from frontal activities which are modulated by southern mid-latitude circulations. Thompson and Wallace (2000) showed that AAO reflects the equator-ward / pole-ward variations in the position of the southern mid latitude storm track. Therefore, the general lack of significant or considerable co-variability between the measures of spread and AAO over WCP and ECP suggests that the predictability of variations in the frequency and intensity of mid-latitude flows structures, such as cut-off-lows, are not related to the variations in the frequency and intensity themselves, at least in a linear way.

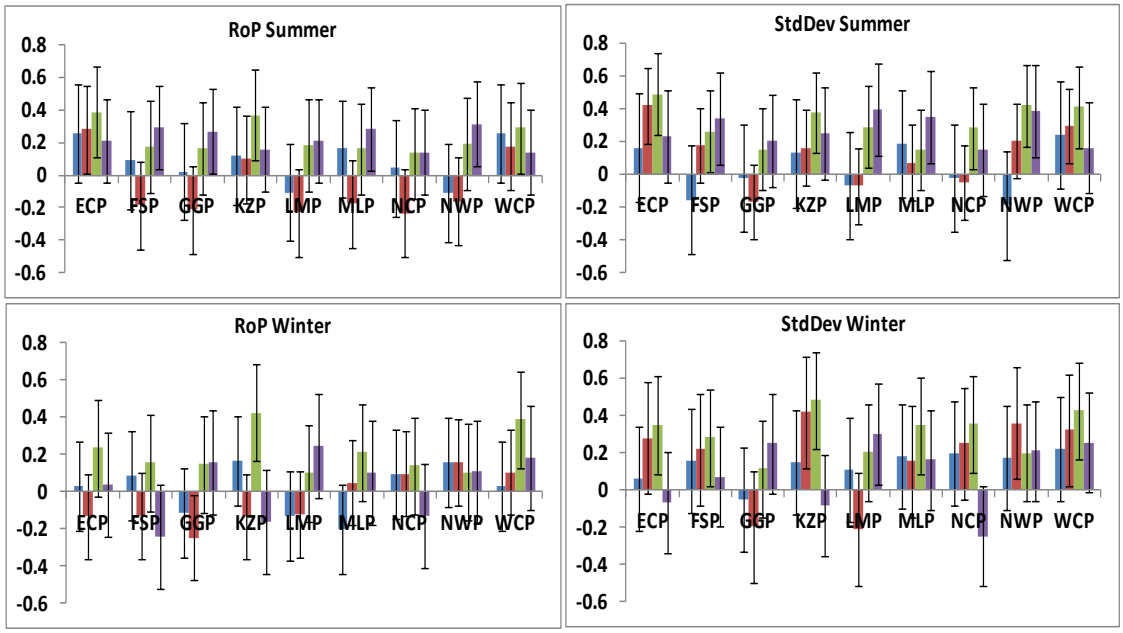

Figure 9.4 Correlations between seasonal temperature measures of spread (for the nine South African Provinces) and climate indices. Error bars indicate 90% confidence intervals estimated through a Monte-Carlo bootstrap procedure; RoP is the 10-90th percentile range and StdDev the standard deviation.

9.3 Summary

Within the HadAM3P-N96/HadRM3P-50km regional modeling framework used in this study, it has been established that the South African provincial measures of predictability significantly co-vary with the observed global SST far and near on seasonal time scale, suggesting that the climatic driving factors / forces may be locally or remotely based.

In order to answer the probing question of whether there are any SST influences on seasonal climate predictability via ensemble spreads, the study further examined the co-variability between the indices of large-scale climate variability and the variations in the ensemble spread of atmospheric model simulations over South Africa. Analyses revealed that the degrees of co-variability differ from index-to-index, season-to-season and province-to-province. There are no clear large-scale patterns in the seasonal-provincial correlations, whether in space or across seasons. Nevertheless, this study affirms that ENSO, as described by MEI, is the most influential in the predictability of seasonal climate over South Africa. It is the only climate index that has more than the required statistical provincial-seasonal realizations during rainfall peak period in summer and even the cold winter. This is in line with the earlier findings of Fauchereau et al. (2009) and Landman and Beraki (2010) that ENSO has the largest influence on South African rainfall anomalies. IOD also appear to have some role in influencing climate predictability in other seasons. This study is therefore indicating that there may be limits to the extent of which year-to-year variations in the predictability of seasonal climate forecasts might be understood, either because - (1) all significant climate predictors are of tropical origin, (2) the responses of predictability measures to predictors are, on the average, weak, (3) predictors are more complex in nature than can be represented by the traditionally simple climate indices, or (4) because the responses in predictability measures are probably nonlinear in nature.

10 Conclusions and Recommendations

Motivated by the importance of seasonal climate information to the socio-economic activities on the African continent, this thesis has analysed multi-years simulation ensembles to study the variability and predictability of seasonal climate over two regions in the continent (i.e. West and Southern Africa). In analysing the simulations, the thesis adopted a methodology that differs from those used by previous studies that have dealt with the subject. While the previous study usually used information about the consensus among the simulation, the thesis has used combined information on both agreement and disagreement of the simulations to investigate variability in dominant seasonal rainfall and temperature classes over West and Southern Africa, to examine the capability of climate models in reproducing the variability, and to study the predictability of the seasonal climates over South Africa. The background and motivation study have been detailed in chapter one of this thesis, and a comprehensive review of past studies on the subject have been provided in chapter two. Chapter three described the data and methodology employed in this thesis, while chapter four to nine presented and described results of the study. The present chapter summaries the results of the thesis with concluding remarks, and gives recommendations for future studies.

10.1 Conclusions

The results of this study can be broadly summarized into two groups. The first group is on the simulation of the characteristics of dominant classes of seasonal climate (rainfall and temperature) over West and Southern Africa using CAM while the second group assesses the predictability of seasonal climate over South Africa.

10.1.1 Simulations of the Characteristics of Dominant Classes of Seasonal Climate over West and Southern Africa

In chapters four to seven we have demonstrated the capability of CAM simulations in reproducing the characteristics of dominant classes / variability of seasonal climate (rainfall and temperature) and in replicating the relative role of various atmospheric

circulation anomalies on the classes/variability over West and Southern Africa. The characteristics considered include the inter-annual and decadal variability, transition, and persistence of the dominant classes. We have also been able to identify those dominant classes that the CAM can simulate adequately, moderately and poorly. The main findings from the application of CAM in simulating seasonal rainfall and temperature can be summarized as follows:

- Though, all the CAM simulations overestimate the magnitude of the inter-annual variability of rainfall, CAM still gives realistic simulations of the atmospheric dynamics that are essential for rainfall mechanisms, as well as factors affecting atmospheric energy budget over West and Southern Africa. The relations between the dominant classes of seasonal climate over the West and Southern African and global SST patterns are consistent between CAM and observations, showing that each class of seasonal climate can be linked to more than one SST index.
- While some simulations substantially perform better than the ensemble mean (average of all the simulations), some others perform substantively worse, however, the best simulations for a particular region / variable combination may not be suitable for another region / variable.
- Over West Africa, there is no preference in CAM's ability to simulate the seasonal variability of rainfall and temperature over West Africa, but the discrepancy among the simulations is higher for temperature than for rainfall, suggesting that, over West Africa, the seasonal predictability of dominant classes of temperature may be lower than that of the dominant classes of rainfall.
- In contrast, over Southern Africa, CAM does a better job in simulating classes of temperature than in simulating classes of rainfall, and the discrepancy among the simulations is lower for temperature than for rainfall, signifying that, over Southern Africa, the predictability of dominant classes of seasonal temperature over Southern Africa may be higher than that of rainfall classes.
- In most aspects, the model simulates the seasonal rainfall variability better over West Africa than over Southern Africa, but the discrepancy among the simulations is higher over West Africa than over Southern Africa, suggesting that

that the predictability of dominant seasonal rainfall may be lower over West Africa than over Southern Africa.

- The model simulates the seasonal temperature variability better over Southern Africa than over West Africa, and the discrepancy among the simulations is higher over West Africa than over Southern Africa, signifying that the predictability of dominant seasonal temperature may be higher over Southern Africa than over West Africa.

The above results have application in the three themes of seasonal climate predictions – characterization, evaluation, and prediction. They show that using information from full sets of trajectories of an ensemble forecasting system is superior to the traditional signal-to-noise paradigms (e.g. above-normal, normal and below-normal) when considering the potential information content of a large ensemble of simulations. A fundamental aspect of this approach is that the three themes are explicitly connected. Sensitivity to selection of ensemble member provides information on the robustness of the dominant classes of rainfall and temperature over our regions of concern; observations lack such information, therefore characterization cannot focus on the observations alone. The signal-to-noise method of evaluation may not be appropriate because this study has shown that an ensemble mean may not be representative of the capability of individual ensemble members. In addition, it is hard to define threshold for a "good" forecast when examining the ensemble mean, whereas the spread of class correlations between ensemble members and observations provides a quantitative calibration for evaluation of class matches. For prediction purposes, this study has shown that there is always at least one ensemble member that is much better than the ensemble mean. Similarly, there are also some ensemble members with extremely poor performance.

Results from this study have shown that the nature of predictability of seasonal climate, over West and Southern Africa, is different both in physics and in the range of goodness and or badness that is possible with a single climate model; and that there are still potentials for further developments in seasonal forecasting over the two near-by regions.

The results may guide on how CAM can be improved to give better seasonal simulations and more reliable future climate projection over these regions so that the socio-economic impacts of extreme rainfall and temperature related disasters within the region will be reduced.

10.1.2 Predictability of South African Seasonal Climate

In chapters eight and nine, we have been able to assess the existence and importance of trends in the spread of South African climate simulations covering 50 years of a large multi-analysis ensemble from a dynamical atmospheric model. We have evaluated and examined the characteristics of long-term trends in the ensemble spread in relation to trends in the ensemble mean and in the observational record, by considering the skill of the monthly mean precipitation and near surface air temperature simulations. In addition, we have been able to investigate the relative role of SSTs and large scale climate indices as predictors of inter-annual variability in the ensemble spreads of seasonal climate (i.e. rainfall and near surface air temperature) simulations from HadRM3P over South African provinces by analyzing the co-variability between the measures of seasonal climate predictability and seasonal anomalies of the SST. The key findings from these chapters are:

- There exist significant long-term trends in the measures of predictability, with a general coastal–inland gradient, suggesting the possibility of the existence of inter-annual variations in the potential range of seasonal climate simulations over South Africa.
- There is evidence that variations in the spreads of the ensemble (generated by the atmospheric model used in this study) reflect the fundamental properties of atmospheric variability in the real climate system. For instance, there are robust relationships between trends in the observational record, in the simulated ensemble means and in measures of the simulated ensemble spread.
- Irrespective of the direction of trends, the correspondence of higher model skill when trends in the ensemble spread are larger suggests that the skill produced by a dynamical modeling system may not be independent of the model's ability to

capture the real atmospheric trends in whatever the model is simulating or forecasting.

- On seasonal time-scales, estimations of the theoretical range of forecasts around the climatological mean, in the context of a single forecasting model system, are a minimum of 34mm and a maximum of 110mm in extreme situations for precipitation over South African; while they are 0.3 ^{o}C and 1 ^{o}C for temperature.
- The co-variability between the indices of large-scale climate variability and the variations in the ensemble spread of atmospheric model simulations over South Africa differs from index-to-index, season-to-season and province-to-province.
- There are no clear large-scale patterns in the correlations between the seasonal-provincial measures of spread and climate indices, whether in space or across seasons.
- ENSO, as described by MEI, is the most influential in the predictability of seasonal climate over South Africa. In the traditional forecasting sense, it is the only climate index that has more than the required statistical provincial-seasonal realizations during rainfall peak period in summer and even the cold winter.

The results presented in chapters eight and nine come from analysis of a single climate modeling system; therefore, the robustness of the results to model selection is unknown. Moreover, this modeling system (HadRM3P) is not particularly modern and certainly does not represent a state-of-the-art model. But this study could not be conducted with a computationally expensive state-of-the-art model, because no computational resources exist, at the moment, for running the large ensembles of simulations required to precisely characterize variations in ensemble spread; therefore, these data sets are currently unique. Whether another model would reveal the same relationship is unknown, consequently the specific values should not be taken too literally. Another concern is that this study only looked for linear relationships between predictors and the variations in predictability. Although significant correlations were found, there was no indication of the mechanism for causation. It may be that climate indices are influencing the atmosphere in a way that affects predictability, or that climate indices are responding to some other driver which is

also affecting the seasonal climate predictability over South Africa; such a driver could be elsewhere within the climate system or could be external in nature, for instance through anthropogenic emissions. Despite the removal of linear trends from the time series of the analysis, nonlinear responses to external drivers may still be present in the data, as suggested by the mostly positive correlations for temperature predictability against SSTs globally. Beyond all these, the mechanisms through which various predictors could affect the spread of simulations over South Africa remain undefined.

Consequently, based on historical data, further understanding of how potential predictability is changing has the prospect to improve the interpretation of current estimates of simulation skill. This study is however indicating that there may be limits to the extent to which year-to-year variations in the predictability of seasonal climate might be understood. The results of the study have applications in improving seasonal forecast and in reducing the negative impact of climate on socio-economic activities of even smaller geographical domain, like South Africa.

10.2 Recommendation for Further Investigation

The results of the thesis can be improved and extended in various ways. First, while the thesis has provided general characteristics of dominant classes of seasonal rainfall and temperature, the intra-seasonal information of each dominant class need further investigation. For example, further study could provide more information on the characteristics of daily or decadal variation of rainfall, rainfall extremes, and dry spells in each dominant rainfall class. It could also provide more information on which of the dominant seasonal temperature class induces heat wave events and on the frequency of the heat wave events. All these information are very important to the socio-economic activities in Africa.

Second, though this study does not evaluate the performance of "worst" ensemble member(s), we however acknowledge that these “worst” ensemble members may also contain some vital elements of the information package. For example, just like the other

("best") ensemble members, the "worst" ensemble member(s) definitely contain information on the boundary and initial conditions, as well as parameterization; therefore, this information can be utilized for the improvement of the climate models.

Third, this study has highlighted some important challenges for the regional climate change projection problem, specifically on the use of the ensemble mean or an arbitrary simulation of climate models. The ensemble mean or a single arbitrary simulation does not possess adequate information on the evaluation of model quality and their utilizations may be misleading. For instance, we found that while the "best performing" ensemble member for Southern Africa is the same for both precipitation and temperature; this however does not hold for West Africa. The "best performing" simulation for precipitation over West Africa is not even notable for temperature over the region. This implies that a good seasonal forecasting system for one region could be bad for a relatively nearby region. Therefore, this study calls for the review of the practice whereby an ensemble mean is based on uniformly-averaging the members rather than the performance of individual ensemble members which may give better prediction.

Fourth, we recall that (in the eighth and ninth chapters) the trends in spread of seasonal simulations over South Africa, given their statistical significance, may be expected to arise from physical responses that are themselves potentially predictable. According to this study, these are drivers and mechanisms that may be remotely forced or locally based. Therefore, possible driving factors may include: trends in sea surface temperature anomaly patterns; changes in atmospheric composition; and, trends in mean surface conditions (which may in turn be driven by the atmospheric composition). Changes in the quality of ocean temperature monitoring could also be involved if they happened to excite mechanisms for increasing simulation spread. The mechanisms involved in translating the driving factors into trends in simulations spread might include: a relationship between the mean climatological state of the atmosphere (and hence its trends) and its variability (e.g. through soil moisture feedbacks); a shift in the frequency of weather patterns; changes in cloud cover that could affect the variability of

temperature by altering the radiative balance of the source of energy. These are some of the issues that have not been explored in this study. In view of this, this study recommends further investigation of the roles of these factors in order to improve seasonal climate predictability.

References

Abiodun BJ, Gutowski WJ, Abatan AA, Prusa JM. 2011. CAM-EULAG: A Non-Hydrostatic Atmospheric Climate Model with Grid Stretching. *Acta Geophysica*, **59 (6)**, 1158 – 1167. DOI: 10.2478/s11600-011-0032-2

Abiodun BJ, Lawal KA, Salami AT, Abatan AA. 2012. Potential Influences of Global Warming on Future Climate and Extreme Events in Nigeria. *Regional Environmental Change*, **13**: 477 – 491. DOI:10.1007/s10113-012-0381-7.

Abraham JP, Baringer M, Bindoff NL, Boyer T, Cheng LJ, Church JA, Conroy JL, Domingues CM, Fasullo JT, Gilson J, Goni G, Good SA, Gorman JM, Gouretski V, Ishii M, Johnson GC, Kizu S, Lyman JM, Macdonald AM, Minkowycz WJ, Moffitt SE, Palmer MD, Piola AR, Reseghetti F, Schuckmann K, Trenberth KE, Velicogna I, Willis JK. 2013. A review of global ocean temperature observations: Implications for ocean heat content estimates and climate change. *Rev. Geophys.*, **51**, 450–483, DOI:10.1002/rog.20022.

Achberger C, Chen D, Alexandersson H. 2006. The surface winds of Sweden during 1999-2000. *Int. J. of Climatol.,* **26**: 159 – 178.

Acheampong PK. 1982. Rainfall anomaly along the coast of Ghana—Its nature and causes. *Geogr. Ann.*, **64A**, 199–211.

AfDB (African Development Bank). 2013. Annual Development Effectiveness Review 2013: Towards sustainable growth for Africa. African Development Bank Group. Tunis. Available via http://www.afdb.org/en/news-and-events/article/africa-is-now-the-fastest-growing-continent-in-the-world-12107/

Afiesimama EA, Pal J, Abiodun BJ, Gutowski WJ, Adedoyin A (2006) Simulation of West African Monsoon using the RegCM3. Part I: Model validation and interannual variability. *Theor Appl Climatol*, **82**: 23–38

Alfani F, Dabalen A, Fisker P, Molini V. 2015. Vulnerability to Malnutrition in the West African Sahel. *Policy Research Working Paper 7171*, World Bank – Poverty Global Practice Group. Available via http://econ.worldbank.org.

Anderson CA, Bushman BJ, Groom RW. 1997. Hot years and serious and deadly assault: Empirical tests of the heat hypothesis. *J Person Soc Psychol,* **73**:1213–1223.

Annamalai H, Xie S-P, McCreary J-P, Murtugudde R. 2005. Impacts of Indian Ocean sea surface temperature on developing El Nino. *J Climatol.*, **18**: 302–319. DOI:10.1175/JCLI-3268.1

Araujo JA, Abiodun BJ, Crespo O. 2014. Impacts of drought on grape yields in Western Cape, South Africa**.** *Theoretical and Applied Climatology***.** DOI:10.1007/s00704-014-1336-3.

Arblaster JM, Alexander LV. 2012. The impact of the El Niño-Southern Oscillation on maximum temperature extremes. *Geophys. Res. Lett.*, **39**, L20702, DOI:10.1029/2012GL053409.

Barnston AG, Ropelewski CF. 1992. Prediction of ENSO episodes using canonical correlation analysis. *J. Clim*., **5**, 1316–1345.

Barnston AG, van den Dool HM, Zebiak SE, Barnett TP, Ji M, Rodenhuis DR, Cane MA, Leetmaa A, Graham NE, Ropelewski CR, Kousky VE, O'Lenic EA, Livezey RE. 1994. Long-lead seasonal forecasts—Where do we stand? *Bull*. *Am*. *Meteorol*. *Soc*., **75**, 2097–2114.

Barreto G, Araujo A. 2001. Time in self-organizing maps: An overview of models. *International Journal of Computer Research*, **10(2)**, 139-179.

Batte L, Deque M. 2010. Seasonal predictions of precipitation over Africa using coupled cean-atmosphere general circulation models: skill of the ENSEMBLES project multimodel ensemble forecasts. *Tellus*, **63A**, 283–299. DOI: 10.1111/j.1600-0870.2010.00493.x

Behera SK, Yamagata T. 2001. Subtropical SST dipole events in the southern Indian Ocean. *Geophysical Research Letters* **28**: 327–330.

Bishop CM. 2006. *Pattern Recognition and Machine Learning*, New York, Springer.

Blench R. 1999. Seasonal climatic forecasting: Who can use it and how should it be disseminated? *Natural Resource perspectives*, **47**, Overseas Development Institute, London

Boer GJ. 2000: A study of atmosphere-ocean predictability on long time scales. *Climate Dynamics*, **15**, 419 – 434.

Boer GJ. 2004. Long time-scale potential predictability in an ensemble of coupled

climate models. *Climate Dynamics,* **23,** 29 – 44. DOI 10.1007/s00382-004-0419-8

Bradley DJ. 1993. Human tropical diseases in a changing environment. *Environmental Change and Human Health.* Ciba Foundation Symposium **175**: 146–162.

Breaker LC. 1989. El NiñO and Related Variability in Sea-Surface Temperature Along the Central California Coast, in Aspects of Climate Variability in the Pacific and the Western Americas (ed D. H. Peterson), American Geophysical Union, Washington, D. C., DOI: 10.1029/GM055p0133

Browne NAK. 2011. Model Evaluation for Seasonal Forecasting over Southern Africa. PhD Thesis submitted to the Faculty of Science, University of Cape Town. 117p.

Browne NAK, Abiodun BJ, Tadross M, Hewitson B. 2009. Simulation of synoptic scale circulation features over southern Africa using GCMs. *ICTP Preprint,* **IC/2009/093.** Available at: http://users.ictp.it/~pub_off/preprints-sources/2009/IC2009093P.pdf

Buckland ST. 1983. Monte-Carlo methods for confidence interval estimation using the bootstrap technique. *Bulletin Applied Statistics* **10,** 194–212.

Buckle C. 1996. *Weather and climate in Africa*. Longman. Malaysia. 312p.

Buhlmann P. 2002. Bootstraps for time series. *Statistical Science,* **vol. 17, no. 1,** 52–72.

Burke MB, Miguel E, Satyanath S, Dykema JA, Lobell DB. 2009. Warming increases the risk of civil war in Africa. *PNAS*, **106(49)**: 20670–20674. Available via www.pnas.org_cgi_doi_10.1073_ pnas.0907998106

Camberlin P, Janicot S, Poccard I. 2001. Seasonality and atmospheric dynamics of the teleconnection between African rainfall and tropical sea-surface temperature: Atlantic vs. ENSO. *Int*. *J*. *Climatol*., **21**: 973–1005. DOI: 10.1002/joc.673

Carleton AM, Travis DJ, Adegoke JO, Arnold DL, Curran S. 2008. Synoptic Circulation and Land Surface Influences on Convection in the Midwest U.S. "Corn Belt" during the Summers of 1999 and 2000. Part II: Role of Vegetation Boundaries. *J. Climate*, **21**, 3617–3641. DOI: http://dx.doi.org/10.1175/2007JCLI1584.1

Cavazos T. 1999. Large-scale circulation anomalies conducive to extreme events and

Simulation of daily rainfall in northeastern Mexico and southeastern Texas. *Journal of Climate*, **12(5)**, 1506–1523.

Cavazos T. 2000. Using self-organizing maps to investigate extreme climate events: An application to wintertime precipitation in the Balkans. *Journal of Climate*, **13(10)**, pp. 1718–1732.

CDC (Centers for Disease Control and Prevention). 2012. Extreme heat: a prevention guide to promote your personal health and safety. Available via www.bt.cdc.gov/disasters/extremeheat/heat _guide.asp.

Chang P, Ji L, Li H. 1997. A decadal climate variation in the Tropical Atlantic Ocean from thermodynamic air-sea interactions. *Nature,* **385**, 516–518.

Chen D, Cane MA, Kaplan A, Zebiak SE, Huang D. 2004. Predictability of El Nino over the past 148 years. *Nature,* **428:** 733–736.

Chen D, Achberger C, Raisenen A, Hellstrom C. 2006. Using statistical downscaling to quantify the GCM-related uncertainty in regional climate change scenarios: A case study of Sweden precipitation. *Advances in Atmospheric Sciences,* **23**: 54 – 60.

Christidis N, Stott PA, Jones GS, Shiogama H, Nozawab T, Luterbacher J. 2012. Human activity and anomalously warm seasons in Europe. *International Journal of Climatology*, **32**: 225–239. DOI: 10.1002/joc.2262

Cocke S, LaRow TE. 2000. Seasonal predictions using a nested regional spectral model embedded in a coupled ocean-atmosphere model. *Mon. Weather Rev.*, **128**, 689–708.

Cocke S, LaRow TE, Shin DW. 2007. Seasonal rainfall predictions over the southeast United States using the Florida State University nested regional spectral model. *J. Geophys. Res.*, **112,** D04106, DOI:10.1029/2006JD007535.

Collins JM. 2011. Temperature variability over Africa. *Journal of Climate*, **24**: 3649–3666, DOI: 10.1175/2011JCLI3753.1.

Collins W, Rasch P, Boville B, Hack J, McCaa J, Williamson D, Kiehl J, Briegleb B, Bitz

C, Lin S-J, Zhang M, Dai Y. 2004. Description of the NCAR Community Atmosphere Model (CAM3.0). Technical Report NCAR/TN-464+STR, National Center for Atmospheric Research, Boulder, Colorado.

Compo GP, Whitaker JS, Sardeshmukh PD, Matsui N, Allan RJ, Yin X, Gleason Jr BE, Vose RS, Rutledge G, Bessemoulin P, Bronnimann S, Brunet M, Crouthamel RI, Grant AN, Groisman PY, Jones PD, Kruk MC, Kruger AC, Marshall GJ, Maugeri M, Mok HY, Nordli O, Ross TF, Trigo RM, Wang XL, Woodruff SD, Worley SJ. 2011. The Twentieth Century Reanalysis Project. *Quarterly Journal of Royal Meteorological Society,* **137**: 1–28. DOI:10.1002/qj.776

Conway G. 2009. The science of climate change in Africa: impacts and adaptation. Discussion paper No 1, Grantham Institute for Climate Change. Available via www.imperial.ac.uk/climatechange/publications.

Cretat J, Pohl B, Richard Y, Drobinski P. 2012a. Uncertainties in simulating regional climate of Southern Africa: sensitivity to physical parameterization using WRF. *Clim. Dyn.*, **38**:613–634

Cretat J, Richard Y, Pohl B, Rouault M, Reason C, Fauchereau N. 2012b. Recurrent daily rainfall patterns over South Africa and associated dynamics during the core of the austral summer. *International Journal of Climatology,* **32**: 261–273. DOI: 10.1002/joc.2266

Demartines P, Blayo F. 1992. Kohonen Self-Organizing Maps: Is the Normalization Necessary? *Complex Systems,* **6**, 105-123.

Deque M, Royer JF. 1992. The skill of extended-range extra-tropical winter dynamical forecasts. *J. Clim*., **5**, 1346–1356.

Diatta S, Fink AH. 2014. Statistical relationship between remote climate indices and West African monsoon variability. *Int. J. Climatol.,* **34**: 3348–3367. DOI: 10.1002/joc.3912

Diedhiou A, Janicot S, Viltard A, de Felice P. 1998. Evidence of two regimes of easterly waves over West Africa and the tropical Atlantic. *Geophys. Res. Lett.* **25**: 2805–2808.

Diedhiou A, Janicot S, Viltard A, de Felice P, Laurent H. 1999. Easterly waves regimes

and associated convection over West Africa and the Tropical Atlantic: Results from the NCEP–NCAR and ECMWF reanalyses. *Clim. Dyn.* **15**: 795–822.

Dike VN, Shimizu MH, Diallo M, Lin Z, Nwofor KO, Chineke TC. 2015. Modelling present and future African climate using CMIP5 scenarios in HadGEM2-ES. *Int. J. Climatol.* **35**: 1784–1799. DOI: 10.1002/joc.4084

Dukic, V, Co-authors. 2012. The role of weather in meningitis outbreaks in Navrango, Ghana: A generalized additive modeling approach. *J. Agric. Biol. Environ. Stat.*, **17**, 442–460, doi:10.1007/s13253-012-0095-9.

Durran DR. 1999. *Numerical Methods for Wave Equations in Geophysical Fluid Dynamics*. Springer-Verlag, Inc.

Eaton BE. 2010. User's Guide to the Community Atmosphere Model CAM-, Technical report, National Center for Atmospheric Research, Boulder, Colorado, 4506. Available online via http://www.cesm.ucar.edu/models/cesm1.0/cam/docs /ug5_0 /ug.pdf

Ehrendorfer M. 1997. Predicting the uncertainty of numerical weather forecasts: A review. *Meteor. Z.,* **6,** 147–183.

Enfield DB, Mestas-Nunez AM, Mayer DA, Cid-Serrano L. 1999. How ubiquitous is the dipole relationship in tropical Atlantic sea surface temperatures? *Journal of Geophysical Research,* **vol. 104, no. C4**, 7841–7848.

Engelbrecht CJ, Engelbrecht FA, Dyson LL. 2013. High-resolution model-projected changes in mid-tropospheric closed-lows and extreme rainfall events over southern Africa. *International Journal of Climatology*, **33**, 173–187. DOI:10.1002/joc.3240

Exenberger A, Pondorfer A. 2011. Rain, temperature and agri-cultural production: The impact of climate change in Sub-Sahara Africa, 1961-2009. *University of Innsbruck - Working Papers in Economics and Statistics*, **26**. Available online via http://eeecon.uibk.ac.at/wopec/

Fauchereau N, Trzaska S, Rouault M, Richard Y. 2003. Rainfall variability and changes in southern Africa during the 20th century in the global warming context. *Natural Hazards*, **29(2)**: 139-154.

Fauchereau N, Pohl B, Reason CJC, Rouault M, Richard Y. 2009. Recurrent daily OLR patterns in the Southern Africa/Southwest Indian Ocean Region, implications for South African rainfall and teleconnections. *Climate Dynamics* **32**: 575–591.

Few R. 2003. Flooding, vulnerability and coping strategies: local responses to a global threat. *Progr. Dev. Studies*, **3(1)**: 43–58

Few R. 2007. Health and climatic hazards: framing social research vulnerability, response and adaptation. *Glob. Environ. Change*, **17**: 281–295

Fink AH, Reiner A. 2003. Spatio-temporal variability of the relation between African easterly waves and West African squall lines in 1998 and 1999. *J. Geophys. Res.* **108**.

Flato G, Marotzke J, Abiodun B, Braconnot P, Chou SC, Collins W, Cox P, Driouech F, Emori S, Eyring V, Forest C, Gleckler P, Guilyardi E, Jakob C, Kattsov V, Reason C, Rummukainen M. 2013. Evaluation of Climate Models. In: Climate Change 2013: The Physical Science Basis. Contribution of Working Group I to the Fifth Assessment Report of the Intergovernmental Panel on Climate Change [Stocker, T.F., D. Qin, G.-K. Plattner, M. Tignor, S.K. Allen, J. Boschung, A. Nauels, Y. Xia, V. Bex and P.M. Midgley (eds.)]. Cambridge University Press, Cambridge, United Kingdom and New York, NY, USA.

Flocas H, Tolika K, Anagnostopoulou C, Patrikas I, Maheras P, Vafiadis M. 2004. Evaluation of maximum and minimum temperature NCEP-NCAR reanalysis data over the Greek area. *Theoretical and Applied Climatology,* **80**: 49–65.

Flynn A, McGreevy C, Mulkerrin EC. 2005. Why do older patients die in a heatwave? *Q. J. M.*, **98(3)**: 227–229. DOI:10.1093/qjmed/hci025

Folland CK, Owen JA, Ward MN, Colman AW. 1991. Prediction of seasonal rainfall in the Sahel region using empirical and dynamical methods. *Journal of Forecasting*, **10**: 21–56.

Folland CK, Palmer TN, Parker DE. 1986. Sahel rainfall and worldwide sea temperatures (1901–1985). *Nature,* **320**: 602–607.

Fontaine B, Janicot S. 1992. Wind-field coherence and its variations over West Africa. *Journal of Climate* **5**: 512–524.

Fontaine B, Janicot S. Moron V. 1995. Rainfall Anomaly Patterns and Wind Field Signals over West Africa in August (1958-1989). *Journal of Climate,* **8**: 1503–1510.

Fontaine B, Janicot S. 1996. Sea surface temperature fields associated with West African rainfall anomaly types. *Journal of Climate* **9**: 2935–2940.

Fontaine B, Janicot S, Monerie PA. 2013. Recent changes in air temperature, heat waves occurrences, and atmospheric circulation in Northern Africa. *J. Geophys. Res. Atmos.*, **118**, 8536–8552. DOI:10.1002/jgrd.50667

Ford J, Katondo KM. 1977. *The distribution of Tsetse Flies in Africa*. London: Hammond and Kell.

Fraley C, Raftery AE. 1998. How Many Clusters? Which Clustering Method? Answers Via Model-Based Cluster Analysis, *The Computer Journal*, **41(8)**: 578-588.

Fraser EDG, Simelton E, Termansen M, Gosling SN, South A. 2013. Vulnerability hotspots: integrating socio-economic and hydrological models to identify where cereal production may decline due to climate change induced drought. *Agricultural and Forest Meteorology*, 170: 195-205.

Frei A, Robinson DA. 1998. Evaluation of snow extent and its variability in the Atmospheric Model Intercomparison Project. *Journal of Geophysical Research,* **Vol. 13, No. D8,** 8859 – 8871. Paper number 98JD00109.

Friederichs P, Paeth H. 2006. Seasonal prediction of African precipitation with ECHAM4-T42 ensemble simulations using a multivariate MOS re-calibration scheme. *Climate Dynamics,* **27,** 761–786. DOI 10.1007/s00382-006-0154-4.

Fritzke B. 1994. Growing cell structures - a self-organizing network for unsupervised and supervised learning. *Neural Networks*, **7(9)**, 1441–1460.

Gadgil S, Joseph PV, Joshi NV. 1984. Ocean-atmosphere coupling over the monsoon region. *Nature,* **312**, 141–143.

Gates WL. 1992. AMIP: The Atmospheric Model Intercomparison Project. *Bulletin American Meteorological Society*, **73**, 1962-1970.

Gbobaniyi E, Sarr A, Sylla MB, Diallo I, Lennard C, Dosio A, Dhi´ediou A, Kamga A,

Browne-Klutse NA, Hewitson B, Nikulina G, Lamptey B. 2013. Climatology, annual cycle and interannual variability of precipitation and temperature in CORDEX simulations over West Africa. *International Journal of Climatology*. DOI: 10.1002/joc.3834

Gray RM, Neuhoff DL. 1998. "Quantization," *IEEE Transactions on Information Theory*, **Vol. 44**, pp. 2325-2384. (Commemorative Issue, 1948-1998)

Grimit EP, Mass CF. 2007. Measuring the ensemble spread-error relationship with a probabilistic approach: Stochastic ensemble results. *Monthly Weather Review,* **135,** 203–221. DOI: 10.1175/MWR3262.1

Grimm AM, Reason CJC. 2011. Does the South American Monsoon influence African rainfall? *Journal of Climate*, **24(4)**, 1226-1238. DOI: 10.1175/2010JCLI3722.1

Grist JP, Nicholson SE. 2001. A study of the dynamic Factors influencing the rainfall variability in the West African Sahel. *Journal of Climate* **14**: 1337–1359.

Guichard F, Coauthors. 2004. Modelling the diurnal cycle of deep precipitating convection over land with cloud-resolving models and single-column models. *Quart. J. Roy. Meteor. Soc.,* **130,** 3139–3172.

Hack J. 1994. Parameterization of moist convection in the National Center for Atmospheric Research community climate model (CCM2). *J. Geophys. Res.*, **99(D3)**: 5551–5568.

Hagos SM, Cook KH. 2008. Ocean warming and late-twentieth century Sahel drought and recovery. *J. Clim.,* **21**: 3797–3814, DOI:10.1175/2008JCLI2055.1.

Halpert MS, Ropelewski CF. 1992. Surface temperature patterns associated with the Southern Oscillation. *J. Clim*., **5**, 577 – 593.

Haltiner GJ, Williams RT. 1980. *Numerical Prediction and Dynamic Meteorology*, 2nd edition. Wiley and Sons, Inc.

Hamill TM, Colucci SJ. 1997. Verification of Eta–RSM short-range ensemble forecasts. *Mon. Wea. Rev.,* **125,** 1312–1327.

Hammer GL, Hansen JW, Phillips JG, Mjelde JW, Hill H, Love A, Potgieter A. 2001. Advances in application of climate prediction in agriculture. *Agric. Syst*., **70**, 515–553.

Hampshire K, Randall S. 1999. Seasonal labour migration strategies in the Sahel: coping with poverty or optimizing security? *Int. J. Popul. Geogr.*, **5**: 367–385

Hansen JW, Mason SJ, Sun L, Tall A. 2011. Review of Seasonal Climate Forecasting for Agriculture in Sub-Saharan Africa. *Expl Agric*., **volume 47 (2)**, pp. 205–240 DOI:10.1017/S0014479710000876

Hansingo K, Reason CJC. 2008. Modeling the atmospheric response to SST dipole patterns in the South Indian Ocean with a regional climate model. *Meteorology and Atmospheric Physics*, **100**, 37–52. DOI:10.1007/s00703-008-0294-7

Hardy A. 1996. On the number of clusters. *Comput. Statist. Data Analysis*, **23**, 83–96.

Harris I, Jones PD, Osborn TJ, Lister DH. 2013. Updated high-resolution grids of monthly climatic observations. In press, *International Journal of Climatology.* DOI: 10.1002joc.3711

Harrison DE, Bond N, Goddard L, Martinez R, Yamagata T. 2014. White Paper #2 – Some societal impacts of ENSO. In Ocean Observation Panel for Climate Change. Report of the Tropical Pacific Observing System 2020 Workshop (TPOS 2020). VOLUME II – White Papers. 27-30th January 2014, Scripps Institution of Oceanography, San Diego, United States

Harrison MSJ. 2005. The development of seasonal and inter-annual climate forecasting. *Climatic Change* 70: 201–220.

Harrison M. 1984. The annual rainfall cycle over the central interior of South Africa. *South Africa Geogr. Journal,* **66**:47–64.

Hegerl GC, Crowley TJ, Allen M, Hyde WT, Pollack HN, Smerdon J, Zorita E. 2006. Detection of Human Influence on a New, Validated 1500-Year Temperature Reconstruction. *Journal of Climate*, **20**: 650 – 666. DOI: 10.1175/JCLI4011.1

Hegerl GC, Zwiers FW, Braconnot P, Gillett NP, Luo Y, Marengo Orsini JA, Nicholls N, Penner JE, Stott PA, et alii. 2007. Understanding and attributing climate change. In: Solomon S, Qin D, Manning M, Chen Z, Marquis M, Averyt KB, Tignor M, Miller HL (eds) Climate Change 2007: The Physical Science Basis. Contribution of Working Group I to the Fourth Assessment Report of the Intergovernmental

Panel on Climate Change, Cambridge University Press, Cambridge, U.K., pp 663–745

Held IM, Delworth TL, Lu J, Findell KL, Knuston TR. 2005. Simulations of Sahel drought in the 20th and 21st centuries. *Proc. Natl. Acad. Sci. U.S.A.* **102**: 17891–17896.

Henderson-Sellers A, Hughes NA. 1982. Albedo and climate theory. *Prog. Phys. Geog.*, **6**, 1-44.

Henderson-Sellers A, Wilson MF. 1983. Surface albedo data for climatic modeling. *Rev. Geophys.,* **21*(8)***, 1743–1778*,* DOI:10.1029/RG021i008p01743.

Heskes T. 2001. Self-organizing maps, vector quantization, and mixture modeling. *IEEE Trans. Neural Networks*, **12(6)**, 1299–1305.

Hewitson BC, Crane RG. 2002. Self-organizing maps: applications to synoptic climatology. *Climate Research*, **22**: 13–26.

Hewitson BC, Crane RG. 2006. Consensus between GCM climate change projections with empirical downscaling. *International Journal of Climate* **26**: 1315–1337.

Hoell A, Funk C, Magadzire T, Zinke J, Husak G. 2014. El Niño–Southern Oscillation diversity and Southern Africa teleconnections during Austral Summer. *Climate Dynamics*. DOI 10.1007/s00382-014-2414-z

Hoerling M, Hurrell J, Eischeid J, Phillips A. 2006. Detection and attribution of twentieth-century northern and southern African rainfall change. *Journal of Climate*, **19(16)**, 3989–4008. http://dx.doi.org/10.1175/JCLI3842.1

Houghton JT. 1991. *The physics of atmosphere.* 2nd Edition. Cambridge Univ. Press. London.

Houghton J. 2004. *Global warming: the complete briefing*. 3rd edition, Cambridge University Press. Cambridge

Hourdin F, Musat I, Guichard F, Ruti PM, Favot F, Filiberti MA, Pham M, Grandpeix JY, Polcher J, Marquet P, Boone A, Lafore JP, Redelsperger JL, Dell'aquila A, Doval TL, Traore AK, Gall´ee H. 2010. AMMA-model intercomparison project. *Bull. Am. Meteorol. Soc.* **91**(1): 95–104.

Houze RA. 2004. Mesoscale convective systems. *Rev. Geophys*., **42**, RG4003,

DOI:10.1029/2004RG000150.

Hudson D, Jones R. 2002. Simulations of present-day and future climate over southern Africa using HadAM3H. *Hadley Centre Technical Note*, 38.

Hulme M, Osborn TJ, Johns TC. 1998. Precipitation sensitivity to global warming: Comparison of observations with HadCM2 simulations. *Geophysical Research Letters*, **25**, 3379– 3382.

Hulme M, Doherty R, Ngara T, New M, Lister D. 2001. African climate change: 1900–2100. *Climate Research* 17, 145–68.

Hurrell JW. 1995. Decadal trends in the North Atlantic Oscillation and relationships to regional temperature and precipitation. *Science,* **Vol. 269 no. 5224**, pp. 676-679. DOI: 10.1126/science.269.5224.676

Hurrell JW. 2001. The North Atlantic Oscillation, *Science,* **291**, 603–605.

IPCC (Intergovernmental Panel on Climate Change). 2007. Climate change 2007: the physical science basis. Contribution of Working Group I to the Fourth Assessment Report of the Intergovernmental Panel on Climate Change, Solomon S, Qin D, Manning M, Chen Z, Marquis M, Averyt KB, Tignor M, Miller HL (eds). CAM-5.1bridge University Press: Cambridge, UK/New York, NY, 996 pp.

IPCC (Intergovernmental Panel on Climate Change). 2013: Summary for Policymakers. In: Climate Change 2013: The Physical Science Basis. Contribution of Working Group I to the Fifth Assessment Report of the Intergovernmental Panel on Climate Change [Stocker TF, Qin D, Plattner G-K, Tignor M, Allen SK, Boschung J, Nauels A, Xia Y, Bex V, Midgley PM (eds.)]. Cambridge University Press, Cambridge, United Kingdom and New York, NY, USA.

Izumo T, Vialard J, Lengaigne M, de Boyer Montegut C, Behera SK, Luo J-J, Cravatte S, Masson S, Yamagata T. 2010. Influence of the state of the Indian Ocean dipole on the following year's El Nino. *Nature Geoscience,* **3:** 168–172, doi:10.1038/NGE0760.

Janicot S. 1992. Spatio-temporal variability of West African rainfall. Part 2: Associated surface and air mass characteristics. *Journal of Climate,* **5**: 499–511.

Jankov I, Gallus Jr. WA, Segal M, Shaw B, Koch SE. 2005. The impact of different

WRF model physical parameterizations and their interactions on warm season MCS rainfall. *Wea. Forecasting,* **20,** 1048–1060.

Jenkins GS, Kamga A, Garba A, Diedhiou A, Morris V, Joseph E. 2002. Investigating the West African climate system using Global/Regional climate models. *Bull. Amer. Mete. Soc.*, **83**: 583–595.

Johns TC, Carnell RE, Crossley JF, Gregory JM, Mitchell JFB, Senior CA, Tett SFB, Wood RA. 2002. Anthropogenic climate change for 1860 to 2100 simulated with the HadCM3 model under updated emissions scenarios. *Climate Dynamics,* **20,** 583–612.

Johnson NC. 2012. How many ENSO flavors can we distinguish? *Journal of Climate*, **26 (13)**: 4816–4827. doi:10.1175/JCLI-D-12-00649.1

Johnson RW. 2001. An introduction to the bootstrap. *Teaching Statictics* **vol. 23, issue 2,** 49–54. DOI:10.1111/1467-9639.00050.

Johnston PA, Archer ERM, Vogel CH, Bezuidenhout CN, Tennant WJ, Kuschke R. 2004. Review of seasonal forecasting in South Africa: producer to end-user. *Climate Research,* **28,** 67–82.

Jones GS, Stott PA, Christidis N. 2008. Human contribution to rapidly increasing frequency of very warm Northern Hemisphere summers. *Journal of Geophysical Reseach,* **113**: DOI:10.1029/2007JD008914.

Jones, PD., Jónsson, T. and Wheeler, D., 1997: Extension to the North Atlantic Oscillation using early instrumental pressure observations from Gibraltar and South-West Iceland. *Int. J. Climatol.* **17**, 1433-1450.

Jones RG, Noguer M, Hassell DC, Hudson D, Willson SS, Genkins GJ, Mitchell JFB. 2004. Generating high resolution climate change scenarios using PRECIS. Technical report, Met Office Hadley Centre, Exeter, U. K., 40pp.

Judd K, Smith LA, Weisheimer A. 2007. How good is an ensemble at capturing truth? Using bounding boxes for forecast evaluation. *Q. J. R. Meteorol. Soc.* **133**, 1309–1325. DOI: 10.1002/qj.111

Jury M, Pathack B. 1993. Composite climatic patterns associated with extreme modes of

summer rainfall over southern Africa: 1975 – 1984. *Theo. & Appl. Climatol.*, **47(3)**, 137 – 145.

Jury MR, Levey KM. 1993. The climatology and characteristics of drought in the Eastern Cape of South Africa. *International Journal of Climatology*, **13**, 629–641.

Kalnay E and twenty-one others. 1996. The NCEP/NCAR 40-year reanalysis project. *Bull. Amer. Meteor. Soc*., **77**, 437-471.

Kaplan A, Cane M, Kushnir Y, Clement A, Blumenthal M, Rajagopalan B. 1998. Analyses of global sea surface temperature 1856-1991, *Journal of Geophysical Research*, **103, 18,** 567–1589.

Keating BA, Carberry PS, Hammer GL, Probert ME, Robertson MJ, Holzworth D, Huth NI, Hargreaves JNG, Meinke H, Hochman Z, Mclean G, Verburg K, Snow V, Dimes JP, Silburn M, Wang E, Brown S, Bristow KL, Asseng S, Chapman S, Mccown RL, Freebairn DM, Smith CJ. 2003. An overview of APSIM, a model designed for farming systems simulation. *Eur. J. Agron*., **18**, 267–288.

Keenlyside NS, Latif M, Jungclaus J, Kornblueh L and Roeckner E. 2008. Advancing decadal-scale climate prediction in the North Atlantic sector. *Nature*, **453**, 84–88.

Kelly PM, Jones PD. 1996. The spatial response of the climate system to explosive volcanic eruptions. *Int. J. Climatol.*, **16**, 537–550.

Klutse NAB, Aboagye-Antwi F, Owusu K, Ntiamoa-Baidu Y. 2014. Assessment of Patterns of Climate Variables and Malaria Cases in Two Ecological Zones of Ghana. *Open Journal of Ecology*, **4**, 764-775. Available via http://dx.doi.org/10.4236/oje.2014.412065

Klutse NAB, Abiodun BJ, Hewitson BC, Gutowski WJ, Tadross MA. 2015. Evaluation of two GCMs in simulating rainfall inter-annual variability over Southern Africa. *Theor. Appl. Climatol*. DOI 10.1007/s00704-014-1356-z

Knippertz P, Fink AH, Schuster R, Trentmann J, Schrage JM, Yorke C. 2011. Ultra-low clouds over the southern West African monsoon region. *Geophys. Res. Lett.*, **38**, L21808, doi:10.1029/2011GL049278.

Kohonen T. 1990. The Self-Organizing Map. *Proceeding of the IEEE*, **78(9)**, 1464-1480.

Kohonen T, Hynninen J, Kangas J, Laaksonen J. 1995. SOM_PAK, The self-organizing map program package version 3.1. Laboratory of Computer and Information Science, Helsinki University of Technology, Finland, 27 pp

Kovats RS, Jendritzky G. 2006. Heat-waves and human health. *Climate Change and Adaptation Strategies for Human Health.* Menne B, Ebi KL, (eds). Springer: Darmstadt, Germany, pp. 63–90.

Kruger AC, Shongwe S. 2004. Temperature trends in South Africa: 1960–2003. *International Journal of Climatology,* **24,** 1929–1945.

Kruger AC. 2006. Observed trends in daily precipitation indices in South Africa: 1910–2004. *International Journal of Climatology,* **26,** 2275–2285.

Kucharik CJ, Serbin SP. 2008. Impacts of recent climate change on Wisconsin corn and soybean yield trends. *Environ. Res. Lett*., (July-September 2008), **3**.

Kumar A, Schubert SD, Suarez MS. 2003. Variability and predictability of 200mb seasonal mean heights during summer and winter. *J. Geophys Res.*, **108**.

Kysely J. 2007. Implications of enhanced persistence of atmospheric circulation for the occurrence and severity of temperature extremes. *Int. J. Climatol.* **27**: 689–695.

Laing AG, Fritsch JM. 1993. Mesoscale convective complexes in Africa. *Mon. Wea. Rev.*, **121**, 2254–2263. DOI:10.1175/1520-0493(1993)121,2254:MCCIA.2.0.CO;2

Laing AG, Fritsch JM. 2000. The large-scale environments of the global populations of mesoscale convective complexes. *Mon. Wea. Rev*., **128**, 2756–2776, DOI:10.1175/1520-0493(2000)128,2756:TLSEOT.2.0.CO;2.

Laing AG, Carbone R, Levizzani V, Tuttle J. 2008. The propagation and diurnal cycles of deep convection in northern tropical Africa. *Quart. J. Roy. Meteor. Soc.*, **134**, 93–109, DOI:10.1002/qj.194.

Landman WA, Beraki A. 2010. Multi – model forecast skill for mid-summer rainfall over southern Africa. *International Journal of Climatology,* **32 (Issue 2),** 303-314. DOI: 10.1002/joc.2273.

Landman WA, Botes S, Goddard L, Shongwe M. 2005. Assessing the predictability of

extreme rainfall over southern Africa. *Geophysical Research Letters,* **32,** L23818. DOI:10.1029/2005GL023965.

Landman WA, Goddard L. 2002. Statistical recalibration of GCM forecasts over southern African using model output statistics. *Journal of Climate,* **15,** 2038–3504.

Landman WA, Goddard L. 2005. Predicting southern African summer rainfall using a combination of MOS and perfect prognosis. *Geophysical Research Letters,* **32,** L15809. DOI:10.1029/2005GL022910.

Landman WA, Kgatuke MM, Mbedzi M, Beraki A, Bartman A, du Piesanie A. 2009. Performance comparison of some dynamical and empirical downscaling methods for South Africa from a seasonal climate modelling perspective. *International Journal of Climatology*, **29,** 1535–1549. DOI:10.1002/joc.1766

Latif M, Grotzner A. 2000. On the equatorial Atlantic oscillation and its response to ENSO. *Clim Dyn.*, **16**: 213-218.

Lavaysse C, Flamant C, Janicot S, Parker DJ, Lafore J-P, Sultan B. 2009. Seasonal evolution of the West African heat low: A climatological perspective. *Clim. Dyn.* **33**: DOI: 10.1007/s00382-009-0553-4.

Lavaysse C, Flamant C, Janicot S, Knippertz P. 2010. Links between African easterly waves, midlatitude circulation and intraseasonal pulsations of the West African heat low. *Q. J. R. Meteorol. Soc.,* **136(s1)**: 141–158. DOI: 10.1002/qj.555

Lawal KA, Stone DA, Aina T, Rye C, Abiodun BJ. 2014. Trends in the potential spread of seasonal climate simulations over South Africa. *International Journal of Climatology,* **35(9)**, 2193 – 2209. DOI:10.1002/joc.4234

Lazenby MJ, Landman WA, Garland RM, DeWitt DG. 2014. Seasonal temperature prediction skill over Southern Africa and human health. *Meteorological Applications*. DOI: 10.1002/met.1449

Le Barbe L, Lebel T, Tapsoba D. 2002. Rainfall variability in West Africa during the years 1950–90. *J. Climate,* **15(2)**: 187–202. DOI: 10.1175/1520-0442(2002)015<0187:RVIWAD>2.0.CO;2.

Lebel T, Delclaux F, Le Barbe L, Polcher J. 2000. From GCM scales to hydrological

scales: Rainfall variability in West Africa. *Stoch. Environ. Res. Risk Assess.,* **14,** 275–295.

Li J, Ding R. 2011. Temporal–Spatial Distribution Of Atmospheric Predictability Limit By Local Dynamical Analogs. *Monthly Weather Review*, **139,** 3265 – 3283. DOI: 10.1175/MWR-D-10-05020.1

Lim Y-H, Park M-S, Kim Y, Kim H, Hong Y-C. 2015. Effects of cold and hot temperature on dehydration: a mechanism of cardiovascular burden. *Int. J. Biometeorol*., **59**: 1035–1043. DOI 10.1007/s00484-014-0917-2

Lin S, Rood R. 1996. Multidimensional flux-form semi-Lagrangian transport schemes. *Mon. Weather Rev.*, **124(9)**: 2046–2070.

Lindesay JA. 1988. South African rainfall, the Southern Oscillation and a Southern Hemisphere semi-annual cycle. *J. Climatol.,* **8**, 17–30.

Lindesay JA, Jury MR. 1991. Atmospheric circulation controls and characteristics of a flood event in central South Africa. *International Journal of Climatology*, **11**: 609–627. DOI: 10.1002/joc.3370110604

Lindesay JA, Vogel CH. 1990. Historical evidence for Southern Oscillation–southern African rainfall relationships. *International Journal of Climatology,* **10,** 679–689.

Lindesay J. 1998. *Present Climates of Southern Africa*. In: Climates of the Southern Continents. Past, present and future. [Hobbs JE, Lindesay JA, Bridgman HA (eds)], John Wiley & Sons, Chichester, 297 pp

Liniger MA, Mathis H, Appenzeller C, Doblas-Reyes FJ. 2007. Realistic greenhouse gas forcing and seasonal forecasts. *Geophysical Research Letters,* **34,** L04705. DOI:10.1029/2006GL028335

Losada T, Rodriguez-Fonseca B, Janicot S, Gervois S, Chauvin F, Ruti P. 2010. A multimodel approach to the Atlantic equatorial mode. Impact on the West African monsoon. *Clim Dyn.*, **35**: 29-43.

Luo J, Behera SK, Masumoto Y and Yamagata T. 2011. Impact of global ocean surface warming on seasonal-to-interannual climate prediction. *J. Climate*, **24,** 1626–1646.

Luo J, Masson S, Behera S, Shingu S and Yamagata T. 2005. Seasonal climate

predictability in a coupled OAGCM using a different approach for ensemble forecasts. *J. Climate*, **18**, 4474–4497.

Luo J, Masson S, Behera S and Yamagata T. 2007. Experimental forecasts of the Indian Ocean dipole using a coupled OAGCM. *J. Climate*, **20**, 2178–2190.

Luo J. 2008. Extended ENSO predictions using a fully coupled ocean-atmosphere model. *J. Climate*, **21**, 84– 93.

Lutjeharms JRE. 2006. *The Agulhas Current.* Springer Verlag, Germany, 329.

Lutz K, Jacobeit J, Rathmann J. 2015. Atlantic warm and cold water events and impact on African west coast precipitation. *Int. J. Climatol.,* **35**: 128–141. DOI: 10.1002/joc.3969

Lyon B, Mason SJ. 2007. The 1997–1998 summer rainfall season in southern Africa. Part I: Observations. *Journal of Climate*, **20**:5134–5148.

Lyon B, Mason SJ. 2009. The 1997–1998 summer rainfall season in southern Africa. Part II: Model simulations and coupled model forecasts. *Journal of Climate*, **22**:3802–3818.

Lyon B. 2009. Southern Africa Summer Drought and Heat Waves: Observations and Coupled Model Behavior. *Journal of Climate*, **22**: 6033 – 6046. DOI: 10.1175/2009JCLI3101.1

MacKellar NC, Hewitson BC, Tadross MA. 2006. Namaqualand's climate: Recent historical and future scenarios. *Journal of Arid Environment,* **70,** 604–614. DOI:10.1016/j.aridenv.2006.03.024.

MacKellar N, New M, Jack C. 2014. Observed and modelled trends in rainfall and temperature for South Africa: 1960–2010. *South African Journal of Science*, **110(7/8)**. http://dx.doi.org/10.1590/sajs.2014/20130353

Makarau A, Jury MR. 1997. Predictability of Zimbabwe summer rainfall. *International Journal of Climatology*, **17**, 1421–1432.

Manhique AJ, Reason CJC, Rydberg L, Fauchereau N. 2009. ENSO and Indian Ocean sea surface temperatures and their relationships with tropical temperate troughs over Mozambique and the Southwest Indian Ocean. *International Journal of Climatology*, **31**. DOI: 10.1002/joc.2050

Martin ER, Thorncroft CD. 2014. The impact of the AMO on the West African monsoon annual cycle. *Q. J. R. Meteorol. Soc.,* **140**: 31–46.

Mason SJ, Joubert AM, Cosijn C, Crimp SJ. 1996. Review of seasonal forecasting techniques and their applicability to Southern Africa. *Water SA*, **22**(3), 203–209.

Mason S, Jury M. 1997. Climatic variability and change over southern Africa: a reflection on underlying processes. *Progress in Physical Geography*, **21(1):**23. ISSN 0309-1333

Mason SJ. 2004. On Using ‘‘Climatology’’ as a Reference Strategy in the Brier and Ranked Probability Skill Scores. *Monthly Weather Review*, **132**, 1891-1895.

Mason SJ, Goddard L. 2001. Probabilistic precipitation anomalies associated with ENSO. *Bull. Amer. Meteor. Soc.,* **82,** 619–638.

Mason SJ. 2008. ‘Flowering walnuts in the wood’ and other bases for seasonal climate forecasting. In *Seasonal Forecasts, Climatic Change and Human Health*, 13–29 (Eds M. C. Thomson, R. Garcia-Herrera and M. Beniston). Dordrecht: Springer.

Mathon V, Laurent H, Lebel T. 2002. Mesoscale convective system rainfall in the Sahel. *J. Appl. Meteorol.* **41**: 1081–1092.

Matthew OJ, Abiodun BJ, Salami AT. 2014. Modelling the impacts of climate variability on crop yields in Nigeria: performance evaluation of RegCM3-GLAM system. *Meteorol. Appl.* DOI: 10.1002/met.1443

McGuffie K, Henderson-Sellers A. 1997. *A Climate Modelling Primer*. John Wiley & Sons. 253pp.

Meehl GA, Tebaldi C. 2004. More intense, more frequent, and longer lasting heat waves in the 21st century. *Science,* **305**: 994–997.

Mera R, Laing AG, Semazzi F. 2014. Moisture Variability and Multiscale Interactions during Spring in West Africa. *Mon. Wea. Rev.*, **142**, 3178–3198. DOI: http://dx.doi.org/10.1175/MWR-D-13-00175.1

Mijindadi NB, Adegbehin JO. 1991. Drought, desertification and food production in Nigeria. *Savanna,* **12**: 25–40.

Misra J. 1991. Phase synchronization. *Inf Process Lett*., **38(2)**: 101–105.

Mitchell TD, Jones PD. 2005. An improved method of constructing a database of

monthly climate observations and associated high resolution grids. *International Journal of Climatology,* **25:** 693–712. DOI:10.1002/joc.1181.

Mohino E, Janicot S, Bader J. 2011. Sahel rainfall and decadal to multi-decadal sea surface temperature variability. *Clim. Dyn.*, DOI:10.1007/s00382-010-0867-2.

Mohr KI, Famiglietti JS, Zipser EJ. 1999. The contribution to tropical rainfall with respect to convective system type, size, and intensity estimated from the 85-GHz ice scattering signature. *J. Appl. Meteor*., **38**, 596–606, DOI:10.1175/1520-0450(1999)038,0596:TCTTRW.2.0.CO;2.

Molesworth AM. 2003. Environmental risk and meningitis epidemics in Africa. *Research Emerging Infectious Diseases*, **9**, 1287-1293.

Murphy AH, Daan H. 1984. 'Impacts of Feedback and Experience on the Quality of Subjective Probability Forecasts: Comparison of Results from the First and Second Years of the Zierikzee Experiment', *Monthly Weather Rev.* **112,** 413-423.

Murphy AH. 1988. Skill score on the mean square error and their relationship to the correlation coefficient. *Monthly Weather Review,* **116,** 2417–2424.

Murphy JM. 1988. The impact of ensemble forecasts on predictability. *Quart. J. Roy. Meteor. Soc.,* **114,** 463–493.

Neale RB. 23 Co-authors. 2010. Description of the NCAR Community Atmosphere Model (CAM 5.0). NCAR Technical Note, June 2010, NCAR/TN-486+STR. Available online via http://www.cesm.ucar.edu/models/cesm1.1/cam/docs /description/cam5_desc.pdf

New M, Hulme M, Jones PD. 2000. Representing twentieth century space-time climate variability. Part 2: development of 1901-96 monthly grids of terrestrial surface climate. *Journal of Climate*, **13**, 2217–2238. DOI:10.1175/1520-0442(2000)013<2217:RTCSTC> 2.0.CO;2

Newton BW, Prowse TD, Bonsal BR. 2012. The Influence of Teleconnections on Synoptic-Scale Circulation Patterns Affecting Western Canadian Water Resources. Science and Technology Infusion Climate Bulletin, NOAA's National Weather Service, *37th NOAA Annual Climate Diagnostics and Prediction Workshop Fort Collins, CO, 22-25 October 2012*

Nicholson SE. 1986. The spatial coherence of African rainfall anomalies: Inter-hemispheric tele-connections. *J. Clim. Appl. Meteorol.* **25**: 1365–1381.

Nicholson SE. 1993. An overview of African rainfall fluctuations of the last decade. *Journal of Climate*, **6**, 1463–1466.

Nicholson SE, Kim J. 1997. The relationship of the El Nino-Southern Oscillation to African rainfall. *Int. J. Climatol*., **17(2),** 117–135. DOI:10.1002/(SICI)1097-0088(199702)17:2 <117:AID-JOC84>3.0.CO;2-O

Nicholson SE. 2001. Climatic and environmental change in Africa during the last two centuries. *Clim. Res*., **17(2)**, 123–144. DOI:10.3354/cr017123.

Nicholson SE, Grist JP. 2003. The seasonal evolution of the atmospheric circulation over West Africa and equatorial Africa. *J. Climate*, **16**, 1013–1030.

Nicholson SE. 2005. On the Question of the "Recovery" of the Ravis in the West African Sahel. *Journal of Arid Environments,* **63**: 615–641.

Nicholson SE. 2009. On the factors modulating the intensity of the tropical rain belt over West Africa. *International Journal of Climatology,* **29**: 673–689. DOI: 10.1002/joc.1702

Nicholson SE, Webster PJ. 2007. A physical basis for the interannual variability of rainfall in the Sahel. *Q. J. R. Meteorol. Soc.* **133**: 2065–2084. DOI: 10.1002/qj.104

Nnamchi HC, Li J, Kang I-S, Kucharski F. 2013. Simulated impacts of the South Atlantic Ocean Dipole on summer precipitation at the Guinea Coast. *Clim. Dyn.* **41**: 677–694.

Null J. 2013. El Nino and La Nina years and intensities based on Oceanic Nino Index (ONI). Available at http://ggweather.com/enso/oni.htm. Date last updated June 10, 2014. Date last visited July 5, 2014.

Odada E, Olago D. 2005. Holcene climatic, hydrological and environmental oscillations in the tropics with special reference to Africa. *Climate Change and Africa*, P. S. Low, Ed., Cambridge University Press, 3–23.

Odekunle TO, Eludoyin AO. 2008. Sea surface temperature patterns in the Gulf of

Guinea: their implications for the spatio-temporal variability of precipitation in West Africa. *Int. J. Climatol.,* **28**: 1507–1517. DOI: 10.1002/joc.1656

Oguntunde PG, Abiodun BJ, Gunnar L. 2012. Spatial and temporal temperature trends in Nigeria, 1901–2000. *Meteorology and Atmospheric Physics*, **118**: 95–105.

Ohunakin OS, Adaramola MS, Oyewola OM, Matthew OJ, Fagbenle RO. 2015. The effect of climate change on solar radiation in Nigeria. *Solar Energy*, **116**, 272–286. http://dx.doi.org/10.1016/j.solener.2015.03.027

Omotosho JB. 1985. The separate contributions of squall lines, thunderstorms and the monsoon to the total rainfall in Nigeria. *J. Climatol.,* **5**: 543–552. DOI:10.1002/joc.3370050507.

Omotosho JB. 2007. Pre-rainy season moisture build-up and storm precipitation delivery in the West Africa Sahel. *International Journal of Climatology*, **28**: 937-946. DOI. 10.1002/joc.1548.

Omotosho JB, Abiodun BJ. 2007. A numerical study of moisture build-up and rainfall over West Africa. *Meteorological Applications*, **14**: 209–225. DOI: 10.1002/met.11

O'Reilly CM, Alin SR, Plisnier DO, Cohen AS, McKee BA. 2003. Climate change decreases aquatic ecosystem productivity of Lake Tanganyika, Africa. *Nature*, **424**, 766–768.

Paeth H, Fink AH, Pohle S, Keis F, Mächel H, Samimi C. 2010. Meteorological characteristics and potential causes of the 2007 flood in sub-Saharan Africa. *Int. J. Climatol.*, **31**, 1908–1926, DOI:10.1002/joc.2199.

Palmer TN. 2000. Predicting uncertainty in forecasts of weather and climate. *Rep. Prog. Phys.,* **63,** 71–116.

Parker DE, Jones PD, Folland CK, Bevan A. 1994. Inter-decadal changes of surface temperature since the late nineteenth century. *Journal of Geophysical Research,* **99, 14,** 373–399.

Pennell C, Reichler T. 2010. On the effective number of climate models. *Journal of Climate,* **24,** 2358–2367.

Pham DT, Dimov SS, Nguyen CD. 2003. Incremental K-means algorithm. *Proc. Instn*

Mech. Engrs, Part C: J. Mechanical Engineering Science, **218**, 783–795.

Pham DT, Dimov SS, Nguyen CD. 2005. Selection of K in K-means clustering. *Proc. IMechE* Part C: *J. Mechanical Engineering Science,* **219**, 103-119.

Pohl B, Fauchereau N, Richard Y, Rouault M, Reason CJC. 2009. Interactions between synoptic, intraseasonal and interannual convective variability over Southern Africa. *Climate Dynamics,* **33**: 1033–1050.

Pohl B, Fauchereau N, Reason CJC, Rouault M. 2010. Relationships between the Antarctic Oscillation, the Madden–Julian Oscillation, and ENSO, and consequences for rainfall analysis. *Journal of Climate,* **Vol. 23,** 238–254. DOI: 10.1175/2009JCLI2443.1

Polo I, Rodriguez-Fonseca B, Losada T, Garcia-Serrano J. 2008. Tropical Atlantic variability modes (1979-2002). Part I: time-evolving SST modes related to West African rainfall. *J. Clim.*, **21**: 6457-6475.

Pielke RA, Matsui T, Leoncini G, Nobis T, Nair US, Lu E, Eastman J, Kumar S, Peters-Lidard CD, Tian Y, Walko RL. 2006. A new paradigm for parameterizations in numerical weather prediction and other atmospheric models. *National Weather Digest,* **30,** 93–99.

Preston-Whyte RA, Tyson PD. 1988. *The Atmosphere and Weather of Southern Africa*, Oxford University Press: Cape Town.

Pyrina M, Hatzianastassiou N, Matsoukas C, Fotiadi A, Papadimas CD, Pavlakis KG, Vardavas I. 2013. Cloud effects on the solar and thermal radiation budgets of the Mediterranean basin. *Atmos. Res*. http://dx.doi.org/10.1016/j.atmosres.2013.11.009.

Randall DA, Wood RA, Bony S, Colman R, Fichefet T, Fyfe J, Kattsov V, Pitman A, Shukla J, Srinivasan J, Stouffer RJ, Sumi A, Taylor KE. 2007. Cilmate Models and Their Evaluation. In: Climate Change 2007: The Physical Science Basis. Contribution of Working Group I to the Fourth Assessment Report of the Intergovernmental Panel on Climate Change [Solomon, S., D. Qin, M. Manning, Z. Chen, M. Marquis, K.B. Averyt, M.Tignor and H.L. Miller (eds.)]. Cambridge University Press, Cambridge, United Kingdom and New York, NY, USA.

Raphael, M., 2003: Recent large scale changes in the extra-tropical southern hemisphere atmospheric circulation. *J. Clim.*, **16(17)**, 2915 – 2924.

Rasch P, Kristjánsson J. 1998. A comparison of the CCM3 model climate using a diagnosed and predicted condensate parameterizations. *J. Clim.*, **11(7)**: 1587–1614.

Rasmussen PE, Collins HP. 1991. Long-term impacts of tillage, fertilizer and crop residue on soil organic matter in temperate semiarid regions. *Advances in Agronomy,* **45**, 93-134.

Rasmusson EM, Carpenter TH. 1982. Variations in the tropical sea surface temperature and surface wind fields associated with the Southern Oscillation / El Nino. *Mon Wea Rev*, **110**: 354–384.

Ratna SB, Ratnam JV, Behera SK, Rautenbach CJW, Ndarana T, Takahashi K, Yamagata T. 2013. Performance assessment of three convective parameterization schemes in WRF for downscaling summer rainfall over South Africa. *Climate Dynamics*. DOI 10.1007/s00382-013-1918-2

Ratnam JV, Behera S, Masumoto Y, Takahashi K, Yamagata T. 2012. A simple regional coupled model experiment for summer-time climate simulation over southern Africa. *Climate Dynamics*, **39**, 2207–2217. DOI:10.1007/s00382-011-1190-2

Ratnam JV, Behera SK, Masumoto Y, Yamagata T. 2014. Remote Effects of El Nino and Modoki Events on the Austral Summer Precipitation of Southern Africa. *Journal of Climate*, **Vol. 27**: 3802-3815. DOI: 10.1175/JCLI-D-13-00431.1

Ratnam JV, Behera SK, Ratna SB, Rautenbach H, Lennard C, Luo J–J, Masumoto Y, Takahashi K, Yamagata T. 2013. Dynamical downscaling of austral summer climate forecasts over southern Africa using a simple regional coupled model. *Journal of Climate*, **26**, 6015–6032. DOI:10.1175/JCLI-D-12-00645.1

Rayner NA, Parker DE, Horton EB, Folland CK, Alexander LV, Rowell DP, Kent EC, Kaplan A. 2003. Global analyses of sea surface temperature, sea ice, and high marine air temperature since late nineteenth century. *J Geophys Res*., **108,** No D14, 4407. doi:10.1029/2002JD002670

Reason CJC, Allan RJ, Lindesay JA, Ansell TJ. 2000. Enso and Climatic Signals Across the Indian Ocean Basin in the Global Context: Part I, Inter-annual Composite Patterns. *Int. J. Climatol*. **20**: 1285–1327.

Reason CJC. 2001. Subtropical Indian Ocean SST dipole events and southern African rainfall. *Geophysical Research Letters*, **28 (11)**, 2225–2227. DOI:10.1029/2000GL012735

Reason CJC. 2002. Sensitivity of the Southern African circulation to dipole Sea-Surface Temperature patterns in the South Indian Ocean. *International Journal of Climatology* **22**: 377–393.

Reason CJC, Hachigonta S, Phaladi RF. 2005. Inter-annual variability in rainy season characteristics over the Limpopo region of southern Africa. *International Journal of Climatology*, **25,** 1835-1853. DOI: 10.1002/joc.1228

Reason CJC, Jagadheesha D. 2005. A model investigation of recent ENSO impacts over southern Africa. *Meteor Atmos Phys*, **89**, 181–205.

Redelsperger J-L, Thorncroft CD, Diedhiou A, Lebel T, Paker DJ, Polcher J. 2006. African Monsoon Multidisciplinary Analysis: An international research project and field CAM-5.1paign. *Bull. Amer. Meteor. Soc.*, **87**, 1739–1746.

Reichler T, Roads JO. 2004. Time–space distribution of long-range atmospheric predictability. *J. Atmos. Sci*., **61**, 249–263.

Reusch DB, Alley RB, Hewitson BC. 2005. Relative performance of self-organizing maps and principal component analysis in pattern extraction from synthetic climatological data. *Polar Geography*, 2005, **29**, No. 3, pp. 188–212.

Reusch DB, Alley RB, Hewitson BC. 2007. North Atlantic climate variability from a self-organizing map perspective, *J. Geophys. Res*., **112**, D02104, doi:10.1029/2006JD007460.

Richard Y, Fauchereau N, Poccard I, Rouault M, Trzaska S. 2001. 20th century droughts in Southern Africa: Spatial and temporal variability, teleconnections with oceanic and atmospheric conditions. *International Journal of Climatology,* **21,** 873–885.

Robine J-M, Cheung SLK, Le Roy S, Van Oyen H, Griffiths C, Michel J-P, Herrmann

FR. 2008. Death toll exceeded 70,000 in Europe during the summer of 2003. *Comptes Rendus Biologies,* **331**: 171–178.

Robinson PJ. 2001. On the Definition of a Heat Wave. *Journal of Applied Meteorology*, **40**, 762 – 775.

Rodriguez-Fonseca B, Janicot S, Mohino E, Losada T, Bader J, Caminade C, Chauvin F, Fontaine B, Garcia-Serrano J, Gervois S, Joly M, Polo I, Ruti P, Roucou P., Voldoire A. 2011. Interannual and decadal SST-forced responses of the West African monsoon. *Atmos Sci Lett.*, **12**: 67-74.

Rogers DJ, Hay SI, Packer MJ. 1996. Predicting the distribution of tsetse flies in West Africa using temporal Fourier processed meteorological satellite data. *Annals of Tropical Medicine and Parasitology*, **90 (3)**, 225-241.

Rotunno R and Synder C. 2008. A generalization of Lorenz's model for the predictability of flows with many scales of motion. J. Atmos. Sci., 65, 1063–1076.

Rouault M, Richard Y. 2003. Intensity and spatial extension of drought in South Africa at different time scales. *Water SA,* **29,** 489–500.

Rouault M, Richard Y. 2005. Intensity and spatial extent of droughts in southern Africa. *Geophysical Research Letters*, **32**, L15702, 4PP., 2005. DOI:10.1029/2005GL022436

Rouault M, Penven P, Pohl B. 2009a. Warming in the Agulhas Current system since the 1980's. *Geophysical Research Letters,* **36,** L12602. DOI:10.1029/2009GL037987.

Rouault M, Servain J, Reason CJC, Bourles B, Rouault MJ, Fauchereau N. 2009b. Extension of PIRATA in the tropical south-east Atlantic: An initial one-year experiment. *African Journal of Marine Science*, 31, 63–71.

Rowell DP, Folland CK, Maskell K, Ward MN. 1995. Variability of summer rainfall over tropical North Africa (1906-1992): observations and modelling. *Quart. J. Roy. Met. Soc.*, 121: 669-704.

Rowell DP. 1998. Assessing potential seasonal predictability with an ensemble of multi-decadal GCM simulations. *J. Climate*, **11**, 109–120.

Rusticucci MM, Kousky VE. 2002. A Comparative study of maximum and minimum

temperatures over Argentina: NCEP-NCAR reanalysis *versus* station data. *Journal of Climate,* **15**: 2089–2101.

Rutherford MC, Powrie LW, Schulze RE. 1999. Climate change in conservation areas of South Africa and its potential impact on floristic composition: A first assessment. *Diversity Distrib.*, **5**, 253–262.

Sachs J, Malaney P. 2002. The Economic and Social Burden of Malaria. *Nature*, **415**, 680-685. http://dx.doi.org/10.1038/415680a

Sastry N. 2002. Forest fires, air pollution and mortality in south-east Asia. *Demography,* **39(1)**: 1–23.

Schulz R, Reggia JA. 2004. Temporally asymmetric learning supports sequence processing in multi-winner self-organizing maps. *Neural Computation*, **16(3)**, 535-561.

Seefeldt MW, Hopson TM, Warner TT. 2012. A Characterization of the Variation in Relative Humidity across West Africa during the Dry Season. *Journal of Applied Meteorology and Climatology,* **51(12)**, pp. 2077-2089. doi: http://dx.doi.org/10.1175/JAMC-D-11-0196.1

Sheffield J, Andreadis KM, Wood EF, Lettenmaier DP. 2009. Global and continental drought in the second half of the twentieth century: Severity-area-duration analysis and temporal variability of large scale events. *Journal of Climate*, **22**, 1962-1981.

Singleton A, Reason CJC. 2007. Variability in the characteristics of cut-off low pressure systems over subtropical southern Africa. *International Journal of Climatology*, **27(3):** 295–310.

Smith TM, Reynolds RW, Peterson TC, Lawrimore J. 2008. Improvements to NOAA's historical Merged Land-Ocean surface temperature analysis (1880–2006). *J Clim*., **21**: 2283–2296

Söhne N, Chaboureau J-P, Guichard F. 2008. Verification of Cloud Cover Forecast with Satellite Observation over West Africa. *Monthly Weather Review*, **Volume 136,** 4421-4434. DOI: 10.1175/2008MWR2432.1

Solomon S, Qin D, Manning M, Chen Z, Marquis M, Averyt KB, et al., editors. 2007.

Climate change: The physical science basis. Contribution of Working Group I to the fourth assessment report of the Intergovernmental Panel on Climate Change. Cambridge: Cambridge University Press; 2007.

Staehelin J, Harris NRP, Appenzeller C, Eberhard J. 2001. Ozone Trends: A Review. *Reviews of Geophysics*, **39 (2)**, pages 231-290.

Stensrud DJ, Bao J-W, Warner TT. 2000. Using initial condition and model physics perturbations in short-range ensemble simulations of mesoscale convective systems. *Mon. Wea. Rev.,* **128,** 2077–2107.

Stensrud DJ, Yussouf N. 2003. Short-range ensemble predictions of 2-m temperature and dew-point temperature over New England. *Mon. Wea. Rev.,* **131,** 2510–2524.

Stewart TR, Glantz MH. 1985. Expert judgment and climate forecasting: a methodological critique of "climate change to the year 2000". *Climatic Change,* **7**, 159 –183.

Stockdale TN, Anderson DLT, Alves JOS, Balmaseda MA. 1998. Global seasonal rainfall forecasts using a coupled ocean-atmosphere model. *Nature*, **392**: 370–373.

Stott PA, Gillett NP, Hegerl GC, Karoly DJ, Stone DA, Zhang X, et al. 2010. Detection and attribution of climate change: A regional perspective. *Wiley Interdisciplinary Reviews: Climate Change*, **1(2)**, 192–211.

Stott PA, Stone DA, Allen MR. 2004. Human contribution to the European heat wave of 2003. *Nature,* **432**: 610–613.

Straus DM, Shukla J. 2005. The known, the unknown and the unknowable in the predictability of weather, Technical Report 175, Center for Ocean-Land-Atmosphere Studies, 20pp.

Su M-C, Chang H-T. 2000. Fast Self-Organizing Feature Map Algorithm. *IEEE Transactions on Neural Networks*, **Vol. 11(3)**, 721-733.

Sultan B, Janicot S. 2000. Abrupt shift of the ITCZ over West Africa and intra-seasonal variability. *Geophys. Res. Lett.,* **27**: 3353–3356.

Sultan B, Janicot S. 2003. The West African monsoon dynamics. Part II: The "preonset" and "onset" of the summer monsoon. *J. Climate,* **16**(21): 3407–3427.

Sundqvist H. 1988. *Parameterization of condensation and associated clouds in models for weather prediction and general circulation simulation. Physically-based modeling and simulation of climate and climatic change*. Springer, New York, pp 433–461.

Sutton RT, Hodson DLR. 2005. Atlantic Ocean forcing of North American and European summer climate. *Science,* **309**: 115–118.

Sylla MB, Dell'Aquila A, Ruti PM, Giorgi F. 2009. Simulation of the intraseasonal and the interannual variability of rainfall over West Africa with RegCM3 during the monsoon period. *Int. J. Climatol.,* **30**: 1865–1883, DOI: 10.1002/joc.2029.

Sylla MB, Gaye AT, Jenkins GS, Pal JS, Giorgi F. 2010. Consistency of projected drought over the Sahel with changes in the monsoon circulation and extremes in a regional climate model projections. *J. Geophys. Res.,* **115**: D16108, DOI: 10.1029/2009JD012983.

Tadross M, Jack C, Hewitson B. 2005. On RCM-based projections of change in southern African summer climate. *Geophysical Research Letters* **32**: L23713, DOI: 10.1029/2005GL024460.

Tarhule A. 2005. Damaging rainfall and flooding: the other Sahel hazards. *Clim. Change*, **72**: 355–377

Tennant W. 1999. Numerical Forecasting Of Monthly Climate In Southern Africa. *Int. J. Climatol*. **19**: 1319–1336.

Tett SFB, Stott PA, Allen MR, Ingram WJ, Mitchell JFB. 1999. Causes of twentieth century temperature change near the Earth's surface. *Nature*, **399**, 569–572.

Teyssou R, Muros-Le Rouzic E. 2007. Meningitis epidemics in Africa, a brief overview. *Vaccine*, **25S**, A3–A7.

Thompson DW, Wallace JM. 2000. Annular modes in the extratropical circulation. Part I: Month-to-month variability. *Journal of Climate*, **13**, 1000–1016.

Thompson LG, Brechera HH, Mosley-Thompsona E, Hardyd DR, Marka BG. 2009. Glacier loss on Kilimanjaro continues unabated. *Proc. Natl. Acad. Sci.*, **106**, 1–6.

Thornton SN. 2010. Thirst and hydration: physiology and consequences of dysfunction. *Physiol. Behav.*, **100(1)**: 15–21. DOI:10.1016/j.physbeh.2010.02.026

Todd M, Washington R. 1999. Circulation anomalies associated with tropical-temperate troughs in southern Africa and the south-west Indian Ocean. *Climate Dynamics*, **15**, 937 – 951.

Tomczak M, Godfrey JS. 2003. *Regional oceanography: an introduction*. 2nd ed, Daya, Delhi.

Tomczyk AM, Bednorz E. 2015. Heat waves in Central Europe and their circulation conditions. *International Journal of Climatology*. DOI: 10.1002/joc.4381

Tozuka T, Abiodun BJ, Engelbrecht FA. 2013. Impacts of convection schemes on simulating tropical-temperate troughs over southern Africa. *Clim Dyn*. DOI 10.1007/s00382-013-1738-4

Trenberth KE, Caron JM, Stepaniak DP. 2000. The atmospheric energy budget and implications for surface fluxes and ocean heat transports. *Climate Dynamics*, **17**, 259 – 276.

Troccoli A. 2010. Seasonal climate forecasting: a review. *Meteorological Applications* DOI: 10.1002/met.184.

Tschakert P. 2007. Views from the vulnerable: understanding climatic and other stressors in the Sahel. *Glob. Environ. Change*, **7**: 381–396

Tschakert P, Sagoe R, Ofori-Darko G, Codjoe SN. 2009. Floods in the Sahel: an analysis of anomalies, memory, and anticipatory learning. *Climatic Change*. DOI 10.1007/s10584-009-9776-y

Tyson P. 1987. *Climatic change and variability in Southern Africa.* Oxford University Press Southern Africa.

Tyson PD, Preston-Whyte RA. 2000. *The weather and climate of Southern Africa.* 2nd Edition. Oxford University Press Southern Africa. Cape Town.

Ujeneza EL, Abiodun BJ. 2014. Drought regimes in Southern Africa and how well GCMs simulate Them. *Climate Dynamics.* DOI 10.1007/s00382-014-2325-z

UNCTAD (United Nation Conference on Trade and Development). 2014. The Economic Development in Africa Report 2014: Catalysing Investment for Transformative Growth in Africa. United Nations publication. UNCTAD/ALDC/AFRICA/2014.

New York and Geneva. Available via http://unctad.org/en/PublicationsLibrary /aldcafrica2014_en.pdf

UNDESA-PD (United Nations Department of Economic and Social Affairs – Population Division). 2013. World Population Prospects: The 2012 Revision, Volume II, Demographic Profiles (ST/ESA/SER.A/345). Available via http://esa.un.org/wpp/ Documentation/pdf/WPP2012_Volume-II-Demographic-Profiles.pdf

UNDP (United Nations Development Programme). 2005. Human Development Report 2005: International cooperation at a crossroads. Aid, trade and security in an unequal world. New York: United Nations Development Programme. ISBN 0-19-530511-6. Available via http://hdr.undp.org/sites/default/files/reports/266/hdr05_ complete.pdf

UNDP (United Nations Development Programme). 2011. Drought risk management in southern Africa. Available via http://web.undp.org/drylands/docs/drought/ AADAF1/1.7.Garanganga.pdf. Date last accessed July 29, 2014.

Unganai LS. 1994. Drought and Southern Africa: A Note from the Harare Regional Drought Monitoring Centre. Available on http://drought.unl.edu/archive/dnn-archive/arch18.pdf. Date last accessed January 29, 2014.

Vardavas IM, Taylor FW. 2011. Radiation and Climate: Atmospheric Energy Budget from Satellite Remote Sensing, International Series of Monographs on Physics 138. Oxford University Press, Oxford.

Verburg P, Kecky RE, Kling H. 2003. Ecological consequences of a century of warming in Lake Tanganyika. *Science*, **301**, 505–507.

von Storch H, Langenberg H, Feser F. 2000. A spectral nudging technique for dynamical downscaling purposes. *Mon. Wea. Rev*., **128**, 3664-3673.

Waha K, Müller C, Rolinski S. 2013. Separate and combined effects of temperature and precipitation change on maize yields in sub-Saharan Africa for mid- to late-21st century. *Global and Planetary Change*, **106**: 1–12. http://dx.doi.org/10.1016/j.gloplacha.2013.02.009

Wanner H, Brönnimann S, Casty C, Gyalistras D, Luterbacher J, Schmutz C, Stephenson

DB, Xoplaki E. 2001. North Atlantic Oscillation – Concepts and Studies. *Surveys in Geophysics,* **22**: 321–382.

Ward MN. 1998. Diagnosis and short-lead time prediction of summer rainfall in tropical north Africa at inter-annual and multi-decadal timescales. *Journal of Climate,* **11**: 3167–3191.

Washington R, Downing TE. 1999. Seasonal forecasting of African rainfall: problems and prospects. *Geogr J*., **165**: 255–274.

Washington R, Preston A. 2006. Extreme wet years over southern Africa: Role of Indian Ocean sea surface temperatures. *Journal of Geophysical Research*, **111**, D15104, DOI:10.1029/2005JD006724

Weigel AP, Liniger MA, Appenzeller C. 2006. The Discrete Brier and Ranked Probability Skill Scores. Monthly *Weather Review*, **135**, 118-124.

WHO (World Health Organization). 1998. Cholera in 1997. *Weekly Epidemiological Record,* **73:** 201–208.

WHO (World Health Organization). 2008. Floods in West Africa raise major health risks. News release August 19, 2008. Available via http://www.who.int/mediacentre /news/releases/2008/pr28/en/index.html. Accessed on 23 July, 2015.

WHO (World Health Organization). 2013. WHO Global Malaria Programme, World Malaria Report. WHO Press, World Health Organization, Geneva.

Wilks DS. 1995. Statistical methods in Atmospheric Sciences: An introduction. Geophy. Series, Second Edition, Academic Press Inc., California, 254 – 275pp.

Williams CJR, Kniveton DR, Layberry R. 2008. Influence of South Atlantic sea surface temperatures on rainfall variability and extremes over southern Africa. *Journal of Climate,* **21**, 6498–6520.

WMO (World Meteorological Organization). 1990a. Report of the International Ozone Trends Panel – 1988. Global Ozone Research and Monitoring Project, Rep. 18, Geneva, Switzerland.

WMO (World Meteorological Organization). 1990b. Scientific Assessment of Stratospheric Ozone – 1989. Global Ozone Research and Monitoring Project, Rep. 20, Geneva, Switzerland.

WMO (World Meteorological Organization). 1992. Scientific Assessment of Ozone Depletion – 1991. Global Ozone Research and Monitoring Project, Rep. 25, Geneva, Switzerland.

WMO (World Meteorological Organization). 2012. Guidelines on Ensemble Prediction Systems and Forecasting. WMO-No 1091.

Wolter K, Timlin MS. 2011. El/Nino Southern Oscillation behavior since 1871 as diagnosed in an extended multivariate ENSO index. *Int J of Climatol*., **31**: 1074–1087. DOI: 10.1002/joc.2336

World Bank. 2006. World Development Report 2005: Equity and Development. Washington: ISBN-10: 0-8213-6412-X. Available via http://siteresources.world bank.org/ INTWDR 2006 /Resources/477383-1127230817535/082136412X.pdf

Wu R, Yang S, Liu S, Sun L, Lian Y, Gao Z. 2010. Changes in the relationship between northeast China summer temperature and ENSO. *J. Geophys. Res.* **115**: D21107, DOI: 10.1029/2010D014422.

Xie S-P, Hu K, Hafner J, Tokinaga H, Du Y, Huang G, Sampe T. 2009. Indian Ocean capacitor effect on Indo–western Pacific climate during the summer following El Nino. *J. Clim.* **22**: 730–747.

Xue Y, De Sales F, Lau WM, Boone A, Feng J, Dirmeyer P, Wu MLC. 2010. Intercomparison and analyses of the climatology of the West African Monsoon in the West African Monsoon Modeling and Evaluation project (WAMME) first model intercomparison experiment. *Climate Dynam.,* **35(1)**: 3–27.

Yarnal B. 1993. *Synoptic Climatology in Environmental Analysis*. Belhaven Press: London.

Zebiak SE, Orlove B, Muñoz AG, Vaughan C, Hansen J, Troy T, Thomson MC, Lustig A, Garvin S. 2014. Investigating El Niño-Southern Oscillation and society relationships. *WIREs Climate Change,* **6 (1)**. 17-34. DOI: 10.1002/wcc.294

Zhang C, Woodworth P, Gu G. 2006. The seasonal cycle in the lower troposphere over West Africa from sounding observations. *Q. J. R. Meteorol. Soc.,* **132**, pp. 2559–2582. DOI: 10.1256/qj.06.23

Zhang F, Snyder C, Rotunno R. 2003. Effects of moist convection on mesoscale

predictability. *J. Atmos. Sci.*, **60(9)**: 1173–1185.

Zhang G, McFarlane N. 1995. Sensitivity of climate simulations to the parameterization of cumulus convection in the Canadian Climate Centre general circulation model. *Atmos. Ocean*, **33**.

Zhang X, Zwiers FW, Hegerl GC, Lambert FH, Gillett NP, Solomon S, Stott PA, Nozawa T. 2007. Detection of human influence on twentieth-century precipitation trends. *Nature*, **448**: 461-466. DOI:10.1038/nature06025

Zwiers FW. 1996. Interannual variability and predictability in an ensemble of AMIP climate simulations conducted with the CCC GCM2, *Climate Dynamics,***12**, 825-847.